Angular analysis of the $B_d^0 \to K^{*0}\mu^+\mu^-$ decay with the ATLAS experiment.

Tamsin Nooney

Submitted in partial fulfillment of the requirements of the Degree of
Doctor of Philosophy

Supervisor: Dr Adrian Bevan

Particle Physics Research Centre
School of Physics and Astronomy
Queen Mary University of London

May 2017

Declaration of Authorship

I, Tamsin Nooney, confirm that the research included within this thesis is my own work or that where it has been carried out in collaboration with, or supported by others, that this is duly acknowledged below and my contribution indicated. Previously published material is also acknowledged below.

I attest that I have exercised reasonable care to ensure that the work is original, and does not to the best of my knowledge break any UK law, infringe any third partys copyright or other Intellectual Property Right, or contain any confidential material.

I accept that the College has the right to use plagiarism detection software to check the electronic version of the thesis.

I confirm that this thesis has not been previously submitted for the award of a degree by this or any other university.

The copyright of this thesis rests with the author and no quotation from it or information derived from it may be published without the prior written consent of the author.

Signature: Date:

I was not involved in the design and construction of the ATLAS experiment; discussion of the experiment in Chapter 3 is included to provide the context for the description of the measurements in subsequent chapters. The production of the data, including the implementation of the event and trigger selection described in Chapter 4, was performed by other members of the analysis group. The reconstruction algorithms employed are attributed to other ATLAS subgroups, as referenced in the text.

The mistag fractions determined from MC are not my own work but the results are included to ensure the evaluation of the results and systematics are adequately described. Various aspects of the fit validation process are not my work, indicated in Sec. 6.3 where relevant. In particular the fits to the control sample MC are not my work but are included to support the work in Chapters 6 through 9.

Acknowledgements

First and foremost I would like to thank my supervisor Adrian Bevan for his continuous support over the past four years. His knowledge and guidance have been truly invaluable throughout my PhD and his blind eye to my travel budget greatly appreciated.

I'd like to extend my gratitude to all those in the ATLAS Rare Decays group for their helpful insight. Special thanks to Ina Carli, Pavel Reznicek and Semen Turchikhin for their vital contributions to this analysis.

I would also like to thank everyone in the PPRC, who have all at some point provided advice, a laugh or a beer when needed. In particular my appreciation goes to Marcella Bona who has helped me in both my analysis and service work on ATLAS.

For their unwavering friendship, even in the face of physics pub talk, I would like to thank Alice Cady, Hannah Carnegy, Alice Grant and Becky Kew.

Thanks also goes to my brilliant army of parents, siblings and niblings: Kay Nooney, Imogen Elsey, Dominic Nooney, Stacey Williams, Zoe Williams, Grace Elsey, Rose Elsey, Dixie Lee, Dot Lee, Thurston Jepps and Harper Jepps. Each have been a great inspiration and morale booster; I hope this mention makes up for some of my absences this past year, as I don't think the subsequent pages will.

Finally I'd like to thank Carl Jeske who bravely took the brunt of my tedious chat, debugging dramas and existential crises whilst offering nothing but calming support and homemade dinners in return. I owe you much more than curry, but it's a good place to start.

Angular analysis of the $B_d^0 \to K^{*0}\mu^+\mu^-$ decay with the ATLAS experiment.

Abstract

An angular analysis of $B_d^0 \to K^0(\to K^+\pi^-)\mu^+\mu^-$ is presented using 20.3 fb^{-1} of pp collision data collected at $\sqrt{s} = 8\ TeV$ with the ATLAS experiment. The angular observables F_L and $S_{3,4,5,7,8}$ were extracted in six bins of q^2, the invariant mass squared of the dimuon system, within the full range $0.04 < q^2 < 6.00\ (GeV/c^2)^2$. The observables were determined from an unbinned maximum likelihood fit using four folded parameterisations of the full angular distribution. The fit results were used to obtain corresponding values for the optimised observables P_1 and $P'_{4,5,6,8}$. The results presented are compatible with Standard Model predictions.

Contents

List of Figures

List of Tables

Chapter 1

Introduction

Our understanding of fundamental particle physics and how it has shaped the world we live in continues to expand, but is not yet complete. The motivation behind any particle physics experiment is to fill these gaps in our knowledge in order to better understand the nature of matter, how the Universe has evolved, what governs it today and its ultimate fate.

Our current understanding of fundamental particles and their interactions is encapsulated in the Standard Model (SM) of particle physics. The foundations of the SM were developed in the mid 1970s [1, 2] and since then nearly all particle physics experimental measurements have either been explained or precisely predicted by SM theory.

Notable accomplishments of the SM include most recently the discovery of the Higgs boson. This was first hypothesised in 1964 [3–5] and was subsequently discovered at the Large Hadron Collider (LHC) [6] in 2012 [7, 8], confirming the origin of the mass of fundamental particles in the SM (see Section 2.1.3). This directly resulted in the Nobel prize in physics, shared between Peter Higgs and Franois Englert for "the theoretical discovery of a mechanism that contributes to our understanding of the origin of mass of subatomic particles" [9]. In addition to the Higgs boson, the SM has been able to predict a number of observables with high precision including the W and Z boson masses[1] [10, 11] and the anomalous

[1] The SM predictions of the W and Z boson masses are (80.390±0.018) GeV/c^2 and (91.1874± 0.0021) GeV/c^2 respectively. The corresponding experimentally measured values are (80.387 ± 0.019) GeV/c^2 and (91.1876 ± 0.0021) GeV/c^2, demonstrating a great technical triumph.

magnetic dipole moment of the electron, a prediction that has a precision better than one part in 10^9 [12].

Despite the overall success of the SM, there are still some holes in the theory. Four fundamental forces are currently known: electromagnetic, weak, strong and gravitational. The SM describes three of these forces, but a theory in which gravity is also incorporated has not yet been established. Furthermore, whilst the SM accounts for all the visible elementary matter, this is believed to constitute only about 5% of the Universe. The rest, which is presently split into approximately 27% dark matter and 68% dark energy, is yet to be understood [13]. A similar question mark resides over the asymmetry seen between matter and antimatter.

All of these open questions point to the existence of new particles, beyond the SM (BSM), which could be discovered and studied at a high energy particle collider. One method to detect new particles at a particle collider is through indirect searches via flavour physics.

An experiment proposed for such searches was the Super$B$ experiment, a project based on the construction of a high luminosity asymmetric electron-positron accelerator [14]. The project was designed as a flavour factory at which physics studies of B, D and Υ meson, and τ lepton decays could be performed in order to precisely measure SM physics as well as study any BSM physics encountered.

The Super$B$ experiment was cancelled at the end of 2012, before detector construction, as a result of economic stability issues found in Europe and consequently all related analyses were terminated. Before its cancellation, a short study into the potential decays that could be studied at the Super$B$ accelerator was performed as part of this PhD, but is not presented in this thesis.

The construction of the Super$B$ detector would have required a low noise pixel vertex detector, able to make fast measurements and withstand the harsh environments of a particle detector. In addition to looking into potential physics analyses on the Super$B$ experiment, a study into a new type of pixel detector with the Arachnid collaboration [15] was performed as part of this PhD.

Arachnid is an R&D programme concentrating on a Complementary Metal Oxide Semiconductor Monolithic Active Pixel Sensor (CMOS MAPS) device called Cherwell [16]. The Cherwell sensor has a wide range of scientific applications and thus this research continued beyond the cancellation of the Super$B$ experiment.

The first experimental results of this sensor were obtained through analysing data from a test-beam at the LHC. These results are not documented here but are summarised in Ref. [17].

This thesis instead focuses on the decay of $B_d^0 \to K^{*0}\mu^+\mu^-$, a flavour physics analysis performed with the ATLAS (A Toroidal LHC ApparatuS) experiment [18] at the LHC. The angular analysis of $B_d^0 \to K^{*0}\mu^+\mu^-$ provides an opportunity to search for new physics, as described in the theoretical overview in Chapter 2.

Chapter 3 describes the LHC and the ATLAS experiment, in particular detailing each of the ATLAS detector components and how they're used for particle detection are given.

The $B_d^0 \to K^{*0}\mu^+\mu^-$ signal events were identified through the vast amount of data saved by the ATLAS experiment. The steps involved in the event selection are given in Chapter 4. The analysis presented here is the second iteration of a $B_d^0 \to K^{*0}\mu^+\mu^-$ angular analysis performed by the ATLAS experiment. Unfortunately problems found in the software meant that the previous analysis using data collected in 2011 was retracted. However, results from the studies performed in the 2011 analysis relating to the event selection have been utilised here.

A description of the background decay modes studied is shown in Chapter 5 and the various techniques used for fitting the collected and simulated data are shown in Chapter 6, including the fit models adopted and their respective validation procedures. Mass fits to the data are documented in Chapter 7. A breakdown of the systematic uncertainties considered in this analysis and their combined contribution are given in Chapter 8. The final results obtained and their comparison with other experimental and theoretical results are given in Chapter 9. A discussion on future work is given in Chapter 10 and the thesis is summarised in Chapter 11.

Additional work was undertaken with the ATLAS semiconductor tracker group as part of an authorship qualification task. This was comprised of installing new off detector optical transmitters and subsequent optical studies to monitor their performance. Smaller tasks in updating the software used for Lorentz angle measurements were also carried out. These service tasks are not discussed further in this thesis.

Chapter 2

Theoretical Overview

This chapter outlines the theory behind the $B_d^0 \to K^{*0}\mu^+\mu^-$ decay and how it's angular distribution can be measured for the purposes of searching for new physics. The basic principles of the SM are outlined in Section 2.1, details of flavour physics are given in Section 2.2 and the measurements made in this angular analysis are described in Section 2.3.

2.1 The Standard Model of Particle Physics

The objective of particle physics is to understand the basic structure and laws in nature, all the way from the largest systems in the Universe to the smallest dimensions. At the smallest scale, there are two classes of fundamental particles, *quarks* and *leptons*, whose interactions are mediated by several *gauge bosons*.

The SM consists of six leptons that are classified according to their charge, electron number L_e, muon number L_μ and tau number L_τ. This classification naturally places them into three generations, as shown in Table 2.1.

Similarly, there are six 'flavours' of quarks: **u**p, **d**own, **s**trange, **c**harm, **b**ottom, and **t**op. These too are grouped into three generations, as given in Table 2.2.

Quarks and leptons are both half integer spin particles ($S = \pm\frac{1}{2}$) belonging to the larger group named *fermions*. Here spin refers to the intrinsic form of angular momentum for all elementary particles. Within the quantum state, the $\pm$ corresponds to the direction in which the spin is pointing and is often referred

TABLE 2.1: A breakdown of selected properties of the three generations of leptons. The charges, denoted by Q, are given in units of e, the absolute value of the electric charge carried by a single electron. All masses quoted are taken from the Particle Data Group [19]. † In the SM all neutrinos are described as massless particles, however in 2015 neutrino oscillations were observed, demonstrating this not to be the case. This discovery led to the 2015 Nobel Prize in Physics being awarded to Takaaki Kajita of the Super-Kamiokande Collaboration and Arthur B. McDonald of the Sudbury Neutrino Observatory Collaboration [20]. The mass of the neutrino is still believed to be extremely small however, so can be approximated as massless for the purpose of this thesis.

1^{st} generation	2^{nd} generation	3^{rd} generation
electron	muon	tau
e	μ	τ
$Q = -1$	$Q = -1$	$Q = -1$
$m_e = 0.511\ MeV/c^2$	$m_\mu = 0.106\ GeV/c^2$	$m_\tau = 1.777\ GeV/c^2$
electron neutrino	muon neutrino	tau neutrino
ν_e	ν_μ	ν_τ
$Q = 0$	$Q = 0$	$Q = 0$
$m_{\nu_e} = 0\ GeV/c^2$ †	$m_{\nu_\mu} = 0\ GeV/c^2$ †	$m_{\nu_\tau} = 0\ GeV/c^2$ †

TABLE 2.2: A breakdown of selected properties of the three generations of quarks. The charges, denoted by Q, are given in units of e, the absolute value of the electric charge carried by a single electron. All masses quoted are taken from the Particle Data Group [19].

1^{st} generation	2^{nd} generation	3^{rd} generation
up	charm	top
u	c	t
$Q = \frac{2}{3}$	$Q = \frac{2}{3}$	$Q = \frac{2}{3}$
$m_u = 2.2\ MeV/c^2$	$m_c = 1.67\ GeV/c^2$	$m_t = 173.34\ GeV/c^2$
down	strange	bottom
d	s	b
$Q = 0$	$Q = 0$	$Q = 0$
$m_d = 4.7\ MeV/c^2$	$m_s = 96\ MeV/c^2$	$m_b = 4.78\ GeV/c^2$

to as 'spin up' or 'spin down'. In addition to the particles listed in Tables 2.1 and 2.2, each fermion has its own antiparticle. Antiquarks and antileptons have the same intrinsic properties in magnitude as their particle partners, but many quantum numbers, such as charge and strangeness, have a reversed sign. Here the strangeness quantum number describes the decay of particles in strong and

electromagnetic interactions. It is defined as the sum of the strangeness of its constituent strange quarks (antiquarks), where $s(\overline{s})$ has strangeness $S = -1(+1)$. All other quark flavours have zero strangeness.

Bound states of quarks are called *hadrons* and can be classified into one of three sub categories, *mesons*, *baryons* or *antibaryons*, each with integer charge. Mesons are composed of one quark and one antiquark, distinct from baryons, which are made up of three quarks, and antibaryons, made up of three antiquarks. The quantum number 'baryon number', B, is assigned to all fundamental particles and is normalised such that baryons have $B = 1$. Subsequently, each quark has $B = \frac{1}{3}$, each antiquark $B = -\frac{1}{3}$, and each lepton $B = 0$.

As well as the individual particles, the SM describes three forces or *gauge fields*: the electromagnetic, weak and strong interactions are mediated by different gauge bosons, all with spin $S = 1$.

The SM has been able to withstand decades of experimental tests, but it also has an aesthetic appeal in its invariance under local gauge transformations. At its foundation, the dynamics of the SM are governed by the Lagrangian density, a function of the fields and their position and time derivatives, which is both Lorentz and gauge invariant. The term gauge refers to the redundant degrees of freedom in the Lagrangian and thus local gauge transformations act independently at each space-time point, changing the potential but having no effect on the fields. Every symmetry innately yields a conservation law and conversely every conservation law reflects an underlying symmetry [21]. A full description of the SM local gauge symmetries is beyond the scope of this thesis, but key points related to the angular analysis of $B^0_d \to K^{*0}\ \mu^+\ \mu^-$ are noted when describing each interaction.

2.1.1 Electromagnetic Interaction

The electromagnetic field is described within the quantum field theory 'Quantum Electrodynamics' (QED), which is invariant under $U(1)$ gauge transformations, for charged spin-$\frac{1}{2}$ particles. Electromagnetic interactions are mediated by the electromagnetic gauge boson, the photon, denoted by γ. In quantum field theory, interactions can be described by adding an additional interaction term, $\mathcal{L}_{int}$, to

the Lagrangian density such that:

$$\mathcal{L} = \mathcal{L}_0 + \mathcal{L}_{int}. \tag{2.1}$$

Here, $\mathcal{L}_0$ is the Dirac Lagrangian density, which describes the kinematics of free fermions as:

$$\mathcal{L}_0 = i\overline{\psi}\gamma^\mu\partial_\mu\psi - m\overline{\psi}\psi, \tag{2.2}$$

where ψ is the fermion field ($\overline{\psi} = \psi^\dagger\ \gamma^0$ is the adjoint spinor), m the fermion mass, $\partial_\mu \equiv \partial/\partial x^\mu$ for the space-time 4-vector x^μ and γ^μ a set of 4×4 matrices that encompass the Pauli matrices σ_i, where $i = 1, 2, 3$.

Local gauge transformations of the form $\psi(x) \rightarrow \psi^{'}(x) = e^{iQ\omega(x)}\psi(x)$ break the gauge invariance of the Lagrangian density in Eq. (2.2). Here, the parameter Q is the charge of the particle involved, whilst $\omega(x)$ are real parameters that depend on the space-time point x. Gauge invariance can be restored by introducing the covariant derivative, D_μ, through which the gauge field and matter interact as

$$D_\mu = \partial_\mu - ieA_\mu. \tag{2.3}$$

The addition of D_μ assumes an interaction between the fermion field and a spin-1 gauge field, A_μ. The new gauge field represents the photon, which transforms as

$$A_\mu \rightarrow A_\mu^{'} = A_\mu - \frac{1}{e}\partial_\mu Q\omega(x) \tag{2.4}$$

under a local gauge transformation. The kinetic term for free photons is constructed from the field strengths $F_{\mu\nu}$, as defined in:

$$\mathcal{L}_{int} = -\frac{1}{4}F_{\mu\nu}F^{\mu\nu}. \tag{2.5}$$

The matrix $F_{\mu\nu}$ can be defined in terms of the commutator of covariant derivatives and consequently is gauge invariant. In the case of QED, $F_{\mu\nu}$ can be expressed as

$$F_{\mu\nu} = \partial_\mu A_\nu - \partial_\nu A_\mu. \tag{2.6}$$

The complete QED Lagrangian, $\mathcal{L}_{QED}$ takes the form

$$\mathcal{L}_{QED} = \overline{\psi}(i\gamma^\mu\partial_\mu - m)\psi + e\overline{\psi}\gamma^\mu\psi Q A_\mu - \frac{1}{4}F_{\mu\nu}F^{\mu\nu}, \tag{2.7}$$

where the term $e\overline{\psi}\gamma^{\mu}\psi Q A_{\mu}$ is treated as a perturbation. A mass term for the electromagnetic gauge boson is forbidden, as a term proportional to $A_{\mu}A^{\mu}$ is not invariant under gauge transformations, thus the photon is massless.

2.1.2 Weak Interaction

The weak interaction is described by a field theory with an underlying $SU(2)_L$ symmetric gauge group, where $SU(n)$ groups refer to the restricted collection of unitary matrices for which the determinant is 1, 'S' stands for 'special' and the subscript L denotes a left-handed *chirality*. The handedness of a particle (left or right) stems from its *helicity*, the direction of a particle's spin relative to its direction of motion. Helicity itself isn't an intrinsic quantum number, as for particles with mass it can be left or right handed depending on the reference frame. Chirality defines a separate property, independent of reference frame; although in the massless limit, a particle's chirality and helicity are equivalent.

The weak force is mediated by three massive vector bosons: two charged bosons, W^+ and W^-, and a neutral boson, Z^0. Experimentally the weak gauge bosons are observed to couple to left handed fermions only, maximally violating *parity* P, an operation defined as the spatial inversion around the origin, where $x' = -x$, $y' = -y$, $z' = -z$ and $t' = t$.

In order to accommodate the parity violation observed in weak interactions, vector currents are extended to have a pseudo-vector component for which parity is invariant. The left and right handed fermion fields are hence be expressed in terms of the projection operators of the chirality states of the fermion, P_L and P_R, respectively as

$$\psi_L = P_L\psi = \frac{1}{2}(1-\gamma^5)\psi \tag{2.8a}$$

$$\psi_R = P_R\psi = \frac{1}{2}(1+\gamma^5)\psi, \tag{2.8b}$$

where γ^5 is defined as the product of the time and space-like matrices in Dirac representation, $\gamma^5 = i\gamma^0\gamma^1\gamma^2\gamma^3$.

The quantum number *weak isospin*, T, is defined as a vector in isospin-space with components T_1, T_2 and T_3. The third component of weak isospin, T_3, is $\pm\frac{1}{2}$ for

left handed fermions, zero for right handed fermions and ± 1 for W bosons. Weak isospin and charge are related by an additional quantum number *hypercharge*, Y, as $Q = T_3 + \frac{1}{2}Y$. Quarks are therefore represented by left handed isospin doublets of $SU(2)$, q_L, with hypercharge $Y = 1/6$ and right handed isospin singlets of $SU(2)$, u_R and d_R with $Y = 2/3$ and $-1/3$, respectively, as in Eq. (2.9):

$$q_L = \left(\begin{pmatrix} u_L \\ d_L \end{pmatrix}, \begin{pmatrix} c_L \\ s_L \end{pmatrix}, \begin{pmatrix} t_L \\ b_L \end{pmatrix} \right) \qquad u_R = (u_R, c_R, t_R) \qquad d_R = (d_R, s_R, b_R). \quad (2.9)$$

The kinetic and interaction terms of the Dirac Lagrangian density can hence be split into left and right handed fermionic parts using the relation:

$$\psi = \psi_L + \psi_R. \quad (2.10)$$

The $SU(2)_L$ gauge transformation under which $\mathcal{L}_0$ is invariant is given by Eq. (2.11), in which α_i are real parameters, $\frac{\sigma_i}{2}$ are the generators of the group and

$$\psi_L \rightarrow \psi_L^{'} = e^{i\alpha_i \frac{\sigma_i}{2}} \psi_L. \quad (2.11)$$

In order to retain the local gauge invariance of the Lagrangian, a new covariant derivative is introduced, defined by Eq. (2.12). The gauge fields W_μ^i, where $i = 1$, 2, 3, are introduced to the $SU(2)_L$ gauge symmetry with coupling g:

$$D_\mu = \partial_\mu - ig\frac{\sigma_i}{2} W_\mu^i. \quad (2.12)$$

The local $SU(2)_L$ gauge transformation becomes:

$$W_\mu^i \rightarrow W_\mu^{i'} = W_\mu^i g \epsilon_{ijk} \Delta^j W_\mu^k + \partial_\mu \Delta^i, \quad (2.13)$$

where $\Delta(x) = (\Delta^1(x), \Delta^2(x), \Delta^3(x))$ and ϵ_{ijk} is the Levi-Civita symbol. The complete weak interaction Lagrangian, $\mathcal{L}_W$, is described by

$$\mathcal{L}_W = \overline{\psi}(i\gamma^\mu \partial_\mu)\psi + g\overline{\psi}\gamma^\mu \sigma_i \psi W_\mu^i - \frac{1}{4} W_{\mu\nu}^i W_i^{\mu\nu}. \quad (2.14)$$

Analogous to the QED Lagrangian, the mass term in the weak Lagrangian is not invariant under $SU(2)_L$ symmetry, indicating massless gauge bosons. However, the world averaged masses of the W and Z bosons are $(80.385 \pm 0.015)\ GeV/c^2$ and $(91.1876 \pm 0.0021)\ GeV/c^2$, respectively [19]. Electromagnetism and the weak force can be combined in a non trivial way to give a unified 'electroweak' theory in

which weak gauge bosons acquire masses through electroweak symmetry breaking.

2.1.3 Electroweak Sector

Electroweak theory is based on an $SU(2)_L \times U(1)_Y$ structure where the generators in $U(1)_Y$ commute with those of $SU(2)_L$. Here the subscript Y differentiates the gauge group of hypercharge from that of QED, $U(1)$.

Two covariant derivatives maintain gauge invariance of the $SU(2)_L \times U(1)_Y$ Lagrangian density, as shown for left and right handed fermions in Eq. (2.15). The gauge field B_μ is analogous to the A_μ field in Section 2.1.1, W_μ^i are the $SU(2)_L$ fields, $g^{'}$ is the $SU(2)$ coupling of the fermionic field to the gauge field and $Y^{L,R}$ represent the left handed isospin doublet and right handed isospin singlet hypercharges:

$$D_{\mu,L} = \partial_\mu - igW_\mu^i - ig^{'}Y^L B_\mu \tag{2.15a}$$

$$D_{\mu,R} = \partial_\mu - ig^{'}Y^R B_\mu. \tag{2.15b}$$

The W_μ^i and B_μ boson fields transform into the physical boson fields $W_\mu^\pm$, Z_μ and A_μ, by:

$$W_\mu^\pm = \frac{1}{\sqrt{2}}(W_\mu^{(1)} \mp W_\mu^{(2)}), \tag{2.16}$$

$$W_\mu^{(3)} = \frac{gZ_\mu + g'A_\mu}{\sqrt{g^2 + g'^2}} \text{ and} \tag{2.17}$$

$$B_\mu = \frac{-g'Z_\mu + gA_\mu}{\sqrt{g^2 + g'^2}}. \tag{2.18}$$

It can be shown that $W_\mu^{(3)}$ and B_μ are an orthogonal mixture of Z_μ and A_μ with weak mixing angle θ_W:

$$\begin{pmatrix} W_\mu^{(3)} \\ B_\mu \end{pmatrix} = \begin{pmatrix} \cos\theta_W & \sin\theta_W \\ -\sin\theta_W & \cos\theta_W \end{pmatrix} \begin{pmatrix} Z_\mu \\ A_\mu \end{pmatrix}. \tag{2.19}$$

The complete electroweak Lagrangian, $\mathcal{L}_{EW}$, is given by

$$\mathcal{L}_{EW} = i\overline{\psi}_L\gamma^\mu D_{\mu,L}\psi_L + i\overline{\psi}_R\gamma^\mu D_{\mu,R}\psi_R - \frac{1}{4}W_{\mu\nu}^i W_i^{\mu\nu} - \frac{1}{4}B_{\mu\nu}B^{\mu\nu}. \tag{2.20}$$

For an $SU(2)_L \times U(1)_Y$ gauge invariant theory, no mass terms are allowed in the Lagrangian density. Under a local gauge transformation of the form $B_\mu \rightarrow B'_\mu = B_\mu + \partial_\mu \Lambda$ for some scalar function Λ, the inclusion of a mass term would lead to $\frac{1}{2}M_B^2 B_\mu B^\mu \neq \frac{1}{2}M_B^2 B'_\mu B'^\mu$. Similarly a mass term for the field W_μ^i, $M_W^2 W_\mu W^\mu$, under the $SU(2)_L$ transformation in Eq. (2.13) would not be invariant. Furthermore, fermionic masses aren't possible without some form of gauge symmetry breaking, owing to the different transformation properties of left and right handed fields, as seen in Eq. (2.15).

The mass terms are generated through the concept of Spontaneous Symmetry Breaking (SSB) via the Higgs mechanism [3–5], which leads to three originally massless gauge fields becoming massive. The details of SSB are not given in this thesis, but an immediate consequence of the theory is that the vector boson masses, given in Eq. (2.21), satisfy the relation $\frac{M_W}{M_Z} = \cos\theta_W$. Here v is the constant vacuum expectation value of the Higgs scalar operator and

$$\begin{aligned} M_W &= \frac{1}{2}gv, \\ M_Z &= \frac{1}{2}\frac{gv}{\cos\theta_W}. \end{aligned} \tag{2.21}$$

2.1.4 Strong Interaction

The dynamics of the strong interaction reside in the quantum field theory, known as Quantum Chromodynamics (QCD). The interaction is mediated by massless gluons, g, which carry the quantum number 'colour', a feature also attributed to quarks.

Within QCD the strong force can be formulated as a field theory with underlying gauge group $SU(N_C)$ with $(N_C^2 - 1)$ corresponding gluons. Experimentally N_C has been found to be equal to three, and the quark fields defined as carrying colours red, green and blue (R, G and B) with eight gluons corresponding to the distinct colour-anticolour combinations. Accordingly the quark fields of flavour f can be described by vectors in colour space $q_f^C \equiv (q_f^R, q_f^G, q_f^B)$. The free Lagrangian density,

$$\mathcal{L}_0 = \sum_f \overline{q}_f (i\gamma^\mu \partial_\mu - m_f) q_f, \tag{2.22}$$

is invariant under global $SU(3)_C$ transformations. The covariant derivative attributed to restoring invariance under local $SU(3)_C$ transformations of the form

$q_f \to q_f^{'} = e^{i\frac{\lambda^a}{2}\omega(x)} q_f$ is given by

$$D_\mu = \partial_\mu - ig_s \frac{\lambda^a}{2} G_\mu^a(x), \tag{2.23}$$

in which g_s is the strong coupling, $\frac{1}{2}\lambda^a$ (a = 1, 2,...,8) the generators of $SU(3)_C$, where λ^a are the Gell-Mann λ-matrices, and G_μ^a the gauge field representing the eight gluons. The final QCD Lagrangian, $\mathcal{L}_{QCD}$, is given by

$$\mathcal{L}_{QCD} = \sum_f \overline{q}_f (i\gamma^\mu D_\mu - m_f) q_f - \frac{1}{4} G_a^{\mu\nu} G^a_{\mu\nu}. \tag{2.24}$$

Assembling all the pieces outlined above presents a SM Lagrangian based on the local gauge symmetry G_{SM}, given by Eq. (2.25), that describes QCD, the chiral $SU(2)_L$ electroweak sector and the hypercharge $U(1)_Y$ sector in which QED is embedded. For the angular analysis of $B_d^0 \to K^{*0}\mu^+\mu^-$, the $SU(3)_C$ symmetry doesn't play a significant role and so shall not be elaborated upon. The $SU(2)_L \times U(1)_Y$ electroweak symmetry determines interactions that permit flavour changing decays of quarks, discussed further in Section 2.2.

$$G_{SM} = SU(3)_c \times SU(2)_L \times U(1)_Y \tag{2.25}$$

2.2 Flavour Physics

Flavour physics aptly refers to the study of different types of quarks in consideration of their flavours, from their unique characteristics to the interactions and transmutations between them. Understanding these processes can lead to stringent constraints on the SM as well as any new models. Specifically, processes in which the flavour quantum number (u, d, s, c, b, t) changes can be used as tools to explore the limits of the SM, and in searches for new physics beyond the SM (BSM). Moreover, charge-parity (CP) violation stems from flavour changing interactions, cementing the importance of the measurements made in flavour physics.

In the SM, the flavour quantum number is conserved in electromagnetic and strong interactions, as well as in neutral current weak processes involving the exchange of a Z^0 boson. In the SM, flavour can only be changed in charged current weak

processes in which either a W^- or W^+ boson is exchanged between an up-type and down-type quark or an anti-up-type and anti-down-type quark, respectively.

2.2.1 Cabibbo-Kobayashi-Maskawa Matrix

Whilst flavour changing is allowed in charged current weak processes in the SM, the relative strength of the weak interaction means the different flavours are approximately conserved. The differences in decay rates between quark flavours are interpreted in the Glashow-Ilipoulos-Maiani (GIM) mechanism in which each physical quark is interpreted as a mixture of mass and weak eigenstates [22].

This interpretation is summarised in Eq. (2.26), in which the first term represents the weak eigenstates and the third term represents the familiar flavours, which are the mass eigenstates. The second term is a 3×3 matrix responsible for the rotation between the mass and weak eigenstates. Known as the Cabibbo-Kobayashi-Maskawa (CKM) matrix [23–25], V_{CKM}, the V_{ij} terms specify the couplings of i to j ($i \to j + W$) in:

$$\begin{pmatrix} d' \\ s' \\ b' \end{pmatrix} = \begin{pmatrix} V_{ud} & V_{us} & V_{ub} \\ V_{cd} & V_{cs} & V_{cb} \\ V_{td} & V_{ts} & V_{tb} \end{pmatrix} \begin{pmatrix} d \\ s \\ b \end{pmatrix}. \tag{2.26}$$

In addition to the 6 quark masses, there are three real physical parameters, and one phase associated with the CKM matrix that can be used to represent V_{CKM} in alternative ways. The standard parameterisation includes the three real rotation angles, θ_{12}, θ_{23} and θ_{13}, and one complex phase factor, δ [26]. Here, $c_{ij} \equiv cos\theta_{ij}$, $s_{ij} \equiv sin\theta_{ij}$ and:

$$V_{CKM} = \begin{pmatrix} c_{12}c_{13} & s_{12}c_{13} & s_{13}e^{-i\delta} \\ -s_{12}c_{23} - c_{12}s_{23}s_{13}e^{i\delta} & c_{12}c_{23} - s_{12}s_{23}s_{13}e^{i\delta} & s_{23}c_{13} \\ s_{12}s_{23} - c_{12}c_{23}s_{13}e^{i\delta} & -s_{23}c_{12} - s_{12}c_{23}s_{13}e^{i\delta} & c_{23}c_{13} \end{pmatrix}. \tag{2.27}$$

2.2.2 Flavour Changing Neutral Currents

Flavour changing neutral currents (FCNCs) are interactions resulting in a change of quark flavour, whilst retaining the same electric charge. These processes involve quark transitions between two up-type quarks, or two down-type quarks. At leading order (LO) or tree level, only 'charged current' interactions, involving the exchange of a $W^{\pm}$, result in a change of quark flavour. Flavour changes are forbidden in 'neutral current' processes, involving a γ or Z^0, as depicted in Figure 2.1(a). At higher orders, however, FCNC processes are allowed in the SM through two successive charged current interactions, for example the transition $b \to (u,c)t \to s$, illustrated in Figure 2.1(b), where the t quark loop contribution dominates over the u and c quark contributions by virtue of $m_t >> m_{u,c}$. Although viable, these processes are more rare than those at tree level, owing to the additional interactions involved. Moreover, as the neutral current is diagonal in flavour space, the interactions are heavily suppressed by the corresponding CKM factors. For a next-to-leading order (NLO) process involving one loop, such as that

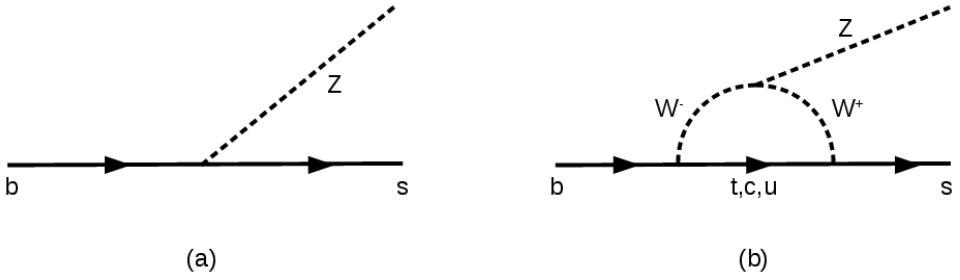

FIGURE 2.1: Diagrammatic representations of flavour changing neutral current interactions involving a $b \to s$ quark transitions that are forbidden in the SM (a) and viable in the SM (b).

in Figure 2.1(b), new particles acting at the weak scale may be able to enter the loop as virtual particles, altering the measured properties of the decay. For rare decays based on the $b \to s$ transition, it is possible to exploit FCNCs as model-independent tests of NP models by making measurements of the decay observables available, such as the CP and angular asymmetries, and branching ratios of both the exclusive and inclusive B decay modes. Any deviations from SM expectations of these measurements may be induced by NP, providing constraints on a number of theoretical parameters.

2.3 The $B_d^0 \to K^{*0}\ \mu^+\ \mu^-$ Decay

The $B_d^0 \to K^{*0}(\to K^+\pi^-)\ \mu^+\ \mu^-$ decay is an FCNC decay involving a $b \to s$ transition. The decay only occurs via loop diagrams in the SM; two Feynman diagrams that contribute at leading order are the γ/Z-penguin, and the FCNC box diagram, as illustrated in Figure 2.2. The final state of this decay has additional contributions from $B_d^0 - \overline{B}_d^0$ mixing, as depicted in Figure 2.3, but this particular contribution does not play a role in this thesis.

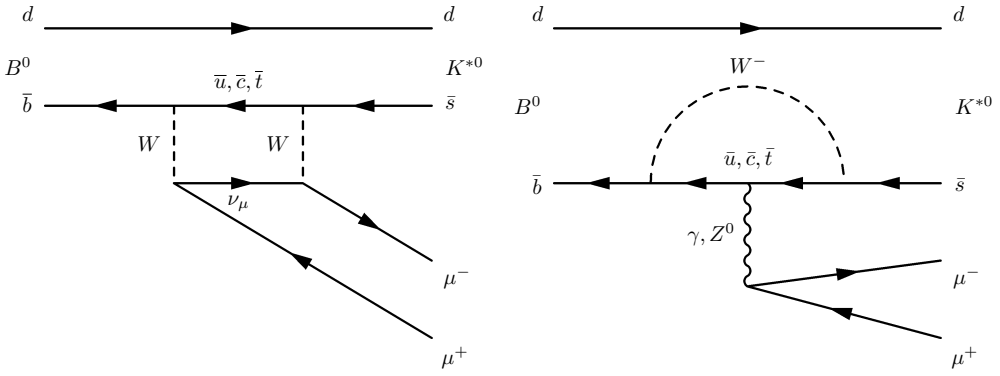

FIGURE 2.2: Box (left) and penguin (right) diagrams of the $B_d^0 \to K^{*0}\mu^+\mu^-$ decay.

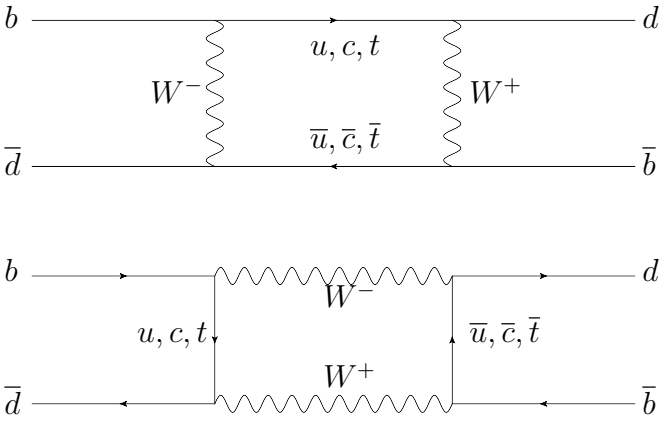

FIGURE 2.3: The B_d^0 - $\overline{B}_d^0$ contributions to $B_d^0 \to K^{*0}\mu^+\mu^-$.

The interference between the diagrams in Figure 2.2 provides an opportunity to search for New Physics (NP), as there are many angular observables available experimentally from this four body final state decay [27]. Discrepancies between SM expectations and the corresponding experimentally measured values of these observables are sensitive probes of BSM scenarios. The SM Lagrangian, $\mathcal{L}_{SM}$, can

be modified to include these NP contributions according to Eq. (2.28), in which c_i are complex coupling coefficients. FCNC processes such as $B_d^0 \to K^{*0}\mu^+\mu^-$ can provide constraints on the term c_i/Λ_{NP}^2, complementing direct searches of new physics, such as SUSY, by imposing bounds on c_i in

$$\mathcal{L} = \mathcal{L}_{SM} + \frac{c_i}{\Lambda_{NP}^2}\mathcal{L}_{NP}. \tag{2.28}$$

The SM branching fraction for this mode is $(1.05\pm0.10) \times 10^6$, hence experimental measurements of these observables at the LHC have been limited by statistics [19]. However, the situation continues to improve as the luminosity and data samples increase; this thesis reports on the first 3D angular analysis of this mode performed by the ATLAS experiment.

2.3.1 The Effective Hamiltonian

Rare semileptonic decays such as $B_d^0 \to K^{*0}\mu^+\mu^-$ are described by an effective Hamiltonian, $\mathcal{H}_{eff}$, of the form

$$\mathcal{H}_{eff} = \frac{4G_F}{\sqrt{2}} V_{tb}V_{ts}^* \frac{e^2}{16\pi^2} \sum_i^{10} \mathcal{C}_i(\mu)\mathcal{O}_i(\mu). \tag{2.29}$$

Here, G_F denotes Fermi's constant, $\mathcal{C}_i$ a set of *Wilson coefficients* and $\mathcal{O}_i$ a set of local operators. As discussed in Section 2.2.2, the loop contributions from the u and c quarks are negligible, hence only the CKM factors related to the t quark, V_{tb} and V_{ts} are considered. The operators $\mathcal{O}_{1,2}$ denote current-current operators, $\mathcal{O}_{3-6}$ the QCD-penguin operators and $\mathcal{O}_{7-10}$ the electroweak operators that govern $b \to s\ l^+l^-$ processes, as given in Eq. (2.30), where $m_b = m_b(\mu)$ is the running mass of the b quark in the $\overline{MS}$ scheme and μ the renormalisation scale. The electroweak operators are [28, 29]:

$$\begin{aligned}
\mathcal{O}_{7(7')} &= \frac{e}{g^2} m_b(\bar{s}\sigma_{\mu\nu}P_{R(L)}b)F^{\mu\nu} \\
\mathcal{O}_{8(8')} &= \frac{1}{g} m_b(\bar{s}\sigma_{\mu\nu}T^a P_{R(L)}b)G^{\mu\nu a} \\
\mathcal{O}_{9(9')} &= \frac{e^2}{g^2}(\bar{s}\gamma_\mu P_{L(R)}b)(\bar{l}\gamma^\mu l) \\
\mathcal{O}_{10(10')} &= \frac{e^2}{g^2}(\bar{s}\gamma_\mu P_{L(R)}b)(\bar{l}\gamma^\mu\gamma_5 l).
\end{aligned} \tag{2.30}$$

The electromagnetic operator $\mathcal{O}_7$ corresponds to $b \to s\gamma$ processes in which the γ decays leptonically to l^+l^-. Operator $\mathcal{O}_8$ is the gluonic equivalent of $\mathcal{O}_7$, but is highly suppressed in the SM so henceforth can be neglected. Semileptonic operators $\mathcal{O}_9$ and $\mathcal{O}_{10}$ represent the penguin and box contributions of $b \to s\ l^+l^-$, respectively, as shown in Figures 2.2 and 2.3.

The Wilson coefficients, $\mathcal{C}_i$, represent the coupling constants of effective vertices, carrying SM information on physics at short distances (scales higher than μ). The values of $\mathcal{C}_i$ can be enhanced by NP contributions, appearing as $\mathcal{C}_i = \mathcal{C}_i^{SM} + \mathcal{C}_i^{NP}$. The decay $B_d^0 \to K^{*0}(K^{*0} \to K^+\pi^-)\mu^+\mu^-$ provides an opportunity for clean precision observables to be measured in order to over-constrain the deviations of $\mathcal{C}_i^{NP}$ [29, 30].

2.3.2 The Angular Basis

The angular distribution of $B_d^0 \to K^{*0}(K^{*0} \to K^+\pi^-)\mu^+\mu^-$ is described by four kinematic variables: the squared invariant mass of the dimuon pair, denoted by 'q^2', and three angles, θ_L, θ_K and ϕ, which describe the geometry of the final state. The angle θ_L is defined as the angle between the direction of the μ^+ (μ^-) and the direction opposite to that of the B_d^0 ($\overline{B}_d^0$) in the dimuon rest frame. The angle θ_K is defined as the angle between the direction of the K^+ (K^-) and the direction opposite to that of the B_d^0 ($\overline{B}_d^0$) in the K^{*0} ($\overline{K}^{*0}$) rest frame. The angle ϕ is the angle between the plane containing the dimuon pair and the plane containing the kaon and pion from the K^{*0} in the B_d^0 rest frame. These definitions are illustrated in Figure 2.4. The three helicity angles $\vec{\Omega} = (\cos\theta_L, \cos\theta_K, \phi)$ appear as factors in

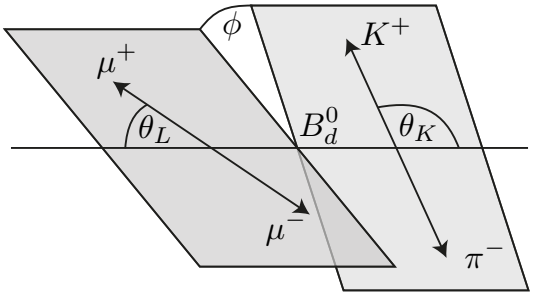

FIGURE 2.4: The three helicity angles used to describe the geometry of the final state of the $B_d^0 \to K^{*0}\mu^+\mu^-$ decay. The angles θ_L, θ_K, and ϕ are defined in the rest frames of the dimuon system, K^{*0} and B_d^0 meson, respectively.

the differential decay rate. For a given basis, a set of observables appear alongside

the helicity angles in the differential decay distribution, expressed as coefficients that depend upon q^2.

In general, the angular distribution of $B_d^0 \to K^{*0}\mu^+\mu^-$ is described by 12 physical observables $I_i^{(a)}$, where $i = 1 - 9$, which contain the complete information that can be obtained through a measurement of this decay. Comparatively the CP-conjugate mode $\overline{B}_d^0 \to \overline{K}^{*0}\mu^+\mu^-$ is described by 12 additional observables, $\overline{I}_i^{(a)}$.

The $B_d^0 \to K^{*0}\mu^+\mu^-$ decay involves the decay of a spin-0 pseudoscalar B_d^0 meson, thus projecting a spin of 0 on the decay axis. As such, the daughter helicities are constrained to $\lambda_1 = \lambda_2 = \lambda$. Furthermore, the daughter K^{*0} meson is a spin-1 particle; consequently there are three independent helicity state amplitudes corresponding to $\lambda = 0$ and $\lambda = \pm 1$. The $\lambda = 0$ state is expressed by the CP-even complex amplitude A_0, whilst the $\lambda = \pm 1$ states are expressed as mixtures of CP-even ($A_\parallel$) and CP-odd ($A_\perp$) amplitudes:

$$A_{\parallel,\perp} = \frac{A_{+1} \pm A_{-1}}{\sqrt{2}}. \tag{2.31}$$

Experimentally the $I_i^{(a)}$ observables represent the angular distribution, but theoretically these observables are expressed in terms of the three decay amplitudes, $A_\parallel$, $A_\perp$ and A_0, as in Eqs (2.32) through (2.43) [31]. The 'L' and 'R' denote left and right handed lepton chirality, m_μ is muon mass and $\beta_\mu = \sqrt{1 - 4m_\mu/q^2}$. In addition to the SM transversity amplitudes, A_S originates from NP-operators and A_t appears as a time-like component of the virtual K^{*0}, which whilst SM-like, contributes in powers of m_μ^2/q^2. The superscripts 's' and 'c' in $I_{1,2,6}$ indicate either a $\sin^2\theta_K$ or $\cos^2\theta_K$ dependence of the corresponding angular term. The 12 observables are defined as:

$$I_1^s = \frac{(2+\beta_\mu^2)}{4}\left[|A_\perp^L|^2 + |A_\parallel^L|^2 + |A_\perp^R|^2 + |A_\parallel^R|^2\right] + \frac{4m_\mu^2}{q^2} Re(A_\perp^L A_\perp^{R*} + A_\parallel^L A_\parallel^{R*}), \tag{2.32}$$

$$I_1^c = |A_0^L|^2 + |A_0^R|^2 + \frac{4m_\mu^2}{q^2}\left[|A_t|^2 + 2Re(A_0^L A_0^{R*})\right] + \beta_\mu^2 |A_S|^2, \tag{2.33}$$

$$I_2^s = \frac{\beta_\mu^2}{4}\left[|A_\perp^L|^2 + |A_\parallel^L|^2 + |A_\perp^R|^2 + |A_\parallel^R|^2\right], \tag{2.34}$$

$$I_2^c = -\beta_\mu^2\left[|A_0^L|^2 + |A_0^R|^2\right], \tag{2.35}$$

$$I_3 = \frac{\beta_\mu^2}{2}\left[|A_\perp^L|^2 - |A_\parallel^L|^2 + |A_\perp^R|^2 - |A_\parallel^R|^2\right], \tag{2.36}$$

$$I_4 = \frac{\beta_\mu^2}{\sqrt{2}}\Big[Re(A_0^L A_\parallel^{L*}) + Re(A_0^R A_\parallel^{R*})\Big], \tag{2.37}$$

$$I_5 = \sqrt{2}\beta_\mu^2\Big[[Re(A_0^L A_\perp^{L*}) - Re(A_0^R A_\perp^{R*}) - \frac{m_\mu}{\sqrt{q^2}}Re(A_\parallel^L A_S^* + A_\parallel^R A_S^*)\Big], \tag{2.38}$$

$$I_6^s = 2\beta_\mu^2\Big[[Re(A_\parallel^L A_\perp^{L*}) - Re(A_\parallel^R A_\perp^{R*})\Big], \tag{2.39}$$

$$I_6^c = 4\beta_\mu^2\frac{m_\mu}{\sqrt{q^2}}Re\Big[(A_0^L A_S^*) - Re(A_0^R A_S^*)\Big], \tag{2.40}$$

$$I_7 = \sqrt{2}\Big[Im(A_0^L A_\parallel^{L*}) - Im(A_0^R A_\parallel^{R*})\Big], \tag{2.41}$$

$$I_8 = \frac{\beta_\mu^2}{\sqrt{2}}\Big[Im(A_0^L A_\perp^{L*}) + Im(A_0^R A_\perp^{R*})\Big] \qquad \text{and} \tag{2.42}$$

$$I_9 = \beta_\mu^2\Big[Im(A_\parallel^L A_\perp^{L*}) + Im(A_\parallel^R A_\perp^{R*})\Big]. \tag{2.43}$$

2.3.3 The Differential Decay Rate

The full angular decay distribution of $B_d^0 \to K^{*0}\mu^+\mu^-$ is described by Eq. (2.44) [29]:

$$\begin{aligned}\frac{d^4\Gamma}{d\cos\theta_L d\cos\theta_K d\phi dq^2} = \frac{9}{32\pi}\Big[&I_1^s \sin^2\theta_K + I_1^c\cos^2\theta_K \\ &+ I_2^s\sin^2\theta_K\cos 2\theta_L + I_2^c\cos^2\theta_K\cos 2\theta_L \\ &+ I_3\sin^2\theta_K\sin^2\theta_L\cos 2\phi + I_4\sin 2\theta_K\sin 2\theta_L\cos\phi \\ &+ I_5\sin 2\theta_K\sin\theta_L\cos\phi + I_6^s\sin^2\theta_K\cos\theta_L + I_6^c\cos^2\theta_K\cos\theta_l \\ &+ I_7\sin 2\theta_K\sin\theta_L\sin\phi + I_8\sin 2\theta_K\sin 2\theta_L\sin\phi \\ &+ I_9\sin^2\theta_K\sin^2\theta_L\sin 2\phi\Big].\end{aligned} \tag{2.44}$$

The corresponding expression for the anti-decay mode is obtained through replacing $I_i^{(a)}$ with its CP-conjugated counterpart $\overline{I}_i^{(a)}$. However, instead of considering these coefficients separately, it can be convenient to combine the decays to form an angular distribution that is only sensitive to the CP averages of each of the angular terms. The (symmetric) CP averages of the $I_i^{(a)}$ terms are denoted by $S_i^{(a)}$, whilst for comparison the CP antisymmetric terms are denoted by $A_i^{(a)}$, where both

are normalised with respect to the combined differential angular distributions of $B^0_d \to K^{*0}\mu^+\mu^-$ and $\overline{B}^0_d \to \overline{K}^{*0}\mu^+\mu^-$, as shown in Eqs (2.45) and (2.46):

$$S_i^{(a)} = (I_i^{(a)} + \overline{I}_i^{(a)}) \Big/ \frac{d(\Gamma+\overline{\Gamma})}{dq^2} \tag{2.45}$$

$$A_i^{(a)} = (I_i^{(a)} - \overline{I}_i^{(a)}) \Big/ \frac{d(\Gamma+\overline{\Gamma})}{dq^2}. \tag{2.46}$$

In this representation of the differential angular distribution, the S_6^c observable is generated by scalar operators only and hence extends the parameterisation to one that is valid generically beyond the SM. However, this term is suppressed by the small lepton masses and consequently the simplification $S_6^s \sin^2\theta_K \cos\theta_l + S_6^c \cos^2\theta_K \cos\theta_l \to S_6 \sin^2\theta_K \cos\theta_l$ is exercised in this analysis. Additionally, in the limit in which the dimuon mass is large compared the muon masses, i.e. $q^2 \gg 4m_\mu^2$, the expressions in Eq. (2.47) hold:

$$\begin{aligned} \frac{m_\mu^2}{q^2} &\approx 0 \\ \beta_\mu^2 &\approx 1 \\ S_1^c &= -S_2^c \\ \frac{4}{3}S_1^s &= 4S_2^s. \end{aligned} \tag{2.47}$$

The differential decay rate can be expressed in terms of the K^{*0} longitudinal polarisation fraction, F_L, using the substitutions

$$\begin{aligned} S_2^c &= -F_L, \\ S_2^c &= -F_L, \\ S_2^s &= \frac{1}{4}(1 - F_L). \end{aligned} \tag{2.48}$$

The forward-backward CP asymmetry, A_{FB}, can also be measured using the relation

$$S_6^s = \frac{4}{3}A_{FB}. \tag{2.49}$$

Intuitively A_{FB} can be thought of as the asymmetry of the forward ($\cos\theta_L > 0$) and backward ($\cos\theta_L < 0$) μ^+s (μ^-s) with respect to the B^0_d ($\overline{B}^0_d$) flight direction in the dimuon rest frame. Both F_L and A_{FB} are defined according to the transversity

amplitudes, expressions for which are given in Eqs (2.50) and (2.51):

$$F_L = \frac{|A_0^L|^2 + |A_0^R|^2}{|A_0^L|^2 + |A_\parallel^L|^2 + |A_\perp^L|^2 + |A_0^R|^2 + |A_\parallel^R|^2 + |A_\perp^R|^2} \tag{2.50}$$

$$A_{FB} = \frac{3}{2}\frac{Re(A_\parallel^L A_\perp^{L*}) - Re(A_\parallel^R A_\perp^{R*})}{|A_0^L|^2 + |A_\parallel^L|^2 + |A_\perp^L|^2 + |A_0^R|^2 + |A_\parallel^R|^2 + |A_\perp^R|^2}. \tag{2.51}$$

Expressing the full angular differential decay rate in terms of S_i, F_L and A_{FB} yields [32]:

$$\begin{aligned}\frac{1}{d\Gamma/dq^2}\frac{d^4\Gamma}{d\cos\theta_L d\cos\theta_K d\phi dq^2} = \frac{9}{32\pi}\Bigg[&\frac{3}{4}(1-F_L)\sin^2\theta_K + F_L\cos^2\theta_K \\ &+ \frac{1}{4}(1-F_L)\sin^2\theta_K\cos 2\theta_L - F_L\cos^2\theta_K\cos 2\theta_L \\ &+ S_3\sin^2\theta_K\sin^2\theta_L\cos 2\phi + S_4\sin 2\theta_K\sin 2\theta_L\cos\phi \\ &+ S_5\sin 2\theta_K\sin\theta_L\cos\phi + \frac{4}{3}A_{FB}\sin^2\theta_K\cos\theta_L \\ &+ S_7\sin 2\theta_K\sin\theta_L\sin\phi + S_8\sin 2\theta_K\sin 2\theta_L\sin\phi \\ &+ S_9\sin^2\theta_K\sin^2\theta_L\sin 2\phi\Bigg].\end{aligned} \tag{2.52}$$

2.3.4 Form Factor Independent Analysis

Heavy-to-light quark transitions, such as the $b \to s$ transition that characterises the $B_d^0 \to K^{*0}$ decay are based on a theoretical framework that is factorised by short and long distance dynamics, in addition to CKM matrix elements. The transversity amplitudes A_0, $A_\parallel$ and $A_\perp$ can be written as functions of these short distance (SD) effects, expressed in terms of Wilson coefficients, and long distance (LD) effects, parameterised by a set of *form factors* (FFs).

Whilst the effects from SD dynamics can be treated perturbatively, the LD FFs are encapsulated in hadronic matrix elements. These matrix elements are related to the local operators generated by EW interactions and QCD, and cannot be calculated in perturbative theory without additional information on the structure of the hadrons. Moreover, a complete lattice solution using non-perturbative QCD isn't yet available; ergo, approximate methods are relied upon to calculate the relevant FFs, allowing large theoretical uncertainties to enter the SM predictions.

Whilst the CP-symmetric (CP-asymmetric) coefficients S_i (A_i) provide an accessible basis, their theoretical cleanliness is compromised by their strong sensitivity to the choice of FFs, thus introducing large uncertainties on any NP searches. An additional *optimised* basis introduces $P_i/P_i^{'}$ observables, which retain the same experimental accessibility as the S_i/A_i coefficients, but allow leading FF uncertainties to cancel [33]. These optimised observables relate to the S_i observables as follows:

$$\begin{aligned} P_1 &= \frac{2S_3}{(1-F_L)} \\ P_2 &= \frac{2}{3}\frac{A_{FB}}{(1-F_L)} \\ P_3 &= \frac{-S_9}{(1-F_L)} \\ P^{'}_{4,5,8} &= \frac{S_{4,5,8}}{\sqrt{F_L(1-F_L)}} \\ P^{'}_6 &= \frac{S_7}{\sqrt{F_L(1-F_L)}}. \end{aligned} \tag{2.53}$$

The $B^0_d \to K^{*0}\mu^+\mu^-$ decay is typically divided into three kinematic regimes; these regimes can be seen in the differential decay rate as a function of q^2 in Figure 2.5 [34]. At low q^2, where the emitted K^{*0} is energetic, QCD factorisation applies. The optimised basis described above allows an exact cancellation of the FFs across the low-q^2 range, $4m^2_\mu < q^2 < 9\ (GeV/c^2)^2$, exploiting the set of theoretically clean $P_i^{(')}$ observables. This is particularly advantageous in the range $1 < q^2 < 6\ (GeV/c^2)^2$, where the interference between the $\mathcal{O}_7$ and $\mathcal{O}_9$ operators increases, leading to an enhanced sensitivity to NP in $\mathcal{C}_9$ (at very low q^2, the virtual γ contribution from $\mathcal{C}_7^{(\prime)}$ dominates). The central region in Figure 2.5 is dominated by the $c\bar{c}$ resonances from $B^0_d \to J/\psi K^{*0}$ and $B^0_d \to \psi(2S)K^{*0}$ decays. At higher values of q^2, where $q^2 = \mathcal{O}(m_b^2)$, the theory encounters a further stumbling block owing to the fact that the FFs are calculated at leading order in a $1/m_b$ operator product expansion [35]. This expansion starts to break down at the precipice of the $c\bar{c}$ threshold, $q^2 < 4m_c^2$, necessitating some level of modelling in order to build a complete profile [36].

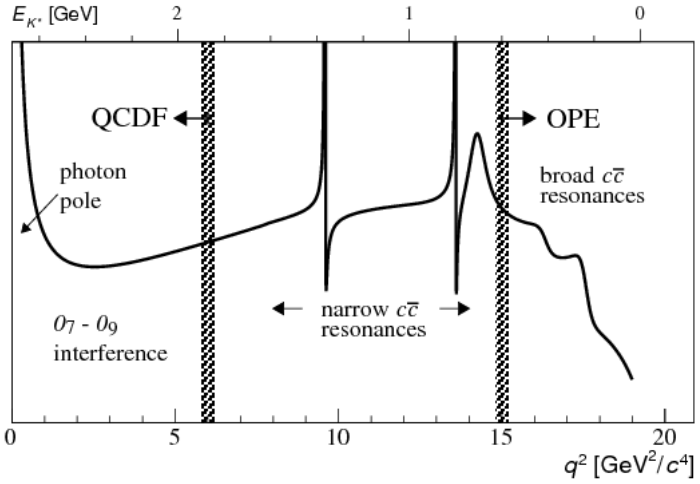

FIGURE 2.5: An illustration of the differential decay rate of $B^0_d \to K^{*0}\mu^+\mu^-$ as a function of q^2 from Ref. [34][34]. The theoretical methods used to predict parameters associated with the decay in the different kinematic regimes are indicated on the distribution. The two narrow $c\bar{c}$ resonances are from $B^0_d \to J/\psi K^{*0}$ (left) and $B^0_d \to \psi(2S)K^{*0}$ (right) decays.

2.3.5 Reducing the Number of Observables

In theory it's possible to measure all values of S_i or $P_i^{(\prime)}$ by fitting the differential decay rate in Eq. (2.52) to the data. Theoretically, this is the preferred way to extract observables [29], but in practice the strategy is limited by the size of a given data-set, which if too small can result in an unstable fit. Instead, one can reduce the number of observables in the fit to a manageable subset, making the observable of interest instantly accessible. This technique of condensing the number of coefficients of interest in the full differential decay rate is known as *folding*[1] and is based on the introduction of specific transformations to cancel out terms in the differential decay rate, thereby projecting out only one remaining angle of the differential decay rate [37]. Four such transformations are performed in this analysis, for the S_4, S_5, S_7 and S_8 parameters, as outlined below.

[1]The folding referred to in this thesis is not related to the more commonly used term unfolding, but instead relies on trigonometric relationships.

In order to disentangle the $S_4/P_4^{'}$ observables, the following transformations are applied:

$$P_4^{'}, S_4 : \begin{cases} \phi \to -\phi & \text{for } \phi < 0 \\ \phi \to \pi - \phi & \text{for } \theta_L > \frac{\pi}{2}. \\ \theta_L \to \pi - \theta_l & \text{for } \theta_L > \frac{\pi}{2} \end{cases} \tag{2.54}$$

Data folded in this way constrains the helicity angle ranges to $\cos\theta_L \in [0,1]$, $\cos\theta_K \in [-1,1]$ and $\phi \in [0,\pi]$. The resulting simplified differential angular distribution is

$$\begin{aligned} \frac{1}{(\Gamma+\overline{\Gamma})}\frac{d^4(\Gamma+\overline{\Gamma})}{d\cos\theta_l d\cos\theta_K d\phi dq^2} =& \frac{9}{8\pi}\Bigg[\frac{3}{4}(1-F_L)\sin^2(\theta_K) + F_L\cos^2(\theta_K) \\ &+ \frac{1}{4}(1-F_L)\sin^2(\theta_K)\cos(2\theta_L) \\ &- F_L\cos^2(\theta_K)\cos(2\theta_L) \\ &+ S_3\sin^2(\theta_K)\sin^2(\theta_L)\cos(2\phi) \\ &+ S_4\sin(2\theta_K)\sin(2\theta_L)\cos(\phi)\Bigg], \end{aligned} \tag{2.55}$$

in which experimental sensitivity to the first five terms of Eq. (2.52) are preserved, as well as the S_4 term of interest. The other terms in Eq. (2.52) cancel, reducing the number of observables in the differential angular distribution from eight to three.

In order to disentangle the $S_5/P_5^{'}$ observables, the following is applied:

$$P_5^{'}, S_5 : \begin{cases} \phi \to -\phi & \text{for } \phi < 0 \\ \theta_L \to \pi - \theta_L & \text{for } \theta_L > \frac{\pi}{2}. \end{cases} \tag{2.56}$$

The ranges become $\cos\theta_L \in [0,1]$, $\cos\theta_K \in [-1,1]$ and $\phi \in [0,\pi]$. The reduced differential decay rate is given by

$$\begin{aligned}\frac{1}{(\Gamma+\overline{\Gamma})}\frac{d^4(\Gamma+\overline{\Gamma})}{d\cos\theta_L d\cos\theta_K d\phi dq^2} = \frac{9}{8\pi}\Bigg[&\frac{3}{4}(1-F_L)\sin^2\theta_K + F_L\cos^2\theta_K \\ &+ \frac{1}{4}(1-F_L)\sin^2\theta_K\cos 2\theta_L \\ &- F_L\cos^2\theta_K\cos 2\theta_L \\ &+ S_3\sin^2\theta_K\sin^2\theta_L\cos 2\phi \\ &+ S_5\sin 2\theta_K\sin\theta_L\cos\phi\Bigg].\end{aligned} \tag{2.57}$$

The transformations for $S_7/P_6^{'}$ are as follows:

$$P_6^{'}, S_7 : \begin{cases} \phi \to \pi - \phi & \text{for } \phi > \frac{\pi}{2} \\ \phi \to -\pi - \phi & \text{for } \phi < -\frac{\pi}{2} \\ \theta_L \to \pi - \theta_L & \text{for } \theta_L > \frac{\pi}{2}. \end{cases} \tag{2.58}$$

The ranges become $\cos\theta_L \in [0,1]$, $\cos\theta_K \in [-1,1]$ and $\phi \in [-\frac{\pi}{2}, \frac{\pi}{2}]$ and the reduced differential decay rate is given by

$$\begin{aligned}\frac{1}{(\Gamma+\overline{\Gamma})}\frac{d^4(\Gamma+\overline{\Gamma})}{d\cos\theta_l d\cos\theta_K d\phi dq^2} =&\frac{9}{8\pi}\Bigg[\frac{3}{4}(1-F_L)\sin^2(\theta_K) + F_L\cos^2(\theta_K) \\ &+ \frac{1}{4}(1-F_L)\sin^2(\theta_K)\cos(2\theta_L) \\ &- F_L\cos^2(\theta_K)\cos(2\theta_L) \\ &+ S_3\sin^2(\theta_K)\sin^2(\theta_L)\cos(2\phi) \\ &+ S_7\sin(2\theta_K)\sin(\theta_L)\sin(\phi)\Bigg].\end{aligned} \tag{2.59}$$

Finally, for S_8 and $P_8^{'}$, these transformations are given by

$$P_8^{'}, S_8 : \begin{cases} \phi \to \pi - \phi & \text{for } \phi > \frac{\pi}{2} \\ \phi \to -\pi - \phi & \text{for } \phi < -\frac{\pi}{2} \\ \theta_L \to \pi - \theta_L & \text{for } \theta_L > \frac{\pi}{2} \\ \theta_K \to \pi - \theta_K & \text{for } \theta_L > \frac{\pi}{2}, \end{cases} \tag{2.60}$$

whilst the resulting differential decay rate is given by

$$\begin{aligned}\frac{1}{(\Gamma+\overline{\Gamma})}\frac{d^4(\Gamma+\overline{\Gamma})}{d\cos\theta_l d\cos\theta_K d\phi dq^2} =& \frac{9}{8\pi}\Bigg[\frac{3}{4}(1-F_L)\sin^2(\theta_K)+F_L\cos^2(\theta_K) \\ &+\frac{1}{4}(1-F_L)\sin^2(\theta_K)\cos(2\theta_L) \\ &-F_L\cos^2(\theta_K)\cos(2\theta_L) \\ &+S_3\sin^2(\theta_K)\sin^2(\theta_L)\cos(2\phi) \\ &+S_8\sin(2\theta_K)\sin(2\theta_L)\sin(\phi)\Bigg].\end{aligned} \tag{2.61}$$

The ranges become $\cos\theta_L \in [0,\ 1]$, $\cos\theta_K \in [\text{-}1,\ 1]$ and $\phi \in [\text{-}\frac{\pi}{2},\ \frac{\pi}{2}]$.

Eqs (2.55), (2.57), (2.59) and (2.61) represent the functional forms of each of the folded angular distributions. In order to avoid using numerical integration in the fits to data, the functional forms were multiplied by the acceptance functions, described in Section 6.2, and integrated in Mathematica using the integration limits defined above. The integrals were performed over $\cos\theta_L$, $\cos\theta_K$ and ϕ, as well as the three additional combinations, $\cos\theta_K$ and $\cos\theta_L$, $\cos\theta_K$ and ϕ, and $\cos\theta_L$ and ϕ to ensure an appropriate probability density function (PDF) could be projected for any one of these angles.

2.3.6 Overview of Experimental and Theoretical Measurements

In addition to the ATLAS experiment, the angular analysis of $B^0_d \to K^{*0}\mu^+\mu^-$ has been performed by the BaBar [38], CMS [39], LHCb [40] and Belle [41] collaborations.

Both the LHCb and Belle experiments performed the FF independent analysis described in Sec 2.3.4 to extract a set of P'_i observables, where $i = 4, 5, 6, 8$. Discrepancies were observed between the experimental results of P'_5 and SM expectations from Ref. [42] in both cases, as seen in Figure 2.6.

However, a number of theoretical approaches to calculating the expected angular observables in the $B^0_d \to K^{*0}\mu^+\mu^-$ analysis exist. The various techniques provide a range of results, dependent on how the non-perturbative hadronic contributions are accounted for. A collection of theoretical predictions for P'_5 are shown in

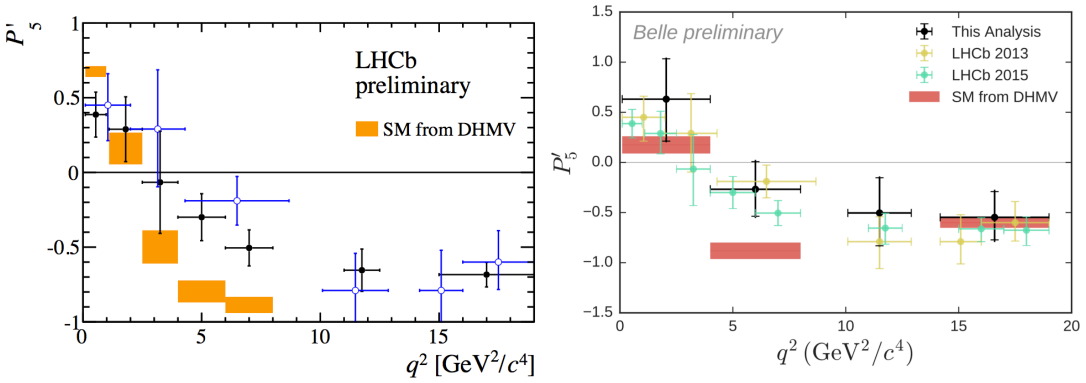

FIGURE 2.6: (left) The Moriond 2015 result for P_5' as a function of q^2 from LHCb [40]. The blue points correspond to the published measurement from 1 fb^{-1} of data and the black points correspond to an update with 3 fb^{-1}. (right) The corresponding result from Belle [41]. Both results are compared to SM expectations from Ref. [42], labelled here as 'DHMV'.

Figure 2.7 from Refs [43–45]. The results show significant differences in both the fitted values of P_5' and their corresponding fitted errors between collaborations. These differences are shown to be more pronounced for higher values of q^2.

The differences between the theoretical computations must be considered when commenting on the agreement of the results shown in this thesis with the SM predictions.

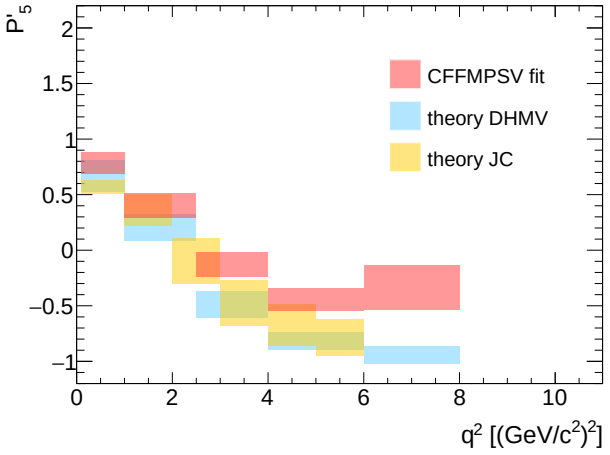

FIGURE 2.7: Comparison of SM predictions for the P_5' parameter in $B_d^0 \to K^{*0}\mu^+\mu^-$ decay from various phenomenological analyses.

Chapter 3

The ATLAS Experiment

The ATLAS experiment is designed to study high energy proton-proton (pp) collisions at the LHC at the European Organisation for Nuclear Research (CERN). The LHC continues to operate at a new frontier of energy, recreating conditions similar to those just after the Big Bang. Hundreds of petabytes of data have been recorded, processed and analysed since data taking began in 2010.

In 2013 the LHC came to the end of its first run which produced a number of successful results. Following an almost two year shut down period, the second run of data taking at the LHC began in June 2015 at nearly double the collision energy of the first run. The ATLAS experiment continues in-depth analyses of the new data but this thesis will only cover data taken in 2012 and the corresponding detector specifications.

This chapter will briefly describe the LHC and its accelerator complex in Section 3.1 before outlining the roles and principles of operation of each of the ATLAS subdetectors. An overview of the ATLAS inner detector is given in Section 3.2.2, the calorimetry system in Section 3.2.3 and the muon system in Section 3.2.4.

3.1 The Large Hadron Collider

The LHC, located beneath the Switzerland-France border, is the world's largest and most powerful particle accelerator to date. It consists of a 27 km ring of superconducting magnets designed to accelerate protons up to a maximum pp centre-of-mass energy of $\sqrt{s} = 14\ TeV$. In 2012, the LHC had reached a little

under 60% of its potential beam energy, running with a collision energy of $\sqrt{s} = 8\ TeV$, delivering 23.3 fb^{-1} total integrated luminosity.

The acceleration of the protons relies on more than the LHC alone and can be divided into five main stages as illustrated in Figure 3.1.

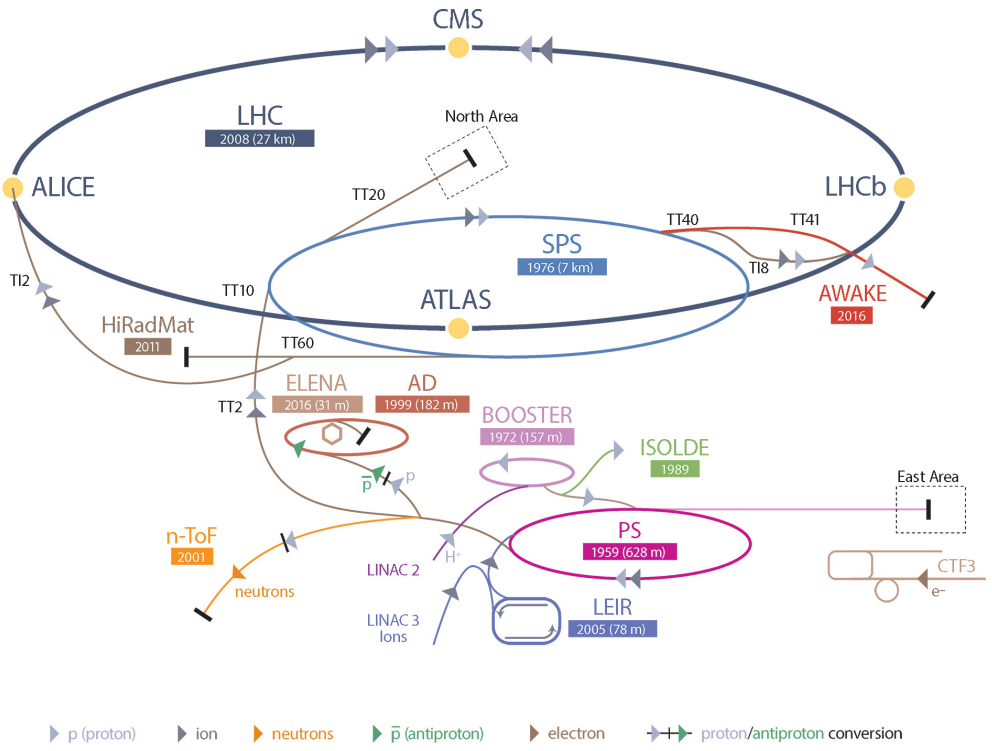

FIGURE 3.1: CERN's accelerator complex. The proton acceleration chain for the LHC is shown as Linac2 (50 MeV) → BOOSTER (1.4 GeV) → PS (25 GeV) → SPS (450 GeV) → LHC (4 TeV). Image © CERN.

In the first stage, hydrogen atoms from a cylinder of compressed hydrogen gas are fed into the source chamber of the first linear accelerator, 'Linac 2'. An electric field is applied to obtain a source of ionised protons which are accelerated to an energy of 50 MeV and injected into the Proton Synchrotron Booster (PSB)[46]. In this second stage, the PSB accelerates the protons to $0.916c$ and an energy of 1.4 GeV before the beams enter the Proton Synchrotron (PS) for the third stage of acceleration. The PS is 628 m in circumference and accelerates protons to over $0.999c$ and 25 GeV. The PS is responsible for providing the bunch packets and bunch spacing at the LHC. In the fourth stage, the proton bunches are injected into the Super Proton Synchrotron (SPS), 7 km in circumference, where they are accelerated to 450 GeV before finally being transferred to the LHC.

The LHC is made up of two vacuum pipes through which protons are accelerated in opposite directions. The counter-rotating beams inside the LHC cross over at four interaction points (IP) around the accelerator ring, corresponding to the positions of four particle detectors, as shown in Figure 3.2. ATLAS and CMS are both general purpose detectors designed to investigate a wide range of physics including Higgs searches and measurements, Standard Model measurements and searches for supersymmetry (SUSY) and exotic signatures. ALICE and LHCb are both smaller specialised detectors, dedicated to studying heavy-ion collisions and physics involving b-quarks, respectively.

In 2012, the LHC was running with a luminosity of $6 \times 10^{33}\ cm^{-2}s^{-1}$. The number of colliding bunches was $\sim$ 1400, with $\sim 10^{11}$ protons per bunch and a bunch spacing of 50 ns. The resulting bunch collision rate was $\sim 32\ MHz$.

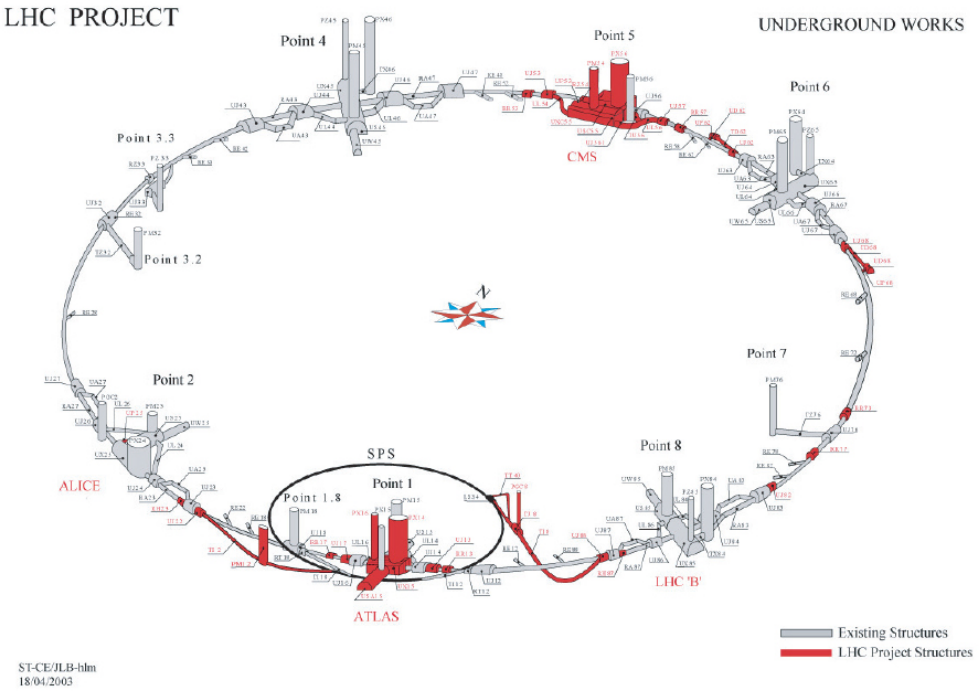

FIGURE 3.2: LHC layout. The ATLAS detector is positioned at Point 1, ALICE at Point 2, CMS at Point 5 and LHCb at Point 8.

3.2 The ATLAS Detector

The largest of the LHC detectors, the ATLAS detector stands 46 m long, 25 m high and 25 m wide in a cavern 100 m below ground at 'Point 1' on the LHC ring, as identified in Figure 3.2. The ATLAS detector consists of many subdetectors,

which in combination are able to measure the different types of particles produced in a given collision.

The inner detector (ID), which is comprised of the Pixel detector, the Semiconductor tracker (SCT) and the Transition Radiation tracker (TRT), immediately surrounds the IP and measures the tracks of charged particles that are bent by the magnetic field of a superconducting solenoidal magnet. Surrounding the ID are two calorimetry devices that measure the energy of the particles. Encasing all of these is the muon spectrometer (MS), used to measure the tracks of muons that are bent in the field of a superconducting toroidal magnet. These subdetectors are constructed around the beam axis in concentric cylinders, as seen in the computer-generated image of the ATLAS detector in Figure 3.3 [18].

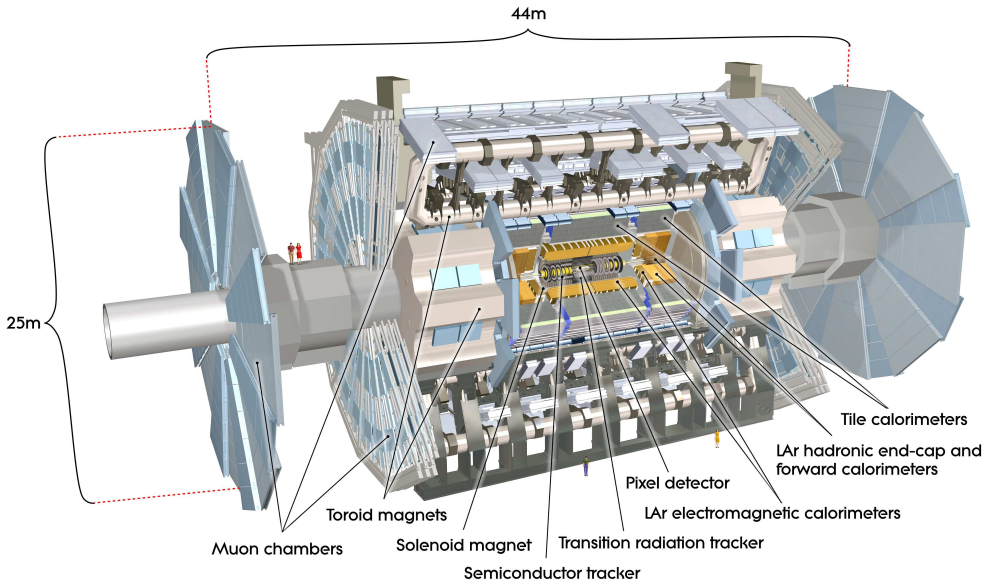

FIGURE 3.3: Cut-away view of the ATLAS detector. The detector is 25 m in height and 46 m in length.

The ATLAS detector is described using a right-handed coordinate system defined with its origin at the nominal IP of the pp collisions. The direction of the beam defines the $z-$axis, which runs counterclockwise; the sides of the detector are labelled A and C for $z > 0$ and $z < 0$ respectively, as illustrated in Figure 3.4 [47]. The $(x - y)$ plane is transverse to the beam direction with the positive $x-$axis pointing from the IP to the centre of the LHC ring and the positive $y-$axis from IP upwards.

In this system, the direction of a particle trajectory is parameterised by two angles, ϕ and θ, where the momentum of the particle is given by p = ($|p|$, θ, ϕ). The

azimuthal angle ϕ is measured around the beam axis and defined as the angle between the projection of the trajectory on the $(x-y)$ plane and the x-axis. The polar angle θ is measured in the $(R-z)$ plane ($R = \sqrt{x^2+y^2}$) as the angle between the trajectory and the $z-$axis.

More commonly in particle physics experiments such as ATLAS, the pseudorapidity defined as $\eta = -\ln\tan(\theta/2)$, is used instead of θ. The transverse momentum $p_T = \sqrt{p_x^2+p_y^2}$ is also preferred thus the linear momentum is represented by $p = (p_T, \eta, \phi)$. These useful angular variables will be referred to in the remainder of this chapter when describing the acceptance ranges of the various detector components. A brief overview of each is given; a full description of the detector can be found in [18].

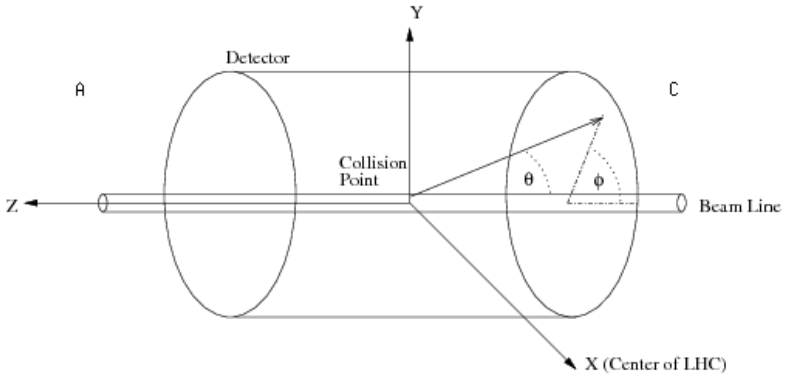

FIGURE 3.4: Illustration of the ATLAS coordinate system.

3.2.1 Magnet System

The ATLAS magnet system is comprised of four large superconducting magnets, providing a magnetic field over a volume of approximately $12,000\ m^3$, where the volume is defined as the region in which the field exceeds $50\ mT$. The layout of the magnet system is shown in Figure 3.5; the four magnets include the central solenoid magnet and three toroid magnets, split into one barrel and two end cap toroids, as indicated. The central solenoid lies within the calorimeters (see Section 3.2.3) and provides a magnetic field to the ID (see Section 3.2.2). The toroid magnets produce a magnetic field to the MS (see Section 3.2.4).

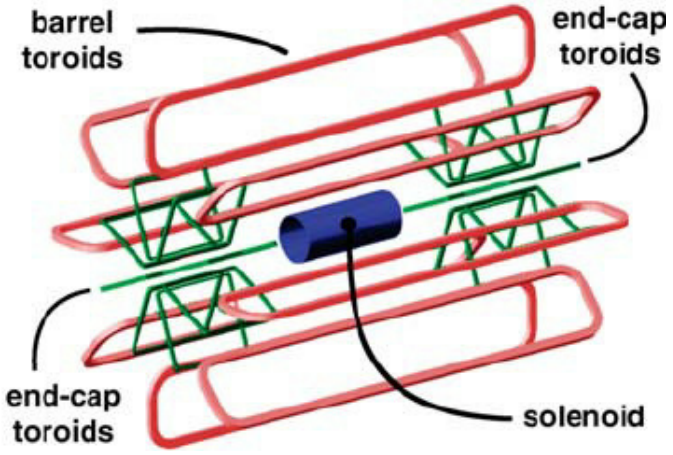

FIGURE 3.5: The layout of the magnet system. The central solenoid and three toroid magnets are indicated. The central solenoid lies inside the calorimeter volume, which is described in Section 3.2.3, whilst the toroid magnets surround the muon spectrometer, discussed in Section 3.2.4.

3.2.1.1 Central Solenoid Magnet

The central solenoid is aligned on the beam axis and provides a 2 T axial magnetic field at the nominal 7.730 kA operational current for the ID, bending charged particles for momentum measurement. The solenoid is placed a short distance in front of the LAr EM calorimeter and thus is designed to be as thin and transparent as possible in order to maintain the calorimeter performance, minimising the number of particle interactions in the coil.

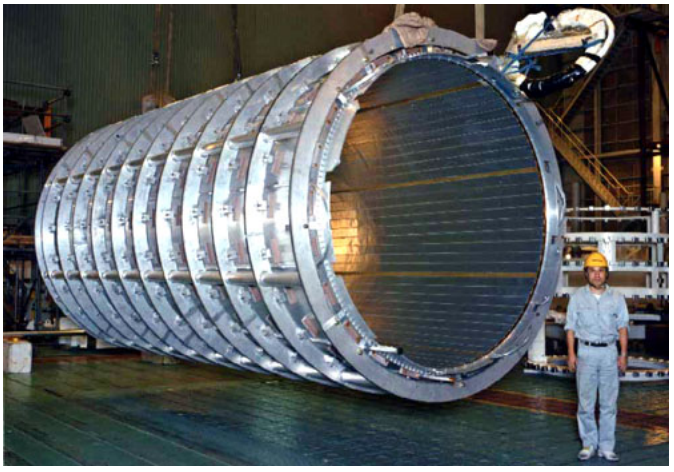

FIGURE 3.6: The ATLAS central solenoid magnet.

The bare solenoid, shown in Figure 3.6, has a length of 26 m with a diameter of 22 m. The single-layer coil is wound with a high-strength Al stabilised superconductor of Rutherford type $NbTi/Cu$, specially developed to minimise the thickness

whilst achieving a high field. The solenoid is installed inside a 12 mm thick Al support cylinder in a common cryostat with the LAr calorimeter to minimise wall material. This design results in a coil transparency of 0.66 radiation lengths at a yield strength greater than 100 MPa. The solenoid is indirectly cooled with two-phase helium flowing in pipes welded to the coil support cylinder.

3.2.1.2 Toroid Magnets

Three large superconducting air-core toroid magnets, one barrel and two end caps, generate the magnetic field for the MS, minimising the amount of material the muons traverse. Each toroid magnet is constructed from eight coils positioned symmetrically about the beam axis. The end cap magnets are rotated 22.5^o relative to the barrel magnet in order to achieve radial overlap and optimise bending power at the interface between the two sections. In the barrel the eight coils of the toroid magnet are positioned in eight individual cryostats, whilst in the end caps these eight coils are stored in their own aluminium-alloy housing. The magnetic field is non-uniform across the barrel and end caps, but provides a field strength of approximately 1 T in the centre of the coils. The respective bending power capabilities of the barrel and the end caps are $1.5 - 5.5\ T \cdot m$ in $0 < |\eta| < 1.4$ and $1.0 - 7.5\ T \cdot m$ in $1.6 < |\eta| < 2.7$, with a slightly lower value in the 'transition region' $1.4 < |\eta| < 1.6$, as shown in Figure 3.7 [48].

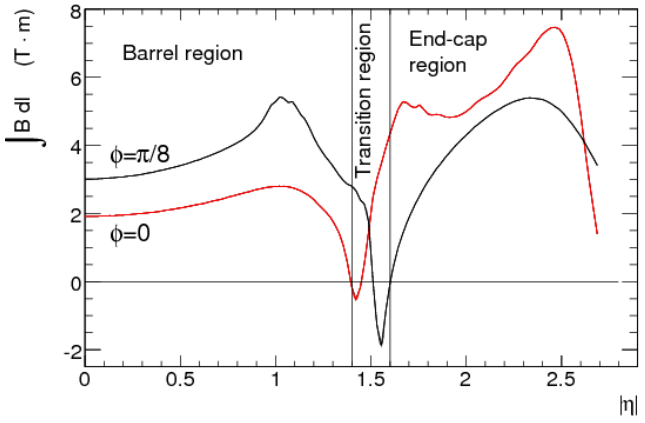

FIGURE 3.7: Predicted field integral in one of the ATLAS toroid octants, as a function of $|\eta|$, for infinite momentum muons. The curves correspond to the azimuthal angles $\phi = 0$ (red) and $\phi = \pi/8$ (black). The image is taken from Ref [18].

3.2.2 Inner Detector

Approximately 360 million inelastic collisions occur within the ATLAS detector each second. This leads to close to 18 inelastic events per crossing and hence a high track density surrounding the IP [49].

One of the challenges ATLAS faces is achieving a sufficient momentum and vertex resolution so as to distinguish between the particle tracks and identify primary and secondary charged particle vertices. Realising these requirements is essential in performing high-precision measurements of the underlying physics processes.

The ATLAS ID comprises three independent subdetectors used in conjunction around the IP to track charged particles of $p_T > 0.5\ GeV/c$ within the pseudorapidity range $|\eta| < 2.5$ [18]. Radially outwards from the nominal IP, these subsystems are the Pixel, SCT and TRT detectors, as illustrated in Figure 3.8. The Pixel and SCT detectors are silicon precision tracking detectors whilst the TRT is a straw tube tracker.

These three subdetectors are arranged in concentric cylindrical layers in the central (barrel) region and disk or wheel like structures, perpendicular to the beam axis, in the forward and backward (end cap) regions. All three are surrounded by a superconducting solenoidal magnet that immerses the ID in an axial magnetic field of 2T. The solenoid bends the tracks of charged particles passing through its field, allowing the particle momenta to be measured.

The integrated ID system has been designed to provide a transverse momentum resolution of $\sigma_{p_T}/p_T = 0.05\%\ p_T\ GeV/c \oplus 1\%$ in the $(x-y)$ plane [50].

3.2.2.1 Pixel and Semiconductor Tracker Detectors

The Pixel system is the innermost detector, responsible for reconstructing primary vertices from pp collisions within ATLAS. Moreover, the Pixel system is critical in the identification and reconstruction of secondary vertices, such as those from B meson decays. The active region of the detector is comprised of three layers in the barrel region (ID layers 0, 1 and 2) and three layers in both of the end cap regions.

The Pixel detector is built up of a total of 1744 'modules', split into 1456 barrel and 288 end cap modules. Each module harbours silicon sensors, front-end (FE)

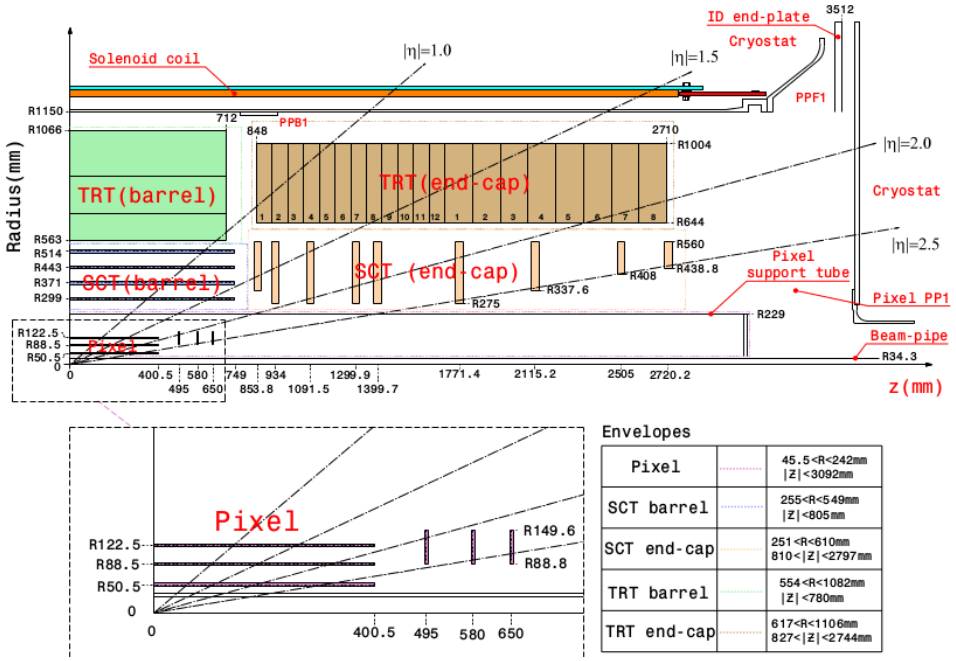

FIGURE 3.8: A schematic diagram of a quarter section of the ATLAS ID. The $R-z$ view shows the different subdetectors of the ID and their dimensions. The silicon pixel detector covers radial distances between 50.5 mm and 150 mm. The SCT covers radial distances from 299 mm to 560 mm and the TRT covers radial distances from 563 mm to 1066 mm.

electronics and flexible circuits or 'readout hybrids' [51]. There are 47,232 pixels in an individual module, each measuring 50 μm in the ϕ direction and 400 μm in the z and R directions. Consequently $\sim$ 80 million pixels span the barrel and end cap layers, creating a total active area of 1.73 m^2.

The Pixel sensors consist of a (256 ± 3) μm thick silicon bulk, constructed from 144 columns by 328 rows of pixels. The high resistivity n-bulk is implanted with an n^+ region on the readout side of the wafer and a p^+ region on the other side to create a p$-$n junction. The p$-$n junction operates in reverse bias with a nominal bias voltage of $(150 - 600)$ V, yielding a depletion region with negligible electric current. Particles passing through the active region ionise the silicon, creating an electric current that is collected and readout at the n-side of the wafer. Electronics channels are connected to the pixel sensors via bump bonding. An analogue block is attached to each pixel and used to amplify the signal charge collected in its associated pixel and compare it to an adjustable threshold using a comparator. If the signal exceeds the discriminating threshold, a digital output of the amplified signal is readout via 16 FE chips. The digital readout includes the hit pixel address

and timestamps for the leading and trailing edges, allowing particle tracks to be measured.

Only hits for which the leading edge rises in the 50 ns window, corresponding to the period of the bunch crossings, are recorded; this offers an average hit efficiency of $(97.8 \pm 0.7)\%$ across the modules. The single-module intrinsic accuracy for the pixels is 10 μm in the $(R - \phi)$ plane for both barrel and end caps and a longer pitch of 115 μm is oriented along the $z-$plane in the barrel and the $R-$plane in the end caps.

The SCT detector consists of 4088 (2112 barrel and 1976 end cap) modules that tile across four additional barrel layers (ID layers 3, 4, 5 and 6) and 9 additional end cap layers (Disks 1-9) on each side, as illustrated in Figure 3.8. The SCT barrel and end cap layers envelope the Pixel detector, providing near full coverage.

Each module is constructed from four identical silicon strip sensors, 6 cm in length and containing 768 strips, each of 80 μm pitch. Pairs of the sensors are daisy chained together creating a combined length of 12 cm and width of ~ 3 cm. One pair of sensors are glued back to back with the other pair at a stereo angle of 40 $mrad$ to produce one module [52]. The module strips in the barrel are aligned along the beam axis providing a constant pitch of 80 μm, whilst those in the end caps are positioned radially with a constant azimuth but a pitch gradient across each module. Installing the modules in this way means that three-dimensional space points can be determined from combining the hits from the two sides of the module. Consequently, approximately eight measurements per charged particle track are made in the SCT, with an intrinsic resolution of 17 μm $(R - \phi)$ and 580 μm $(z)(R)$.

The SCT sensors are (285 ± 15) μm thick and are constructed from n-type bulk silicon with p-type implants, employing single sided p-in-n technology with a nominal reverse bias voltage of $(150 - 350)$ V. The readout strips are capacitatively coupled to the implant strips such that each module possesses a thermal and mechanical core structure (baseboard), sandwiched between the pairs of silicon microstrip sensors. Akin to the Pixel detector, the hits in the SCT are readout using radiation hard FE chips mounted to flexible readout hybrids responsible for nearly 6.3 million readout channels. The detector registers a hit if the pulse height exceeds a preset threshold of 1 fC, a value based on the performance specification for the

detection efficiency and noise occupancy. The average intrinsic hit efficiency in the SCT was measured to be $(99.74 \pm 0.04)\%$.

3.2.2.2 Transition Radiation Tracker Detector

The outermost of the three tracking subsystems of the ATLAS ID is the TRT, a drift-tube system designed to accompany the precision tracking chambers in providing robust tracking information. In addition to its role in the ID triad, the TRT has stand-alone pattern recognition and electron/pion separation capabilities.

The TRT consists of 370,000 polyimide drift or straw tubes, each 4 mm in diameter with a $\sim$ 31.5 μm diameter gold plated tungsten wire anode through the centre [53]. These straw tubes are filled with a gas mixture of 70% Xe, 27% CO_2 and 3% O_2. In the barrel region, 50,000 straw tubes form up to 73 longitudinal layers, covering a pseudorapidity range of $|\eta| < 1$. These layers are split into three rings of 36 modules, as seen in Figure 3.9 [18]. The end cap regions divide 320,000 straws into 160 radial planes. These planes form the body of two sets of independent wheels at either end of the barrel, covering an η range of $1 < |\eta| < 2$.

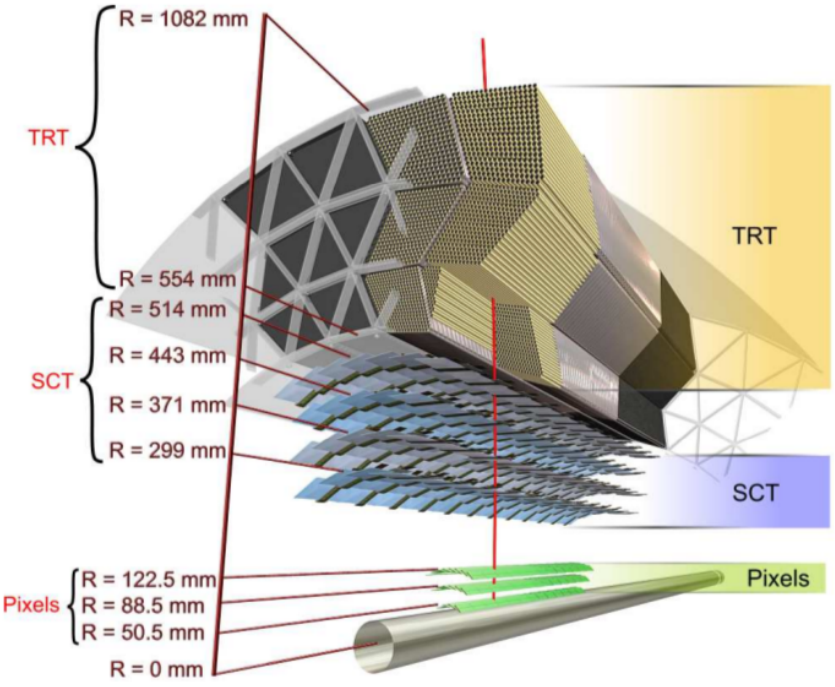

FIGURE 3.9: Layout of the sensors and structural elements of the ATLAS ID as a 10 GeV charged particle passes through at $|\eta| \sim 0$.

The walls of the tubes are kept at a voltage of $-1.6\ kV$, whilst the anode wires are grounded. Hence when a charged particle passes through the TRT, it ionises the gas inside the straws yielding free electrons that drift towards the anodes. Here they are amplified and read out at each end; in this fashion each tube acts as a proportional counter.

When charged particles traverse the interface between the straw tubes and the gas mixture, photons are generated with an intensity dependent on the particle's Lorentz factor $\gamma = E/m$, a phenomena known as transition radiation (TR) [54]. Typically, photon energy deposits from electron induced TR are $8-10\ keV$ whilst for pions, which are minimally ionising particles (MIPs), the photon energy deposits are around 2 keV [53]. The straws are fixed in a matrix of fibres and foils in the barrel and end cap regions respectively, to provide electron identification through TR measurements.

The maximum drift time in the gas is about 40 ns and the basic straw hit efficiency is around 96%. The TRT only provides $(R-\phi)$ information, for which it has a resolution of 130 μm for charged tracks. However, this is atoned for by providing over 30 hits per track, complementing the other two ID subsystems and significantly contributing to the overall tracking performance [18].

3.2.3 Calorimetry

The ID is able to accurately reconstruct the primary and secondary vertices of particle decays. These decays continue to cascade beyond the ID, but it's financially infeasible to have the level of granularity achieved in the ID throughout the whole $\sim 23000\ m^3$ structure. An alternative approach is used to identify and measure the properties of particles to a precision that satisfies the requirements of the prospective physics studies.

The ATLAS calorimeters are designed to measure the energy a particle loses as it passes through the detector. These sampling calorimeters consist of layers of absorbing high-density materials interleaved with layers of an active medium, covering the full ϕ range. The system encircles the ID and solenoid magnets and is broadly split into two calorimeters, designed to provide particle identification. The liquid argon (LAr) electromagnetic (EM) calorimeter, discussed in Section 3.2.3.1, is the closer of the two calorimeters to the beam line and its primary role is to detect

and measure photons and electrons within pseudorapidity range $|\eta| < 3.2$. The hadronic calorimeter, discussed in Section 3.2.3.2, complements the EM calorimeter, providing hadronic energy measurements with $|\eta| < 1.7$. Both calorimeters include LAr forward detectors that extend the total pseudorapidity range covered by the calorimeters to $|\eta| = 4.9$.

The energy resolution of the calorimeters have been studied as a function of energy range and the experimental measurements, after noise subtraction, have been fitted with the expression

$$\frac{\sigma(E)}{E} = \frac{a}{\sqrt{E(GeV)}} \oplus b, \tag{3.1}$$

where a is the stochastic term and b is the constant term reflecting local non-uniformities in the response of the calorimeter. The combined ATLAS calorimetry system is able to achieve an energy resolution of $\sigma(E)/E = (52.0 \pm 1.0)\%/\sqrt{E(GeV)} \oplus (3.0 \pm 0.1)\%$ and an electronic-noise term of $(1.6\ GeV \pm 0.1)\%$ [55]. This leads not only to particle identification, but accurate measurements of the shapes of particle cascades, both in electromagnetic showers and hadronic jets. In addition, the calorimeters are capable of giving us information on neutrinos through missing transverse energy.

3.2.3.1 LAr Electromagnetic Calorimeter

Similarly to the ID, the EM calorimeter has one barrel (EMB) and two end cap regions (EMEC), but unlike the ID each component is embedded within its own cryostat. The EMB is made up of two identical half barrels separated by a distance of 4 mm at $z = 0$. Each EMEC is comprised of two coaxial wheels, located at either end of the barrel. The EM calorimeter employs an accordion-shaped architecture of lead absorbers with copper electrodes positioned between them. The corrugated planes of absorbers radiate outwards in the EMB, in effect stacking upon one another to provide full coverage in ϕ without azimuthal cracks. A total of 1024 of these planes are used in each half barrel. In the EMECs, the accordion structure lies parallel to the radial direction and 'stacks' axially with each end cap employing 768 absorbers. Photographs of the EMB and EMEC construction are shown in Figure 3.10 [18].

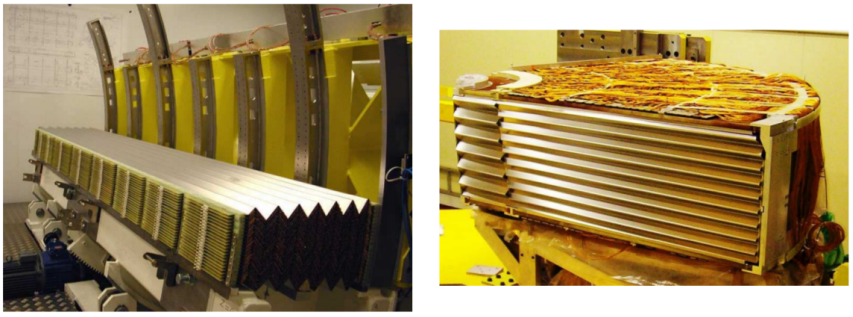

FIGURE 3.10: Photographs of a partly stacked barrel electromagnetic LAr module (left) and a side view of an electromagnetic end cap LAr module (right).

As an electron passes through the lead absorbers, it interacts with the material to produce a shower of low energy electrons, positrons and photons. The electron will continue to pass through several layers of the absorbers, creating an increasingly complex shower before it eventually stops. The EM calorimeter uses LAr cooled to -185^oC as the active detector medium. The low energy particles created in the showers pass into the LAr, ionising its atoms. Emersed in the LAr is a copper grid which acts as an electrode to readout the output signal which is proportional to the incident particle energy absorbed by the lead.

The EM calorimeters are longitudinally segmented into three layers: front, middle and back, as viewed from the IP. The first layer, known as the strip layer, has the finest resolution in η and is designed to provide high resolution direction information. For a pseudorapidity $|\eta| < 1.4$, the strip cell size provides a granularity of $\Delta\eta \times \Delta\phi = 0.0031 \times 0.1$ and for $1.4 < |\eta| < 1.475$ this increases to 0.025×0.025. The second (middle) layer is designed to contain the majority of the EM shower. This middle layer has a resolution four times higher in ϕ, but eight times lower in η than the strip layer for low η. As $|\eta|$ increases, the granularity in the middle layer increases to $\Delta\eta \times \Delta\phi = 0.075 \times 0.025$. The final layer, known as the back layer, has a coarse granularity of $\Delta\eta \times \Delta\phi = 0.050 \times 0.025$ for $|\eta| < 1.35$ and is used to collect the small residual energy of the shower. The described segmentation in η, ϕ and depth is depicted in Figure 3.11, where a slice through a barrel module of the LAr EM calorimeter is shown [18]. The readout electronics are also used to provide an analogue signal to the first level trigger system (see Section 3.3) from the energy deposited in the trigger towers.

The overall thickness of the EM calorimeter is 11 interaction lengths (λ) at $\eta = 0$,

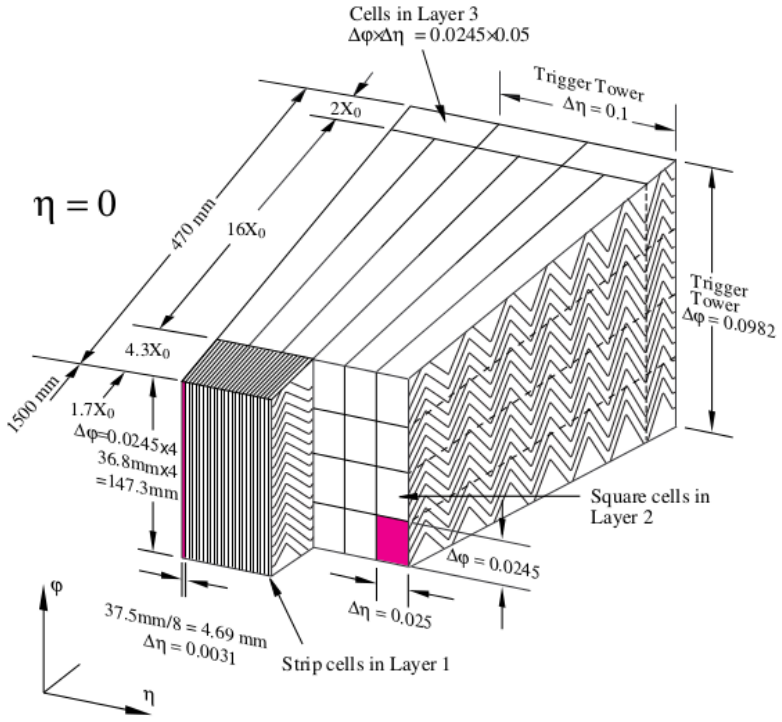

FIGURE 3.11: A diagram of a barrel module, highlighting the granularity in η and ϕ of the cells of each of the three layers. The granularity in η and ϕ of the trigger towers is also shown.

which is both adequate for resolution of high energy jets and reducing punch-through to well below the level of prompt muons. Here punch-through refers to the occasions in which non-muon particle types are not stopped in the calorimeter and thus creating a signal. After noise subtraction ($\sigma_{noise} = 250\ MeV$), the LAr EM calorimeter has a measured energy resolution of $\sigma(E)/E = (10.1 \pm 0.4)\%/\sqrt{E(GeV)} \oplus (0.17 \pm 0.04)\%$ in the energy range 10 to 245 GeV at $|\eta| = 0.687$ [56]. Furthermore the LAr EM calorimeter achieves a polar angle resolution in the range $50 - 60\ mrad/\sqrt{E\ (GeV)}$ over both barrel and end cap regions [55].

3.2.3.2 Hadronic Calorimeter

The hadronic calorimeter is a collection of three calorimeters; the tile calorimeter, the LAr hadronic end cap calorimeter (HEC) and the LAr forward calorimeter (FCal). These are used to measure the energies of hadrons.

The tile calorimeter is a sampling calorimeter employing a large array of interleaved steel and scintillator sheets or 'tiles' covering the region $|\eta| < 1.7$. When a

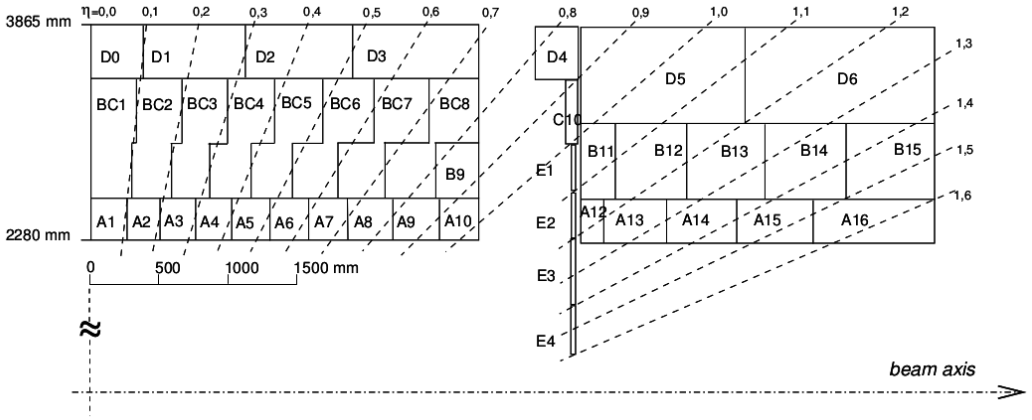

FIGURE 3.12: The segmentation in depth and η of a tile calorimeter module in the barrel (left) and an extended barrel (right). The cells are labelled 'A' and 'D' for the innermost and outermost layers of the tile calorimeter module. The middle layer is labelled 'BC' for the central barrel and 'B' for the extended barrel. Four scintillators, labelled E1-E4, are also shown.

high energy hadron passes through the steel, it interacts with the atomic nuclei, initiating a torrent of particles. The tiles are positioned both radially and normal to the beam line with a radial depth of approximately 7.4 λ. Similarly to the EM calorimeter, the geometry of the tile calorimeter yields seamless azimuthal coverage. The produced particle shower enters the scintillator, where light is radiated. The light intensity from the affected tiles is measured and readout through long wavelength-shifting fibres to photomultiplier tubes (PMTs) where it's converted into an electric current. From this electric current, it's possible to measure the energy possessed by the hadron that entered the calorimeter.

The tile calorimeter is divided into a barrel and two extended barrel sections, which are each segmented into 64 modules with a cell ϕ-segmentation of $\Delta\phi \sim 0.1$ [57]. Each module is radially segmented into three layers as shown in Figure 3.12 [57]. The inner two layers have a cell η-segmentation of $\Delta\eta = 0.1$ while the third layer the η-segmentation doubles ($\Delta\eta = 0.2$). The fractional energy resolution as a function of beam energy and impact angle is $\sigma(E)/E = (56.4 \pm 0.4)\%/\sqrt{E(GeV)} \oplus (5.5 \pm 0.1)\%$ for isolated pions [18].

The HEC is a LAr-copper sampling calorimeter covering the pseudorapidity range $1.5 < |\eta| < 3.2$. The HEC consists of two independent wheels immersed in an end cap cryostat, shared by the EMEC and FCal. Each wheel has 32 wedge-shaped modules and each module is divided into two segments in depth. The wheels use flat copper plates interleaved with 8.5 *mm* LAr gaps as the active

medium. The granularity in the HEC is $\Delta\eta \times \Delta\phi = 0.1 \times 0.1$ for $|\eta| < 2.5$ and $\Delta\eta \times \Delta\phi = 0.2 \times 0.2$ for higher values of $|\eta|$. The fractional energy resolution for pions is $\sigma(E)/E = (70.6 \pm 1.5)\%/\sqrt{E\ (GeV)} \oplus (5.8 \pm 0.2)\%$ in the HEC; the measured resolution increases for electrons to $\sigma(E)/E = (21.4 \pm 0.1)\%/\sqrt{E(GeV)}$ [18].

The FCal provides calorimetry in the remaining high η range, $3.1 < |\eta| < 4.9$. The FCal is made up of three modules, FCal1, FCal2 and FCal3 in each end cap. FCal1 uses copper to optimise resolution and heat removal required for electromagnetic measurements. FCal2 and FCal3 both employ tungsten to provide containment and reduce the lateral spread of hadronic showers in order to measure the energy of hadronic interactions. All modules consist of a metal matrix with electrodes in the longitudinal channels and small gaps for the active medium, LAr. The energy resolutions for pions and electrons in the FCal are $\sigma(E)/E = \sim 70\%/\sqrt{E\ (GeV)} \oplus \sim 3.0\%$ and $\sigma(E)/E = (28.5 \pm 1.0)\%/\sqrt{E(GeV)} \oplus (3.5 \pm 0.1)\%$ respectively [18].

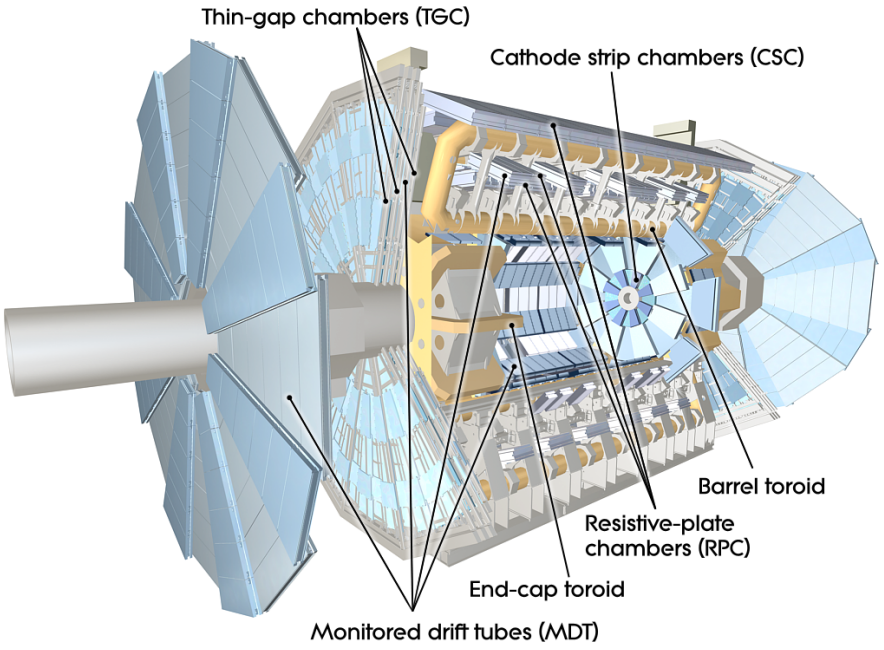

FIGURE 3.13: The layout of the Muon Spectrometer.

3.2.4 Muon Spectrometer

Muons are minimally ionising particles (MIPs), which means their mean energy loss rate is close to minimum. Muons are therefore able to penetrate through

several metres of iron and as such pass through ATLAS's ID and calorimeters without stopping. An additional component to the ATLAS detector is therefore required outside the calorimeters to provide accurate muon track measurements. The ATLAS Muon Spectrometer (MS) is the outermost part of the detector and uses a combination of powerful magnets and high precision tracking chambers to measure charged particles, typically muons, exiting the calorimeters. The barrel and end cap toroid magnets discussed in Section 3.2.1.2 produce a magnetic field with a $B \cdot dl$ of between $2-6\ T \cdot m$ [58]. The MS accounts for most of the volume of the entire detector and is designed to measure muons with $p_T > 3\ GeV/c$ with a resolution of 4% up to $p_T = 100\ GeV/c$ and approximately 10% for 1 TeV/c tracks [48]. In addition to three toroid magnets, the MS consists of Monitored Drift Tubes (MDTs) and Cathode Strip Chambers (CSCs) for precision-measurement tracking in the bending plane and Resistive Plate Chambers (RPCs) and Thin Gap Chambers (TGCs) for triggering. The layout of the MS is illustrated in Figure 3.13.

3.2.4.1 Precision Tracking Chambers

The two precision tracking chambers in the ATLAS MS are the MDTs the CSCs.

The MDTs provide precision measurements of track coordinates in the bending plane $(R-z)$ of the toroid magnetic field. There are 1088 chambers, grouped into 18 main types of detector associated with the MDT. Broadly speaking these chamber sizes and the layer dimensions scale with distance from the IP, but in order to minimise acceptance losses, some of these chambers are constructed with atypical shapes.

The MDT chambers are built from a collection of aluminium pressurised drift tubes operating with a mixture of 93% Ar and 7% CO_2 gas at 3 bar. As an incident muon moves through the drift tube, it ionises the gas leaving a trail of ions and electrons that drift to the sides and centres of the tubes. A tungsten-rhenium wire extends through the centre of each tube that collects the ionisation electrons. A custom designed monolithic ASC (Amplifier/Shaper/Discriminator) chip converts the raw tube data signals to a binary output that is channelled to a Time-to-Digital Converter (TDC). By measuring the time it takes for these charges to drift from the starting point, it's possible to determine the position of the muon as it passed through. The average drift speed is 20 $\mu m/ns$, corresponding to an error of

10 μm on the distance travelled by the muon before being collected at the wire of the drift tube. The drift radius of the hit as a function of the drift time $(r-t)$ was measured to have a mean residual width of 96 μm, equating to a track resolution of approximately 80 μm for $r > 6$ mm [58]. The MDT covers the majority of the range $|\eta| < 2.7$ but is only able to safely operate up to ≈ 150 Hz/cm^2 [59]. For $|\eta| > 2$, the counting rate limit is exceeded, reaching ≈ 2500 Hz/cm^2 at $|\eta| = 2.7$. Consequently, CSCs are employed in the innermost layer $2 < |\eta| < 2.7$.

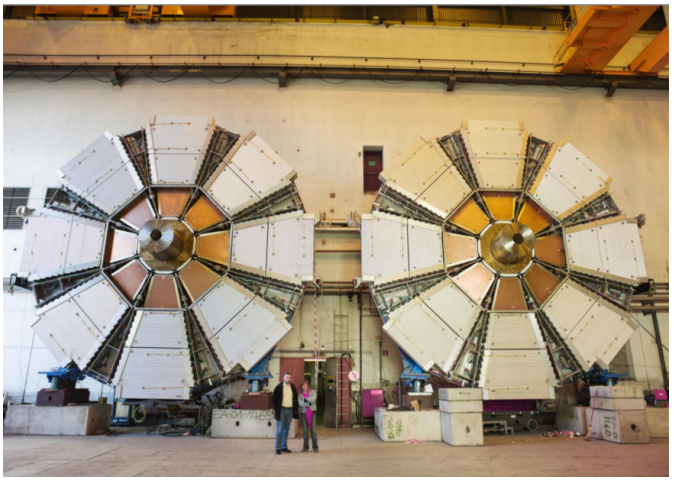

FIGURE 3.14: The ATLAS Small Wheels with eight large and eight small overlapping chambers. The Cathode Strip Chambers can be seen at the inner part of the wheel.

CSCs are multiwire proportional chambers with segmented cathode readout, which provide a higher granularity than the MDTs. The whole CSC system consists of two end cap disks, each made up of 16 chambers that are further segmented into eight large and eight small chambers in ϕ, as depicted in Figure 3.14 [59]. Each chamber is constructed from four identical CSC planes layered behind one another, allowing four independent measurements in η and ϕ to be made for each track.

Each of the planes within a chamber have 192 precision $x-$strips, which run perpendicular to the anode wires and 48 transverse $y-$strips, which run parallel. The $x-$strips have a readout pitch of 5.567 mm and 5.308 mm for the small and large chambers, respectively. The position of the muon is determined by interpolating the charge on three to five adjacent cathode strips, resulting in a spatial resolution of 60 μm per plane. The $y-$strips measure the transverse coordinate to ~ 5 mm providing good two-track resolution.

3.2.4.2 Trigger Chambers

The ATLAS trigger chambers are designed to perform two main functions: the first aim is to discriminate muon p_T tracks, providing fast measurements in the non-bending ϕ-projection to complement the MDT measurements. The second is to reduce the event rate from the level of $\sim 10^9\ Hz$ to a more feasible level of the order 100 Hz without jeopardising any analyses. An outline of the trigger chambers and how they operate is given below, while a more detailed description of the trigger system is given in Section 3.3 and the specific triggers used for event selection in this analysis are given in Section 4.1.

Two varieties of trigger chambers are employed to provide fast muon p_T track measurements with approximately uniform accuracy across the the full ϕ scope and in $|\eta| \leq 2.4$. Two different technologies are employed to address the significant differences between the barrel and end cap environments, relating to the muon kinematics, detector geometry and radiation levels.

In the barrel, where $|\eta| \leq 1.05$, Resistive Plate Chambers (RPCs) are located above and below the MDTs to form three concentric cylinders about the beam axis, as depicted in Figure 3.15 [18]. The three layers or 'stations' are labelled RPC1, RPC2 and RPC3 from the innermost to outermost layer. The RP1 and RP2, which sandwich the middle MDT layer, are responsible for low p_T triggers for $6-9\ GeV$ particle tracks. The RP3, which sits above the outer MDT in the large sectors and below it in the small sectors, provides a high p_T trigger for $9-35\ GeV$ particle tracks.

A total of 1116 RPCs reside in the MS, encompassing 380 stations. Each station has two rectangular detector 'units', positioned with a 65 mm overlap to maximise the area in which curved tracks can be measured. In turn, each unit consists of two independent parallel high resistivity plastic plates. The positively-charged anode plate and the negatively-charged cathode plate measure in η and ϕ and are separated by a gas volume 2 mm in height. An electric field of 4.9 kV/mm is maintained across the gap; when a particle passes through, it creates a gas avalanche along the ionising track in the gas gap [18]. The readout from the RPCs is via metallic strips that are mounted on the outer faces of the plates, giving four readout channels per unit, amounting to 3.5×10^4 readout channels in total.

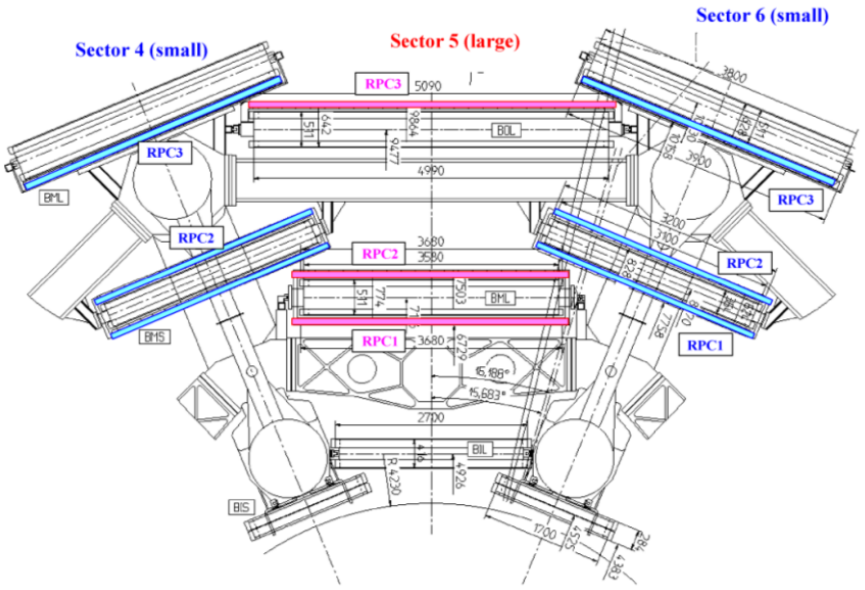

FIGURE 3.15: A cross-section through one part of the barrel. The RPCs are marked in colour in the small (blue) and large (pink) sectors.

The RPCs operate in avalanche mode meaning all primary electron clusters form avalanches simultaneously, producing one instantaneous signal. The charge multiplication for a given avalanche continues until the avalanche reaches the anode, giving rise to a gas gain dependent on the distance between the primary electron cluster and the receiving anode. The electrons from the gas avalanche are collected at the anodes and the pattern of hit strips gives a quick measure of muon momentum. The RPCs have a time resolution of 1.3 ns at 100 Hz/cm^2 and 1.8 ns at 1 kHz/cm^2, a spatial resolution of 10 mm in z and ϕ and a rate capability of 1 kHz/cm^2 [18]. Good time and spatial resolution in the RPCs is critical in order to make immediate decisions about whether data is stored in a bunch crossing period of 50 ns.

In the end caps, $1.05 < |\eta| < 2.4$, Thin Gap Chambers (TGCs) trigger on muons and perform azimuthal measurements of their tracks. Much like the RPCs in the barrel, the TGCs are positioned in four layers in the end cap to complement the radial measurements made by the end cap MDTs. The middle MDT layer has three associated TGC layers: 'TGC1' located in front of the MDT and 'TGC2' and 'TGC3' behind it. A fourth layer, 'TGC4', is located in front of the inner MDT layer. This partnership of MDTs and TGCs allows both radial and azimuthal coorinates to be determined. At the outer MDT layer, the azimuthal measurement is extrapolated from the inner TGCs.

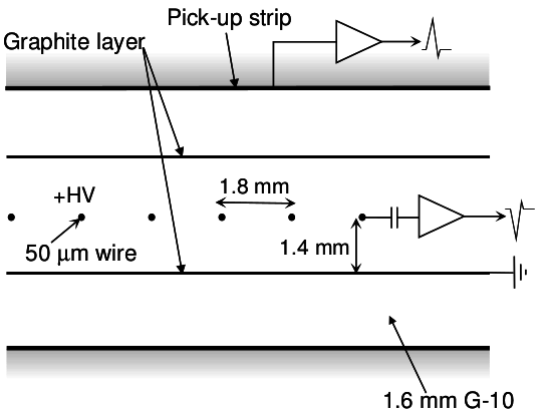

FIGURE 3.16: The Thin Gap Chamber structure showing anode wires, graphite cathodes, G-10 layers and a pick-up strip. The G-10 layers represent 1.6 mm thick glass-reinforced epoxy laminate sheets.

The TGCs are multiwire proportional chambers, operating in a similar manner to the CSCs in Section 3.2.4.1. The anodes are 50 μm diameter tungsten wires, which are kept at a high positive voltage of 2900 ± 100 V [18]. The anode wires are sandwiched between resistive grounded graphite plates, 1.6 mm in thickness. The distance between the wires and the graphite layers is 1.4 mm, slightly shorter than the wire-to-wire distance of 1.8 mm; the characteristic TGC structure is shown in Figure 3.16 [18, 60].

The region between the cathodes is filled with a highly quenching mixture of CO_2 and n-Pentane ($n - C_5H_{12}$), allowing the TGCs to operate in a saturated mode leading to strong signals with reduced Landau tails and a high signal to noise ratio. The geometry of the system shown in Figure 3.16 reduces the drift component of ionisation clusters, leading to a time resolution good enough to provide an efficiency greater than 99% for bunch-crossing identification for a 50 ns gate. Critically, the TGCs have a large rate capability of more than 20 kHz/cm^2 compared to the RPC limit of ~ 1 kHz/cm^2.

3.3 The Trigger and Data Acquisition

The event rate in the ATLAS detector is the product of the total integrated luminosity and the total pp cross section from inelastic collisions. In 2012 the event rate was approximately 10^9 Hz, but storing such a high data rate would require

unrealistic computing power and storage. An online trigger system is therefore required to utilise the information from the calorimeters and muon trigger chambers in order to accept or reject events. The ATLAS trigger system consists of three levels, namely Level 1 (L1), Level 2 (L2) and the Event Filter (EF).

The L1 trigger is the first stage of event selection and is responsible for reducing the rate to below 75 kHz by identifying regions of interest (RoI) for further processing. Signals corresponding to events containing features such as missing transverse energy or high momentum electrons, muons, taus, photons, jets and B hadrons are fed to the L1 trigger from trigger hardware in the calorimeter (L1Calo) and muon detector systems (L1Muon). These signals are processed through the Central Trigger Processor (CTP) with a decision time of 2.5 μs [61].

The L2 trigger and EF are both software based triggers, which in conjunction are known as the High Level Trigger (HLT). The L2 trigger uses fast algorithms to request data from the readout systems in the RoI identified by the L1 trigger for processing. The reconstruction software is used to better determine the event properties and in so doing, further reduces the data rate to ~ 3.5 kHz, with an average processing time of 40 $ms/event$.

The EF is based on offline algorithms used to fully reconstruct the events provided by the L2 trigger, finally reducing the data rate to ~ 200 Hz, with an average processing time of 4 $s/event$.

Most analyses have signatures that rely on triggering on multiple objects. The signature of the $B_d^0 \to K^{*0}(\to K^+\pi^-)\mu^+\mu^-$ decay demands at least two oppositely signed muons are selected and moreover the four body final state of this decay leads to a reduced p_T of these muons. ATLAS employs a muon trigger system, designed to identify and select an extensive spectrum of muons, including lower momentum dimuon pairs.

3.3.1 Muon Trigger

The muon trigger follows the same three stage process described above, starting with an L1 hardware response.

The L1 trigger relies on information from custom built hardware in the RPCs and TGCs within the MS. It aims to reconstruct muon tracks through the trigger

chambers, identifying coincidences of hits in the different layers. The position information or RoI of the hits is then stored for the L2 trigger to process. In addition to the RoI, the L1 trigger classifies the muons according to their estimated momentum. The curvature of the muon track in the magnetic field of the MS and the distance from the IP the muons are seen to traverse, are used to measure the muons' p_T. Broadly, coincidence hits in two layers of the trigger chambers correspond to "low p_T" muons and hits through three layers correspond to "high p_T" muons. Equally, those with a large degree of deviation from a straight line will have a lower momentum than those on a straight path.

The L1 trigger quantifies this with a set of p_T thresholds, which are labelled as MU11 for $p_T > 11\ GeV/c$, for example. MU10 and lower are then classified as "low p_T" muons and MU11 and higher as "high p_T" muons [62].

The muon L2 and EF identify muons using three distinct strategies. Standalone muons are reconstructed in the MS only. The trajectories reconstructed in the MS are subsequently extrapolated to the beam line to determine the parameters of the muons at the IP. Combined muons arise when track reconstruction is performed independently in the MS and the ID, and then the tracks are formed from successfully combining an MS track with an ID track. Finally, in instances in which a muon candidate is not found, the EF starts with tracks in the ID, as indicated by the L1 ID RoI, and extrapolates to nearby tracks in the MS. In this instance, muon tracks reconstructed in the ID only are referred to as tagged muons.

The signature muons in the decay $B_d^0 \to K^{*0}\mu^+\mu^-$ are low p_T muons; in cases where the trigger thresholds are relaxed to guarantee event selection, the event rate inevitably increases significantly. In order to control this, isolation, I^μ, was added as an extra requirement to the muon candidate. The isolation is defined as

$$I^\mu = \frac{\sum p_T - p_T^\mu}{p_T^\mu}, \tag{3.2}$$

where $\sum p_T$ is the sum of all tracks with $p_T > 1\ GeV/c$ in a cone of radius R centred on the muon candidate of momentum $p_T(\mu)$.

To further control the data rate, whilst allowing a lower p_T threshold, some triggers are prescaled, so that only a fraction of the triggered events are stored. Particles that pass the trigger requirements are stored in different data streams corresponding to the trigger they passed; hence muons that pass a given trigger are stored

in the muon stream. The B physics triggers are largely muon based algorithms, thus muons passing this different set of trigger requirements are stored in the B physics stream. This leads to many particles being stored in multiple streams, thus measures must be taken to avoid double counting.

The streams are further subcategorised in order of priority for offline reconstruction to take place, as well as by the fraction of event information written to them. Streams containing events to be reconstructed quickly are called 'prompt' streams, whilst those that store data to be processed later are called 'delayed' streams. The trigger tests a large number of hypotheses independently and the whole decision sequence for each hypothesis is known as a 'trigger chain'. The trigger system is therefore defined by a menu of trigger chains starting from the L1 trigger. A full description of the trigger chains used in this analysis are given in Section 4.1.

3.4 Monte Carlo Simulation

The ability to interpret the data collected at high-energy physics detectors is a major theoretical challenge. Hundreds of processes involving all known particles and potentially some additional particles occur across a broad momentum range. To tackle this problem, the data collected by the ATLAS experiment is compared to theoretical predictions using Monte Carlo (MC) simulated events.

MC methods encompass many computational algorithms that generate random numbers to obtain numerical solutions to multi-dimensional integrals for which analytical solutions are not known. The MC event simulation can be broadly split into four main stages, namely the event generation, simulation, digitisation and reconstruction.

Most event generators divide a process according to the scales of momentum transfer involved, as shown in Figure 3.17.

Here, the black lines correspond to hard scattering and the red, green and blue lines represent colour singlets. The pink filled circle represents the soft underlying event and the grey filled elipses represent colourless clusters. The backward parton evolution and the (QED) initial/final state radiation are shown by the purple and pink lines, respectively. Finally the teal lines correspond to nonperturbative gluon splitting and the yellow regions to hadronic decays.

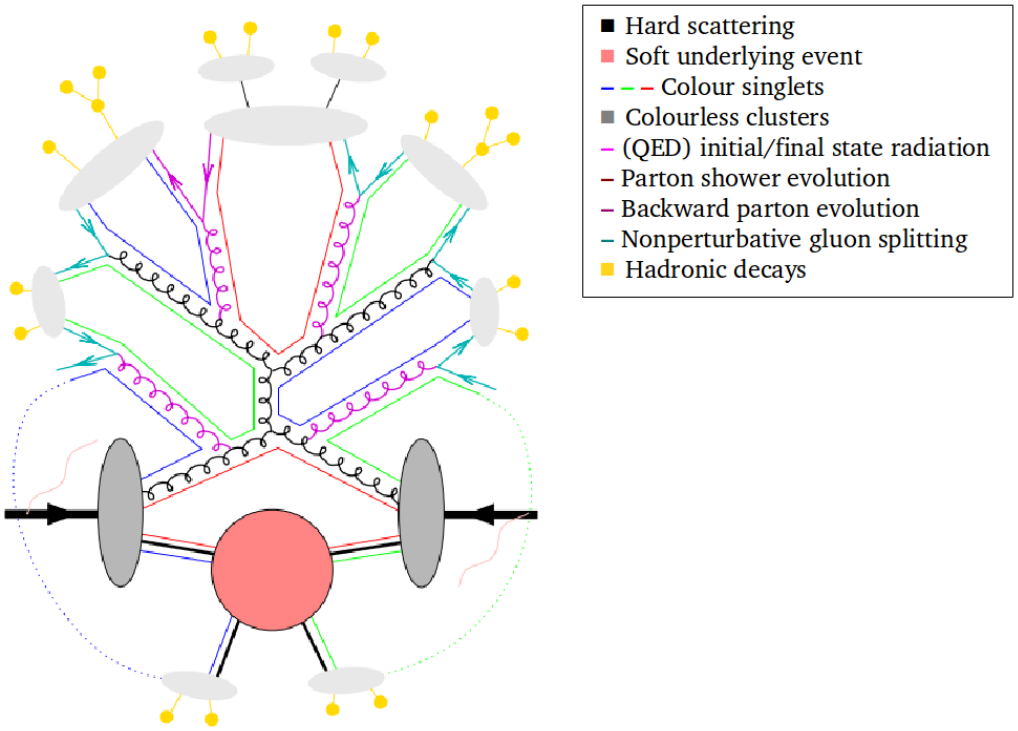

FIGURE 3.17: The structure of a pp collision, showing the different stages involved in dijet production via $gg \rightarrow gg$. Image taken from Ref. [63].

Event generation starts by calculating the probability distribution of a particular hard scatter, which are the subprocesses with the largest invariant momentum transfer. The incoming partons are described by PDFs whilst the matrix elements of the hard subprocesses are perturbatively computable, giving a probabilistic distribution of the outgoing partons.

Parton shower algorithms are used to simulate higher order processes, describing the incoming and outgoing partons associated with the hard collision. A cascade of partons, largely gluons, are produced by the colour charges that are created or annihilated in a pair creation process, or accelerated in a scattering process. The parton shower can be simulated as a series of interactions, starting at the hard process and working downwards to low momentum scales. The evolution of this momentum transfer stops at scales of the order 1 GeV, at which point perturbation theory breaks down.

At momentum scales below this, hadronisation models are used. Hadronisation denotes the process by which the set of coloured partons, after showering, are

transformed into a set of colour-singlet primary hadrons.

The underlying event is made up of any secondary interactions between the remaining partons in the initial protons. These interactions produce soft hadrons, which contaminate the hard process already simulated.

Finally, many of the simulated hadrons are unstable particles that go on to decay. Efforts to model the decay of these heavy resonances are also made within the event generator software.

Several event generators are available on the market, but only those used in this thesis are mentioned here.

Pythia is a general-purpose event generator widely used by the LHC collaborations. The Pythia program is designed specifically for generating high energy particle collisions such as the pp collisions at the LHC, incorporating a wide range of theories and models from research and literature. This includes the hard and soft interactions between the proton constituents as well as parton distributions, parton showers, multiparton interactions, fragmentation and decay. Here, the Pythia8B branch of Pythia [64] was used to produce b-events using repeated hadronisation. The events with b quarks in the fiducial volume were selected and used to provide information of the strong and electroweak B decays.

The MC samples used in this thesis (see Chapter 5) were generated using parton distributions obtained by the Coordinated Theoretical-Experimental Project on QCD (CTEQ) Collaboration in a global fit using the LO hard cross sections in Ref. [65]. The physics approximations made by Pythia allow for a number of free parameters that must be tuned to the experimental data. The tuning of the event generator was set to the `AU2` (denoting 'ATLAS Underlying event 2') tune series for simulation of the underlying event [66]. This allowed Pythia's response to each parameter variation to be measured and optimised. Following the Pythia generation, the appropriate B meson type was input to EvtGen [67] to decay according to the channel specified.

EvtGen is a MC generator developed for B decays and specialised for each experiment using it. EvtGen has a wide but not exhaustive list of decay models to describe potential B decay modes of interest in generated MC. A summary of the EvtGen decay models used in this analysis and their associated nomenclature is given in Table 3.1.

TABLE 3.1: A list of the EVTGEN decay models used in the generation of signal and background MC samples.

Decay model	Description
PHSP	Decays generic phase space to n-bodies.
PHOTOS	Generates final state photons on a generated decay.
VLL	Decays a vector meson to a pair of charged leptons.
VSS	Decays a vector particle into two scalars.
SVV_HELAMP	Decays a scalar to two vectors. The decay amplitude is specified by the helicity amplitudes which are given as arguments for the decay.
VVP	Decays a vector to a vector and a photon.
SVS	Decays a scalar to a vector and a scalar.
TSS	Decays a tensor particle to two scalar mesons.
ETA_DALITZ	Decays η to 3 πs with measured dalitz amplitude.
BTOSLLALI	Decays $b \to sll$ according to Ali '02 et al.

Following the event generation, simulation of the ATLAS detector geometry is performed by several detector description and simulation tools. These are GEometry ANd Tracking (GEANT4) [68], ATLFASTII [69], Fast ATLAS Track Simulation (FATRAS) [70] and Integrated Simulation Framework (ISF) [71].

The GEANT4 system describes the experimental setup of the ATLAS detector, the particle trajectories as they pass through the different subdetector mediums and the response of the electronic components of the detector. For each subdetector the GEANT4 system includes a model of how the ionisation in the active detector element is changed into the digital output of the readout electronics, a step known as digitisation.

Simulations can be very demanding on the computing power and thus the remaining three detector simulation software tools provide a simplified detector description providing much faster simulations whilst retaining a sufficient level of detail of the physical and real material effects.

FATRAS is a software used for the fast simulation of processes inside the ATLAS ID and MS. Compared to GEANT4, FATRAS describes the detector components as thin discrete layers and spends less time simulating secondary particles

in interactions with the detector material. These factors provide simulations 100 times faster than GEANT4.

AtlFastII combines a fast calorimeter simulation [72] with the full GEANT4 simulation of the ID and MS. In AtlFastII, muons are the only particles simulated with GEANT4 in the calorimeter. These muons can reach the MS, providing a factor of ten increase in speed compared to GEANT4.

ISF provides the user interface to specify which particles, subdetectors and phase space regions will be simulated by GEANT4 and which will be handled by the fast simulation packages. This allows only particles or events relevant to the user to be simulated with high precision whilst the rest are approximated, saving time and computing power.

The final step in the event simulation involves the reconstruction of the kinematic information and particle identification. The tracks are reconstructed from the hits in the individual detector elements in the ID and the MS, and clusters of deposited energy within the calorimeter cells. The information obtained from each of the steps in the event simulation is combined to provide the full kinematic information of the event. This information is subsequently used in the MC event selection, described in Chapter 4.

Chapter 4

Event Selection

This chapter describes the selection of signal events for the angular analysis of the decay $B_d^0 \to K^{*0}\ \mu^+\mu^-$. The event information was retrieved from 20.3 fb^{-1} of data recorded in 2012 primarily by the ATLAS ID and MS. The technical details of the individual tracking and trigger sub-detectors were described in Chapter 3. The event selection outlined below is based on studies performed as part of the ATLAS $B_d^0 \to K^{*0}\ \mu^+\mu^-$ angular analysis using 2011 data. The 2011 version of the analysis was retracted due to issues related to the software that affected the final result, but information obtained from the studies in this previous iteration were relied upon here, where possible.

The identification, reconstruction and optimisation of the signal decay was carried out in four phases. In the first phase, all events passing a set of trigger requirements were selected, as discussed in Section 4.1. The second phase was the 'pre-selection' phase, in which the basic event reconstruction was performed, as described in Section 4.2. A set of more stringent 'final selection' criteria were imposed in the third phase in order to distinguish the signal from other very similar background decays, as outlined in Section 4.3. The final phase removed any remaining multiple candidates in an event using the procedure described in Section 4.4.

4.1 Trigger Selection

The trigger selection for this analysis exploited the dimuon signature of the signal candidates, searching for events that satisfied triggers designed to select one or

more muons in an event from the prompt muon and delayed B physics trigger streams.

However, not all of the triggered events could be used inclusively. The analysis relied upon MC simulation, where not all data trigger configurations were included. One example of the data-MC trigger differences was related to the trigger prescales, which were found to vary for certain trigger chains in data but were not simulated in MC. Consequently only events that passed trigger chains in both the data and MC were accepted.

The data trigger selection strategy was based on the set of offline selection requirements and best candidate selection criteria for $q^2 < 6\ (GeV/c^2)^2$ described in Sections 4.2-4.4. A list of events that passed these criteria and their corresponding trigger chains were used to iteratively build a list of the most efficient trigger chains based on their availability during 2012 running and prescale factor. The trigger chain that contributed the highest fraction of events was selected and each of the events collected by it excluded one-by-one. The procedure was repeated for the remaining chains until a voluntary stop, set at 15 trigger chains.

The dominant contribution was found to come from chains corresponding to $B \to \mu^+\mu^- X$ events (`BmumuX` chains), where X represents one or more hadronic tracks in the final state. The `BmumuX` triggers stem from L1 dimuon triggers. The HLT uses these L1 muons in conjunction with hit information from the ID to build tracks corresponding to events with a $B \to \mu^+\mu^- X$ topology, including $B_d^0 \to \mu^+\mu^- K^{*0}$ candidates. These events are closely related to each other, thus for consistency reasons they were used altogether, adding four additional trigger chains to the final list.

The remaining trigger chains were made up of low-p_T single-muon (`mu`), two-muon (`2mu`), three-muon (`3mu`) and dimuon (`DiMu`) vertex chains, seeded from L1, L2 and EF triggers. In some instances an Event Filter Full Scan (EFFS) was performed over the whole detector volume. A full scan at the EF has the potential to identify a second softer muon in cases where only one muon fired an L1 trigger. As the trigger efficiency at L1 is relatively low compared to L2 and EF (see Section 3.3.1), EFFS increases the trigger efficiency for dimuon pairs. However, these full scans are computationally expensive so cannot be performed for every event.

The combination of the 15 most contributing trigger chains and four additional trigger chains was found to preserve 93% of events in the data sample, triggering

a total of 1497 events. A description of the terms used in the trigger chain names is given in Table 4.1 and a breakdown of the number of events retrieved from each trigger chain is shown in Table 4.2. The 19 trigger chains were able to achieve sensitivity in even the lowest q^2 region, resulting in triggered events across the full q^2 range of interest for this thesis, $(0.04 < q^2 < 6.00)$ $(GeV/c^2)^2$.

TABLE 4.1: A breakdown of the trigger chain naming scheme.

Naming convention	Criteria
`Bmumux_v2`	Requires events with a $B \to \mu^+\mu^- x$ topology, where x represents one or more hadronic tracks in the final state.
`NmuX(T)`	Requires N muons with $p_T > X$ GeV/c.
`EF`	Requires the trigger chain to be present in the event filter.
`EFFS`	Requires a full scan at the EF. The FS is used to identify softer muons in cases where only one muon fired an L1 trigger.
`L2StarB`	Requires the L2Star algorithm framework is used [73]. The L2 algorithms were implemented and optimised within this framework for 2012 data taking.
`j65_a4tchad`	Requires a jet with transverse energy above 65 GeV.
`xen`	Requires the missing transverse energy, based on calibrated clusters of calorimeter cells without postfix, to be above n GeV.
`tclcw`	Requires the topocluster-based algorithm [74] is used, where the calibrated topological clusters are summed at the EF.
`loose/tight`	Requires either cut-based loose or tight identification.
`BarrelOnly`	Requires candidates in the barrel detector region.
`MSonly`	Requires candidates in the muon spectrometer.
`DiMu_noVtx_noOS`	Requires two muons at L1, but does not require vertex or opposite sign conditions.

By only considering triggers that were available in both data and MC, the MC was strategically reweighted in order to replicate the effect of the prescaling in the data. The trigger chains were categorised into three groups, according to their prescaling. A summary of the trigger weights is given in Table 4.3.

The first group contained unprescaled triggers that were operational throughout the entirety of 2012, with a luminosity fraction $\mathcal{L}_{frac} = 0.999779$ of the total luminosity. Events passing any of the unprescaled triggers had a weight, $w = 1$, applied. If none of the eight triggers in group 1 were fired, the second group was checked.

TABLE 4.2: The 15 most efficient trigger chains from data and four additional `BmumuX` chains.

Iteration	Most effective trigger chain	Events recorded	Events left
	Total		1603
1	EF_mu4Tmu6_Bmumux_v2	889	714
2	EF_2mu4T_Bmumux_v2_L2StarB	182	532
3	EF_mu4T_j65_a4tchad_xe60_tclcw_loose	120	412
4	EF_mu18_tight_mu8_EFFS	90	322
5	EF_2mu8_EFxe30_tclcw	50	272
6	EF_mu36_tight	40	232
7	EF_2mu4T_Bmumux_v2	23	209
8	EF_3mu4T	23	186
9	EF_2mu4T_Bmumux_BarrelOnly_v2_L2StarB	22	164
10	EF_mu24_j65_a4tchad_EFxe40_tclcw	20	144
11	EF_mu24_tight_mu6_EFFS	9	135
12	EF_mu24_tight	7	128
13	EF_2mu6_Bmumux_v2_L2StarB	7	121
14	EF_mu40_MSonly_barrel_tight	7	114
15	EF_2mu6_DiMu_noVtx_noOS	5	109
	EF_2mu6_Bmumux_v2	1	108
	EF_mu4Tmu6_Bmumux_v2_L2StarB	1	107
	EF_2mu4T_Bmumux_Barrel_v2_L2StarB	1	106
	EF_mu4Tmu6_Bmumux_Barrel_v2_L2StarB	0	106

The second group contained 12 of the aforementioned `Bmumux` trigger chains. These were not available for about 30% of the integrated luminosity collected in 2012, due to their introduction part way through running. Additionally, some of these triggers were switched off at a specific instantaneous luminosity, as their rates became too high. Each of the `Bmumux` chains had to be weighted according to their respective collected luminosity, ranging between $0.58 - 0.70$ of the total integrated luminosity.

If neither the first nor second group of triggers were fired, those from the third group were checked. The third group contained the remaining two triggers. These triggers were operational throughout 2012, but were heavily prescaled. Under the assumption their prescales are uncorrelated, the trigger weight defined was:

$$w = 1 - \prod_{i=1}^{n} (1 - \mathcal{L}^{i}_{frac}), \tag{4.1}$$

where $\mathcal{L}^{i}_{frac}$ is the luminosity fraction collected by the i^{th} trigger chain and the product is taken over all triggers of the third group which are fired. The weight of these triggers was calculated to be 0.15.

TABLE 4.3: A breakdown of the trigger weights applied to the 19 trigger chains for MC reweighting.

Group	Trigger chains	Weight
1 (unprescaled)	EF_mu4T_j65_a4tchad_xe60_tclcw_loose	1.0
	EF_mu18_tight_mu8_EFFS	1.0
	EF_2mu8_EFxe30_tclcw	1.0
	EF_mu36_tight	1.0
	EF_3mu4T	1.0
	EF_mu24_j65_a4tchad_EFxe40_tclcw	1.0
	EF_mu24_tight_mu6_EFFS	1.0
	EF_mu40_MSonly_barrel_tight	1.0
2 (moderate prescaling)	EF_2mu6_Bmumux_v2	0.69
	EF_2mu6_Bmumux_v2_L2StarB	0.69
	EF_2mu4T_BarrelOnly_Bmumux_v2	0.69
	EF_2mu4T_BarrelOnly_Bmumux_v2_L2StarB	0.69
	EF_mu4Tmu6_Bmumux_v2	0.68
	EF_mu4Tmu6_Bmumux_v2_L2StarB	0.68
	EF_2mu4T_Bmumux_Barrel_v2	0.65
	EF_2mu4T_Bmumux_Barrel_v2_L2StarB	0.65
	EF_mu4Tmu6_Barrel_Bmumux_v2	0.64
	EF_mu4Tmu6_Barrel_Bmumux_v2_L2StarB	0.64
	EF_Barrel_Bmumux_v2_L2StarB	0.58
	EF_2mu4T_Bmumux_v2	0.58
3 (heavily prescaled)	EF_mu24_tight	0.15
	EF_2mu6_DiMu_noVtx_noOS	0.15

Finally, if an event didn't pass any of the three stages of trigger weighting, it was rejected.

The effective trigger efficiency for $B_d^0 \to K^{*0}\ \mu^+\mu^-$ was estimated using the sum of weights as applied to the signal MC. The efficiencies were calculated to be $28.0 \pm 0.2\%$ for the flat MC, $29.4 \pm 0.1\%$ for SM MC and $29.1 \pm 0.1\%$ for $\overline{B}_d^0 \to \overline{K}^{*0}\ \mu^+\mu^-$ SM MC. These three signal MC samples are described in detail in Section 5.1.

4.2 Pre-Selection

The selection of events in the data was based on their topology: signal-like events had two muon tracks and two hadronic tracks, coming from the same decay vertex. In reality the kaon and pion hadronic tracks come from a secondary decay vertex

of $K^{*0} \to K^+\pi^-$, but due to the short lifetime of K^{*0} of approximately 10^{-20} s, the detector is not able to resolve the two vertices.

The reconstructed data was analysed for all possible signal candidates. The algorithms used to find and record these candidates were from the B-physics analysis packages in the ATLAS Athena framework [75]. The Athena framework is an enhanced version of the Gaudi Common Framework Project [76] designed by the LHCb experiment for a wide range of physics data-processing applications. The packages used in this thesis were valid for Athena release `17.2.X`.

Candidate events from decays of J/ψ or Υ mesons ('Onia' decays) to two muons were selected from the combined muon and B data containers. The full decay sequences were retrieved, down to the final state tracks and loose cuts on candidate masses, p_T, and vertex χ^2 per degree of freedom were imposed. Dimuon pairs of opposite sign were considered if their combined mass fell within the range $(0 < M(\mu^+\mu^-) < 5500)\ MeV/c^2$ and their vertex χ^2 per degree of freedom was $\chi^2/n.d.f. < 20$.

B candidates were identified by fitting four tracks to a common vertex. Two of these tracks were required to come from muons with $p_T > 0.5\ GeV/c$, identified by the trigger, and two tracks were required to be oppositely signed particles, not identified as muons.

The primary vertex (PV) of the B candidate was chosen as the vertex with the smallest impact parameter, d_0, to the reconstructed 4-momentum of the B.

Secondary vertices for the B and K^{*0} candidates were refitted, the primary vertices were refitted without the four tracks from $K^+\pi^-$ $\mu^+\mu^-$ and additional cuts were applied:

- B vertex $\chi^2/n.d.f. < 15$
- B mass in the range $(4600 < M_{B_d^0} < 6000)\ MeV/c^2$
- K^{*0} mass in the range $(600 < M_{K^{*0}} < 1050)\ MeV/c^2$.

All B candidates were recorded for subsequent analysis. Some events had more than one B candidate per event and often these arose from the K and π track assignment for the K^{*0} daughter tracks. The methodology for reducing this to a single candidate per event is discussed in Section 4.4.

4.3 Final Candidate Selection

After pre-selection, final analysis cuts were implemented on the reconstructed n-tuples. The final selection cuts can be subdivided into three main stages. In the first stage a set of quality cuts connected to the track reconstruction of the muons and hadrons were applied. The second stage applied a set of baseline cuts relating to the $B_d^0 \to K^{*0}(\to K^+\pi^-)\ \mu^+\mu^-$ analysis. The signal to background ratio was optimised through a third set of cuts.

Track reconstruction in the ID, described in Section 3.2.2, begins with a pre-processing stage in which the raw data collected by the pixel and SCT detectors is converted into clusters based on silicon sensors in which a signal was recorded. The SCT uses information from both sides of the module to convert these clusters into space-points.

Prompt tracks were identified close to the IP and track seeds are built by joining clusters in the three pixel layers and the first SCT layer. These track seeds then e extended through the rest of the SCT. If the fitted track crosses a cluster, it is classified as a hit; if the fitted track crosses a silicon sensor that does not have a generated cluster associated with it, it is classified as a hole. The selected tracks were then extended to the TRT to be refitted with the full ID information.

The performance of muon reconstruction during the first run of data taking on ATLAS was studied in Ref. [77]. A selection of requirements to optimise the quality of ID tracks used for combined muons is given. This analysis required at least one of the muons in the final state dimuon pair to be a combined muon, therefore the following requirements were imposed:

- at least 1 Pixel hit;
- at least 5 SCT hits;
- at most 2 active Pixel or SCT sensors traversed by the track but without hits;
- at least 9 TRT hits in the region of full TRT acceptance, $0.1 < |\eta| < 1.9$.

The baseline cuts for $B_d^0 \to K^{*0}(\to K^+\pi^-)\ \mu^+\mu^-$ were adopted from the 2011 ATLAS analysis of $B_d^0 \to J/\psi K^{*0}$ [78] to impose more stringent constraints on

the $|\eta|$ of the tracks, B_d^0 mass, K^{*0} mass, final state particle p_T, K^{*0} p_T, and the B and dimuon vertex $\chi^2/n.d.f.$.

In order to account for ID acceptance effects, the four tracks corresponding to the $K^+\pi^-\mu^+\mu^-$ final state particles, as well as the K^{*0}, B and dimuon candidates were required to have $|\eta| < 2.5$. The world average K^{*0} mass is (891.66 ± 0.26) MeV/c^2 with an average width of (50.8 ± 0.9) MeV/c^2 [19]. Likewise, the world average B_d^0 mass is (5279.55 ± 0.26) MeV/c^2.

The mass range of the K^{*0} was restricted to $[846, 946]$ MeV/c^2, representing one K^{*0} width either side of its PDG mass.

The B candidate mass range was initially defined in the same way to be $[4900, 5700]$ MeV/c^2, however this range was reduced to $[5150, 5700]$ MeV/c^2 in order to remove a background caused by partially reconstructed decays peaking at low B masses. These decays and the subsequent mass cut are discussed fully in Chapters 8 and 9.

The p_T cuts imposed were $p_T(\mu) > 3500$ MeV/c and $p_T(K, \pi) > 500$ MeV/c. Finally the muon pairs were refitted to a common vertex with $\chi^2/n.d.f. < 10$ to exclude random combinations of the tracks.

The cuts described above were optimised using the MC samples, introduced in Chapter 5, to select the signal decay and suppress the background by maximising the estimator:

$$P(N_{sig}, N_{bckg}) = \frac{N_{sig}}{N_{sig} + N_{bckg}}, \tag{4.2}$$

where N_{sig} is the number of selected signal events and N_{bckg} the number of background events.

The B_d^0 meson has a relatively long lifetime, $\tau_{B^0} = (1.520 \pm 0.004) \times 10^{-12}$ s [19], which was exploited to remove background contributions from short lived hadrons. A large proportion of $b\bar{b} \to \mu^+\mu^- X$ events along with most $c\bar{c} \to \mu^+\mu^- X$ and Drell-Yan events were removed by applying a cut on the lifetime significance, τ/σ_τ, where the decay time uncertainty σ_τ was calculated for each candidate from the covariance matrices associated with the four-track vertex fit and with the primary vertex fit.

The 3D pointing angle, θ, is defined as the angle between the reconstructed direction of flight of the B and its reconstructed 3-momentum vector. This translates into the vector that runs between the primary vertex and the reconstructed B_d^0 vertex, which optimally is equal to zero such that $\cos\theta$ is very close to one for real B_d^0 decays.

In order to ensure the reconstructed K^{*0} candidates were produced in B decays rather than from separate interactions, a further cut on $p_T(K^{*0})$ was imposed.

The quality of the measured B candidates was improved further by a tighter B vertex $\chi^2/n.d.f.$ cut.

A final selection requirement was applied to constrain radiative charmonium decays originating from decays such as $B_d^0 \to (J/\psi, \psi(2S))K^{*0}$, in which the $c\bar{c}$ meson decays to $\mu^+\mu^-\gamma$, with the photon escaping undetected. These were removed via the requirement that $|(m(B_d^0)_{rec} - m(B_d^0)_{PDG}) - (m(\mu^+\mu^-)_{rec} - m(J/\psi)_{PDG})| < \Delta m$.

To find the optimal values of these selection parameters, a discrete scan through parameter space was performed. The highest estimator value corresponded to the following cuts:

- $\tau/\sigma_\tau > 12.75$
- $\cos\theta > 0.999$
- $p_T(K^{*0}) > 3000\ MeV$
- B vertex $\chi^2/n.d.f. < 2.0$
- $\Delta m = 130\ MeV/c^2$.

4.4 Best Candidate Selection

After all the selection requirements described in Sections 4.2 and 4.3 were applied, approximately 15% of the remaining events contained multiple candidates. In order to select the best candidate in each event for fitting the following procedures were adopted in order, in a two-step process:

The first procedure was to identify the candidate with the best reconstructed B vertex $\chi^2/n.d.f$ for each event, removing about 4% of multiple candidates.

Of the remaining events, the four final state particles, split into a dimuon and dihadron pair, were reconstructed to a common vertex. The dihadron pair h^+h^- were assigned the $K^+\pi^-$ and π^+K^- masses in turn with both combinations saved in the selection process. The second procedure for removing multiple candidates picked the combination of h^+h^- with $m(K\pi)$ closest to the PDG value of $m(K^{*0})$. This was found to be the dominant source of multiple candidates in events after the selection was imposed.

The 4-track combination with better K^{*0} mass significance from the reconstruction of $M_{K\pi}$ was selected. (In contrast, the 2011 analysis selected the candidate with $M_{K\pi}$ closest to the K^0 mass. This candidate selection procedure biases the $M_{K\pi}$ distribution, which is the reason why it was not considered for inclusion as a discriminating variable in the fit.)

The final average number of candidates per event in data was 1.123. Similar values were recorded for the signal, control sample and background MC samples, as seen in Table 4.4. The nomenclature used in Table 4.4 to describe the decays is described fully in Chapter 5.

TABLE 4.4: Average number of candidates per event in different samples after the full event selection has been applied.

MC type	Mode	Av. candidates/event
–	Data	1.123
Signal	$B_d^0 \to K^{*0}\mu^+\mu^-$ (EVTGEN, PHSP)	1.173
	$B_d^0 \to K^{*0}\mu^+\mu^-$ (EVTGEN, SM)	1.173
	$\overline{B}_d^0 \to \overline{K}^{*0}\mu^+\mu^-$ (EVTGEN, SM)	1.173
Control channel	$B_d^0 \to K^{*0}J/\psi$ (EVTGEN)	1.160
	$B_d^0 \to K^{*0}\psi(2S)$ (EVTGEN)	1.178
S-wave	$B_d^0 \to K^+\pi^-\mu^+\mu^-$ (EVTGEN)	1.107
Peaking background	$B_d^0 \to \phi J/\psi$ (PYTHIA)	1.049
	$\Lambda_b \to \Lambda J/\psi$ (PYTHIA)	1.047
	$\overline{\Lambda}_b \to \overline{\Lambda} J/\psi$ (PYTHIA)	1.037
	$B_d^0 \to K_S J/\psi$ (PYTHIA)	1.050
	$B_d^0 \to K_S\psi(2S)$ (PYTHIA)	1.084
	$\Lambda_b \to \Lambda\psi(2S)$ (PYTHIA)	1.130
	$\overline{\Lambda}_b \to \overline{\Lambda}\psi(2S)$ (PYTHIA)	1.094
	$B_u^+ \to K^+ J/\psi$ (PYTHIA)	1.014
	$B_u^+ \to \pi^+ J/\psi$ (PYTHIA)	1.010
	$B_u^+ \to K^- J/\psi$ (PYTHIA)	1.016
	$B_u^+ \to K^{*0}\mu^+\mu^-$ (EVTGEN)	1.115
	$B_s^0 \to \phi\mu^+\mu^-$ (EVTGEN)	1.051
	$B_u^+ \to K^{*+}(K^0\pi^+)\mu^+\mu^-$ (EVTGEN)	1.027
	$B_s^0 \to K^{*0}J/\psi$ (EVTGEN)	1.171
	$B_d^0 \to K^{*0}\phi$ (EVTGEN)	1.147
	$\Lambda_b \to \Lambda\mu^+\mu^-$ (EVTGEN)	1.093
	$\Lambda_b \to \Lambda(pK^-)\mu^+\mu^-$ (EVTGEN)	1.125
Comb. background	$b\bar{b} \to \mu^+\mu^- X$ (PYTHIA)	1.142
	$b\bar{b} \to \mu^+\mu^- X$ (EVTGEN)	1.159
	$b\bar{b} \to \mu^+\mu^- X$ (PYTHIA, AA)	1.223
	$b\bar{b} \to \mu^+\mu^- X$ (PYTHIA, AB)	1.213
	$b\bar{b} \to \mu^+\mu^- X$ (PYTHIA, BA)	1.209
	$b\bar{b} \to \mu^+\mu^- X$ (PYTHIA, BB)	1.268
	$c\bar{c} \to \mu^+\mu^- X$ (PYTHIA)	1.146

Chapter 5

Backgrounds

This chapter documents the background studies performed in order to establish a comprehensive model of the channels that contribute significantly to the signal region. The signal was simulated using the MC samples described in Section 5.1. The background was described by two components: a smooth combinatorial background and a peaking background. These two types of background were studied separately using MC samples described in Section 5.2 and 5.3 for combinatorial and peaking backgrounds, respectively.

To conclude on the relevant background MC samples, an extensive list of decays with a similar topology to the signal were considered. Given the quark breakdown of the signal $d\bar{b} \to d\bar{s}\mu^+\mu^-$, these decays were categorised as follows:

- A change in the spectator quark.
- A change in the non-spectator quark.
- Hadron misidentification.
- Three body decays, in which an independent fourth particle is misreconstructed as part of the decay.
- Five body decays, in which one particle is neglected in the reconstruction.

Many of these channels were immediately omitted owing to significant differences between their invariant mass ranges and the signal mass region, or through incompatible daughter particles. Decays that were considered but found to be negligible

are summarised in Appendix A in Tables A.1, A.2 and A.3 for B_d^0, B_s^0 and B_u^+ decays, respectively.

Decays involving *fake muons* were considered, referring to either true muons measured in the MS but not produced promptly in the decay of a B meson or to hadronic punch through, whereby hadrons are not contained within the calorimeter but instead produce a track in the MS. The combined contribution of fake muons is measured to be $< 0.5\%$ ($< 0.3\%$) for kaon (pion) tracks in the MS [79], making these modes insignificant relative to the signal in this analysis.

Modes predicted to be negligible as a result of the considerations above are not discussed further and were not officially requested for generation and reconstruction. Several other modes required more in-depth investigations via event simulation in order to assess whether they needed to be treated as a source of background in this analysis.

The initial MC tests were performed at truth level after applying the first stage of simulation, before detector effects and trigger information was applied. Once the cuts and distributions had been validated, the propagation of the EvtGen outgoing particles and their properties through the ATLAS detector were simulated. The signals corresponding to interactions between the decay particles and the detector layers were digitised before the trigger and offline reconstruction software was applied to provide consistency with the data.

The distributions describing each decay were obtained and the remaining final selection requirements described in Section 4.3 were applied.

In instances when the cross section of the relevant process was known, the expected yields were calculated using the analysed integrated luminosity, $\mathcal{L}_{analysed}$, and cross section, σ; otherwise the number of B mesons in data, N_B, and the branching fractions of the decay chain[1], $\mathcal{BR}$, were used:

$$\begin{aligned} N_{data} &= \mathcal{L}_{analysed} \times \sigma \times \epsilon, \\ &= N_B \times \mathcal{BR} \times \epsilon \times Z, \end{aligned} \tag{5.1}$$

[1]The branching fractions included the entire decay chain from the primary B meson decay through to a set of particles resembling the signal final state. The $K^{*0} \to K^+\pi^-$ rate was taken as the corresponding Clebsch-Gordon coefficient (2/3) with an assumed error of zero.

where $\epsilon = N_i/N_{tot}$ for N_i events in a given q^2 bin of the MC simulated data out of N_{tot} events across all q^2 bins. Here Z is the scale and represents the normalisation required to account for the relevant ratio of b quark fragmentation fractions. The b quark fragmentation fractions, f_x, correspond to the probability that the b quark is bound to a quark of flavour x. For B^0_d decays Z is equal to one, representing f_d/f_d. Similarly for B^+_u decays the approximation $Z = f_u/f_d \approx 1$ was made by assuming $SU(2)$ isospin symmetry. For B^0_s decays, the scale $Z = f_s/f_d = 0.240 \pm 0.010$ was applied using the result from the ATLAS analysis at $\sqrt{s} = 7\,TeV$ in Ref. [80]. The Λ_b normalisation $f_{\Lambda_b}/f_d = 0.629 \pm 0.0006$ was calculated as $f_{\Lambda_b}/f_d = (f_{\Lambda_b}/f_s) \times (f_s/f_d)$ where $(f_{\Lambda_b}/f_s) = 1.65 \pm 0.10$ was calculated as the naive average from LHCb [81] and CDF results [82][2].

The majority of the potential background modes were found to have negligible contributions, where a significant background contribution was defined as more than 0.25 events in a given 1 $(GeV/c^2)^2$ wide q^2 bin after selection requirements. The full list of the channels requested for MC simulation is given in Table 5.1 with their expected yields per q^2 bin. The exclusive decays were produced using a combination of Pythia8B and EvtGen event generators, where the nomenclature used for the EvtGen decay models is given in Table 3.1. The signal and background decays that passed the 0.25 event threshold in a 1 $(GeV/c^2)^2$ wide q^2 bin are described in the following sections. The Pythia8B $b\bar{b} \to \mu^+\mu^- X$ samples are labelled AA-BB, representing four different dimuon combinations that could contribute to the combinatorial background. These are described in more detail in Section 5.2.

5.1 Signal MC

In the previous iteration of this analysis, using data collected in 2011 by the ATLAS experiment, signal MC was produced using Pythia8B. For consistency, the equivalent sample was generated here. However, Pythia8B was found to generate an incorrect q^2 distribution such that all of the events fell into the lowest bin $q^2 \in [0.04, 2.00]$ $(GeV/c^2)^2$, thus this MC sample was not used in further studies.

[2]Both LHCb and CDF have measured f_{Λ_b}/f_s as $f_{\Lambda_b}/f_s[LHCb] = 1.544$ and $f_{\Lambda_b}/f_s[CDF] = 1.75$.

TABLE 5.1: The different background MC samples studied at truth level, broken down by bins of q^2. The bin number corresponds to the lower bound on q^2 for a 1 $(GeV/c^2)^2$ wide bin. The S-wave and non-resonant contributions are assumed to be at 5% of the level of the resonant contributions.

Process	bin 0	bin 1	bin 2	bin 3	bin 4	bin 5
$b\bar{b} \to \mu\mu X$ (PYTHIA8B)	–	–	–	–	–	–
$b\bar{b} \to \mu\mu X$ (EVTGEN)	–	–	–	–	–	–
$b\bar{b} \to \mu\mu X$ (PYTHIA8B: AA)	–	–	–	–	–	–
$b\bar{b} \to \mu\mu X$ (PYTHIA8B: AB)	–	–	–	–	–	–
$b\bar{b} \to \mu\mu X$ (PYTHIA8B: BA)	–	–	–	–	–	–
$b\bar{b} \to \mu\mu X$ (PYTHIA8B: BB)	–	–	–	–	–	–
$c\bar{c} \to \mu\mu X$	–	–	–	–	–	–
$B_s \to J/\psi\phi$	0	0	0	0	0	0.096
$\Lambda_b \to \Lambda J/\psi$	0	0	0	0	0	0
$\overline{\Lambda}_b \to \overline{\Lambda} J/\psi$	0	0	0	0	0	0
$B_d \to J/\psi K^0_S$	0	0	0	0	0	0
$B_d \to \psi(2S) K^0_S$	0	0	0	0	0	0
$\Lambda_b \to \Lambda\psi(2S)$	0	0	0	0	0	0
$\overline{\Lambda}_b \to \overline{\Lambda}\psi(2S)$	0	0	0	0	0	0
$B^+ \to J/\psi K^+$	0	0	0	0	0	0
$B^+ \to J/\psi \pi^+$	0	0	0	0	0	0
$B^- \to J/\psi K^-$	0	0	0	0	0	0
$B^\pm \to K^{*+}\mu\mu$	0.17	0.12	0.025	0.25	0.12	0.22
$B_s \to \phi\mu\mu$	0.4	0.19	0.22	0.23	0.25	0.28
$B_d \to K^*\mu\mu$ (PHSP)	1200	1200	1500	1500	1600	1700
$B_d \to K^*\mu\mu$ (SM)	160	72	77	81	90	102
$\overline{B}_d \to K^*\mu\mu$ (SM)	160	70	73	80	88	102
$B_d \to J/\psi K^*$	0	0	0	0	1.0	2.1
$B_d \to \psi(2S) K^*$	0	0	0	0.08	0.08	0.24
$B^\pm \to K^+\mu\mu$	0.89	0.81	1.0	1.3	1.5	1.9
$B^0_d \to K^+\pi^-\mu\mu$	2.5	2.6	3.0	3.2	3.4	3.4
$B_s \to J/\psi K^*$	0	0	0.0045	0.0045	0	0.013
$B^0_d \to \phi K^*$	0.28	0.4	0	0	0	0
$\Lambda_b \to \Lambda(1520)\mu\mu$	3.9	4	4.5	4.8	4.9	5.2
$\Lambda_b \to Kp\mu\mu$	0.052	0.046	0.059	0.062	0.062	0.065

Four alternative signal MC samples were fully generated and reconstructed for this analysis, summarised in Table 5.2. The selection efficiencies for the MC samples

are quoted, where the efficiency is defined as the number of candidates that pass the selection requirements in Chapter 4 divided by number of candidates before these criteria are imposed.

TABLE 5.2: Description of the signal MC samples generated. The selection efficiencies for the MC samples are quoted for all q^2.

Process	Generator	Decay Models	Events generated	Efficiency (%)
$B_d^0 \to K^{*0}\mu^+\mu^-$	EVTGEN	PHSP	50M	8.3
$B_d^0 \to K^{*0}\mu^+\mu^-$	EVTGEN	PHOTOS BTOSLLBALL, VSS	5M	5.6
$\overline{B}_d^0 \to \overline{K}^{*0}\mu^+\mu^-$	EVTGEN	PHOTOS BTOSLLBALL, VSS	5M	5.5
$B_d^0 \to K^+\pi^-\mu^+\mu^-$	EVTGEN	PHSP	20M	0.27

A large sample of $B_d^0 \to K^{*0}\mu^+\mu^-$ MC was generated using the generic phase space decay model, PHSP [67], in which all the spins of the particles in the initial and final state are averaged. The configuration of this model specifies the amplitudes between the initial and final states of the decay chain such that the helicity angles are generated flat in phase space. This assumes no phase difference between the three amplitudes in Eq. (2.31) with $A_\lambda = 1.0$ and hence an F_L value equal to $\frac{1}{3}$. This signal MC sample was used to model the detector acceptance effects, as described in Section 6.2.

A second signal MC sample was generated using the BTOSLLBALL model [67], designed to implement $b \to sll$ decays according to the semileptonic and penguin FFs calculated using the parameterisation in Ref. [36]. This model produces SM-like angular distributions, with expected F_L and A_{FB} values corresponding to those shown in Figure 5.1. The equivalent MC sample was also generated for the anti-decay $\overline{B}_d^0 \to \overline{K}^{*0}\mu^+\mu^-$. In both cases, the K^{*0} mesons were decayed via the VSS decay model describing a vector meson to a pair of scalar mesons and the PHOTOS package [67] was included to incorporate effects of final state radiation on the generated decays.

The final signal MC sample generated was the non-resonant $B_d^0 \to K^+\pi^-\mu^+\mu^-$ S-wave contribution, with the same final state as the P-wave signal. Interference between the S- and P-waves causes the angular distributions of the final state particles to differ from the case of the pure P-wave state, hence this MC sample was used to measure these effects, as described in Section 6.3.1.

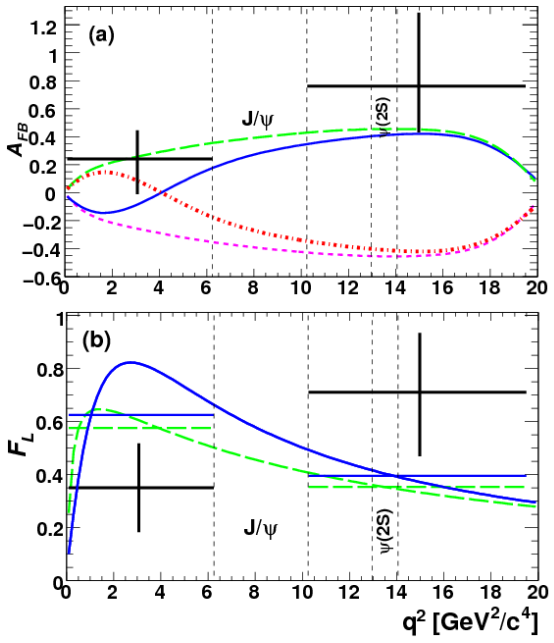

FIGURE 5.1: A_{FB} (left) and F_L (right) measured using the decay $B^0_d \to K^0 l^+ l^-$ by the BaBar Collaboration [36]. Comparisons with SM predictions according to the BTOSLLBALL model are shown (blue solid). The results from implementing a sign flip in the Wilson coefficients in the Hamiltonian are also shown for $C_7^{eff} = -C_7^{eff}$ (green long dash); $C_9^{eff} C_{10}^{eff} = -C_9^{eff} C_{10}^{eff}$ (pink short dash); $C_7^{eff} = -C_7^{eff}$, $C_9^{eff} C_{10}^{eff} = -C_9^{eff} C_{10}^{eff}$ (red dash-dot).

Truth level MC distributions using the four generator models for the signal channel are shown in Figures 5.2-5.7. Figures 5.2 and 5.3 show the B^0_d mass and mass error distributions, respectively, as produced by the four models. The distributions are largely consistent, with the exception of the non-resonant S-wave mass distribution, which has an excess of events in the lower mass region and a reduced peak. The broader mass distribution of the S-wave MC sample may introduce a bias on the fit, but this should be in the direction of pushing some of the S-wave out of the fitted signal component and into the background. This is a desirable pathology from the perspective of extracting information. Figures 5.4-5.6 show the helicity angle distributions of the four MC samples. The ϕ distribution is flat for all four MC samples, but differences are seen in the $\cos\theta_L$ and $\cos\theta_K$ distributions between samples generated using PHSP and SM-like BTOSLLBALL decay models. These differences are also seen in the q^2 distribution in Figure 5.7, indicating the MC samples produced using the PHSP decay model cannot be used to reliably extract information on the angular distributions. However, the PHSP MC samples were still used in determining the detector and simulation effects, as described in Section 6.2.

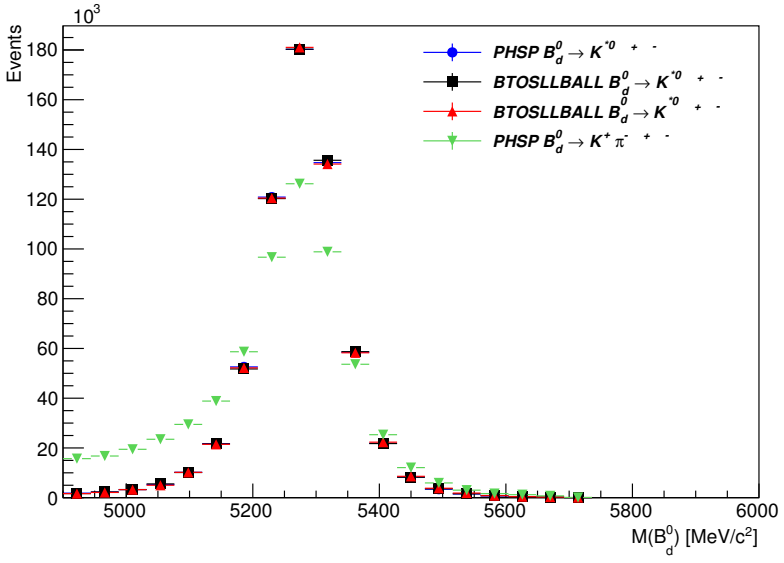

FIGURE 5.2: Truth level signal MC distributions of the B^0_d mass, using four different models for generation.

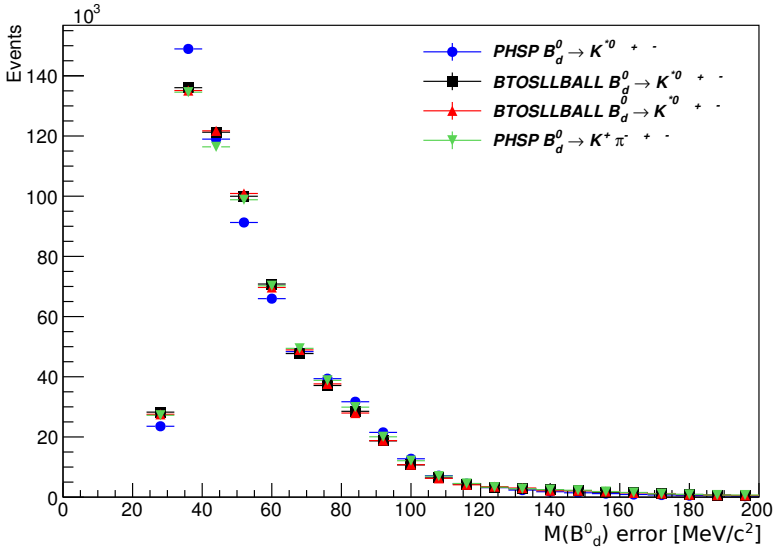

FIGURE 5.3: Truth level signal MC distributions of the B^0_d mass error, using four different models for generation.

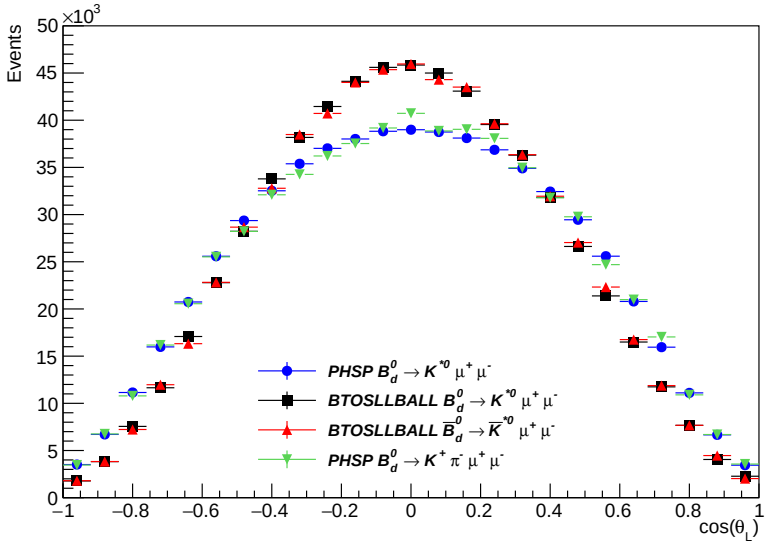

FIGURE 5.4: Truth level signal MC distributions of the helicity angle $\cos\theta_L$, using four different models for generation.

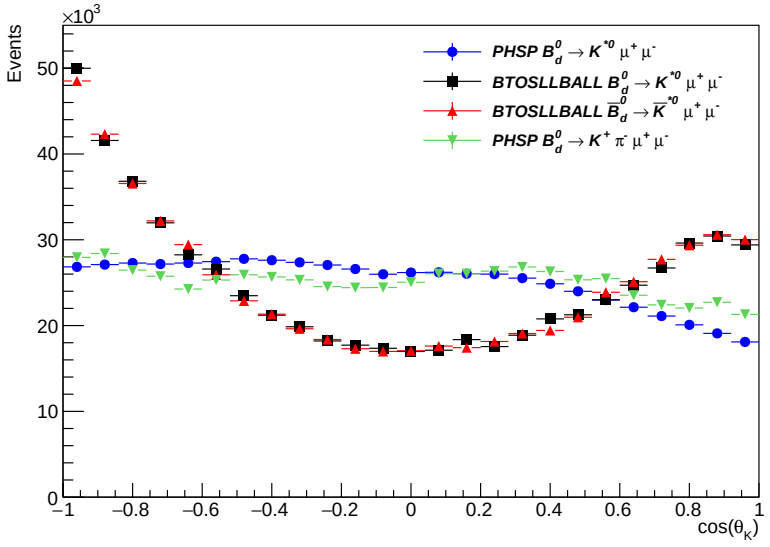

FIGURE 5.5: Truth level signal MC distributions of the helicity angle $\cos\theta_K$, using four different models for generation.

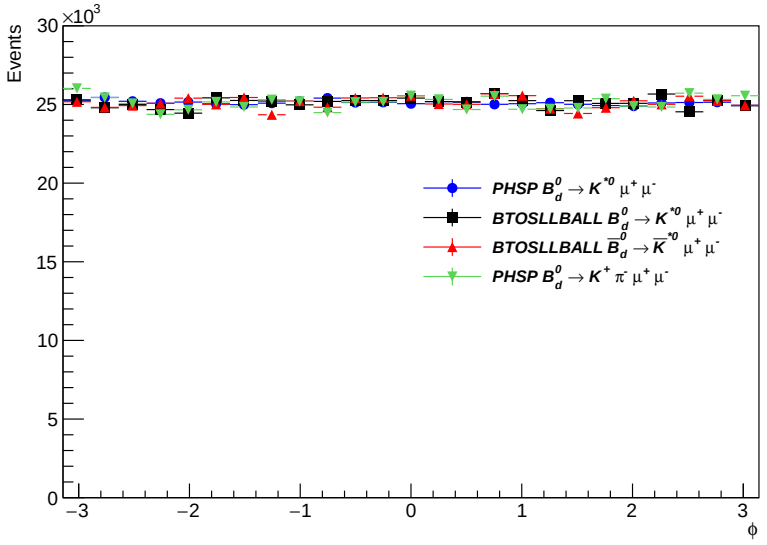

FIGURE 5.6: Truth level signal MC distributions of the helicity angle ϕ, using four different models for generation.

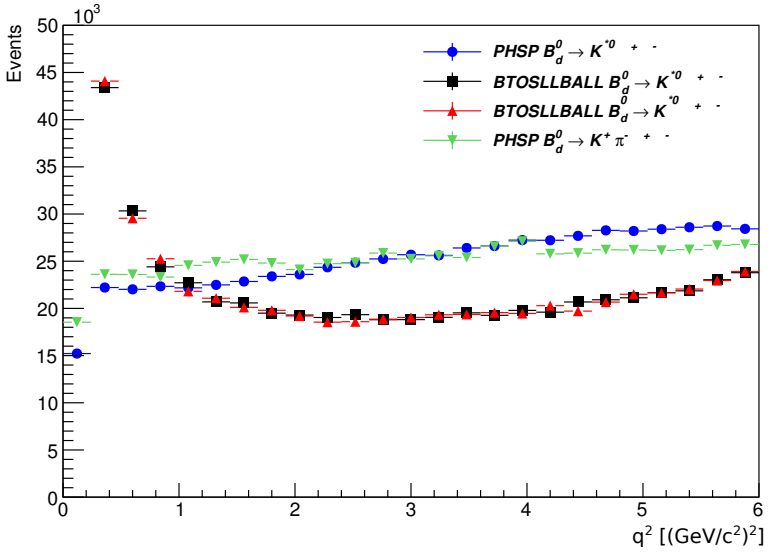

FIGURE 5.7: Truth level signal MC distributions of q^2, using four different models for generation.

A series of studies were performed using MC truth in order to establish the appropriate selection requirements for the final state particles in data. The transverse momentum threshold for final state particles in the hard subprocess, $\hat{p}_T^{min}$, is directly dependent on $p_T(\mu)$. PYTHIA8B by default generates B mesons rather than $\overline{B}$ mesons, hence the selection requirements were imposed on the antiquarks, $\overline{q}$, and not the quarks, q. The η and p_T of the $\overline{b}$ antiquark, the final state muons and the final state hadrons, $h^{\pm}$, were sequentially varied with the aim of finding a sufficiently high cut to increase the speed of the simulation without affecting the resulting $p_T(B)$ spectrum.

The final selection criteria are shown in Table 5.3, where the quark η limit is set to an arbitraily high value to indicate the absence of a selection requirement. Repeated hadronisation was not performed for any of the signal samples.

TABLE 5.3: Truth level selection requirements implemented in the signal MC samples, including hard process kinematics and heavy quark selection. All p_T cuts are in units of GeV/c.

Generator	$\hat{p}_T^{min}$	q p_T	$\overline{q}$ p_T	q η	$\overline{q}$ η	$\mu^{\pm}$ p_T	$\mu^{\pm}$ η	$h^{\pm}$ p_T	$h^{\pm}$ η
EVTGEN	7.0	>0.0	>7.0	<102.6	<2.6	>3.5	<2.6	>0.5	<2.6
PYTHIA	7.0	>0.0	>7.0	<102.6	<2.6	>3.5	<2.6	-	-

5.2 Combinatorial Background MC

Measuring the B_d^0 mass and angular variables of the signal decay relies on reconstructing the correct $K^+\pi^-\mu^+\mu^-$ four body final state. The algorithms and event selection outlined in Section 4 were designed to select the correct combination of particles, based on their properties. Combinatorial background arises from the reconstruction of a random combination of uncorrelated tracks, which leads to a decreased signal-to-background ratio N_{sig}/N_{bckg}. The combinatorial background for $B_d^0 \to K^{*0}\ \mu^+\mu^-$ consists mainly of $b\overline{b} \to \mu^+\mu^- X$ decays that distort the measured mass and angular distributions if not modelled correctly.

Six inclusive MC samples were generated to study this. Four samples, denoted PYTHIA:AA through PYTHIA:BB, were generated as a 4-corners sample in the ATLAS $B_s \to \mu^+\mu^-$ analysis using 2012 data [79]. The purpose of the MC was to simulate the dimuon combinations from semileptonic B decays; each sample

originates from primary $b \to c\mu^-\overline{\nu}$ decays and secondary $c\mu^-\overline{\nu} \to s\mu^+\nu\mu^-\overline{\nu}$ decays. The PYTHIA AA sample prevents both semileptonic b and $\overline{b}$ decays, the AB and BA samples prevent either semileptonic b and $\overline{b}$ decays, respectively, whilst the BB sample allows semileptonic decays of both b and $\overline{b}$. The remaining two inclusive modes were generated with the parameters summarised in Table 5.4. The six samples are defined as follows:

- $b\overline{b} \to \mu\mu X$ (PYTHIA)
- $b\overline{b} \to \mu\mu X$ (EVTGEN)
- $b\overline{b} \to \mu\mu X$ (PYTHIA: AA)
- $b\overline{b} \to \mu\mu X$ (PYTHIA: AB)
- $b\overline{b} \to \mu\mu X$ (PYTHIA: BA)
- $b\overline{b} \to \mu\mu X$ (PYTHIA: BB)

Each of these samples were used in preliminary checks for any significant peaking structures; however very few events passed the full selection criteria.

TABLE 5.4: Truth level selection criteria implemented in the background MC samples, including hard process kinematics and heavy quark selection. All p_T requirements are in units of GeV/c.

Process	$\hat{p}_T^{min}$	$q\ p^T$	$\overline{q}p^T$	$q\ \eta$	$\overline{q}\eta$	$\mu^{\pm}p^T$	$\mu^{\pm}\eta$	$h^{\pm}\ p^T$	$h^{\pm}\ \eta$
$b\overline{b} \to \mu^+\mu^- X$	7.0	>0.0	>7.0	<102.6	<2.6	>3.5	<2.6	>0.5	<2.6
$c\overline{c} \to \mu^+\mu^- X$	15.0	>7.0	>7.0	<4.5	<4.5	>3.5	<2.6	-	-

5.3 Peaking Background MC

The exclusive backgrounds that were found to contribute to the signal region in MC tests are shown in Table 5.5; the respective truth level selection requirements are the same as those listed for $b\bar{b} \to \mu^+\mu^- X$ in Table 5.4.

TABLE 5.5: Description of the background MC samples generated.

Process	Decay	Decay Model	Events	Efficiency (%)
$B_d^0 \to J/\psi K^{*0}$	$B_d^0 \to J/\psi K^{*0}$ $J/\psi \to \mu^+\mu^-$ $K^{*0} \to K^+\pi^-$	SVV_HELAMP 1.0 0.0 $\sqrt{2}$ 0.0 1.0 0.0 PHOTOS VLL VSS	5M	9.9
$B_d^0 \to \psi(2S)K^{*0}$	$B_d^0 \to \psi(2S)K^{*0}$ $\psi(2S) \to \mu^+\mu^-$ $K^{*0} \to K^+\pi^-$	SVV_HELAMP 1.0 0.0 $\sqrt{2}$ 0.0 1.0 0.0 PHOTOS VLL VSS	5M	9.9
$B_d^0 \to \phi K^{*0}$	$B_d^0 \to \phi K^{*0}$ $\phi \to \mu^+\mu^-$ $K^{*0} \to K^+\pi^-$	PHSP PHOTOS VLL VSS	5M	1.2
$B_s \to \phi\mu^+\mu^-$	$B_s \to \phi\mu^+\mu^-$ $\phi \to K^+K^-$	BTOSLLALI VSS	5M	0.5
$B^+ \to K^{*+}\mu^+\mu^-$	$B^+ \to K^{*+}\mu^+\mu^-$ $K^{*+} \to K^0\pi^+$	PHOTOS BTOSLLBALL VSS	5M	0.05
$B^+ \to K^+\mu^+\mu^-$	$B^+ \to K^+\mu^+\mu^-$	PHOTOS BTOSLLBALL	5M	0.27
$\Lambda_b \to \Lambda\mu^+\mu^-$	$\Lambda_b \to \Lambda\mu^+\mu^-$ $\Lambda(1520) \to pK^-$	PHSP PHSP	5M	2.1
$\Lambda_b \to pK^-\mu^+\mu^-$	$\Lambda_b \to pK^-\mu^+\mu^-$	PHSP	5M	0.34

The first two exclusive decays are $B_d^0 \to K^{*0}J/\psi$ and $B_d^0 \to K^{*0}\psi(2S)$, where the $c\bar{c}$ resonances J/ψ and $\psi(2S)$ both decay to a dimuon pair. The EVTGEN MC decay model for both channels was 'SVV_HELAMP', representing the decay of a scalar meson to two vector mesons [67]. The helicity amplitudes corresponding to the three polarisation states of the vector mesons were given as arguments for the decay. In both cases $H_+ = 1.0$, $H_0 = \sqrt{2}$ and $H_- = 1.0$. The helicity amplitudes, H_λ, where $\lambda = +1, 0, -1$, are related to the decay amplitudes, A_λ, by the Jacob and Wick convention [83]:

$$H_\lambda = \sqrt{\frac{4\pi}{2J+1}} A_\lambda, \tag{5.2}$$

where J is the spin of the B meson. This set of arguments yields $F_L = 0.5$ through Eq. (2.50). The $c\bar{c}$ resonances were decayed via the 'VLL' decay model describing the decay of a vector meson to a pair of charged leptons.

The $B_d^0 \to K^{*0}J/\psi$ and $B_d^0 \to K^{*0}\psi(2S)$ decays dominate in the regions $8.0 < q^2 < 11.0$ $(GeV/c^2)^2$ and $12.5 < q^2 < 15.0$ $(GeV/c^2)^2$, respectively, as seen in the

truth level MC distributions in Figure 5.8. The two modes can't be distinguished from the signal by topology selection and the fraction of B mesons that decay via these charm resonances is high. The branching fraction of the $B_d^0 \to K^{*0} J/\psi$ decay is 1000 times higher than that of the signal decay. Similarly, the branching fraction of $B_d^0 \to K^{*0}\psi(2S)$ is 600 times higher than that of signal. These two modes were used as control regions in order to minimise the reliance on MC, as outlined in Section 6.3.1. However, the low mass tail of the $B_d^0 \to K^{*0} J/\psi$ decay was still observed to provide a source of background at low q^2, as seen in Table 5.1.

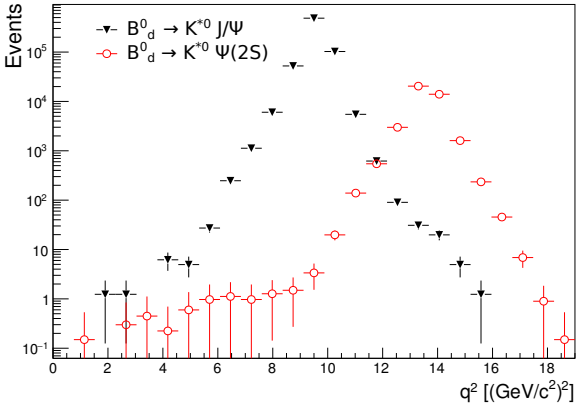

FIGURE 5.8: The truth level q^2 distributions of the $B_d^0 \to K^{*0} J/\psi$ (black) and $B_d^0 \to K^{*0}\psi(2S)$ (red) MC samples generated by EVTGEN.

Alternatively, the dimuon pair can be produced from a ϕ decay, leading to pollution from $B_d^0 \to K^0\phi(\to \mu^+\mu^-)$ decays. Any contribution from $B_d^0 \to K^0\phi(\to \mu^+\mu^-)$ decays occur at very low q^2, as seen in Figure 5.9. Correspondingly the veto $q^2 \in [0.98, 1.10]$ $(GeV/c^2)^2$ was applied to remove this contribution and should be assumed hereafter.

The flavour symmetry described in Section 2.1.2 for the weak interaction can be extended to quarks, such that the strong interaction can be assumed to treat all quark flavours equally. This implies an approximate $SU(2)$ isospin symmetry in strong interactions. Therefore the comparable masses of u and d quarks mean the interaction between the quarks is independent of their flavour. If this set of rules is extended to the strange quark, which has a slightly higher mass, an approximate $SU(3)$ flavour symmetry under $u \leftrightarrow d \leftrightarrow s$ can be assumed.

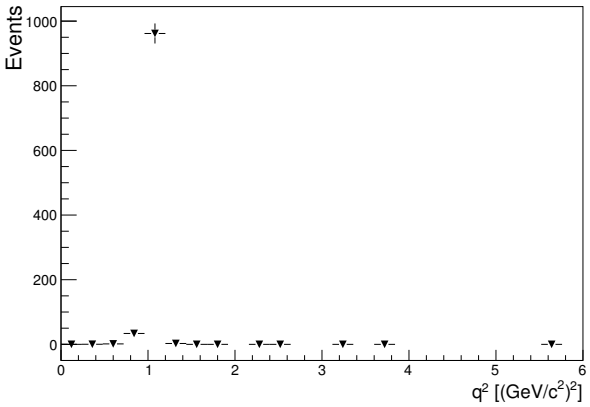

FIGURE 5.9: The truth level q^2 distribution of the $B_d^0 \to K^{*0}\phi$ MC sample generated by EVTGEN. A veto in $q^2 \in [0.98, 1.10]$ $(GeV/c^2)^2$ was applied to remove this contribution.

The second set of backgrounds were investigated under the assumption of $SU(3)$ flavour symmetry, where the spectator d quark was sequentially replaced with a u and s quark to yield the channels $B_u^+ \to K^+\mu^+\mu^-$, $B_u^+ \to K^{*+}\mu^+\mu^-$ and $B_s^0 \to \phi\mu^+\mu^-$ in Table 5.5.

The K^{*0} decays into $K\pi$ in almost all cases, which can be thought of as h^+h^- owing to the lack of particle ID in the ATLAS detector. The $B_u^+ \to K^+\mu^+\mu^-$ decay therefore requires an additional h^- meson to be picked up in the reconstruction to resemble the signal. The K^{*+} meson similarly decays into $K\pi$, or more generally as h^0h^+, and requires the h^0 to be neglected in favour of an h^- in the reconstruction of the tracks. Both hadrons, $h^\pm$, are daughter particles in the decay of a B_u^+ meson, which has a mass $M_{B_u^+} = (5279.26 \pm 0.17)\ MeV/c^2$ (c.f. $M_{B_d^0} = (5279.58 \pm 0.17)\ MeV/c^2$).

The $B_s^0 \to \phi\mu^+\mu^-$ mode was generated using the 'BTOSLLALI' decay model [67] in which the FFs for $b \to sll$ were taken from Ref. [84]. The B_s^0 meson peaks at a higher mass of $M_{B_s^0} = (5366.79 \pm 0.23)\ MeV/c^2$ and the ϕ meson decays to K^+K^- in nearly half of all cases, potentially distorting the signal region at higher mass.

The MC truth mass distributions of these three peaking backgrounds are compared to that of the signal, generated according to the BTOSLLBALL decay model, in Figure 5.10. The peaking background distributions are normalised to the size of the signal. The $B_u^+ \to K^{*+}\mu^+\mu^-$ decay contributes to the low mass region, the $B_u^+ \to K^+\mu^+\mu^-$ to the high mass region and the $B_s^0 \to \phi\mu^+\mu^-$ decay produces a

broader signal-like mass distribution. The mass error distributions of these modes are reasonably consistent with the signal, as seen in Figure 5.11 and consistency is also seen in the $\cos\theta_L$, ϕ and q^2 distributions in Figures 5.12, 5.13 and 5.14, respectively. A comparison of the $\cos\theta_K$ distributions of the peaking backgrounds relative to the signal is shown in Figure 5.15. An excess of events is seen as q^2 approaches -1.0 in the $B_s^0 \to \phi\mu^+\mu^-$ distribution and an additional excess is seen in the $B_u^+ \to K^+\mu^+\mu^-$ distribution as q^2 approaches +1.0.

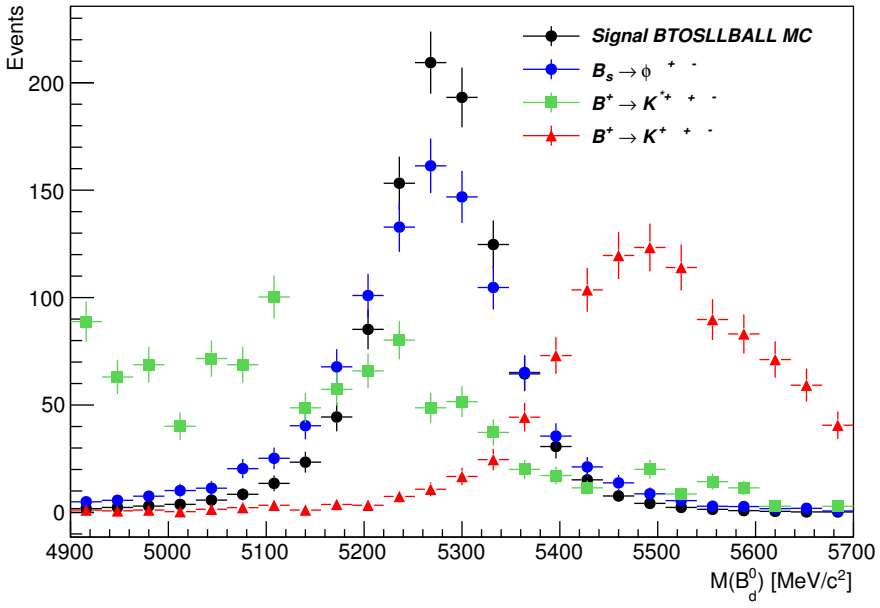

FIGURE 5.10: The truth level $M(B_d^0)$ distributions of the $B_d^0 \to K^{*0}\mu^+\mu^-$ MC sample generated using the BTOSLLBALL model in EVTGEN (black), the $B_u^+ \to K^{*+}\mu^+\mu^-$ MC sample (green), the $B_u^+ \to K^+\mu^+\mu^-$ MC sample (red) and the $B_s^0 \to \phi\mu^+\mu^-$ MC sample (blue).

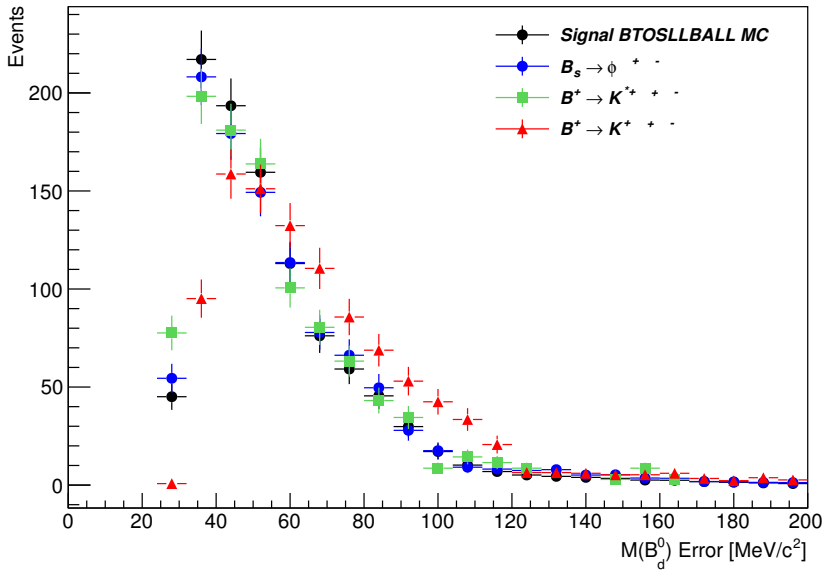

FIGURE 5.11: The truth level $\cos\theta_K$ distributions of the $B^0_d \to K^{*0}\mu^+\mu^-$ MC sample generated using the BTOSLLBALL model in EVTGEN (black), the $B^+_u \to K^{*+}\mu^+\mu^-$ MC sample (green), the $B^+_u \to K^+\mu^+\mu^-$ MC sample (red) and the $B^0_s \to \phi\mu^+\mu^-$ MC sample (blue).

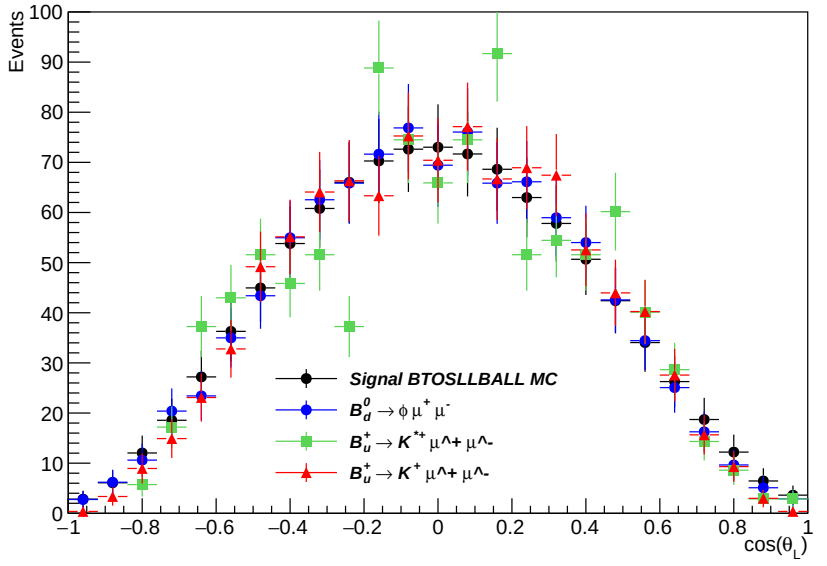

FIGURE 5.12: The truth level $\cos\theta_K$ distributions of the $B^0_d \to K^{*0}\mu^+\mu^-$ MC sample generated using the BTOSLLBALL model in EVTGEN (black), the $B^+_u \to K^{*+}\mu^+\mu^-$ MC sample (green), the $B^+_u \to K^+\mu^+\mu^-$ MC sample (red) and the $B^0_s \to \phi\mu^+\mu^-$ MC sample (blue).

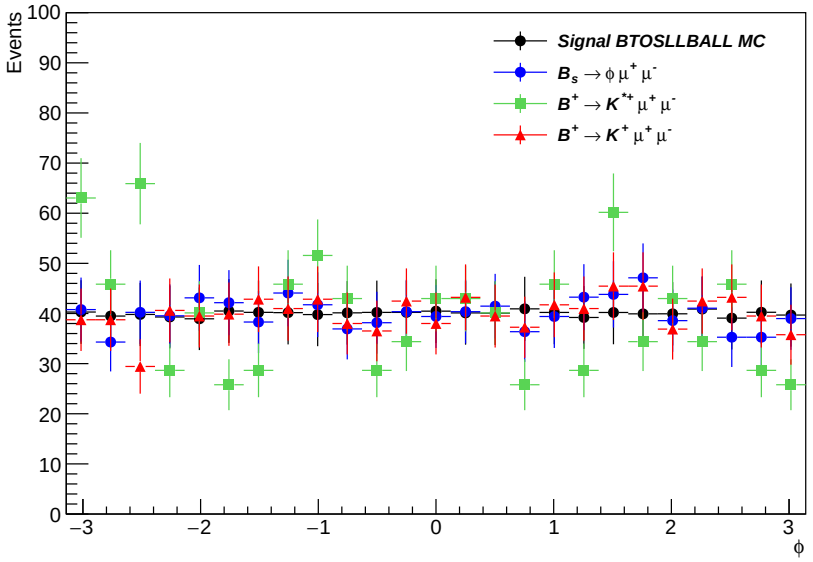

FIGURE 5.13: The truth level $\cos\theta_K$ distributions of the $B_d^0 \to K^{*0}\mu^+\mu^-$ MC sample generated using the BTOSLLBALL model in EVTGEN (black), the $B_u^+ \to K^{*+}\mu^+\mu^-$ MC sample (green), the $B_u^+ \to K^+\mu^+\mu^-$ MC sample (red) and the $B_s^0 \to \phi\mu^+\mu^-$ MC sample (blue).

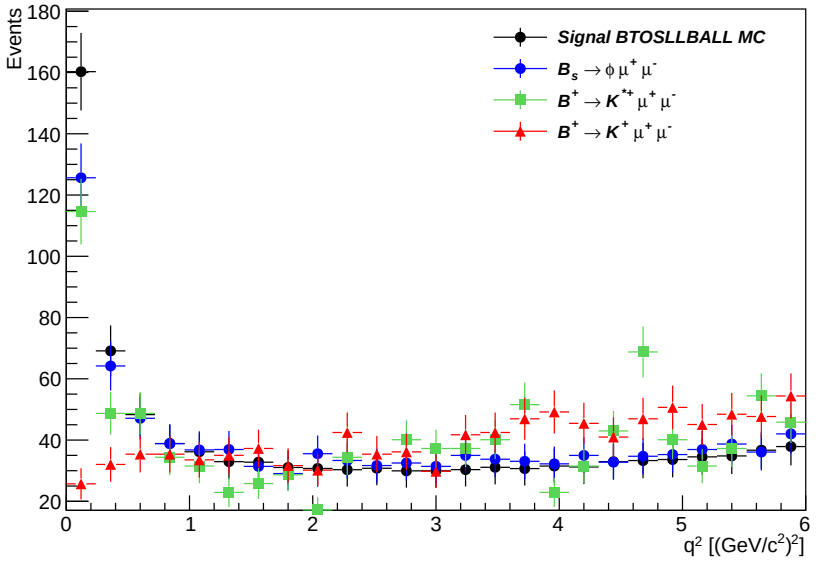

FIGURE 5.14: The truth level $\cos\theta_K$ distributions of the $B_d^0 \to K^{*0}\mu^+\mu^-$ MC sample generated using the BTOSLLBALL model in EVTGEN (black), the $B_u^+ \to K^{*+}\mu^+\mu^-$ MC sample (green), the $B_u^+ \to K^+\mu^+\mu^-$ MC sample (red) and the $B_s^0 \to \phi\mu^+\mu^-$ MC sample (blue).

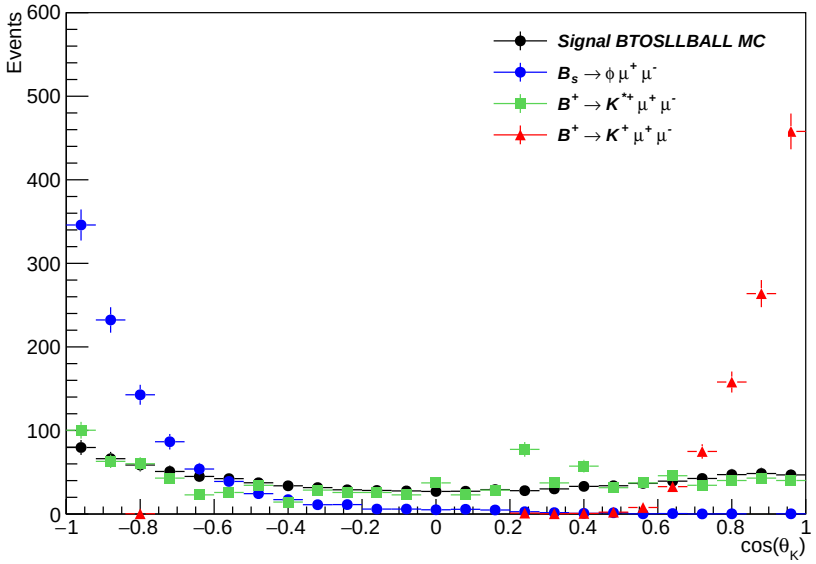

FIGURE 5.15: The truth level $\cos\theta_K$ distributions of the $B^0_d \to K^{*0}\mu^+\mu^-$ MC sample generated using the BTOSLLBALL model in EVTGEN (black), the $B^+_u \to K^{*+}\mu^+\mu^-$ MC sample (green), the $B^+_u \to K^+\mu^+\mu^-$ MC sample (red) and the $B^0_s \to \phi\mu^+\mu^-$ MC sample (blue).

The decay $\Lambda_b \to pK^-\mu^+\mu^-$, which can proceed via the $\Lambda(1520)$ resonance, can be a source of peaking background if the proton is misidentified as a pion. The underlying models of the decays of the Λ_b modes are unknown and thus the phase space decay model was relied upon in the absence of a definitive solution.

The expected yield from the PHSP-generated Λ_b MC samples are shown in Table 5.1 for different q^2 bins. High contributions are observed in each q^2 bin for $\Lambda_b \to \Lambda(1520)\mu^+\mu^-$ using this decay model, indicating the need to model this channel in the background composition. The non-resonant channel $\Lambda_b \to pK^-\mu^+\mu^-$ was also found to be exceed the threshold defined for non-negligible backgrounds but to a lesser extent, therefore the $\Lambda_b \to pK^-\mu^+\mu^-$ contribution could be accounted for in a systematic uncertainty in the same manner as the other peaking backgrounds.

The simulated q^2 distribution for the PHSP-generated $\Lambda_b \to \Lambda(1520)\mu^+\mu^-$ MC sample is given in Figure 5.16. This spectrum was compared to the related mode $\Lambda_b \to \Lambda^0\mu^+\mu^-$, measured by the LHCb Collaboration in Ref. [85] and shown in Fig 5.17 with the SM predictions from Ref. [86] superimposed. The SM q^2 distribution for $\Lambda_b \to \Lambda^0\mu^+\mu^-$ is shown to be suppressed at low q^2 (< 6 $(GeV/c^2)^2$),

akin to the signal SM q^2 distribution shown in Figure 5.18 for $(0.04 < q^2 < 19.00)$ $(GeV/c^2)^2$, but with a slightly harder spectrum owing to the higher mass of the Λ^0 baryon relative to that of the K^{*0} meson.

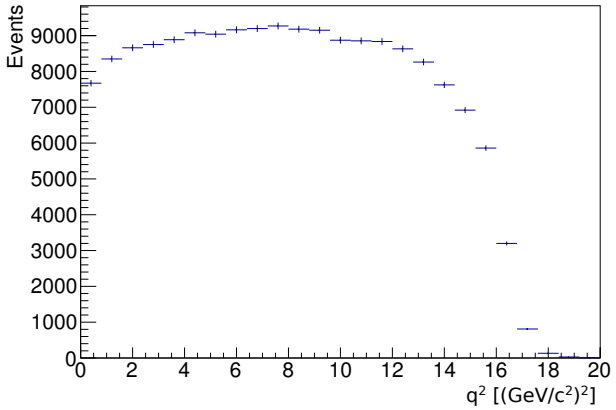

FIGURE 5.16: The truth level q^2 distribution of the $\Lambda_b \to \Lambda(1520)\mu^+\mu^-$ MC sample generated using the phase space decay model in EVTGEN.

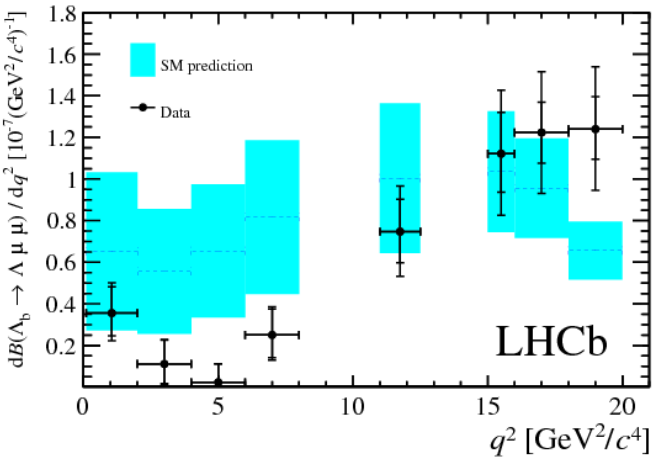

FIGURE 5.17: LHCb-measured $\Lambda_b \to \Lambda\mu^+\mu^-$ branching fraction as a function of q^2 with the predictions of the SM superimposed, from Ref. [85].

The intermediate Λ^0 measured in the LHCb analysis is lighter than the $\Lambda(1520)$ studied here ($M_\Lambda = (1115.683 \pm 0.006)$ MeV/c^2) and decays predominantly to $p\pi^-$ as opposed to pK^-. Although the modes are not identical, the two are related by isospin, hence it was deemed reasonable to assume the q^2 spectrum for $\Lambda_b \to \Lambda^0\mu^+\mu^-$ as a conservative bound, where the true q^2 distribution was expected to be slightly harder by virtue of the heavier Λ baryon. The expected yields of $\Lambda_b \to \Lambda(1520)\mu^+\mu^-$ and $\Lambda_b \to pK^-\mu^+\mu^-$ assuming the branching fractions for

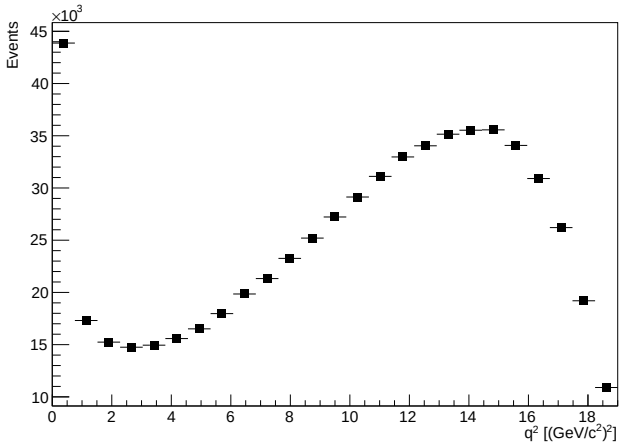

FIGURE 5.18: The truth level q^2 distribution of the $B^0_d \to K^{*0}\mu^+\mu^-$ MC sample generated using the BTOSLLBALL decay model in EVTGEN.

$\Lambda_b \to \Lambda^0\mu^+\mu^-$ given in Ref. [85] for each q^2 bin are given in Table 5.6. The resonant background is reduced by a factor of eight in the lowest q^2 bin and up to a factor of 320 in the highest q^2 bin. The non-resonant background contribution increases but doesn't exceed a few events per q^2 bin. Both backgrounds were subsequently treated in the same way as the other peaking modes, as detailed in Section 6.1.2.2.

TABLE 5.6: The breakdown by q^2 for the Λ_b background samples, where branching fractions from the LHCb analysis in Ref. [85] of $\Lambda_b \to \Lambda^0\mu^+\mu^-$ are assumed. The bin number indicates the lower bound of the q^2 bin for a 1 $(GeV/c^2)^2$ binning scheme.

Process	bin 0	bin 1	bin 2	bin 3	bin 4	bin 5
$\Lambda_b \to \Lambda(1520)\ \mu^+\mu^-$	1.83	1.88	0.61	0.66	0.09	0.08
$\Lambda_b \to pK^-\ \mu^+\mu^-$	0.99	0.87	0.46	0.48	0.10	0.11

Chapter 6

Fitting

This chapter documents the various techniques used for fitting the data and MC and their respective validation procedures. Fit models to distinguish the signal, combinatorial background and peaking backgrounds are described in Section 6.1. Acceptance functions were defined to account for detector effects on the angular variables; a description of the acceptance as a function of q^2 for the signal is given in Section 6.2. The performance of the fit models, including acceptance effects, were validated using a range of toy MC studies and the level of biases found are reported in Section 6.3. The fit models were reproduced in each q^2 bin within a 1 $(GeV/c^2)^2$ binning scheme:

- $q^2 \in [0.04, 0.98]$ $(GeV/c^2)^2$,
- $q^2 \in [1.10, 2.00]$ $(GeV/c^2)^2$,
- $q^2 \in [2.00, 3.00]$ $(GeV/c^2)^2$,
- $q^2 \in [3.00, 4.00]$ $(GeV/c^2)^2$,
- $q^2 \in [4.00, 5.00]$ $(GeV/c^2)^2$,
- $q^2 \in [5.00, 6.00]$ $(GeV/c^2)^2$.

We perform a two stage fit; first to the mass distribution and subsequently to mass and angular distributions. During the fit validation stage, a high number of angular variable fits were found to fail for bins with a signal-to-background ratio $(S/B) \lessapprox 0.25$. Yield expectations extrapolated from the ATLAS 2011 analysis of

$B_d^0 \to K^{*0}\,\mu^+\mu^-$ for the relative changes in integrated luminosity and $b\bar{b} \to \mu^+\mu^- X$ cross-section in 2012 revealed these levels of S/B in half of the q^2 bins listed above [87]. Therefore without an increased data sample, the fit models described below were found to be unsuitable using this binning.

A 2 $(GeV/c^2)^2$ binning scheme was subsequently adopted, in which the fit models were replicated for the bins $q^2 \in [0.04, 2.00]$ $(GeV/c^2)^2$, $q^2 \in [2.00, 4.00]$ $(GeV/c^2)^2$ and $q^2 \in [4.00, 6.00]$ $(GeV/c^2)^2$, where the ϕ veto $q^2 \in [0.98, 1.10]$ $(GeV/c^2)^2$ was applied throughout. Three additional wide low q^2 bins were studied, the first $q^2 \in [0.04, 6.00]$ $(GeV/c^2)^2$ covers the entire q^2 range in this analysis. The second wide bin $q^2 \in [0.04, 4.00]$ $(GeV/c^2)^2$ represents the lower q^2 bin adopted in the angular analysis of $B^0 \to K^*(892)^0\ell^+\ell^-$ performed by the Belle Collaboration [41]. The third wide bin $q^2 \in [1.10, 6.00]$ $(GeV/c^2)^2$ mirrors the widest low-q^2 bin reported by the CMS Collaboration [88], removing the virtual γ contribution that dominates at very low q^2.

A good level of fit convergence was found for the expected S/B in the wider bins and thus this was the binning scheme employed.

6.1 Fit Models

An extended maximum likelihood function, defined for each q^2 bin was used to fit the data and MC. This consisted of maximising the likelihood $\mathcal{L}$, which used PDFs, P_{ij}, to describe the distribution of discriminating variables m, $\cos\theta_K$, $\cos\theta_L$ and ϕ as

$$\mathcal{L} = \frac{e^{-n'}}{n!} \prod_{i=1}^{n} \sum_{j} n_j P_{ij}(m, \cos\theta_L, \cos\theta_K, \phi; \hat{p}, \hat{\theta}) \epsilon(\cos\theta_L, \cos\theta_K, \phi). \tag{6.1}$$

In practice $-\ln\mathcal{L}$ was minimised, which is equivalent to maximising $\mathcal{L}$. The product was evaluated for all the events in a given sample up to the total number of events, n. The likelihood was summed over the signal and background components, denoted by j. The Poisson nature of the event yields was taken into account, where the fitted yield is represented by n_j for the j^{th} component and the total fitted event yield $n' = \sum n_j$. Here $\hat{p}$ and $\hat{\theta}$ represent the parameters of interest and the nuisance parameters, respectively. The final term, $\epsilon(\cos\theta_L, \cos\theta_K, \phi)$, represents

the acceptance as a function of the angular observables; the background acceptance was set to 1.0 whilst the non-trivial signal acceptance is described in Section 6.2. The resolution was expected to vary on an event by event basis, due, in part, to the different detector resolutions in the different regions within the acceptance, as detailed in Section 3.2. This dependence of the PDF on both the mass and per event mass error requires corrections to be applied to the likelihood, such that a PDF sampled from a histogram of the conditional variable $\sigma(m)_i$ was included in order to avoid biases from the so-called 'Punzi effect' [89].

Given the limited data and the number of parameters in the fit, a two stage fit strategy was devised in which the B_d^0 mass and mass error were fitted in the first iteration to extract the signal and combinatorial background yields.

These yields were then fixed in the next iteration in which the three helicity angles $\cos\theta_L$, $\cos\theta_K$ and ϕ were also used as discriminating variables and the angular observables F_L, S_3 and S_i, where $i = 4$, 5, 6, 7 and 8, were subsequently extracted.

The signal PDF, $\mathcal{P}_{\text{sig}}$, is discussed in Section 6.1.1 and the background PDFs, subdivided into combinatorial background, $\mathcal{P}_{\text{comb.bckg}}$, and peaking background, $\mathcal{P}_{\text{peak.bckg}}$, are outlined in Sections 6.1.2.1 and 6.1.2.2, respectively.

6.1.1 Signal Fit Model

The signal was modelled by a single Gaussian function with per-candidate errors on the reconstructed mass, $\sigma(m)$, as follows:

$$P_{\text{sig}}(m) = \frac{1}{S\sigma(m)\sqrt{2\pi}} e^{-(m-m_0)^2/2S^2\sigma^2(m)}. \tag{6.2}$$

Here m_0 is the mean fitted B_d^0 mass and S is a dimensionless scale factor that measures the deviation between the fitted signal width, σ_i, and the width obtained from the per-candidate mass errors, such that:

$$\sigma_i = S\sigma(m). \tag{6.3}$$

If the per-candidate mass errors are calculated correctly in the reconstruction, S is expected to be approximately one. These nuisance parameters were determined from fits to the control region of the data, described in Section 6.3.3 and fixed to these extracted values in all subsequent fits.

6.1.1.1 Kaon-Pion Misidentification

The ATLAS detector doesn't have the ability to definitively identify hadrons such as the kaons and pions in the signal final state, leading to multiple h^+h^- candidates per event being saved. In order to select the correct candidate per event, the strategy outlined in Section 4.4 was followed.

The procedure led to both $K^+\pi^-$ and π^+K^- mass combinations being saved, which correspond to the K^{*0} and $\overline{K}^{*0}$ decay products in $B^0_d \to K^{*0}\mu^+\mu^-$ and $\overline{B}^0_d \to \overline{K}^{*0}\mu^+\mu^-$ processes. The B^0_d and $\overline{B}^0_d$ events were distinguished by the sign of the final state kaon, which was assigned based on the flavour of the s quark of the $K^{*0}(d\bar{s})$ ($\overline{K}^{*0}(s\bar{d})$). Once the sign of the kaon was defined, the B meson was inferred through the decay chain $\bar{b} \to \bar{q}_u \to \bar{s}$ for a B^0_d meson or $b \to q_u \to s$ for a $\overline{B}^0_d$ meson.

In order to establish if the assignment of the kaon charge was correct, the reconstructed data was compared to the generated B^0_d and $\overline{B}^0_d$ MC samples, outlined in Section 5. Discrepancies between the assignment of the tagged kaon at MC truth level and after reconstruction were accounted for by a dilution term

$$D = (1 - 2\omega) \simeq 1 - \omega - \overline{\omega}, \tag{6.4}$$

where ω is the mistag probability for an event to misidentify a pion as a kaon in the reconstruction and likewise $\overline{\omega}$ is the probability a kaon is reconstructed as a pion. The dilution was factored out of the affected parameters, inflating their errors to account for the occasions in which a b quark and hence B meson was incorrectly tagged. The mistag fractions determined from MC are shown in Table 6.1[1]. Comparable values of ω were extracted from each of the MC samples. Furthermore, the SM $\overline{B}^0_d \to \overline{K}^{*0}\mu^+\mu^-$ MC was used to derive a value of $\overline{\omega}$ that was consistent with ω, i.e. $\Delta\omega = \omega - \overline{\omega}$ values consistent with zero.

[1]The mistag fractions determined from MC were not obtained by the author, but is relevant work from the analysis group.

TABLE 6.1: Mistag fractions determined from signal and control sample MC. The mistag probability for an event to misidentify a pion as a kaon in the reconstruction is given by ω, the probability a kaon is reconstructed as a pion is given by $\overline{\omega}$ and $\Delta\omega = \omega - \overline{\omega}$.

MC sample	ω	$\overline{\omega}$	$\Delta\omega$
Signal (phase space)	0.1092 ± 0.0002	–	–
Signal (SM)	0.1097 ± 0.0007	0.1087 ± 0.0007	0.0010 ± 0.0010
$J/\psi\ K^{*0}$	0.1041 ± 0.0007	–	–
$\psi(2S)\ K^{*0}$	0.1102 ± 0.0007	–	–

Mistagging events leads to the transformation $\theta_K \to (\pi - \theta_K)$ in the differential decay rate, hence a sign flip in all factors of $\sin 2\theta_K$. From Eq. (2.52) the angular observables directly affected by this sign flip are S_4, S_5, S_7 and S_8. Moreover, there is an additional sign flip in ϕ arising from the fact that ϕ is defined relative to the assigned kaon in the final state. The parameters affected when taking both of these mistagging effects into account are S_4, S_5 and S_9.

The mistag fractions determined from MC broken down by q^2 bin are shown in Table 6.2. No evidence of a q^2 dependence on the mistag fraction was observed for the phase space MC, but the values of ω and $\overline{\omega}$ were found to vary with q^2 for the two SM MC samples with deviations $> 2\sigma$ seen in the range $(0.04 < q^2 < 6.00)\ (GeV/c^2)^2$. Despite the observed q^2 dependence of the SM signal MC mistag fraction, the absolute value $\Delta\omega$, equal to $\omega - \overline{\omega}$ for the SM MC samples, was found to be consistent with zero.

TABLE 6.2: Mistag fractions determined from MC broken down by q^2 bin.

q^2 bin $((GeV/c^2)^2)$	Phase space ω	SM (B^0_d) ω	SM $(\overline{B}^0_d)$ $\overline{\omega}$	SM $\Delta\omega$
$[0.04, 2.00]$	0.1069 ± 0.0008	0.1092 ± 0.0026	0.1043 ± 0.0026	0.0050 ± 0.0037
$[2.00, 4.00]$	0.1066 ± 0.0007	0.0953 ± 0.0030	0.0968 ± 0.0030	-0.0016 ± 0.0043
$[4.00, 6.00]$	0.1072 ± 0.0007	0.0985 ± 0.0027	0.1011 ± 0.0028	-0.0026 ± 0.0039
$[0.04, 4.00]$	0.1066 ± 0.0005	0.1034 ± 0.0020	0.1011 ± 0.0019	0.0022 ± 0.0028
$[1.10, 6.00]$	0.1069 ± 0.0005	0.0980 ± 0.0019	0.0985 ± 0.0019	-0.0006 ± 0.0026
$[0.04, 6.00]$	0.1069 ± 0.0004	0.1018 ± 0.0016	0.1011 ± 0.0016	0.0007 ± 0.0023

6.1.2 Background Fit Model

This subsection describes the fit model of the combinatorial and peaking backgrounds. A summary of all the backgrounds studied in this analysis is given in Table 5.1. The combinatorial background model is described in Section 6.1.2.1 and the peaking background model is described in Section 6.1.2.2.

6.1.2.1 Combinatorial Background

The combinatorial background was described by the product of two PDFs, the first describing the combinatorial background in the mass distribution and the second describing the combinatorial background in the angular distributions. The mass distribution background was modelled using the exponential distribution

$$P_{\text{comb.bckg}}(m_{K\pi\mu\mu}) = e^{-\lambda m}, \tag{6.5}$$

where λ is the rate of change of the distribution.

The background to the angular distributions was modelled using a second order Chebyshev polynomial, with coefficients a_i, b_i and c_i, as:

$$\begin{aligned} P_{\text{bckg}}(\cos\theta_L, \cos\theta_K, \phi) =& (1 + a_1 T_1(\cos\theta_L) + a_2 T_2(\cos\theta_L)) \times \\ & (1 + b_1 T_1(\cos\theta_K) + b_2 T_2(\cos\theta_K)) \times \\ & (1 + c_1 T_1(\phi) + c_2 T_2(\phi)), \end{aligned} \tag{6.6}$$

where the Chebyshev polynomial terms $T_{1,2}$ are given by

$$T_1(x) = x, \tag{6.7}$$

$$T_2(x) = 2x^2 - 1. \tag{6.8}$$

As was the case for the signal, each of the combinatorial background parameters was determined from fits to the data in each q^2 bin. In this way, the systematic dependence of the signal parameters on the combinatorial background shape was accounted for in the uncertainties extracted from the fit.

6.1.2.2 Peaking Background

A number of decay modes have a similar topology to the signal and appear in the B_d^0 mass region of interest. A description of these modes is given in Section 5, in which the yield expectations of each background are reported for each q^2 bin. The majority of the decays studied were estimated to have insignificant yields per q^2 bin relative to the signal expectation. A threshold of 0.25 events in a given q^2 bin was applied to the list of exclusive background samples in Table 5.1, narrowing the list down to the five decays, shown separately in Table 6.3.

Toy MC studies were used to evaluate any systematic bias resulting from these backgrounds, based on the number of events approximated in Table 6.3. The toy MC studies performed are summarised in Sections 6.3.4.1 and 6.3.4.2.

Control sample fits to $B_u^+ \to K^+ J/\psi$, $B_s^0 \to K^{*0} J/\psi$ and $\Lambda_b \to \Lambda J/\psi$ MC simulated data were used to describe the peaking backgrounds.

A single Gaussian with mean μ and width σ was used to model the $B_u^+ \to K^+ J/\psi$ background, where the per-event error scaling of the width was accounted for, as before.

A single Gaussian function was, however, found to be insufficient to model both the core and outlier parts of the peaking background distributions for the $B_u^+ \to K^+ J/\psi$ and $\Lambda_b \to \Lambda J/\psi$ modes. In this case triple Gaussian PDFs were used to model these channels, with nuisance parameters μ_i and $\sigma(m)_i$ for each Gaussian distribution:

$$\mathcal{P} = f_2 \left(\frac{f_1}{S_1 \sigma(m)_1 \sqrt{2\pi}} e^{-\frac{(m-\mu_1)^2}{2S_1^2 \sigma(m)_1^2}} + \frac{(1-f_1)}{S_2 \sigma(m)_2 \sqrt{2\pi}} e^{-\frac{(m-\mu_2)^2}{2S_2^2 \sigma(m)_2^2}} \right) + \frac{(1-f_2)}{S_3 \sigma(m)_3 \sqrt{2\pi}} e^{-\frac{(m-\mu_3)^2}{2S_3^2 \sigma(m)_3^2}}. \tag{6.9}$$

Validations of these models and the per event error correlations are described in Section 6.3.2.

TABLE 6.3: Peaking background contributions (number of events) for each q^2 bin.

Peaking background	q^2 range $((GeV/c^2)^2)$					
	[0.04, 0.98]	[1.10, 2.00]	[2.00, 3.00]	[3.00, 4.00]	[4.00, 5.00]	[5.00, 6.00]
$B^+ \to K^{*+}\mu^+\mu^-$	0.17	0.12	0.03	0.25	0.12	0.22
$B^+ \to K^+\mu^+\mu^-$	0.89	0.81	1.00	1.30	1.50	1.90
$B_s^0 \to \phi\mu^+\mu^-$	0.40	0.19	0.22	0.23	0.25	0.28
$\Lambda_b \to \Lambda(1520)\ \mu^+\mu^-$	1.83	1.88	0.61	0.66	0.09	0.08
$\Lambda_b \to pK^-\ \mu^+\mu^-$	0.99	0.87	0.46	0.48	0.10	0.11
Total	4.28	3.87	2.32	2.92	2.06	2.59

6.2 Signal Acceptance Functions

A crucial step in understanding the angular distributions of the $K^+\pi^-\mu^+\mu^-$ final state came from establishing how the data and MC were distorted by various aspects of the detection and production. The selection criteria and reconstruction, including the triggering and detector configuration, all contribute to so-called 'acceptance effects' that had to be accounted for.

The large sample of phase space signal MC described in Section 5 was used as the reference for measuring the acceptance effects contributing to the data and MC samples in this analysis.

Before detector simulation, studies performed at MC truth level revealed flat helicity angle distributions across the entire q^2 range, as expected. Deviations from the uniform shapes seen in Figure 6.1 for $\cos\theta_L$, $\cos\theta_K$ and ϕ distributions for $B^0_d \to K^{*0}\,\mu^+\mu^-$ (EvtGen, PHSP) MC after the full simulation has been applied can therefore be attributed to acceptance effects.

Acceptance functions were defined in each q^2 bin via polynomial fits to the $B^0_d \to K^{*0}\,\mu^+\mu^-$ (EvtGen, PHSP) MC. Following preliminary tests, sixth order polynomials for both $\cos\theta_L$ and $\cos\theta_K$ were found to provide the best fit agreement. In the full 3D PDF given by Eq. (2.52) and in the three folded 3D PDFs in terms of S_5, S_7 and S_8 as given by Eqs (2.57), (2.59) and (2.61), respectively, the ϕ distribution was assumed to be unaffected by acceptance effects. This was owing to the fact that ϕ is defined in the B^0_d rest frame, as the angle between the uncorrelated decay planes of the $K\pi$ and $\mu\mu$ systems. The acceptance functions are thus given by:

$$\begin{aligned}\epsilon(\cos\theta_L,\cos\theta_K) = N(1.0 + L_1\cos\theta_L + L_2\cos^2\theta_L + L_3\cos^3\theta_L + L_4\cos^4\theta_L \\ + L_5\cos^5\theta_L + L_6\cos^6\theta_L)\times \\ (1.0 + K_1\cos\theta_L + K_2\cos^2\theta_L + K_3\cos^3\theta_L + K_4\cos^4\theta_L \\ + K_5\cos^5\theta_L + K_6\cos^6\theta_L),\end{aligned} \tag{6.10}$$

where N is a normalisation constant folded into the overall normalisation of the efficiency times angular PDF and L_i and K_j are the polynomial coefficients taken

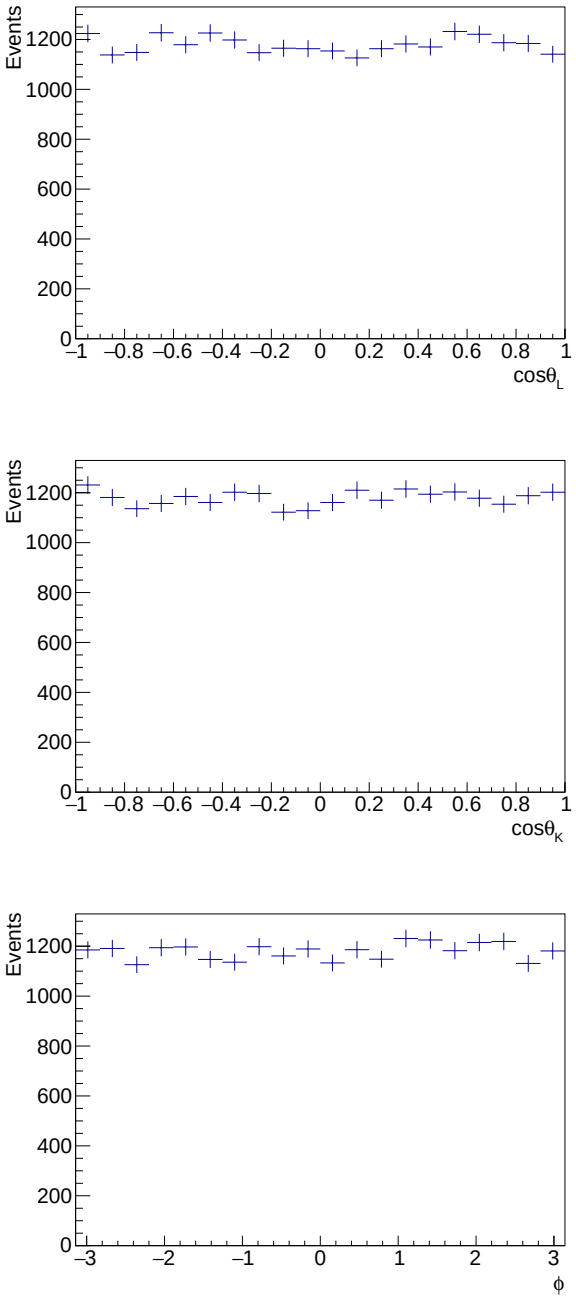

FIGURE 6.1: $B_d^0 \to K^{*0}\ \mu^+\mu^-$ (EVTGEN, PHSP) MC helicity angle distributions using truth information only, across the full range $q^2 \in [0.04, 6.00]\ (GeV/c^2)^2$. The original flat distributions were generated using the phase space decay model, corresponding to $A_\lambda = 1$ for $\lambda = -1, 0, +1$ and hence $F_L = \frac{1}{3}$.

as the acceptance parameters for $\cos\theta_L$ and $\cos\theta_K$, respectively. The acceptance of ϕ, $\epsilon(\phi) = 1$, is implied.

Implementing the folding transformations in Eq. (2.54) to obtain a PDF in terms of S_4 introduced distortions to the $\cos\theta_L$ distribution for $\phi > \frac{\pi}{2}$. As such, a ϕ term was introduced into the acceptance function for this PDF. Ensuing tests found that a 2^{nd} order polynomial function in ϕ provided the best compromise between goodness of fit and appropriate level of computation. The acceptance function for this PDF therefore becomes

$$\begin{aligned}\epsilon(\cos\theta_L, \cos\theta_K, \phi) = N'(1.0 + L_1\cos\theta_L + L_2\cos^2\theta_L + L_3\cos^3\theta_L + L_4\cos^4\theta_L \\ + L_5\cos^5\theta_L + L_6\cos^6\theta_L)\times \\ (1.0 + K_1\cos\theta_L + K_2\cos^2\theta_L + K_3\cos^3\theta_L + K_4\cos^4\theta_L \\ + K_5\cos^5\theta_L + K_6\cos^6\theta_L)\times \\ (1.0 + P_1\phi + P_2\phi^2),\end{aligned} \tag{6.11}$$

where N' is the modified normalisation constant. The initial configuration for the fits assumed constant parameters of $F_L = 0.3333$ and $S_i = 0.0$, where $i = 3$, 4, 5, 6s, 7, 8 and 9. The angular distributions were observed to have a significant q^2 dependence and accordingly fits were performed for the six q^2 bins independently. For each q^2 bin, $6L_j$ and $6K_j$ for $j = 1 - 6$, or $6L_j$, $6K_j$ and $2P_k$ ($k = 1, 2$) polynomial coefficients were extracted from fits to the $B_d^0 \to K^{*0}\,\mu^+\mu^-$ (EvtGen, PHSP) MC.

In order to verify these acceptance parameters, a closure test was performed in which the fits to the phase space signal MC were repeated with the inclusion of the newly extracted coefficients. In this cross-check, the acceptance parameters were fixed as constants, whilst the angular observables F_L and S_i were allowed to float. Fit functionality required no significant biases between the final angular observable values and the initial values used in the MC generation. The fit functionality was therefore determined by the pull distributions of the parameters from the closure test fits; the pull for a given fitted parameter x_{fitted} obtained with an uncertainty σ for the corresponding true value $x_{\text{generated}}$ was defined as

$$p = \frac{x_{\text{fitted}} - x_{\text{generated}}}{\sigma}, \tag{6.12}$$

expected to be distributed as a unit Gaussian with a mean of zero and width of one in the limit of high statistics for an unbiased sample with uncertainties correctly extracted from the fit.

The methodology above was repeated using the signal MC generated with the BTOSLLBALL decay model in EvtGen. As detailed in Section 5, this model decays the particles with SM-like angular distributions, applying amplitudes related to a set of angular observables with a non-trivial q^2 dependence. The initial parameters used in the fits were taken an analysis of the angular distributions in the decay $B \to K^* l^+ l^-$ performed by the BaBar Collaboration [90]. Specifically the distributions observed by the BaBar Collaboration, given in Figure 5.1, were digitised in order to extract values of F_L and A_{FB}. The digitised data was used to compute numerical integrals in the relevant q^2 bins for the distributions; the resulting SM predictions are summarised in Table 6.4. The remaining observables (S_3, S_4, S_5, S_7, S_8 and S_9) were assumed to be zero in this configuration with the caveat that a q^2 dependence for the S_3, S_4 and S_5 parameters has been reported in theory papers, for example [30], [42] and [91]. However, the theoretical calculations are reported for a set of q^2 ranges that differ from the binning adopted in this analysis. Furthermore, it isn't straightforward to convert the BTOSLLBALL parameters into the optimised observable basis and a number of different approaches have been adopted for the form factor computations, as outlined in Section 2.3.6. As such, the ability to robustly interpret the fit bias from this MC was compromised and instead the bias was approximated as the offset from zero for each S observables (bar S_{6s}) across all bins.

Table 6.4: SM expectations of F_L digitised from BaBar results and numerically integrated for the 2 $(GeV/c^2)^2$ and wide q^2 bins studied in this analysis.

q^2 range $((GeV/c^2)^2)$	$F_L \pm \sigma(F_L)$
$[0.04, 2.00]$	0.546 ± 0.0002
$[2.00, 4.00]$	0.813 ± 0.0004
$[4.00, 6.00]$	0.732 ± 0.0003
$[0.04, 4.00]$	0.681 ± 0.0002
$[1.10, 6.00]$	0.765 ± 0.0003
$[0.04, 6.00]$	0.698 ± 0.0002

Given the uncertainty surrounding the fit bias using the SM signal MC, the parameters extracted from the phase space signal MC were chosen to be the most reliable determination of the acceptance effects, as the expected distributions were well known, allowing a precise determination of any biases. Nonetheless, the SM

acceptance parameters were measured as a cross-check and these results are summarised in Appendix B, along with the corresponding results from the $\overline{B}{}^0_d \to \overline{K}{}^{*0}$ $\mu^+\mu^-$ (EvtGen, SM) MC sample.

The acceptance parameters, results from the closure tests and corresponding plots using the $B^0_d \to K^{*0}$ $\mu^+\mu^-$ (EvtGen, PHSP) MC are given in Section 6.2.1 for each of the folded MC samples and PDFs.

Large acceptance effects are seen at the extremities of the $\cos\theta_L$ distribution, where $\cos\theta_L$ approaches ± 1. These distortions arise from the muon p_T cut ($> 3.5\ GeV/c$) defined in the MC generation, designed to replicate the trigger used for data selection. These cuts don't discriminate between positive and negative muons resulting in the symmetric spectrum seen. The momentum dependence of this effect means it is accentuated at lower values of q^2 and diminishes as q^2 increases.

The significance of the acceptance effects can be seen to change for two different q^2 bins within the q^2 range studied here, $q^2 \in [0.04, 6.00]$ $(GeV/c^2)^2$, as demonstrated in Figure 6.2.

The $\cos\theta_K$ distribution is asymmetric in the generated MC, an effect that arises as a result of unequal momenta between the charged kaon and pion daughters in the K^{*0} decay. For $\cos\theta_K$ close to ± 1, the K^{*0} daughters manifest themselves as a fast kaon and slow pion in the lab frame. The track reconstruction efficiency for low p_T charged kaons is higher than that of low p_T charged pions, resulting in a larger acceptance effect as $\cos\theta_K$ tends to 1, where slow pion contributions begin to dominate.

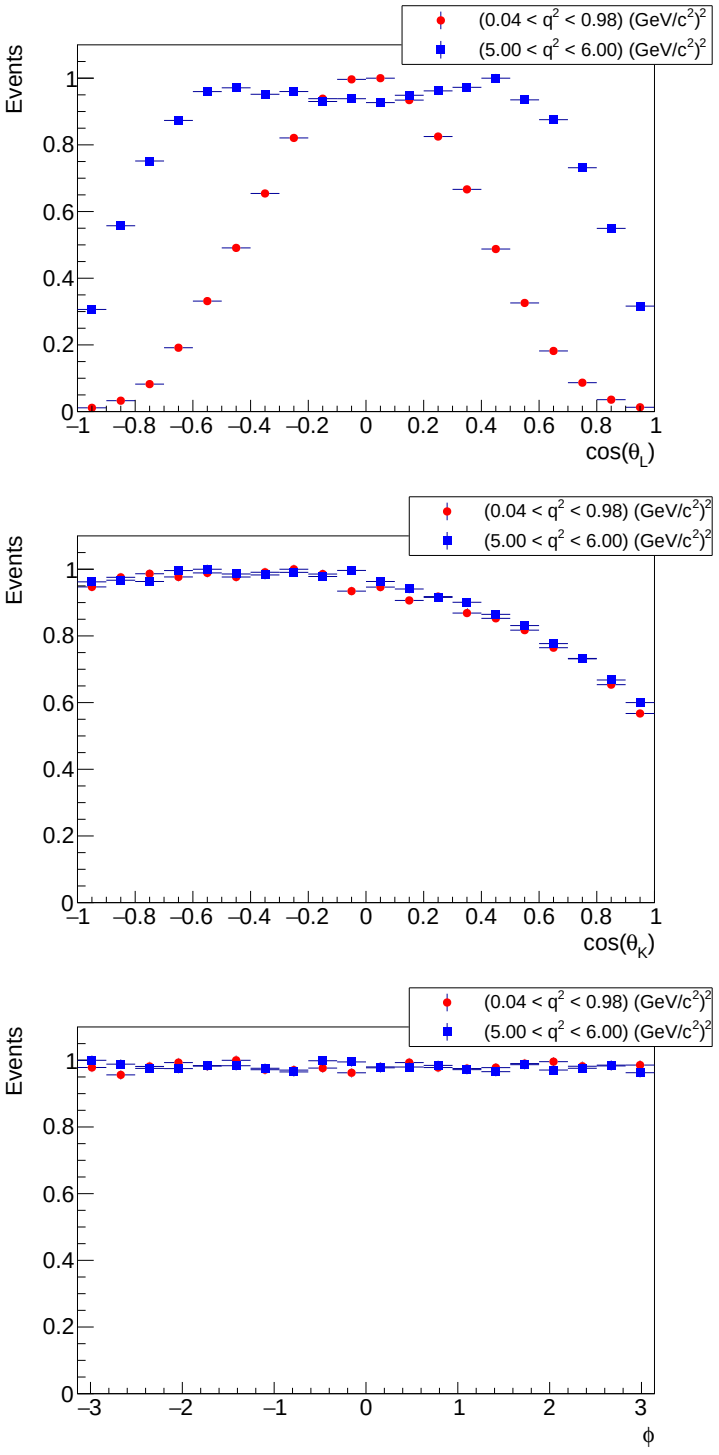

FIGURE 6.2: Helicity angle distributions from the $B^0_d \to K^{*0}\,\mu^+\mu^-$ (EVTGEN, PHSP) MC for $q^2 \in [0.04, 0.98]$ $(GeV/c^2)^2$ (red) and $q^2 \in [5.00, 6.00]$ $(GeV/c^2)^2$ (blue).

6.2.1 Folded PDFs, in terms of S_4, S_5, S_7 and S_8

S_4 folded PDF

The first folding procedure, given in Eq. (2.54), results in a PDF dependent on the F_L, S_3 and S_4 angular observables only. The coefficients from 6th order polynomial fits to the $\cos\theta_L$ and $\cos\theta_K$ distributions and a 2^{nd} order polynomial fit to the ϕ distribution to the folded S_4 $B^0_d \to K^{*0}$ $\mu^+\mu^-$ (EvtGen, PHSP) MC were extracted. The helicity angle distributions per q^2 bin are shown in Figures 6.3-6.8. These extracted acceptance parameters were fixed in a subsequent closure test fit to the folded S_4 $B^0_d \to K^{*0}$ $\mu^+\mu^-$ (EvtGen, PHSP) MC sample and a measure of the fit bias can be inferred from Table 6.5.

Fit biases were observed in the F_L and S_4 parameters from the closure test, whilst the S_3 parameter was unbiased across all q^2 bins. The MC fitted helicity angle distributions were subsequently used as 'acceptance maps' to account for detector acceptance effects in the fits to data. The acceptance maps were found to show reasonable agreement, although small discrepancies between the fitted PDF and MC are observed, most notably in the $\cos\theta_K$ distribution for $4.00 < q^2 < 6.00$. Several tests were done to achieve the best agreement and the results shown below reflect this best case scenario. The intrinsic fit bias is explored in more detail in Section 6.3.

Table 6.5: Results from the acceptance parameter closure test using the folded S_4 $B^0_d \to K^{*0}$ $\mu^+\mu^-$ (EvtGen, PHSP) MC and the extracted acceptance parameters. The initial value of F_L was 0.3333, whilst S_3 and S_4 were both 0.0.

q^2 range $((GeV/c^2)^2)$	$F_L \pm$ error	$S_3 \pm$ error	$S_4 \pm$ error
$[0.04, 2.00]$	0.330 ± 0.001	0.000 ± 0.001	-0.051 ± 0.002
$[2.00, 4.00]$	0.325 ± 0.001	0.001 ± 0.001	-0.070 ± 0.002
$[4.00, 6.00]$	0.319 ± 0.001	0.002 ± 0.001	-0.069 ± 0.001
$[0.04, 4.00]$	0.327 ± 0.001	0.001 ± 0.001	-0.062 ± 0.001
$[1.10, 6.00]$	0.323 ± 0.001	0.001 ± 0.001	-0.068 ± 0.001
$[0.04, 6.00]$	0.324 ± 0.001	0.001 ± 0.001	-0.065 ± 0.001

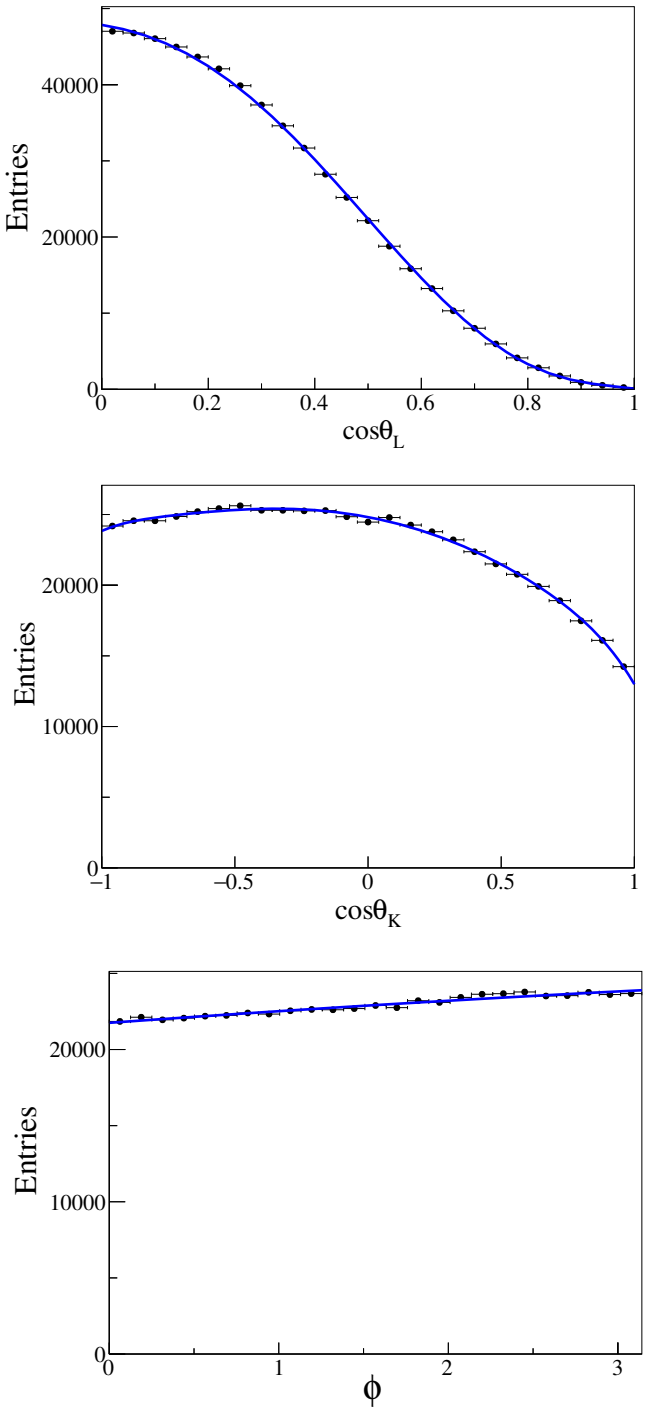

FIGURE 6.3: 6th order polynomial fits to the folded S_4 $B^0_d \to K^{*0}\ \mu^+\mu^-$ (EVTGEN, PHSP) MC for $q^2 \in [0.04, 2.00]$ $(GeV/c^2)^2$. The (black) points represent the MC distribution and the (blue) lines represent the fits to MC using the extracted acceptance parameters.

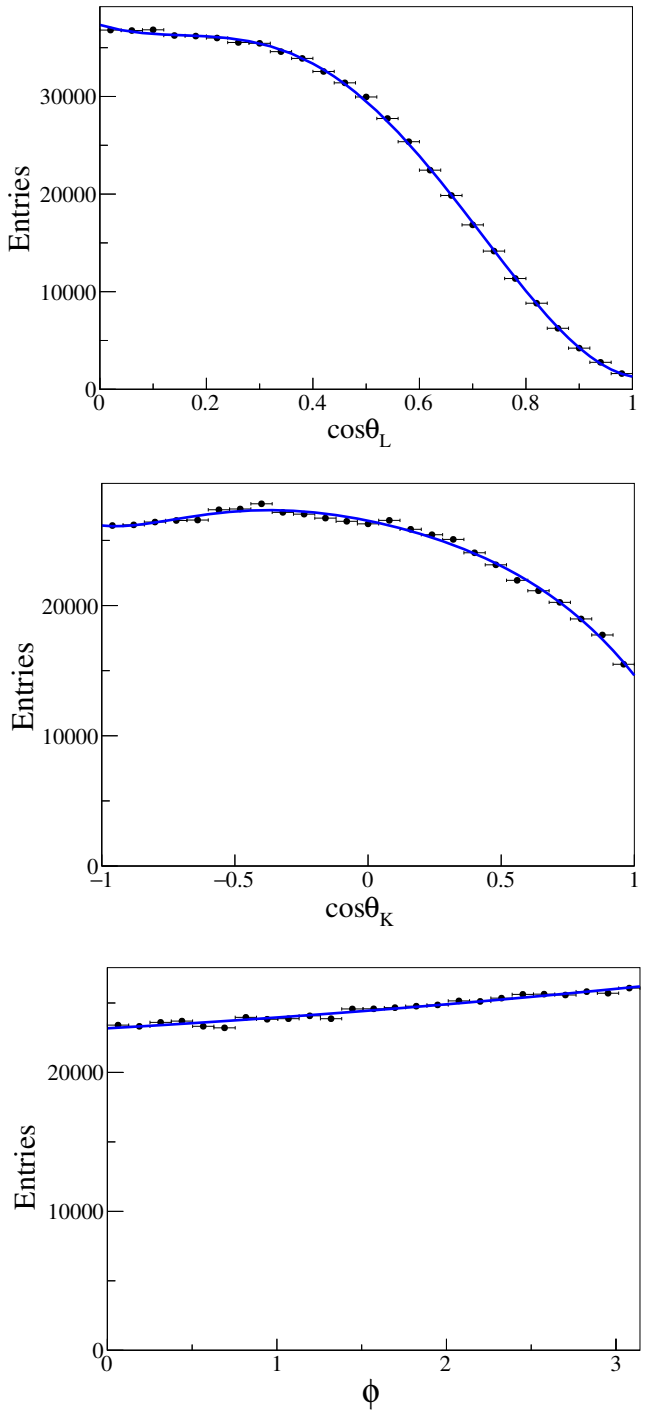

FIGURE 6.4: 6th order polynomial fits to the folded S_4 $B_d^0 \to K^{*0}\ \mu^+\mu^-$ (EVTGEN, PHSP) MC for $q^2 \in [2.00, 4.00]$ $(GeV/c^2)^2$. The (black) points represent the MC distribution and the (blue) lines represent the fits to MC using the extracted acceptance parameters.

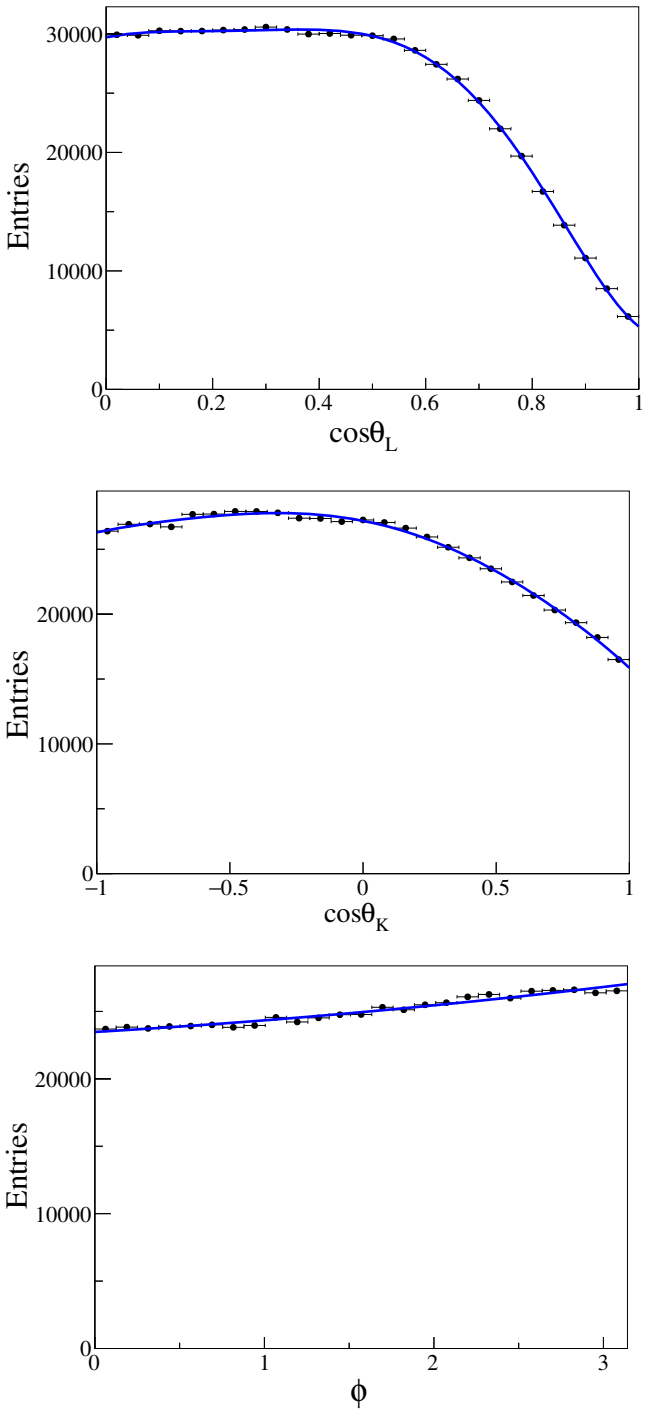

FIGURE 6.5: 6th order polynomial fits to the folded S_4 $B_d^0 \to K^{*0}\ \mu^+\mu^-$ (EVTGEN, PHSP) MC for $q^2 \in [4.00, 6.00]$ $(GeV/c^2)^2$. The (black) points represent the MC distribution and the (blue) lines represent the fits to MC using the extracted acceptance parameters.

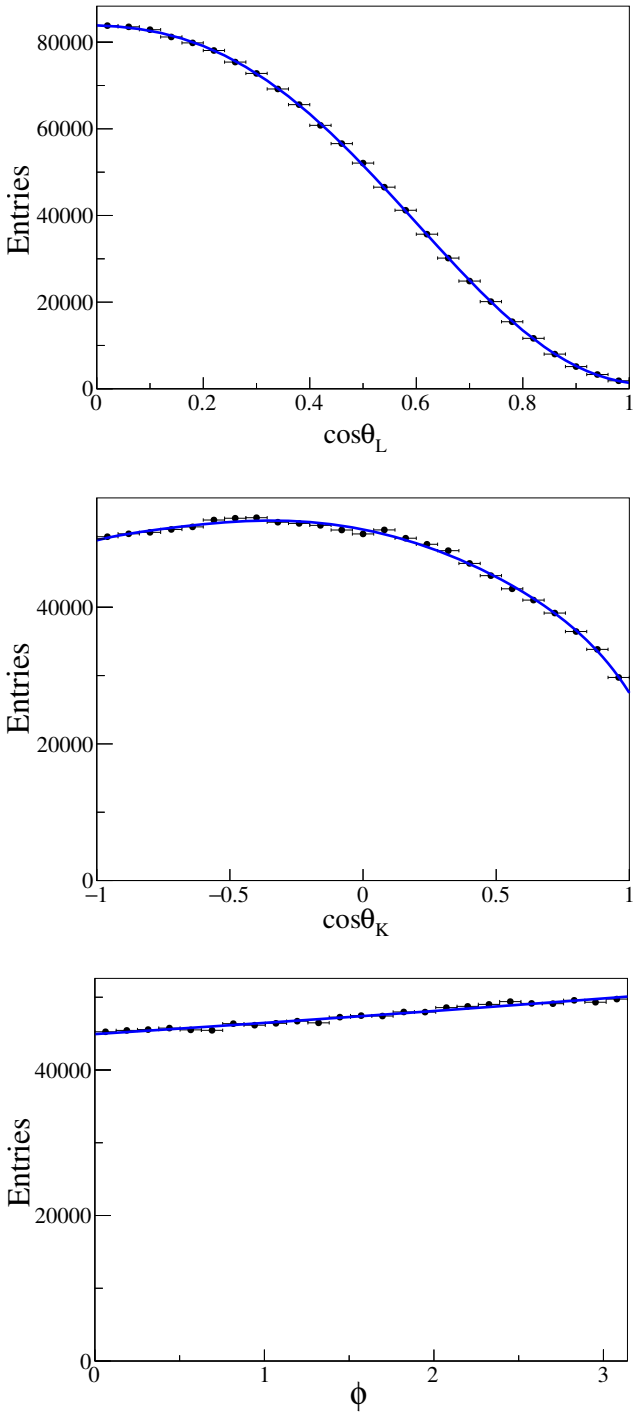

FIGURE 6.6: 6th order polynomial fits to the folded S_4 $B_d^0 \to K^{*0}$ $\mu^+\mu^-$ (EVTGEN, PHSP) MC for $q^2 \in [0.04, 4.00]$ $(GeV/c^2)^2$. The (black) points represent the MC distribution and the (blue) lines represent the fits to MC using the extracted acceptance parameters.

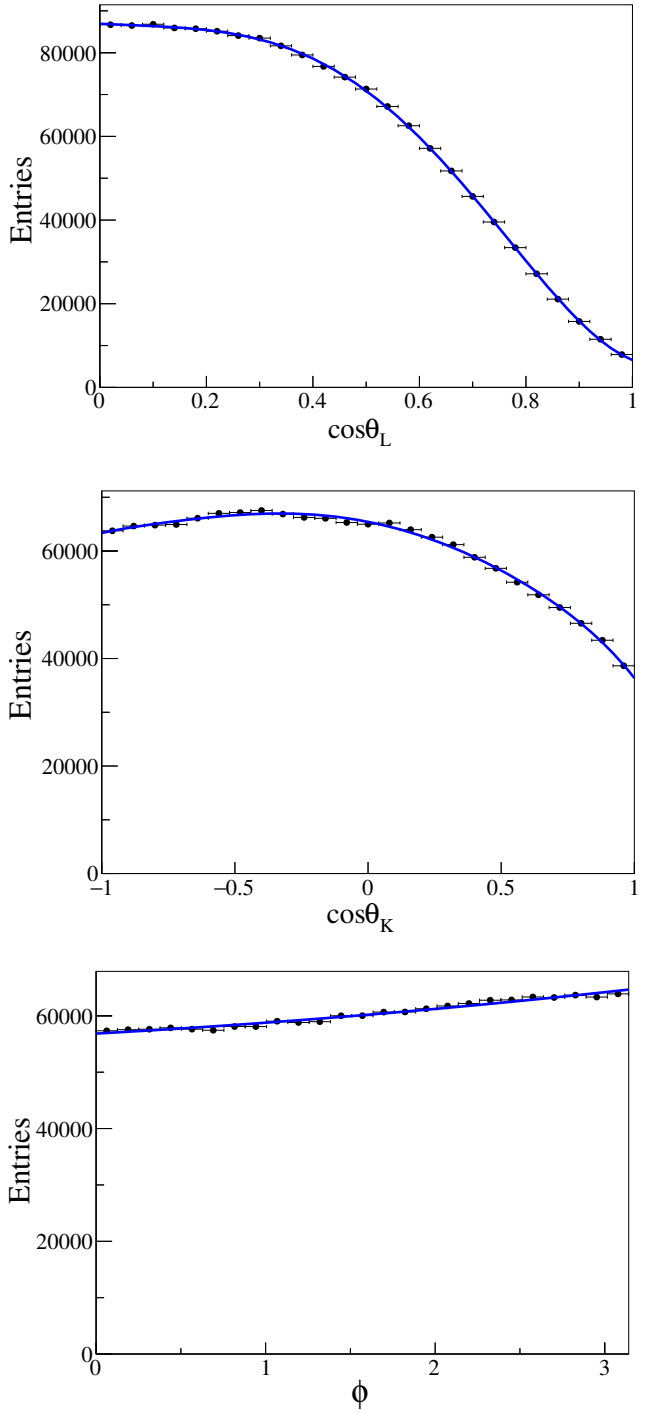

FIGURE 6.7: 6th order polynomial fits to the folded S_4 $B^0_d \to K^{*0}\ \mu^+\mu^-$ (EVTGEN, PHSP) MC for $q^2 \in [1.10, 6.00]$ $(GeV/c^2)^2$. The (black) points represent the MC distribution and the (blue) lines represent the fits to MC using the extracted acceptance parameters.

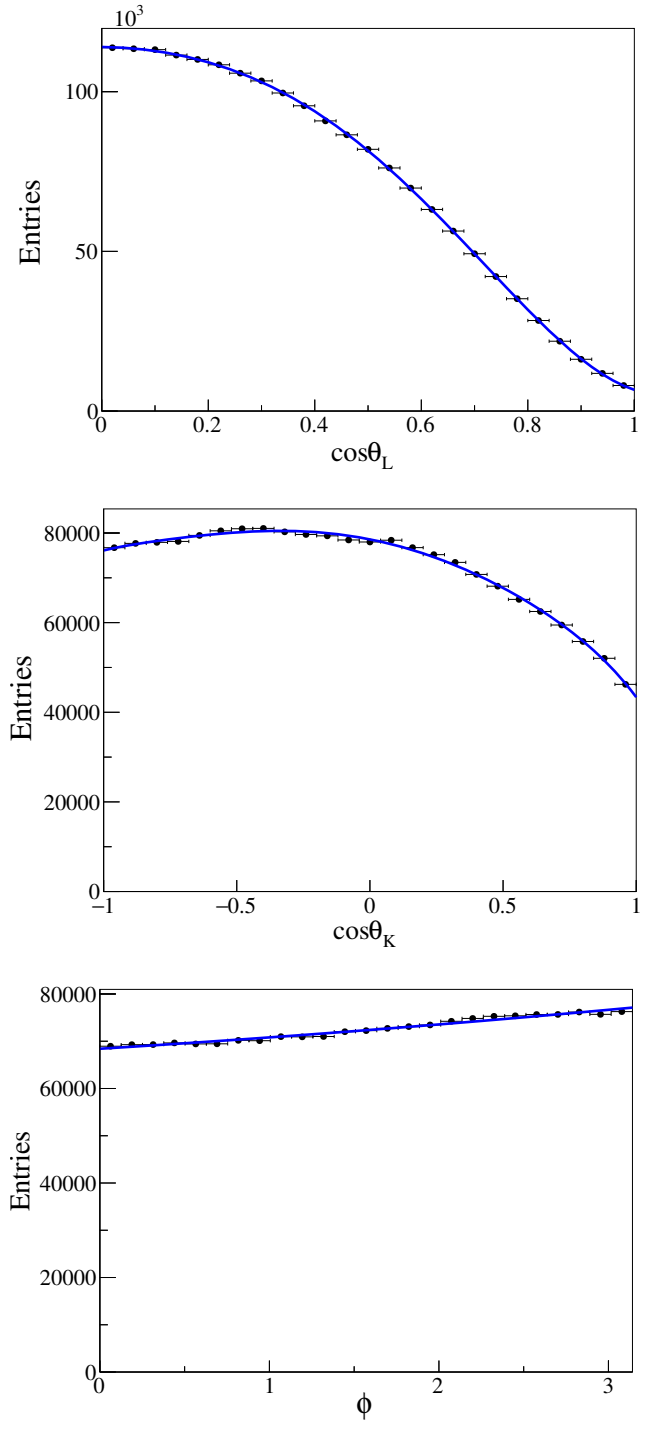

FIGURE 6.8: 6th order polynomial fits to the folded S_4 $B^0_d \to K^{*0}\ \mu^+\mu^-$ (EVTGEN, PHSP) MC for $q^2 \in [0.04, 6.00]$ $(GeV/c^2)^2$. The (black) points represent the MC distribution and the (blue) lines represent the fits to MC using the extracted acceptance parameters.

S_5 folded PDF

The second folding procedure, given in Eq. (2.56), results in a PDF dependent on the F_L, S_3 and S_5 angular observables only. The coefficients from 6th order polynomial fits to the $\cos\theta_L$ and $\cos\theta_K$ distributions from the folded S_5 $B^0_d \to K^{*0}\,\mu^+\mu^-$ (EvtGen, PHSP) MC were extracted and results from the closure test are shown in Table 6.6. The angular distributions are shown in Figures B.1−B.6 in Appendix B.

The closure test shows small biases for the fitted F_L, S_3 and S_5 parameters to the same level as observed in the case of the S_4 folded MC.

Table 6.6: Results from the acceptance parameter closure test using the folded S_5 $B^0_d \to K^{*0}\,\mu^+\mu^-$ (EvtGen, PHSP) MC and extracted acceptance parameters. The initial value of F_L was 0.3333, whilst S_3 and S_5 were both 0.0.

q^2 range $((GeV/c^2)^2)$	$F_L \pm$ error	$S_3 \pm$ error	$S_5 \pm$ error
$[0.04, 2.00]$	0.330 ± 0.001	-0.001 ± 0.001	0.001 ± 0.001
$[2.00, 4.00]$	0.326 ± 0.001	0.003 ± 0.001	0.001 ± 0.001
$[4.00, 6.00]$	0.320 ± 0.001	0.005 ± 0.001	-0.004 ± 0.001
$[0.04, 4.00]$	0.327 ± 0.001	0.001 ± 0.001	0.001 ± 0.001
$[1.10, 6.00]$	0.323 ± 0.001	0.003 ± 0.001	-0.001 ± 0.001
$[0.04, 6.00]$	0.324 ± 0.001	0.002 ± 0.001	-0.001 ± 0.001

S_7 folded PDF

The third folding procedure results in a PDF dependent on the F_L, S_3 and S_7 angular observables only via the transformations in Eq. (2.58). As for the case of the S_5 folding, 6th order polynomial fits to the $\cos\theta_L$ and $\cos\theta_K$ distributions from the folded S_7 folded MC were performed. The fits to the $\cos\theta_L$, $\cos\theta_K$ and ϕ MC distributions are illustrated in Figures B.7-B.12 and a measure of the intrinsic fit bias is given in Table 6.7.

Small biases are once again seen in the fitted values of F_L and S_3, whilst no bias is seen in the S_7 parameter.

S_8 folded PDF

The final folding procedure, given in Eq. (2.60), results in a PDF dependent on the F_L, S_3 and S_8 angular observables only. The coefficients from 6th order polynomial fits to the $\cos\theta_L$ and $\cos\theta_K$ distributions to the folded S_8 $B^0_d \to K^{*0}$

TABLE 6.7: Results from the acceptance parameter closure test using the folded S_7 $B^0_d \to K^{*0}\ \mu^+\mu^-$ (EVTGEN, PHSP) MC and extracted acceptance parameters. The initial value of F_L was 0.3333, whilst S_3 and S_7 were both 0.0.

q^2 range $((GeV/c^2)^2)$	$F_L \pm$ error	$S_3 \pm$ error	$S_7 \pm$ error
$[0.04, 2.00]$	0.330 ± 0.001	-0.001 ± 0.001	0.000 ± 0.001
$[2.00, 4.00]$	0.326 ± 0.001	0.003 ± 0.001	0.000 ± 0.001
$[4.00, 6.00]$	0.320 ± 0.001	0.005 ± 0.001	-0.000 ± 0.001
$[0.04, 4.00]$	0.327 ± 0.001	0.001 ± 0.001	0.000 ± 0.001
$[1.10, 6.00]$	0.323 ± 0.001	0.003 ± 0.001	-0.000 ± 0.001
$[0.04, 6.00]$	0.324 ± 0.001	0.002 ± 0.001	0.000 ± 0.001

$\mu^+\mu^-$ (EVTGEN, PHSP) MC were extracted and the corresponding fitted angular observables from the closure test are given in Table 6.8 and the helicity angle distributions per q^2 bin are shown in Figures B.13–B.18.

Similarly to the S_5 and S_7 acceptance closure tests, small biases in F_L and S_3 were observed whilst S_8 was found to be unbiased.

TABLE 6.8: Results from the acceptance parameter closure test using the folded S_8 $B^0_d \to K^{*0}\ \mu^+\mu^-$ (EVTGEN, PHSP) MC and extracted acceptance parameters. The initial value of F_L was 0.3333, whilst S_3 and S_8 were both 0.0.

q^2 range $((GeV/c^2)^2)$	F_L	S_3	S_8
$[0.04, 2.00]$	0.330 ± 0.001	-0.001 ± 0.001	-0.002 ± 0.002
$[2.00, 4.00]$	0.326 ± 0.001	0.003 ± 0.001	-0.001 ± 0.002
$[4.00, 6.00]$	0.320 ± 0.001	0.005 ± 0.001	0.003 ± 0.001
$[0.04, 4.00]$	0.327 ± 0.001	0.001 ± 0.001	-0.001 ± 0.001
$[1.10, 6.00]$	0.323 ± 0.001	0.003 ± 0.001	0.001 ± 0.001
$[0.04, 6.00]$	0.324 ± 0.001	0.002 ± 0.001	0.000 ± 0.001

6.3 Fit Validation

This section summarises the tests performed in order to validate the methods used for extracting the signal parameters of interest. Fit validations were required to understand the intrinsic fit bias, performance of the models and acceptance functions outlined in Sections 6.1 and 6.2. Signal and control sample MC were used to validate the signal fit model; the fitted yields and signal parameters of interest are summarised in Section 6.3.1. Fits to MC peaking background samples were performed in order to extract background nuisance parameters, as documented in 6.3.2. Additionally, fits to the control region of the data were used to extract certain signal parameters of interest, outlined in Section 6.3.3.

Toy MC studies were used to validate the likelihood model; these studies are described for the nominal PDF including signal and combinatorial background components in Section 6.3.4.1 and with the inclusion of embedded peaking backgrounds in 6.3.4.2.

6.3.1 Fits to the Signal and Control Sample MC

As a consistency check, fits to the signal MC samples were performed in order to verify that the fit was able to extract the signal yield and determine the shape parameters. The aim was to determine the percentage of signal events that were misreconstructed as combinatorial background, referred to as 'cross-feed', in order to validate the PDF assumed was reasonable for fitting data.

Mass fits to the three signal MC samples were performed and the fitted yields were used to determine the difference between the true distributions estimated from MC and the PDF distributions used to fit the samples. The typical cross-feed was found to range between $2.8-3.8\%$ for the phase space signal MC, as seen in Table 6.9, with comparable ranges seen in the SM signal MC and SM $\overline{B}{}^0_d$ MC in Tables 6.10 and 6.11, respectively. The fitted mass distributions per q^2 bin are shown in Figure 6.9 for the phase space MC, with similar distributions seen for the SM MC samples.

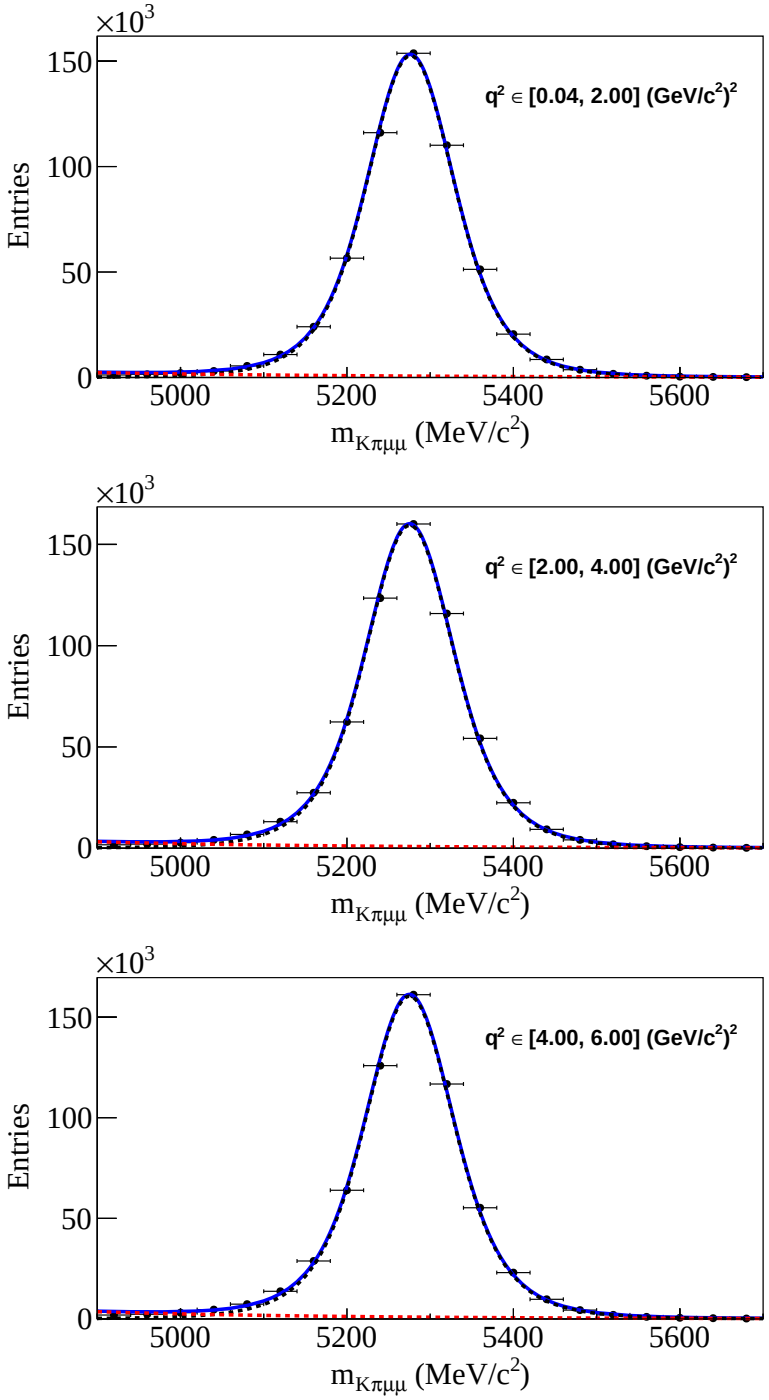

FIGURE 6.9: Mass distributions from fits to the phase space signal MC for q^2 bins $[0.04, 2.00]$ $(GeV/c^2)^2$ (top), $[2.00, 4.00]$ $(GeV/c^2)^2$ (middle) and $[4.00, 6.00]$ $(GeV/c^2)^2$ (bottom). The blue (solid) line is the total fitted PDF, the black (dashed) is the fitted signal component and the red (dashed) is the fitted combinatorial background component.

TABLE 6.9: Signal and combinatorial background yields from fits to the $B^0_d \to K^{*0}\ \mu^+\mu^-$ (EVTGEN, PHSP) MC for different bins of q^2.

q^2 range $((GeV/c^2)^2)$	Initial N_{sig}	Fitted N_{sig}	Fitted N_{bckg}	Cross-feed (%)
$[0.04, 2.00]$	572160	555710^{+763}_{-760}	16451^{+202}_{-201}	2.88
$[2.00, 4.00]$	613640	592380^{+790}_{-789}	21269^{+230}_{-228}	3.47
$[4.00, 6.00]$	626150	602530^{+792}_{-805}	23619^{+243}_{-241}	3.77

TABLE 6.10: Signal and combinatorial background yields from fits to the $B^0_d \to K^{*0}\ \mu^+\mu^-$ (EVTGEN, SM) MC for different bins of q^2.

q^2 range $((GeV/c^2)^2)$	Initial N_{sig}	Fitted N_{sig}	Fitted N_{bckg}	Cross-feed (%)
$[0.04, 2.00]$	57184	55679^{+241}_{-240}	15049^{+618}_{-603}	2.63
$[2.00, 4.00]$	31733	30515^{+180}_{-179}	12182^{+552}_{-538}	3.84
$[4.00, 6.00]$	35579	34076^{+192}_{-189}	15024^{+611}_{-597}	4.22

TABLE 6.11: Signal and combinatorial background yields from fits to the $\overline{B}^0_d \to \overline{K}^{*0}\ \mu^+\mu^-$ (EVTGEN, SM) MC for different bins of q^2.

q^2 range $((GeV/c^2)^2)$	Initial N_{sig}	Fitted N_{sig}	Fitted N_{bckg}	Cross-feed (%)
$[0.04, 2.00]$	56731	55297^{+239}_{-241}	14355^{+604}_{-699}	2.53
$[2.00, 4.00]$	31198	30025^{+179}_{-178}	11729^{+557}_{-542}	3.76
$[4.00, 6.00]$	35095	33650^{+189}_{-189}	14451^{+603}_{-589}	4.11

The signal PDF assumes that a common scale factor multiplying the error on the reconstructed mass is a reasonable approach to follow, as detailed in Section 6.1.1. In order to validate the scaling assumed for the model, the mean B_d mass and RMS error obtained from fits to signal MC were studied in slices of per event error. Linearity was observed for the RMS error as a function of the per event error, verifying the scaling strategy adopted, as shown in Figures 6.10, 6.11 and 6.12 for the phase space, SM and $\overline{B}{}^0_d$ SM MC samples, respectively. Although the mean mass was also found to vary linearly as a function $\sigma(m_B)$, the fit performance was sufficient to proceed without also replacing m_0 with $m_0(\sigma(m_B))$.

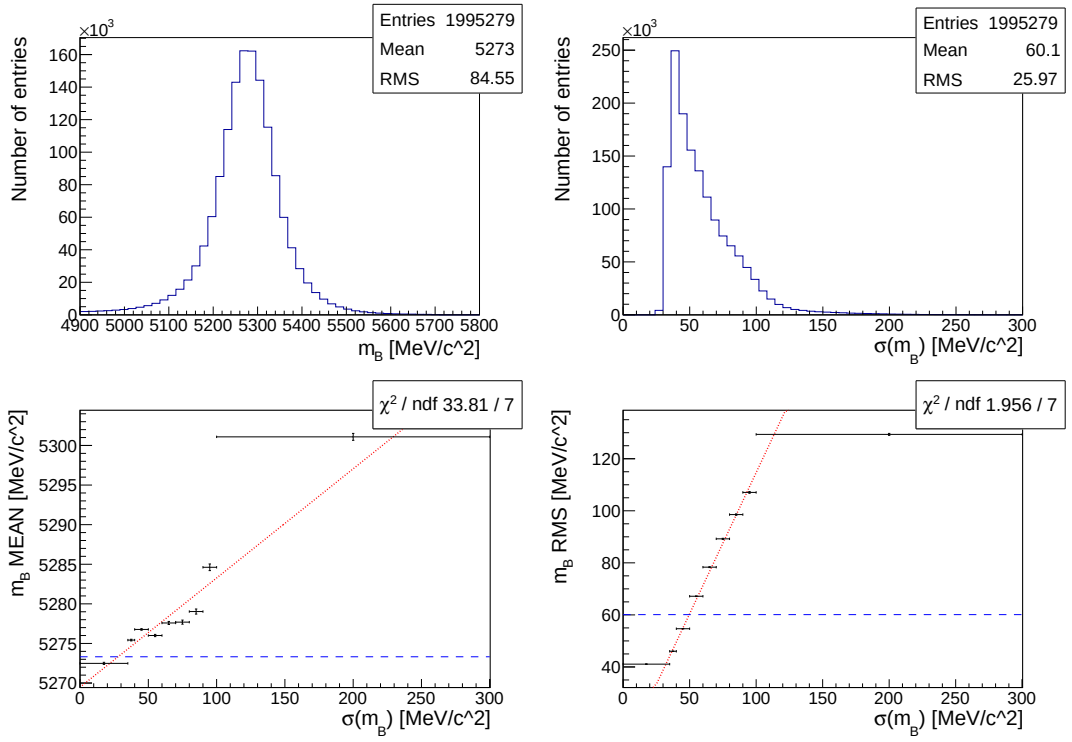

FIGURE 6.10: The reconstructed mass (top left), error on the mass (top right), mean mass as a function of the per event error on the mass (bottom left) and RMS on the mass as a function of the per event error on the mass (bottom right) for the phase space signal MC. The red (dashed) lines represent the best fit and the blue (dashed) lines represent the mean fitted mass and RMS on the mass from the top plots.

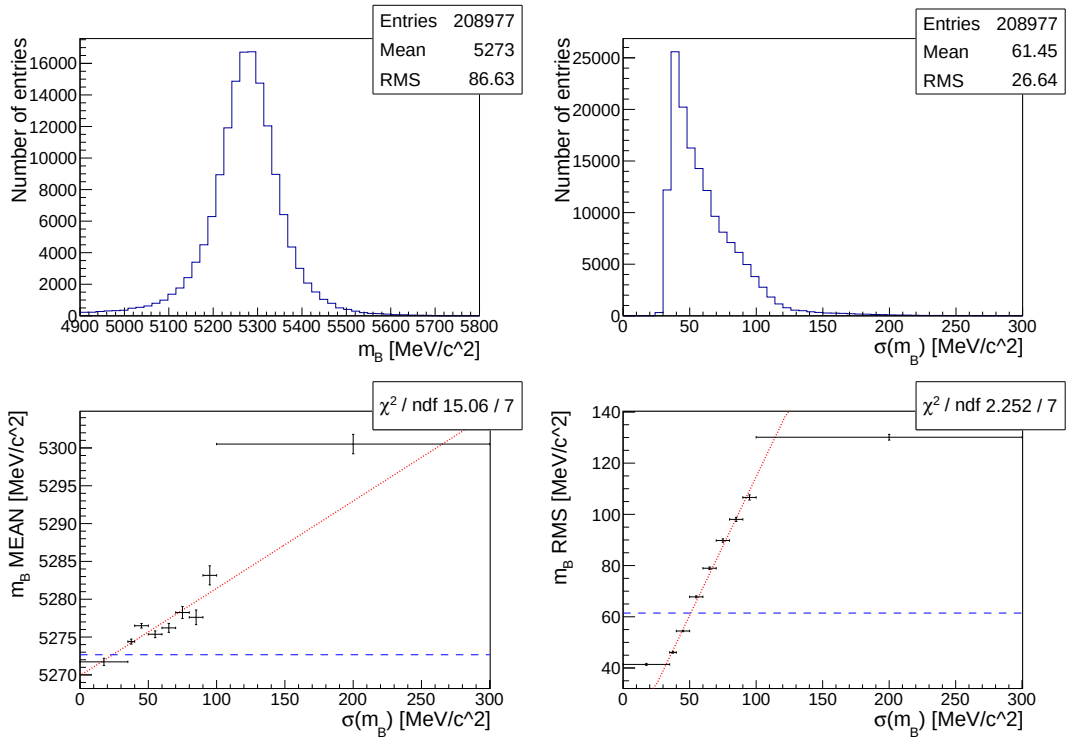

FIGURE 6.11: The reconstructed mass (top left), error on the mass (top right), mean mass as a function of the per event error on the mass (bottom left) and RMS on the mass as a function of the per event error on the mass (bottom right) for the SM signal MC. The red (dashed) lines represent the best fit and the blue (dashed) lines represent the mean fitted mass and RMS on the mass from the top plots.

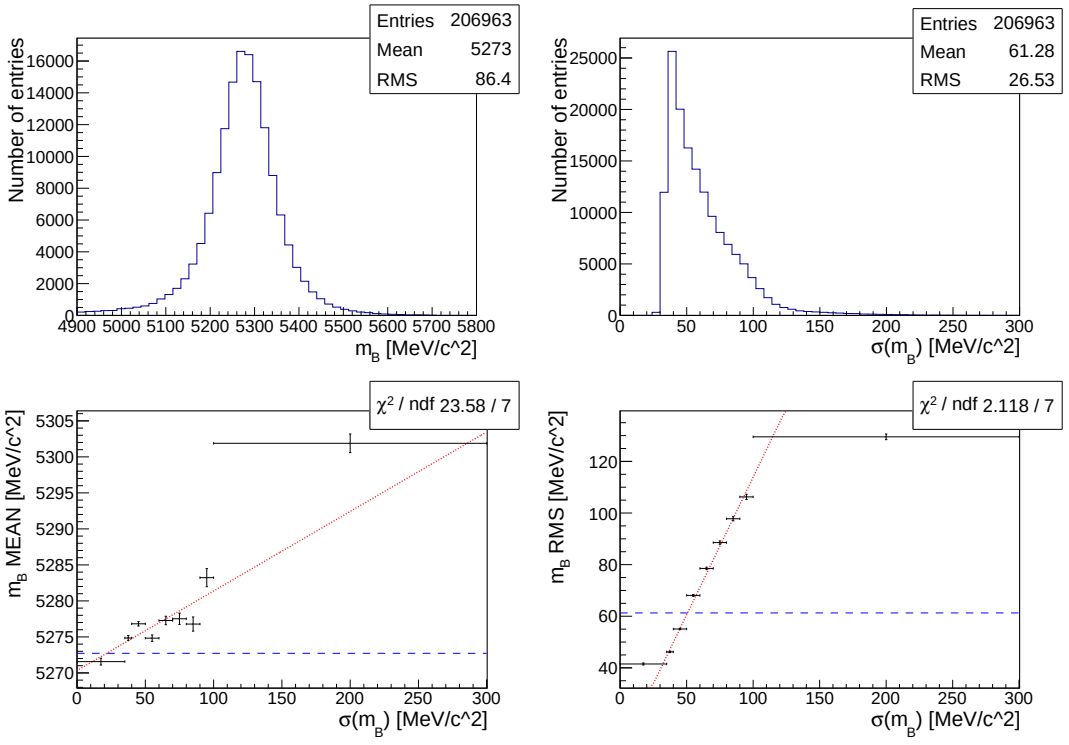

FIGURE 6.12: The reconstructed mass (top left), error on the mass (top right), mean mass as a function of the per event error on the mass (bottom left) and RMS on the mass as a function of the per event error on the mass (bottom right) for the SM $\overline{B}{}^0_d$ signal MC. The red (dashed) lines represent the best fit and the blue (dashed) lines represent the mean fitted mass and RMS on the mass from the top plots.

The signal parameters m_0 and S were extracted from all three of the signal MC samples for each q^2 bin and compared to the corresponding results extracted from the control sample MC. The signal MC results are summarised in Figure 6.13, which shows a decline of a few MeV/c^2 in m_0 as the fits move from the lowest to highest q^2 bin, most significantly for the SM signal MC. Deviations up to 2 σ were observed between q^2 bins in the measured S values and up to 3 σ between the signal MC samples in a given q^2 bin.

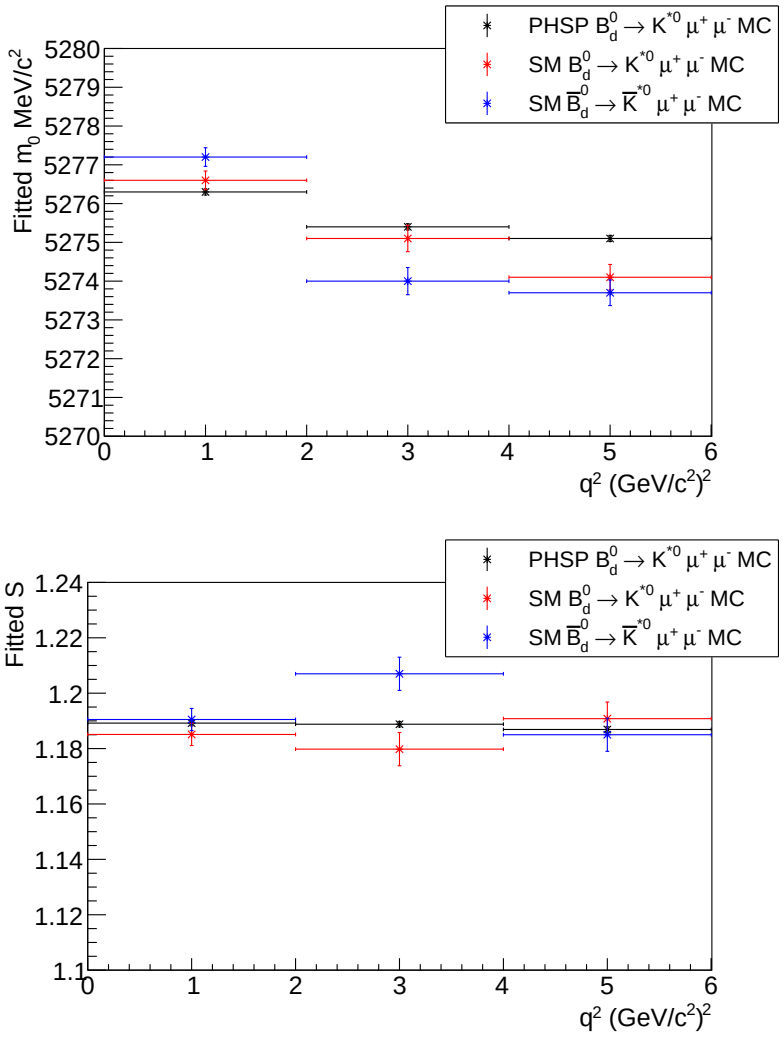

FIGURE 6.13: The mean fitted B_d^0 mass, m_0, (top) and the fitted scale factor, S, (bottom) as a function of q^2 for the three signal MC samples. The black markers correspond to the phase space signal MC, the red markers to the SM signal MC and the blue markers to the SM $\overline{B}_d^0$ MC decays.

Fits to the $B_d^0 \to J/\psi K^{*0}$ control sample MC yielded the following fitted values of m_0 and S:

$$\begin{aligned} m_0(J/\psi K^{*0}) &= 5276.0 \ \pm 0.1 \ MeV/c^2, \\ S(J/\psi K^{*0}) &= 1.1836 \ \pm 0.0023. \end{aligned} \tag{6.13}$$

The corresponding results for the $B_d^0 \to \psi(2S)K^{*0}$ control sample are:

$$\begin{aligned} m_0(\psi(2S)K^{*0}) &= 5275.8 \ \pm 0.1 \ MeV/c^2, \\ S(\psi(2S)K^{*0}) &= 1.1779 \ \pm 0.0022. \end{aligned} \tag{6.14}$$

A comparable level of agreement in m_0 and S is seen between the two control MC samples as between the signal MC samples. Moreover, each of the control MC results is comparable to those extracted from the signal MC samples in Figure 6.13, although the S values extracted from the control samples are slightly closer to one.

These results indicate that it's possible to fit the control region(s) and translate information on the mass scale to the signal region without incurring a significant bias in the experimental procedure.

6.3.2 Fits to the Peaking Background MC Samples

Mass fits to the peaking background MC samples $B_s^0 \to K^{*0}J/\psi$, $B_u^+ \to K^+J/\psi$ and $\Lambda_b \to \Lambda J/\psi$ were performed in order to extract nuisance parameters for modelling the contributions from the backgrounds listed in Table 6.3 correctly.

A single Gaussian PDF was found to adequately fit the mass distribution of the $B_s^0 \to K^{*0}J/\psi$ MC and the fitted parameters were found to be:

$$\begin{aligned} m_0(J\psi K^{*0}) &= (5362.9 \ \pm 0.1) \ MeV/c^2 \\ S(J\psi K^{*0}) &= 1.1779 \ \pm 0.0021, \end{aligned} \tag{6.15}$$

where the PDG B_s^0 mass is 5366.79 ± 0.23 MeV/c^2 [19]. The single Gaussian PDF is shown overlaid on the MC simulated data for $B_s^0 \to J/\psi K^0$ in Figure 6.14. For comparison, the result from using a triple Gaussian PDF to fit this mode is shown. The mass and mass error information is also summarised in Figure 6.14; linearity was observed between the mean m_B and $\sigma(m_B)$, as well as between the RMS on m_B and $\sigma(m_B)$.

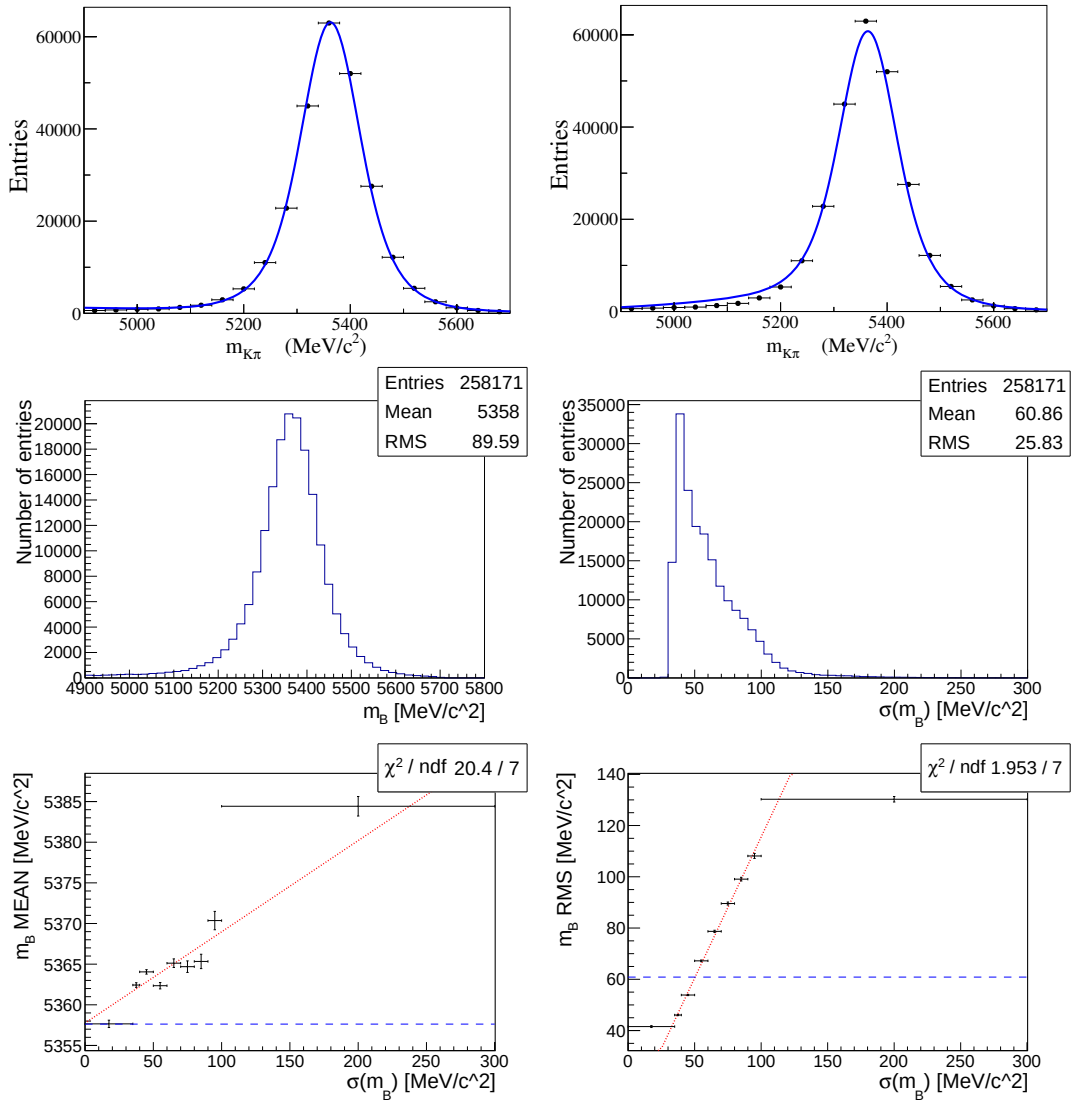

FIGURE 6.14: The single (top-left) and triple (top-right) Gaussian PDF model overlaid on MC simulated data for $B_s^0 \to J/\psi K^{*0}$. Also shown are the reconstructed mass (middle-left), error on the mass (middle-right), mean mass as a function of the error on the mass (bottom-left) and RMS on the mass as a function of the error on the mass (bottom-right).

Triple Gaussian PDFs were used to fit the mass distributions for $B_u^+ \to K^+ J/\psi$ and $\Lambda_b \to \Lambda J/\psi$. Two mass fits to $B_u^+ \to K^+ J/\psi$ using the triple Gaussian model are shown in Figure 6.15. In one instance the widths are scaled by the per event errors and in the other they are not. The PDF was observed to overestimate the low mass tail and slightly underestimate the peak position when incorporating the mass-mass error correlation in the Gaussian widths. The corresponding shape neglecting that correlation information provided better agreement between the PDF and MC simulated data.

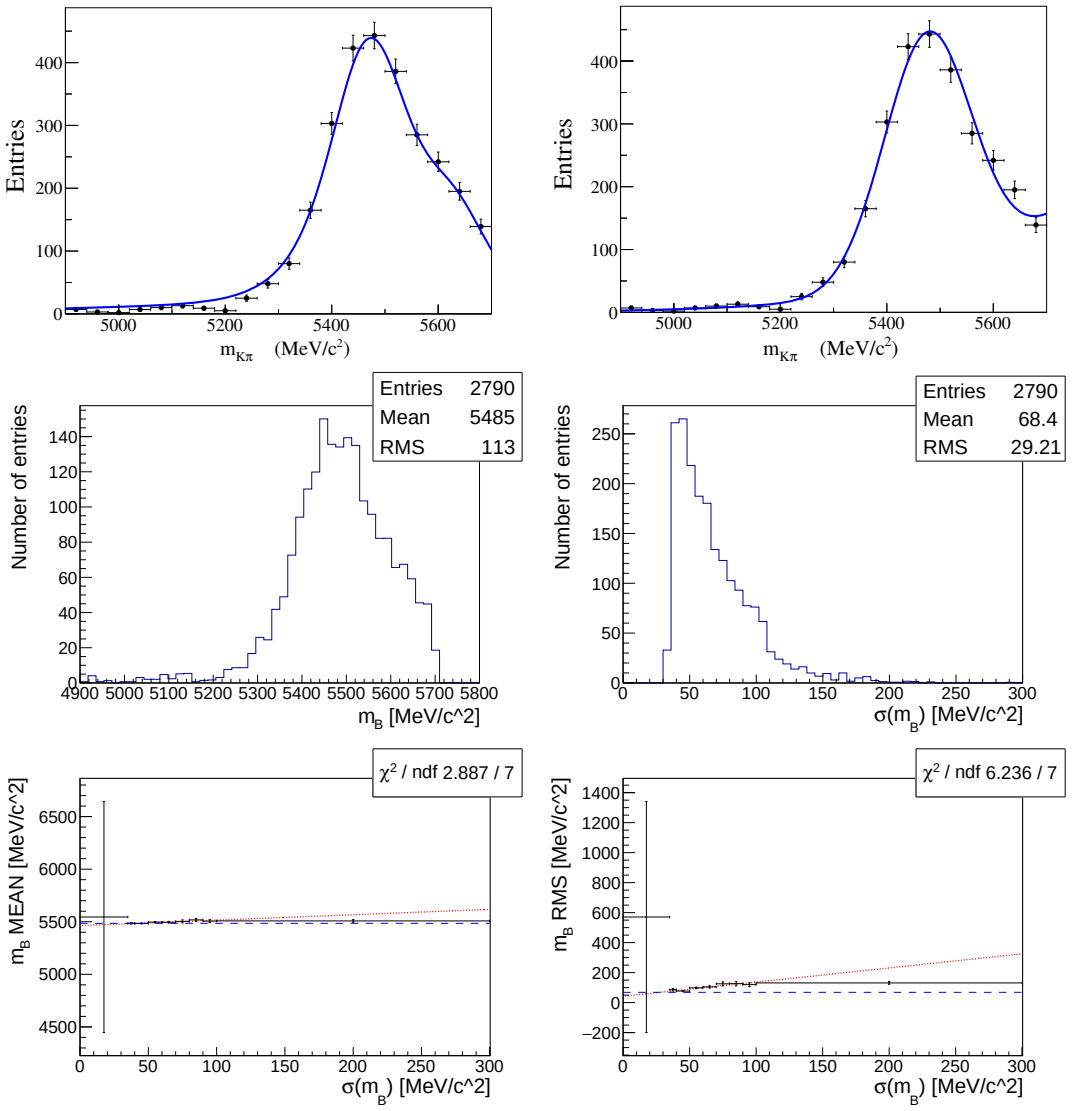

FIGURE 6.15: The triple Gaussian PDF model overlaid on MC simulated data for $B^+ \to J/\psi K^{*+}$, where the widths are scaled by the per event errors (top-left) and left unscaled (top-right). Also shown are the reconstructed mass (middle-left), error on the mass (middle-right), mean mass as a function of the error on the mass (bottom-left) and RMS on the mass as a function of the error on the mass (bottom-right).

The $\Lambda_b \to \Lambda J/\psi$ mass fit and mass-mass error information is shown in Figure 6.16. The mass fits were performed without the inclusion of the mass-mass error correlation, yielding good agreement between the PDF and MC.

As linearity was not observed between the mean m_B and $\sigma(m_B)$, or the RMS on m_B and $\sigma(m_B)$ in fits to both $B_u^+ \to K^+ J/\psi$ and $\Lambda_b \to \Lambda J/\psi$ MC samples, scaling was not used.

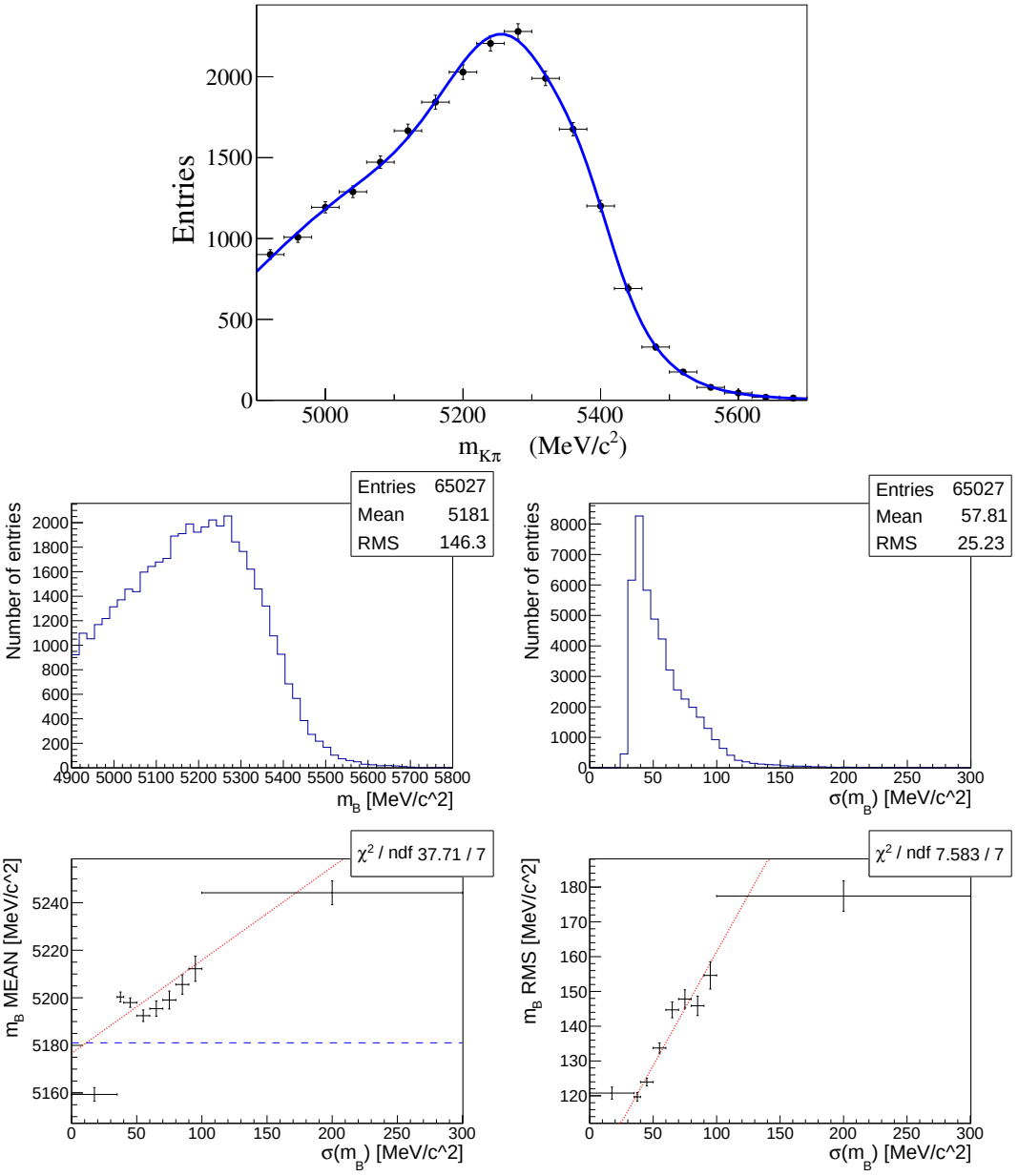

FIGURE 6.16: The triple Gaussian PDF model overlaid on MC simulated data for $\Lambda_b \to \Lambda\mu^+\mu^-$, where the widths are not scaled by the per event errors (top). Also shown are the reconstructed mass (middle-left), error on the mass (middle-right), mean mass as a function of the error on the mass (bottom-left) and RMS on the mass as a function of the error on the mass (bottom-right).

6.3.3 Fits to the Data Control Regions

The control sample based on $B_d^0 \to J/\psi K^{*0}$, described in Section 5, was used to determine values of m_0 and S for subsequent signal fits. The second control sample corresponding to the $B_d^0 \to \psi(2S)K^{*0}$ decay was used to replicate all fits in the $B_d^0 \to J/\psi K^{*0}$ region as a cross check of the derived values.

The PDF described for the signal in Section 6.1.1 was employed to fit the control regions in $q^2 \in [8.0, 11.0]$ $(GeV/c^2)^2$ and $q^2 \in [12.0, 15.0]$ $(GeV/c^2)^2$ for J/ψ and $\psi(2S)$, respectively. All event selection requirements were applied and the fit configuration included signal and combinatorial background components. Variants of the configuration, including the embedded peaking backgrounds were used to assess the effect of the exclusive modes. Each of the backgrounds in Section 6.3.2 were added sequentially, resulting in six separate fits for each control region (signal + combinatorial background + one or more exclusive modes). The statistical errors on the fitted m_0 and S parameters were taken as the largest of the three statistical errors from these fits. The systematic uncertainty was derived from the fits as half of the total spread.

Fits to the $B_d^0 \to J/\psi K^{*0}$ control region resulted in the fitted parameters:

$$\begin{aligned} m_0 &= (5276.6 \ \pm 0.3 \ \pm 0.5) \ MeV/c^2, \\ S &= 1.219 \ \pm 0.005 \ \pm 0.0017. \end{aligned} \tag{6.16}$$

The corresponding fitted parameters from the $B_d^0 \to \psi(2S)K^{*0}$ control region were used as a cross-check:

$$\begin{aligned} m_0 &= (5275.5 \ \pm 1.2 \ \pm 1.7) \ MeV/c^2, \\ S &= 1.191 \ \pm 0.020 \ \pm 0.006. \end{aligned} \tag{6.17}$$

The result from the $\psi(2S)K^0$ region is in agreement with that from the $J/\psi K^{*0}$ region, but with large statistical and systematic uncertainties. A difference of 0.6 MeV/c^2 (0.01%) and 0.035 (2.9%) was observed between $B_d^0 \to J/\psi K^{*0}$ data and MC for m_0 and S, respectively (see Eq. (6.13)), indicating using values of m_0 and S extracted from MC may not be a robust fit model. These shape parameters were instead taken from fits to the $J/\psi K^{*0}$ control region of the data.

Furthermore, the effect of including exclusive background contributions in the fit was assessed and the results are summarised in Table 6.12, in which the following exclusive backgrounds were included in variants of this fit:

$$\begin{aligned} \Lambda_b &\to \Lambda J/\psi \\ B^+ &\to K^+ J/\psi \\ B_s &\to J/\psi K^{*0} \end{aligned} \tag{6.18}$$

The values of m_0 and S extracted from these fits show that the shape of the signal PDF is not strongly dependent on the exclusive background components included, as long as at least one is added to the model. The yields obtained in each of the fits with the exclusive backgrounds were consistent with each other, with the exception of the fit variation including signal, combinatorial background and Λ_b components for $B_d^0 \to \psi(2S)K^{*0}$ in which a negative Λ_b yield was observed. This yield returned to positive once the B^+ component was added. Figure 6.17 shows mass plots for two different background hypotheses in the J/ψ region of data; the mass is not modeled well in this region unless at least one peaking background component is included.

TABLE 6.12: Fitted signal, combinatorial background and peaking background yields, m_0 and S for the $B^0_d \to J/\psi K^{*0}$ and $B^0_d \to \psi(2S)K^{*0}$ control regions. These results were obtained from fits to the entire 2012 data sample. The row marked † uses a single Gaussian mass PDF for the B_s component.

Sample	N_{sig}	N_{bckg}	N_{Λ_b}	N_{B^+}	N_{B_s}	$m_0(MeV/c^2)$	S
$B^0_d \to J/\psi K^{*0}$	150329 ± 510	106411 ± 465	–	–	–	5276.8 ± 0.2	1.235 ± 0.004
	144144 ± 867	100435 ± 816	12164 ± 1382	–	–	5277.0 ± 0.2	1.215 ± 0.005
	141676 ± 882	82671 ± 1591	26725 ± 1591	5668 ± 376	–	5276.3 ± 0.2	1.203 ± 0.005
	141596 ± 889	83395 ± 1929	25801 ± 2320	5508 ± 451	4402 ± 678	5276.1 ± 0.3	1.202 ± 0.005
	141677 ± 883	82726 ± 1838	26657 ± 1838	5657 ± 427	2541 ± 650	5276.3 ± 0.3	1.203 ± 0.005†
$B^0_d \to \psi(2S)K^{*0}$	11861 ± 161	14905 ± 170	–	–	–	5277.2 ± 0.8	1.188 ± 0.015
	11862 ± 161	14904 ± 170	0.0 ± 72	–	–	5277.2 ± 0.8	1.188 ± 0.015
	12035 ± 309	11665 ± 574	2061 ± 714	1005 ± 96	–	5274.8 ± 0.8	1.196 ± 0.018
	12100 ± 300	12448 ± 842	1034 ± 1043	878 ± 152	304 ± 243	5273.8 ± 1.2	1.185 ± 0.020
	12092 ± 309	12370 ± 933	1148 ± 1156	892 ± 163	264 ± 263	5273.9 ± 1.2	1.197 ± 0.019†

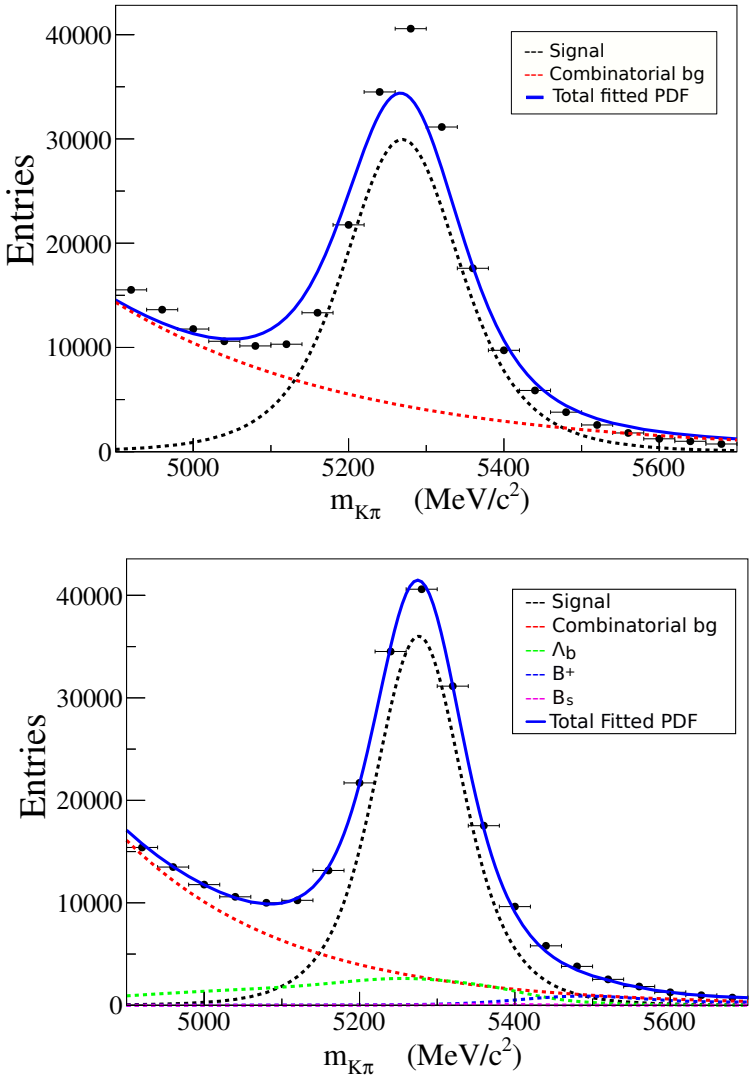

FIGURE 6.17: Control sample mass fit projection for $J/\psi K^{*0}$ from a fit assuming signal and combinatoric background components only (left) and a fit that also includes Λ_b, B^+ and B_s background components (right). These results are obtained using the whole 2012 data sample.

6.3.4 Toy MC Validation of the Likelihood Model

The intrinsic fit bias of the likelihood estimator given in Eq. (6.1) was validated by performing toy MC studies. These studies involved generating signal and backgrounds according to expectations of the likelihood, fitting these samples and then measuring the pull mean and width of the fitted observables.

Validation of the likelihood model was performed for two fit configurations through toy MC studies. The first type, described in Section 6.3.4.1, generated toy MC according to the folded angular PDFs in terms of F_L, S_3 and $S_{i=4,5,7,8}$ using a fit configuration that included signal and combinatorial background components, with the B_d^0 mass, B_d^0 mass error and angular distributions used as discriminating variables. The event yields used for each ensemble of toys were randomly distributed as a Poisson with a mean corresponding to the nominal expected yield, extracted from the mass fits to data summarised in Table 7.1. The mean B_d^0 mass, m_0, and scale factor, S, were fixed at (5276.6 $\pm$ 0.6) MeV/c^2 and 1.219 $\pm$ 0.0018, respectively, according to results from fits to the $B_d^0 \to J/\psi K^{*0}$ control sample, as given in Eq. (6.16).

The second set of toys, referred to as 'embedded toys', were performed by oversampling the number of events in Table 6.3 to represent the peaking background contributions from $B_u^+ \to K^{*+}\ \mu^+\mu^-$, $B_u^+ \to K^+\ \mu^+\mu^-$, $B_s^0 \to \phi\ \mu^+\mu^-$, $\Lambda_b \to \Lambda(1520)\ \mu^+\mu^-$ and $\Lambda_b \to pK^-\ \mu^+\mu^-$. The remaining fit configuration was identical to that used for the nominal PDF toy MC studies, as described in 6.3.4.2.

6.3.4.1 PDF Toy MC Validation

The two-stage fitting stategy outlined in Section 6.1 was adopted and the results from these fits are given in Tables 6.13 to 6.16. A Gaussian function was used to fit the pull distributions and the corresponding constant scaling factor, mean and width from the fit are given for the signal and background yields in each q^2 bin studied.

The S_4, S_5 S_7 and S_8 MC toys were found to be largely unbiased with correctly extracted errors, such that the pull means were consistent with zero and pull widths consistent with one. Linearity tests were performed in which a further set of signal only toys were generated for different initial F_L and S_i values within the physical parameter space. Fits to the generated MC found there was good linearity throughout the parameter space.

In instances for which the biases were slightly higher, an additional test scaled the signal and combinatorial background yields in the same angular distribution toy outlined here by a factor of ten before fitting. In the high statistics toys, all fits converged and the biases previously seen in the pull means were no longer

present. This was consistent with the other studies and led to the conclusion that the biases reported were the intrinsic bias from the fit performed. The intrinsic fit bias highlights that for Run 2 on the ATLAS experiment, an increase in the data samples is required to perform the same angular analysis of $B_d^0 \to K^{*0}\mu^+\mu^-$. Furthermore additional work on controlling the background to reduce the bias is necessary.

TABLE 6.13: Fitted angular observables from 500 angular distribution toys using the S_4 folded PDF. The fit model included signal and combinatorial background components with fixed m_0 and S values in order to fit the angular observables F_L, S_3 and S_4.

q^2 range $((GeV/c^2)^2)$	Param.	Constant	Pull mean	Pull width	Bias (σ)
$[0.04, 2.00]$	F_L	18.851 ± 1.201	-0.083 ± 0.046	0.936 ± 0.042	-1.791
	S_3	18.840 ± 1.198	-0.052 ± 0.046	0.940 ± 0.042	-1.121
	S_4	20.273 ± 1.295	-0.014 ± 0.043	0.853 ± 0.038	-0.324
$[2.00, 4.00]$	F_L	18.378 ± 1.168	-0.121 ± 0.046	0.942 ± 0.042	-2.546
	S_3	17.337 ± 1.124	-0.076 ± 0.050	0.970 ± 0.045	-1.511
	S_4	18.009 ± 1.159	-0.014 ± 0.048	0.934 ± 0.042	-0.284
$[4.00, 6.00]$	F_L	18.360 ± 1.193	0.070 ± 0.049	0.895 ± 0.042	1.414
	S_3	18.260 ± 1.156	0.092 ± 0.047	0.876 ± 0.037	1.968
	S_4	17.762 ± 1.206	0.047 ± 0.049	0.904 ± 0.046	0.966
$[0.04, 4.00]$	F_L	17.928 ± 1.096	0.007 ± 0.049	0.996 ± 0.041	0.145
	S_3	18.527 ± 1.233	0.012 ± 0.047	0.963 ± 0.048	0.263
	S_4	18.947 ± 1.256	0.008 ± 0.047	0.950 ± 0.047	0.170
$[1.10, 6.00]$	F_L	17.845 ± 1.132	-0.022 ± 0.050	1.005 ± 0.045	-0.442
	S_3	20.166 ± 1.276	0.047 ± 0.046	0.925 ± 0.043	1.022
	S_4	18.636 ± 1.121	-0.003 ± 0.049	0.993 ± 0.041	-0.053
$[0.04, 6.00]$	F_L	18.495 ± 1.131	0.064 ± 0.049	1.002 ± 0.044	1.295
	S_3	17.254 ± 1.060	0.077 ± 0.055	1.067 ± 0.049	1.396
	S_4	18.581 ± 1.144	-0.028 ± 0.047	0.963 ± 0.040	-0.589

TABLE 6.14: Fitted angular observables from 500 angular distribution toys using the S_5 folded PDF. The fit model included signal and combinatorial background components with fixed m_0 and S values in order to fit the angular observables F_L, S_3 and S_5.

q^2 range $((GeV/c^2)^2)$	Param.	Constant	Pull mean	Pull width	Bias (σ)
$[0.04, 2.00]$	F_L	15.570 ± 0.980	0.058 ± 0.058	1.116 ± 0.051	1.004
	S_3	17.440 ± 1.128	0.041 ± 0.049	0.979 ± 0.045	0.839
	S_5	17.627 ± 1.116	-0.035 ± 0.053	1.018 ± 0.047	-0.667
$[2.00, 4.00]$	F_L	14.890 ± 1.077	0.068 ± 0.051	0.903 ± 0.045	1.345
	S_3	16.525 ± 1.245	0.127 ± 0.047	0.806 ± 0.045	2.729
	S_5	17.996 ± 1.166	0.008 ± 0.045	0.868 ± 0.037	0.183
$[4.00, 6.00]$	F_L	18.097 ± 1.309	-0.020 ± 0.044	0.771 ± 0.041	-0.444
	S_3	18.045 ± 1.366	-0.026 ± 0.041	0.714 ± 0.038	-0.626
	S_5	18.706 ± 1.257	0.005 ± 0.044	0.851 ± 0.040	0.108
$[0.04, 4.00]$	F_L	19.424 ± 1.290	0.012 ± 0.045	0.907 ± 0.044	0.272
	S_3	18.768 ± 1.208	0.042 ± 0.048	0.971 ± 0.045	0.874
	S_5	18.853 ± 1.118	-0.117 ± 0.047	0.982 ± 0.038	-2.467
$[1.10, 6.00]$	F_L	17.787 ± 1.099	-0.055 ± 0.054	1.030 ± 0.046	-1.018
	S_3	18.024 ± 1.178	0.080 ± 0.050	0.993 ± 0.048	1.622
	S_5	16.598 ± 1.044	-0.122 ± 0.054	1.026 ± 0.045	-2.275
$[0.04, 6.00]$	F_L	18.497 ± 1.208	-0.053 ± 0.051	0.975 ± 0.050	-1.012
	S_3	17.663 ± 1.072	-0.014 ± 0.054	1.096 ± 0.050	-0.266
	S_5	18.098 ± 1.112	-0.027 ± 0.051	1.041 ± 0.046	-0.527

TABLE 6.15: Fitted angular observables from 500 angular distribution toys using the S_7 folded PDF. The fit model included signal and combinatorial background components with fixed m_0 and S values in order to fit the angular observables F_L, S_3 and S_7.

q^2 range $((GeV/c^2)^2)$	Param.	Constant	Pull mean	Pull width	Bias (σ)
$[0.04, 2.00]$	F_L	16.418 ± 1.077	0.017 ± 0.053	1.054 ± 0.051	0.326
	S_3	17.401 ± 1.084	-0.019 ± 0.051	1.034 ± 0.045	-0.382
	S_7	18.597 ± 1.129	0.036 ± 0.048	0.979 ± 0.041	0.747
$[2.00, 4.00]$	F_L	17.705 ± 1.091	-0.122 ± 0.049	0.938 ± 0.037	-2.502
	S_3	18.994 ± 1.259	0.026 ± 0.045	0.890 ± 0.042	0.592
	S_7	16.882 ± 1.077	0.034 ± 0.052	1.010 ± 0.046	0.653
$[4.00, 6.00]$	F_L	17.477 ± 1.101	0.050 ± 0.049	0.965 ± 0.041	1.032
	S_3	20.112 ± 1.298	-0.047 ± 0.042	0.828 ± 0.037	-1.130
	S_7	18.686 ± 1.171	-0.050 ± 0.048	0.949 ± 0.042	-1.042
$[0.04, 4.00]$	F_L	17.775 ± 1.109	-0.025 ± 0.051	1.029 ± 0.047	-0.497
	S_3	18.396 ± 1.138	0.035 ± 0.050	1.002 ± 0.044	0.745
	S_7	19.482 ± 1.172	0.106 ± 0.047	0.960 ± 0.039	2.261
$[1.10, 6.00]$	F_L	17.843 ± 1.156	0.055 ± 0.049	0.988 ± 0.046	1.131
	S_3	18.563 ± 1.093	0.007 ± 0.049	1.008 ± 0.039	0.142
	S_7	18.052 ± 1.091	0.003 ± 0.051	1.041 ± 0.044	0.060
$[0.04, 6.00]$	F_L	18.347 ± 1.142	0.026 ± 0.049	0.970 ± 0.042	0.545
	S_3	18.061 ± 1.190	0.019 ± 0.049	0.962 ± 0.047	0.386
	S_7	18.341 ± 1.130	-0.013 ± 0.050	1.007 ± 0.044	-0.262

TABLE 6.16: Fitted angular observables from 500 angular distribution toys using the S_8 folded PDF. The fit model included signal and combinatorial background components with fixed m_0 and S values in order to fit the angular observables F_L, S_3 and S_8.

q^2 range $((GeV/c^2)^2)$	Param.	Constant	Pull mean	Pull width	Bias (σ)
$[0.04, 2.00]$	F_L	16.211 ± 1.155	0.087 ± 0.051	0.932 ± 0.051	1.706
	S_3	16.149 ± 1.148	-0.052 ± 0.051	0.910 ± 0.050	-1.003
	S_8	19.225 ± 1.237	-0.026 ± 0.045	0.795 ± 0.036	-0.582
$[2.00, 4.00]$	F_L	14.684 ± 1.098	-0.002 ± 0.057	0.913 ± 0.055	-0.034
	S_3	14.558 ± 1.141	0.080 ± 0.052	0.839 ± 0.050	1.544
	S_8	18.686 ± 1.338	-0.001 ± 0.042	0.740 ± 0.038	-0.012
$[4.00, 6.00]$	F_L	15.440 ± 1.128	0.021 ± 0.052	0.868 ± 0.047	0.417
	S_3	16.425 ± 1.221	-0.037 ± 0.047	0.807 ± 0.045	-0.782
	S_8	16.123 ± 1.183	-0.033 ± 0.047	0.800 ± 0.041	-0.711
$[0.04, 4.00]$	F_L	17.635 ± 1.159	-0.072 ± 0.050	0.990 ± 0.048	-1.437
	S_3	19.040 ± 1.176	-0.071 ± 0.046	0.923 ± 0.039	-1.548
	S_8	18.032 ± 1.136	0.007 ± 0.047	0.881 ± 0.037	0.153
$[1.00, 6.00]$	F_L	17.452 ± 1.106	0.005 ± 0.050	0.971 ± 0.042	0.092
	S_3	19.190 ± 1.167	-0.027 ± 0.049	0.927 ± 0.041	-0.555
	S_8	19.128 ± 1.243	0.118 ± 0.043	0.829 ± 0.036	2.708
$[0.04, 6.00]$	F_L	18.085 ± 1.120	0.010 ± 0.050	1.009 ± 0.044	0.207
	S_3	19.264 ± 1.200	-0.007 ± 0.046	0.952 ± 0.041	-0.153
	S_8	19.269 ± 1.134	0.155 ± 0.046	0.951 ± 0.036	3.358

6.3.4.2 Embedded Toy MC Validation

The embedded toy MC studies were performed for both the mass and the angular distributions, employing the same procedure outlined above. Mass fit toys with embedded peaking backgrounds are summarised in Section 6.3.4.3 and embedded angular distribution toys are detailed in Section 6.3.4.4.

6.3.4.3 Mass Fit Toys

The fitted average values of the signal and background yields and their errors, based on 500 toys, are given in Table 6.17. The pull widths are compatible with one, indicating that the fit is able to extract the uncertainty from the data accurately. The signal yield pull means are compatible with zero, demonstrating that the fit is able to extract the signal yield with an acceptable bias relative to the statistical uncertainty. The combinatorial backround yield pull means are biased by amounts ranging between 2.8 σ and 7.4 σ for the different q^2 bins. These biases are consistent with the respective embedded background contributions from Table 6.3, indicating that the peaking backgrounds are included in the combinatorial background model, rather than the signal model.

TABLE 6.17: Mass fit toy results for a configuration that includes signal and combinatorial background components with embedded peaking background contributions as summarised in Table 6.3.

q^2 range $((GeV/c^2)^2)$	Param.	Constant	Pull mean	Pull width	Bias (σ)
$[0.04, 2.00]$	N_{sig}	19.931 ± 1.253	-0.001 ± 0.046	0.917 ± 0.040	-0.020
	N_{bckg}	19.086 ± 1.136	0.177 ± 0.048	0.953 ± 0.039	3.686
$[2.00, 4.00]$	N_{sig}	17.653 ± 1.083	0.017 ± 0.052	1.034 ± 0.045	0.333
	N_{bckg}	17.772 ± 1.086	0.150 ± 0.053	1.029 ± 0.046	2.846
$[4.00, 6.00]$	N_{sig}	18.455 ± 1.178	-0.078 ± 0.048	1.000 ± 0.046	-1.617
	N_{bckg}	18.640 ± 1.184	0.161 ± 0.047	0.953 ± 0.042	3.457
$[0.04, 4.00]$	N_{sig}	18.401 ± 1.118	0.028 ± 0.052	1.031 ± 0.048	0.527
	N_{bckg}	19.315 ± 1.184	0.158 ± 0.046	0.940 ± 0.039	3.469
$[1.10, 6.00]$	N_{sig}	18.072 ± 1.125	-0.006 ± 0.050	0.986 ± 0.044	-0.130
	N_{bckg}	18.923 ± 1.220	0.283 ± 0.049	0.975 ± 0.048	5.791
$[0.04, 6.00]$	N_{sig}	19.759 ± 1.288	0.004 ± 0.047	0.892 ± 0.042	0.076
	N_{bckg}	18.664 ± 1.306	0.339 ± 0.046	0.914 ± 0.049	7.413

6.3.4.4 Angular Distribution Toys

The results from the embedded angular distribution toys are given in Tables 6.18 to 6.21 below. Overall the biases seen were small, indicating the fit was able to correctly extract the angular parameters when the peaking background contributions were included. However, some significant biases were seen in F_L, particularly in two of wide q^2 bins, $q^2 \in [1.10, 6.00]$ $(GeV/c^2)^2$ and $q^2 \in [0.04, 6.00]$ $(GeV/c^2)^2$.

TABLE 6.18: Fitted angular observables from 500 embedded angular distribution toys using the S_4 folded PDF. The fit model included signal and combinatorial background components with embedded peaking background contributions from Table 6.3.

q^2 range $((GeV/c^2)^2)$	Param.	Constant	Pull mean	Pull width	Bias (σ)
$[0.04, 2.00]$	F_L	19.398 ± 1.260	-0.094 ± 0.044	0.887 ± 0.041	-2.133
	S_3	18.170 ± 1.171	0.004 ± 0.047	0.933 ± 0.041	0.076
	S_4	21.091 ± 1.346	-0.048 ± 0.041	0.813 ± 0.036	-1.169
$[2.00, 4.00]$	F_L	17.962 ± 1.149	-0.155 ± 0.049	0.969 ± 0.044	-3.168
	S_3	17.448 ± 1.120	-0.015 ± 0.050	0.995 ± 0.046	-0.296
	S_4	17.388 ± 1.148	-0.023 ± 0.049	0.944 ± 0.045	-0.469
$[4.00, 6.00]$	F_L	18.422 ± 1.184	0.008 ± 0.049	0.901 ± 0.042	0.165
	S_3	17.431 ± 1.094	0.089 ± 0.049	0.909 ± 0.038	1.822
	S_4	18.113 ± 1.230	0.061 ± 0.047	0.862 ± 0.043	1.297
$[0.04, 4.00]$	F_L	17.426 ± 1.195	0.011 ± 0.053	1.029 ± 0.058	0.209
	S_3	19.117 ± 1.292	-0.042 ± 0.047	0.951 ± 0.050	-0.883
	S_4	19.250 ± 1.208	-0.012 ± 0.047	0.960 ± 0.043	-0.256
$[1.10, 6.00]$	F_L	18.504 ± 1.260	-0.196 ± 0.048	0.956 ± 0.050	-4.045
	S_3	19.273 ± 1.288	-0.022 ± 0.046	0.924 ± 0.047	-0.477
	S_4	18.283 ± 1.108	-0.008 ± 0.051	1.031 ± 0.045	-0.163
$[0.04, 6.00]$	F_L	18.503 ± 1.081	-0.046 ± 0.049	1.011 ± 0.038	-0.955
	S_3	18.407 ± 1.145	0.048 ± 0.048	0.943 ± 0.041	0.990
	S_4	18.787 ± 1.243	-0.068 ± 0.045	0.889 ± 0.041	-1.529

TABLE 6.19: Fitted angular observables from 500 embedded angular distribution toys using the S_5 folded PDF. The fit model included signal and combinatorial background components with embedded peaking background contributions from Table 6.3.

q^2 range $((GeV/c^2)^2)$	Param.	Constant	Pull mean	Pull width	Bias (σ)
$[0.04, 2.00]$	F_L	16.936 ± 1.046	0.030 ± 0.054	1.074 ± 0.047	0.554
	S_3	17.802 ± 1.119	0.058 ± 0.051	1.023 ± 0.047	1.150
	S_5	18.117 ± 1.118	-0.082 ± 0.051	1.033 ± 0.047	-1.604
$[2.00, 4.00]$	F_L	3.679 ± 0.588	0.086 ± 0.137	1.047 ± 0.184	0.626
	S_3	3.572 ± 0.645	0.119 ± 0.140	1.060 ± 0.223	0.848
	S_5	4.994 ± 0.640	-0.085 ± 0.106	0.974 ± 0.111	-0.799
$[4.00, 6.00]$	F_L	17.188 ± 1.254	-0.065 ± 0.044	0.769 ± 0.039	-1.492
	S_3	16.704 ± 1.292	0.051 ± 0.047	0.805 ± 0.049	1.089
	S_5	17.638 ± 1.209	-0.022 ± 0.046	0.872 ± 0.043	-0.479
$[0.04, 4.00]$	F_L	19.102 ± 1.260	0.034 ± 0.045	0.904 ± 0.042	0.766
	S_3	18.441 ± 1.180	-0.043 ± 0.047	0.979 ± 0.044	-0.895
	S_5	18.594 ± 1.117	-0.078 ± 0.050	1.005 ± 0.043	-1.560
$[1.10, 6.00]$	F_L	18.339 ± 1.117	-0.191 ± 0.050	1.024 ± 0.044	-3.834
	S_3	17.405 ± 1.160	0.048 ± 0.051	1.020 ± 0.052	0.953
	S_5	17.113 ± 1.034	-0.107 ± 0.054	1.061 ± 0.045	-1.989
$[0.04, 6.00]$	F_L	18.962 ± 1.208	-0.197 ± 0.046	0.906 ± 0.040	-4.320
	S_3	17.949 ± 1.124	-0.035 ± 0.050	1.026 ± 0.047	-0.686
	S_5	18.003 ± 1.104	-0.046 ± 0.049	1.009 ± 0.043	-0.943

TABLE 6.20: Fitted angular observables from 500 embedded angular distribution toys using the S_7 folded PDF. The fit model included signal and combinatorial background components with embedded peaking background contributions from Table 6.3.

q^2 range $((GeV/c^2)^2)$	Param.	Constant	Pull mean	Pull width	Bias (σ)
$[0.04, 2.00]$	F_L	16.241 ± 1.054	0.017 ± 0.056	1.085 ± 0.053	0.303
	S_3	17.357 ± 1.096	-0.037 ± 0.052	1.048 ± 0.048	-0.718
	S_7	18.844 ± 1.144	0.034 ± 0.047	0.973 ± 0.040	0.717
$[2.00, 4.00]$	F_L	16.859 ± 1.071	-0.155 ± 0.053	0.991 ± 0.044	-2.909
	S_3	19.237 ± 1.262	0.057 ± 0.045	0.895 ± 0.042	1.272
	S_7	17.743 ± 1.085	0.049 ± 0.052	1.010 ± 0.043	0.938
$[4.00, 6.00]$	F_L	18.141 ± 1.176	-0.057 ± 0.046	0.918 ± 0.041	-1.229
	S_3	19.721 ± 1.296	-0.022 ± 0.044	0.852 ± 0.040	-0.500
	S_7	18.971 ± 1.252	-0.087 ± 0.046	0.895 ± 0.042	-1.917
$[0.04, 4.00]$	F_L	17.325 ± 1.067	-0.042 ± 0.053	1.059 ± 0.047	-0.798
	S_3	18.332 ± 1.076	-0.013 ± 0.051	1.045 ± 0.042	-0.262
	S_7	19.156 ± 1.165	0.070 ± 0.049	0.989 ± 0.044	1.418
$[1.10, 6.00]$	F_L	17.867 ± 1.175	-0.092 ± 0.050	1.000 ± 0.050	-1.820
	S_3	18.514 ± 1.093	-0.032 ± 0.049	0.998 ± 0.039	-0.654
	S_7	17.995 ± 1.093	0.002 ± 0.051	1.038 ± 0.044	0.043
$[0.04, 6.00]$	F_L	17.661 ± 1.124	0.064 ± 0.051	0.998 ± 0.045	1.268
	S_3	19.283 ± 1.196	0.005 ± 0.044	0.902 ± 0.037	0.114
	S_7	18.751 ± 1.131	-0.051 ± 0.049	1.002 ± 0.042	-1.043

TABLE 6.21: Fitted angular observables from 500 embedded angular distribution toys using the S_8 folded PDF. The fit model included signal and combinatorial background components with embedded peaking background contributions from Table 6.3.

q^2 range $((GeV/c^2)^2)$	Param.	Constant	Pull mean	Pull width	Bias (σ)
$[0.04, 2.00]$	F_L	15.345 ± 1.050	0.046 ± 0.054	0.982 ± 0.050	0.843
	S_3	15.849 ± 1.092	-0.005 ± 0.052	0.919 ± 0.046	-0.100
	S_8	17.569 ± 1.178	-0.014 ± 0.048	0.806 ± 0.039	-0.295
$[2.00, 4.00]$	F_L	13.480 ± 1.093	0.032 ± 0.054	0.827 ± 0.051	0.597
	S_3	14.752 ± 1.093	-0.014 ± 0.051	0.842 ± 0.044	-0.274
	S_8	18.262 ± 1.352	-0.032 ± 0.043	0.724 ± 0.040	-0.740
$[4.00, 6.00]$	F_L	16.107 ± 1.120	-0.017 ± 0.050	0.859 ± 0.042	-0.347
	S_3	16.429 ± 1.187	-0.092 ± 0.048	0.831 ± 0.044	-1.907
	S_8	16.348 ± 1.173	-0.032 ± 0.048	0.817 ± 0.042	-0.668
$[0.04, 4.00]$	F_L	18.229 ± 1.186	-0.060 ± 0.048	0.953 ± 0.045	-1.259
	S_3	18.081 ± 1.157	-0.122 ± 0.047	0.945 ± 0.042	-2.588
	S_8	18.099 ± 1.103	-0.090 ± 0.050	0.957 ± 0.041	-1.803
$[1.10, 6.00]$	F_L	17.784 ± 1.138	-0.077 ± 0.051	0.972 ± 0.045	-1.490
	S_3	19.554 ± 1.201	-0.071 ± 0.046	0.891 ± 0.038	-1.544
	S_8	18.260 ± 1.171	0.119 ± 0.047	0.907 ± 0.041	2.529
$[0.04, 6.00]$	F_L	17.756 ± 1.111	-0.146 ± 0.051	1.031 ± 0.046	-2.889
	S_3	18.909 ± 1.240	0.046 ± 0.047	0.932 ± 0.043	0.989
	S_8	19.404 ± 1.152	0.055 ± 0.046	0.920 ± 0.035	1.204

Chapter 7

Mass Fits

This chapter documents the fits to the mass distributions in data, performed in the different q^2 regions under study. Projection plots of the mass distribution fitted for each of the q^2 regions are shown, along with the corresponding set of likelihood ratio (LR) plots. The LR was computed as $\mathcal{L}_{sig}/(\mathcal{L}_{sig}+\mathcal{L}_{bckg})$ on an event-by-event basis, where $\mathcal{L}_{sig}$ and $\mathcal{L}_{bckg}$ are the likelihoods for a given event to be signal or background, respectively. The green component of the LR plots corresponds to the signal toy MC and the red component to the combinatorial background toy MC, both generated from the likelihood normalised to the yields fitted on data. The mass fits were nominally performed allowing for a $\Lambda_b \to \Lambda(1520)(pK^-)\ \mu^+\mu^-$ component in the fit, however a significant Λ_b yield was not observed. Taking into consideration the discussion in Sec. 6.3.2 regarding the expected yields and observed fitted yields consistent with zero, the Λ_b component was removed from subsequent fits. The strategy to account for this peaking background was instead replaced with that used for the other exclusive background modes. For the mass distribution plots here, the black (dashed) line corresponds to the fitted signal, the red (dashed) line to the combinatorial background and the blue (solid) line to the total fitted PDF.

The fit configuration for mass fits is described in Sec. 6.1, and the signal m_0 and S parameters were fixed to the values obtained from fits to the $B^0_d \to J/\psi K^{*0}$ control sample region in the data, given in Eq. (6.16). The results shown here are broken down into 2 $(GeV/c^2)^2$ and wide low-q^2 bin mass fits.

The fitted parameters from mass fits to data in the 2 $(GeV/c^2)^2$ and wide low-q^2 binning schemes are summarised in Table 7.1; the fitted signal yield N_{sig}, background yield N_{bckg} and background shape parameter λ are all given. The mass distributions are shown in Figs 7.1 through 7.6, where the high minimum mass cut is attributed to the selection requirement to remove the background observed at low B masses, as discussed in Chapter 4. The S/B in each bin allowed for a sufficient percentage of fits converging ($> 80\%$) for the angular analysis.

TABLE 7.1: Fitted yields and λ from mass fits to data in the 2 $(GeV/c^2)^2$ and wide low-q^2 binning schemes.

q^2 Range $((GeV/c^2)^2)$	N_{sig}	N_{bckg}	λ
$[0.04, 2.0]$	128^{+22}_{-22}	122^{+22}_{-21}	$-0.0013^{+0.0010}_{-0.0008}$
$[2.0, 4.0]$	106^{+23}_{-22}	113^{+23}_{-22}	$-0.0021^{+0.0011}_{-0.0009}$
$[4.0, 6.0]$	114^{+24}_{-23}	204^{+26}_{-25}	$-0.0030^{+0.0006}_{-0.0006}$
$[0.04, 4.0]$	236^{+32}_{-31}	233^{+32}_{-31}	$-0.0016^{+0.0007}_{-0.0006}$
$[1.1, 6.0]$	275^{+35}_{-34}	363^{+36}_{-35}	$-0.0024^{+0.0005}_{-0.0005}$
$[0.04, 6.0]$	342^{+39}_{-38}	445^{+40}_{-39}	$-0.0023^{+0.0004}_{-0.0004}$

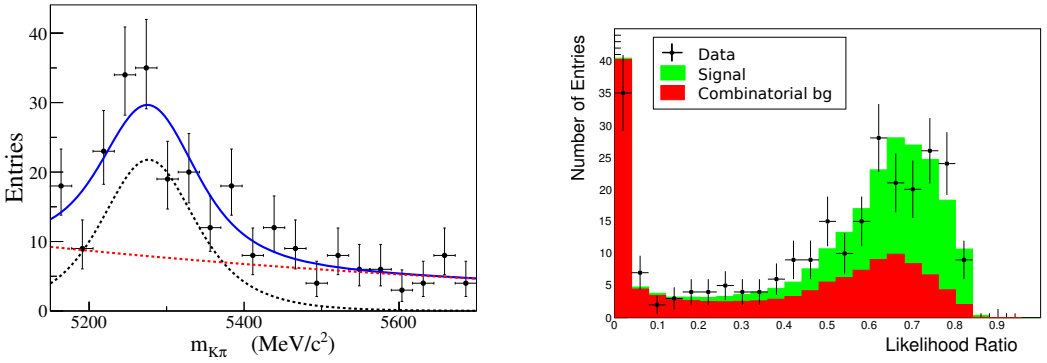

FIGURE 7.1: (left) Mass fit projection and (right) LR distribution $\mathcal{L}_{sig}/(\mathcal{L}_{sig} + \mathcal{L}_{bckg})$ for $q^2 \in [0.04, 2.00]$ $(GeV/c^2)^2$. In the mass fit projection, the black (dashed) line corresponds to the fitted signal, the red (dashed) line to the combinatorial background and the blue (solid) line to the total fitted PDF.

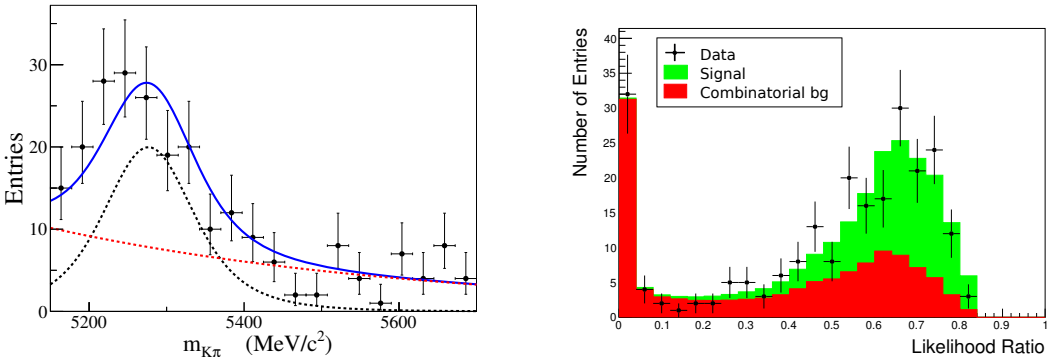

FIGURE 7.2: (left) Mass fit projection and (right) LR distribution $\mathcal{L}_{sig}/(\mathcal{L}_{sig} + \mathcal{L}_{bckg})$ for $q^2 \in [2.00, 4.00]$ $(GeV/c^2)^2$. In the mass fit projection, the black (dashed) line corresponds to the fitted signal, the red (dashed) line to the combinatorial background and the blue (solid) line to the total fitted PDF.

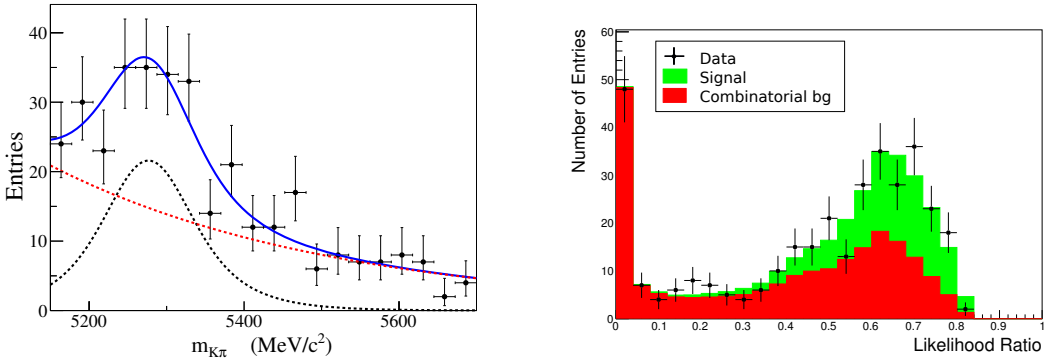

FIGURE 7.3: (left) Mass fit projection and (right) LR distribution $\mathcal{L}_{sig}/(\mathcal{L}_{sig} + \mathcal{L}_{bckg})$ for $q^2 \in [4.00, 6.00]$ $(GeV/c^2)^2$. In the mass fit projection, the black (dashed) line corresponds to the fitted signal, the red (dashed) line to the combinatorial background and the blue (solid) line to the total fitted PDF.

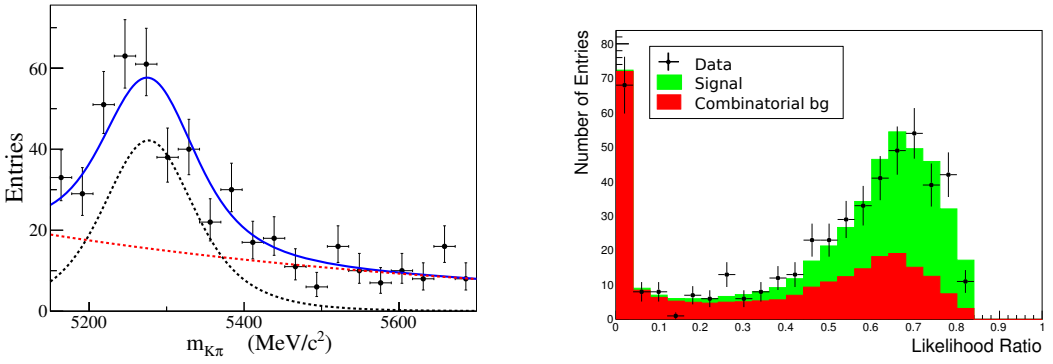

FIGURE 7.4: (left) Mass fit projection and (right) LR distribution $\mathcal{L}_{sig}/(\mathcal{L}_{sig} + \mathcal{L}_{bckg})$ for $q^2 \in [0.04, 4.00]$ $(GeV/c^2)^2$. In the mass fit projection, the black (dashed) line corresponds to the fitted signal, the red (dashed) line to the combinatorial background and the blue (solid) line to the total fitted PDF.

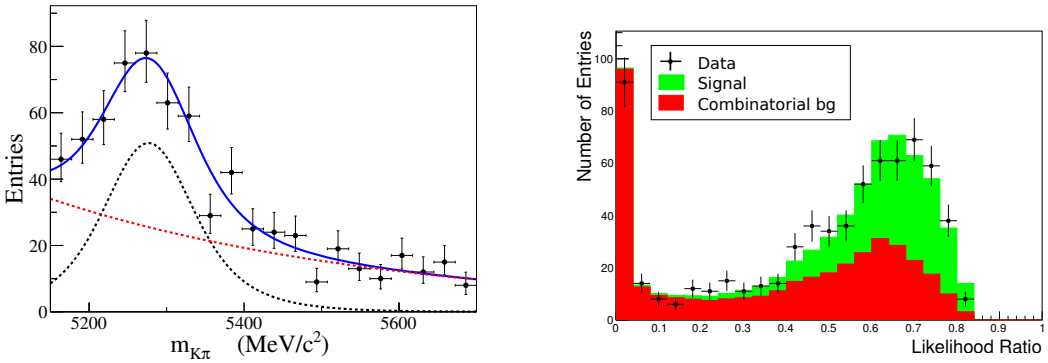

FIGURE 7.5: (left) Mass fit projection and (right) LR distribution $\mathcal{L}_{sig}/(\mathcal{L}_{sig} + \mathcal{L}_{bckg})$ for $q^2 \in [1.10, 6.00]$ $(GeV/c^2)^2$. In the mass fit projection, the black (dashed) line corresponds to the fitted signal, the red (dashed) line to the combinatorial background and the blue (solid) line to the total fitted PDF.

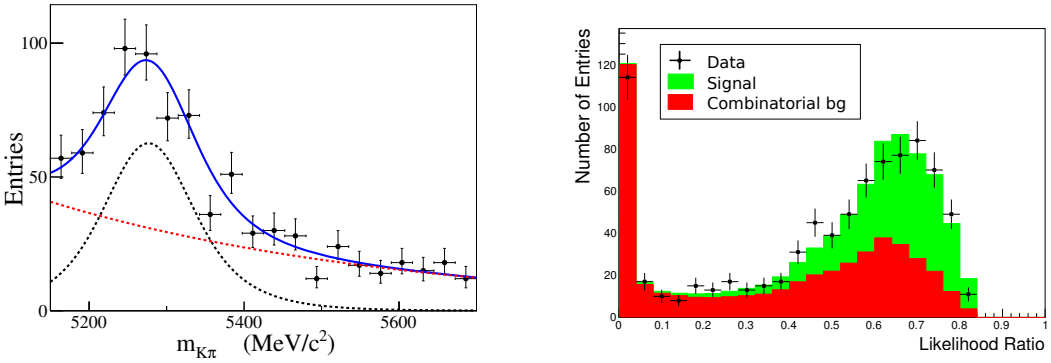

FIGURE 7.6: (left) Mass fit projection and (right) LR distribution $\mathcal{L}_{sig}/(\mathcal{L}_{sig} + \mathcal{L}_{bckg})$ for $q^2 \in [0.04, 6.00]$ $(GeV/c^2)^2$. In the mass fit projection, the black (dashed) line corresponds to the fitted signal, the red (dashed) line to the combinatorial background and the blue (solid) line to the total fitted PDF.

Chapter 8

Systematic Uncertainties

This chapter documents the sources of systematic uncertainty that were considered for this analysis. The following subsections outline the results from ten sources of systematic uncertainty, each assigned to correct for potential angular or q^2 dependent biases introduced to the analysis:

- PDF nuisance parameters (See Sec. 8.1).
- Background description in the angular distributions (See Sec. 8.2).
- Peaking background (See Sec. 8.3).
- Data-MC differences (See Sec. 8.4).
- Fit bias (See Sec. 8.5).
- Kaon-pion misidentification (See Sec. 8.6).
- S-wave contribution (See Sec. 8.7).
- Misreconstructed decays (See Sec. 8.8).
- Acceptance functions (See Sec 8.9).
- Mass fit range (See Sec. 8.10).

For each systematic uncertainty analysed, the errors from the nominal fit result and varied fit result were found to be consistent, hence the systematic uncertainties described here were assumed to be additive and the errors combined in quadrature.

The one exception to this was the systematic uncertainty from the dilution factor, which was multiplicative.

8.1 PDF Nuisance Parameters

The systematic uncertainty contribution from the fixed model parameters in the nominal angular fit were calculated. The relevant PDF nuisance parameters were:

- Background yield,
- background slope parameter λ,
- $\cos\theta_K$ acceptance parameters K_1 - K_6,
- $\cos\theta_L$ acceptance parameters L_1 - L_2,
- ϕ acceptance parameters P_1 - P_2 (for the S_4 PDF only).

The specified parameters were varied by $\pm$ 1 σ from their nominal values and the data was refitted. The deviation between the nominal fitted angular observables given in Table 9.1 and the fitted angular observables when moving the PDF parameters up and down by 1 σ were computed as the systematic uncertainty from this source. These uncertainties are shown in Appendix C in Table C.1 for each q^2 bin.

The dominant contribution to the systematic uncertainties given in Table C.1 come from varying the signal and background yields.

8.2 Background Description in Angular Distributions

The combinatorial background angular shapes were modelled using second order Chebyshev polynomials, as given by Eq. (6.6). The uncertainty associated with the choice of order for the polynomials was evaluated by increasing the order to three and repeating the fits to data. The uncertainty associated with the parameterisation was taken to be the difference between the fitted angular parameter

results in the two fits. These uncertainties are shown in Table C.2 for the folded PDFs in terms of S_4 to S_8, categorised by q^2 bin.

8.3 Peaking Background Contribution

The nominal fit model neglected peaking background contributions from $B^+ \to K^{*+}\mu^+\mu^-$, $B^+ \to K^+\mu^+\mu^-$, $B_s^0 \to \phi\mu^+\mu^-$, $\Lambda_b \to \Lambda(1520)\ \mu^+\mu^-$ and $\Lambda_b \to pK^-\ \mu^+\mu^-$ decays. Toy MC was used to sequentially neglect and over-sample the expected number of events in each q^2 bin, given in Table 6.3, in order to establish the effect the peaking backgrounds have on the fit. A systematic uncertainty to account for this effect was calculated as the difference between the fitted angular parameters in the toy MC results for PDF and embedded toys, as summarised in Secs 6.3.4.1 and 6.3.4.2, respectively. The results are shown in Table C.3 for the S_4, S_5, S_7 and S_8 folded PDFs in each q^2 bin.

8.4 Data-MC Agreement

A set of systematic uncertainties were evaluated to account for differences between data and MC. The trigger weighted $J/\psi K^{*0}$ control region of the data, where $q^2 \in [8.00, 11.00]\ (GeV/c^2)^2$, was used to study the B_d^0 p_T spectrum in three B_d^0 mass windows. The low and high mass regions $(5150 < M(B_d^0) < 5200)\ MeV/c^2$ and $(5450 < M(B_d^0) < 5700)\ MeV/c^2$, respectively) were defined as the left and right sidebands and the central mass region, $5200 < M(B_d^0) < 5450$, as the window encompassing the majority of the $J/\psi K^{*0}$ peak.

A simple fit comprised of a Gaussian plus a linear function was performed on the B_d^0 mass distribution in the central mass range in order to evaluate the fraction of signal and background events in this region. The B_d^0 p_T distribution corresponding to the right mass sideband was subsequently normalised to the extracted background yield in the central mass region and subtracted from the central B_d^0 p_T distribution[1].

[1]The process was repeated for the left sideband. The difference between the subtraction of the two sidebands was found to be negligible. The right sideband required the least amount of scaling to the background yield and thus was picked over the left to propagate through to the systematic uncertainty.

The $B_d^0 \to J/\psi K^{*0}$ MC B_d^0 p_T spectrum for $q^2 \in [8.00, 11.00]$ $(GeV/c^2)^2$ and $(5200 < M(B_d^0) < 5450)$ MeV/c^2 was normalised to the sideband subtracted p_T distribution from data and the ratio of data/MC calculated.

The trigger weight applied to the phase space signal MC was modified to include the $J/\psi K^{*0}$ data/MC weight and the fits to the signal MC performed in Sec. 6.2 were repeated. The systematic uncertainty was calculated as the difference in fitted angular variables before and after the data/MC ratio was applied to the event weight. The results are summarised in Table C.4.

8.5 Fit Bias

A systematic uncertainty was assigned to account for the intrinsic fit bias of the likelihood estimator, determined from PDF toy MC studies, as described in Sec. 6.3. The systematic uncertainty was evaluated as the difference between the nominal results from the PDF toy MC outlined in Sec. 6.3.4.1 and toy MC generated using these nominal fit results corrected for their fit bias. Results are shown in Table C.5 for each of the folded $S_{i=4,5,7,8}$ PDFs in each q^2 bin.

8.6 Kaon-Pion Misidentification

A systematic uncertainty to account for kaon-pion misidentification effects was applied. The mistag probability of B_d^0 events to be reconstructed as $\overline{B}_d^0$ events as a result of a pion being misidentified as a kaon in the reconstruction is given by ω, as described in Sec. 6.1.1.1. Likewise, the mistag probability of $\overline{B}_d^0$ events to be reconstructed as B_d^0 events as a result of a kaon being misidentified as a pion in the reconstruction is given by $\overline{\omega}$. The two SM signal MC samples were used to determine the value of ω and $\overline{\omega}$ for each q^2 region under study. The angular parameters S_4 and S_5 are directly affected by this mistag and hence the dilution $D = 1 - 2\langle\omega\rangle$ was factored out of the data folded for these two observables. Here the approximation $1 - \omega - \overline{\omega} = 1 - 2\langle\omega\rangle$ was assumed, validated by $\Delta\omega = \omega - \overline{\omega}$ values consistent with zero, as shown in Table 6.2. The uncertainty on ω and $\overline{\omega}$ was determined by the MC statistical uncertainty; accordingly the systematic uncertainty arising from the dilution factor on data was taken to be $\Delta\omega/2$, given in Table C.6.

8.7 S-Wave

In addition to the resonant P-wave contribution to the $K^+\pi^-\mu^+\mu^-$ final state, in which the hadronic pair are daughters from a K^{*0} decay, the $K^+\pi^-$ system can also be in an S-wave configuration, as described in Sec 5.1. The S-wave MC sample has a broader B mass distribution than the signal one; in the fits to data the only discrimination between the two configurations is in the angular distributions. Thus, a significant S-wave contribution could lead to distortions in the angular profile of the signal.

The S-wave event yield, N_{Swave}, is expected to be approximately 5% of the P-wave contribution [40], as summarised in Table 8.1 using the fitted signal yields in Table 7.1. A systematic uncertainty to account for the effect of the S-wave contribution on the angular distribution was evaluated for the folded PDFs in each q^2 bin through toy MC studies. The third column in Table 8.1 is the result of subtracting the S-wave yields from the observed signal yields. These new S-wave subtracted yields were used in a set of MC toys in which S-wave events were embedded in an approach akin to the embedded peaking background toys described in Sec 6.3.4.2, in order to assess the effect the embedded S-wave contribution has on the signal and background yields, and subsequent fitted angular parameters.

The systematic uncertainties were calculated as the difference between the fitted angular observables from the previous PDF toy MC studies, given in Tables 6.13 - 6.16 and the embedded S-wave toy MC studies. The systematic uncertainties from this source are given in Table C.7.

TABLE 8.1: The expected S-wave contribution and corresponding S-wave subtracted signal yield for each q^2 bin.

q^2 range $((GeV/c^2)^2)$	N_{Swave}	$N_{sig} - N_{Swave}$
$[0.04, 2.00]$	6.4	121.6
$[2.00, 4.00]$	5.3	100.7
$[4.00, 6.00]$	5.7	108.3
$[0.04, 4.00]$	11.8	224.2
$[1.10, 6.00]$	13.8	261.3
$[0.04, 6.00]$	17.1	324.9

8.8 Misreconstructed Decays

A systematic uncertainty was assigned to account for mis-reconstructed signal, in which a wrong sign flavour tag is assigned for the signal mode. The wrong flavour tag assignment results in a migration of events from one area of the angular distribtion space to another. Acceptance parameters were extracted from both the SM $B^0_d \to K^{*0}\mu^+\mu^-$ and $\overline{B}^0_d \to \overline{K}^{*0}\mu^+\mu^-$ MC. Both sets of parameters were used to fit the SM $B^0_d \to K^{*0}\mu^+\mu^-$ MC and the difference between the fitted angular parameters were calculated as a symmetric systematic uncertainty from this source. The results are shown in Table C.8 for each of the folded PDFs.

8.9 Acceptance functions

The systematic uncertainty arising from the acceptance functions was calculated as the difference between the generated angular parameter values in the phase space signal MC and the fitted values from the closure tests, described in Sec 6.2 and summarised in Tables 6.5, 6.6, 6.7 and 6.8 for the S_4, S_5, S_7 and S_8 PDF folded signal MC samples, respectively. These systematic uncertainties are shown in Table C.9.

8.10 Mass Fit Range

In addition to the peaking backgrounds listed in Table 6.3, the background was observed to peak at masses lower than the B^0_d mass. This was interpreted as partially reconstructed decays (PRDs), in which one or more particles are missed on reconstructing the 4-track final state. These PRD backgrounds were observed to peak at $|\cos\theta_L| = 0.7$, with the effect being more prominent at higher q^2.

The lower mass selection requirement at 5150 MeV/c^2 significantly reduced the contribution of PRD background into the signal. The mass fit range was then varied from $[5150, 5700]$ MeV/c^2 to $[5200, 5700]$ MeV/c^2 in order to study the stability of the results. A set of systematic uncertainties to account for the effect on the extracted signal parameters from reducing the fit range by 50 MeV/c^2 on the low side are summarised in Table C.10 for each of the PDFs used.

8.11 Combined Systematic Uncertainty

The systematic uncertainties outlined in this chapter were combined and the total systematic uncertainty on the fitted angular variables are shown in Table 8.2 for the S observables and in Table 8.3 for the $P^{(\prime)}$ observables. The dominant sources of systematic uncertainty on the S parameters (and hence on the $P^{(\prime)}$ observables) are from the mass fit range, fit bias and the background angular shape. For the S_4 parameter the acceptance function also provides dominant systematic contribution for the q^2 bin $[0.04, 2.00]$ $(GeV/c^2)^2$.

TABLE 8.2: The combined systematic uncertainties on the fitted angular variables F_L, S_3 and $S_{i=4,5,7,8}$ for each PDF folding.

q^2 range $((GeV/c^2)^2)$	PDF	$\sigma(F_L)$	$\sigma(S_3)$	$\sigma(S_i)$
$[0.04, 2.00]$	S_4	$^{+0.019}_{-0.019}$	$^{+0.013}_{-0.013}$	$^{+0.059}_{-0.059}$
	S_5	$^{+0.023}_{-0.024}$	$^{+0.016}_{-0.016}$	$^{+0.031}_{-0.031}$
	S_7	$^{+0.020}_{-0.021}$	$^{+0.028}_{-0.026}$	$^{+0.012}_{-0.012}$
	S_8	$^{+0.034}_{-0.034}$	$^{+0.037}_{-0.037}$	$^{+0.042}_{-0.042}$
$[2.00, 4.00]$	S_4	$^{+0.057}_{-0.058}$	$^{+0.057}_{-0.058}$	$^{+0.074}_{-0.074}$
	S_5	$^{+0.042}_{-0.042}$	$^{+0.060}_{-0.061}$	$^{+0.031}_{-0.031}$
	S_7	$^{+0.062}_{-0.062}$	$^{+0.055}_{-0.055}$	$^{+0.052}_{-0.052}$
	S_8	$^{+0.036}_{-0.037}$	$^{+0.053}_{-0.053}$	$^{+0.051}_{-0.051}$
$[4.00, 6.00]$	S_4	$^{+0.081}_{-0.082}$	$^{+0.054}_{-0.054}$	$^{+0.072}_{-0.072}$
	S_5	$^{+0.070}_{-0.070}$	$^{+0.054}_{-0.054}$	$^{+0.060}_{-0.060}$
	S_7	$^{+0.047}_{-0.047}$	$^{+0.067}_{-0.067}$	$^{+0.061}_{-0.061}$
	S_8	$^{+0.046}_{-0.045}$	$^{+0.057}_{-0.057}$	$^{+0.034}_{-0.034}$
$[0.04, 4.00]$	S_4	$^{+0.031}_{-0.031}$	$^{+0.030}_{-0.030}$	$^{+0.072}_{-0.072}$
	S_5	$^{+0.033}_{-0.033}$	$^{+0.032}_{-0.032}$	$^{+0.033}_{-0.033}$
	S_7	$^{+0.030}_{-0.030}$	$^{+0.033}_{-0.033}$	$^{+0.029}_{-0.029}$
	S_8	$^{+0.021}_{-0.021}$	$^{+0.041}_{-0.041}$	$^{+0.029}_{-0.029}$
$[1.10, 6.00]$	S_4	$^{+0.058}_{-0.058}$	$^{+0.016}_{-0.017}$	$^{+0.071}_{-0.071}$
	S_5	$^{+0.055}_{-0.055}$	$^{+0.015}_{-0.015}$	$^{+0.017}_{-0.017}$
	S_7	$^{+0.051}_{-0.051}$	$^{+0.013}_{-0.013}$	$^{+0.043}_{-0.043}$
	S_8	$^{+0.038}_{-0.038}$	$^{+0.016}_{-0.017}$	$^{+0.054}_{-0.054}$
$[0.04, 6.00]$	S_4	$^{+0.042}_{-0.042}$	$^{+0.021}_{-0.021}$	$^{+0.068}_{-0.068}$
	S_5	$^{+0.041}_{-0.041}$	$^{+0.018}_{-0.018}$	$^{+0.008}_{-0.008}$
	S_7	$^{+0.036}_{-0.036}$	$^{+0.014}_{-0.014}$	$^{+0.036}_{-0.036}$
	S_8	$^{+0.026}_{-0.026}$	$^{+0.014}_{-0.015}$	$^{+0.035}_{-0.035}$

TABLE 8.3: The combined systematic uncertainties on the fitted angular variables P_1, $P'_{i=4,5,6,8}$ for each PDF folding.

q^2 range $((GeV/c^2)^2)$	PDF	$\sigma(P_1)$	$\sigma(P'_i)$
$[0.04, 2.00]$	S_4	$^{+0.045}_{-0.045}$	$^{+0.152}_{-0.152}$
	S_5	$^{+0.057}_{-0.057}$	$^{+0.081}_{-0.081}$
	S_7	$^{+0.091}_{-0.098}$	$^{+0.024}_{-0.024}$
	S_8	$^{+0.124}_{-0.124}$	$^{+0.086}_{-0.086}$
$[2.00, 4.00]$	S_4	$^{+0.299}_{-0.305}$	$^{+0.195}_{-0.195}$
	S_5	$^{+0.335}_{-0.329}$	$^{+0.082}_{-0.082}$
	S_7	$^{+0.286}_{-0.286}$	$^{+0.108}_{-0.108}$
	S_8	$^{+0.277}_{-0.277}$	$^{+0.106}_{-0.106}$
$[4.00, 6.00]$	S_4	$^{+0.194}_{-0.194}$	$^{+0.186}_{-0.186}$
	S_5	$^{+0.204}_{-0.204}$	$^{+0.153}_{-0.153}$
	S_7	$^{+0.233}_{-0.233}$	$^{+0.123}_{-0.123}$
	S_8	$^{+0.203}_{-0.203}$	$^{+0.069}_{-0.069}$
$[0.04, 4.00]$	S_4	$^{+0.125}_{-0.125}$	$^{+0.183}_{-0.183}$
	S_5	$^{+0.133}_{-0.133}$	$^{+0.085}_{-0.085}$
	S_7	$^{+0.136}_{-0.136}$	$^{+0.058}_{-0.058}$
	S_8	$^{+0.164}_{-0.164}$	$^{+0.058}_{-0.058}$
$[1.10, 6.00]$	S_4	$^{+0.072}_{-0.077}$	$^{+0.182}_{-0.182}$
	S_5	$^{+0.069}_{-0.069}$	$^{+0.044}_{-0.044}$
	S_7	$^{+0.059}_{-0.059}$	$^{+0.087}_{-0.087}$
	S_8	$^{+0.076}_{-0.072}$	$^{+0.109}_{-0.109}$
$[0.04, 6.00]$	S_4	$^{+0.085}_{-0.085}$	$^{+0.173}_{-0.173}$
	S_5	$^{+0.073}_{-0.073}$	$^{+0.023}_{-0.023}$
	S_7	$^{+0.055}_{-0.055}$	$^{+0.072}_{-0.072}$
	S_8	$^{+0.058}_{-0.055}$	$^{+0.070}_{-0.070}$

Chapter 9

Results

This analysis was performed with a mass-prefit such that the mass and mass-error discriminating variables were used to extract the yields and background slope parameter from the data. A subsequent fit was then performed after extending the likelihood to include $\cos\theta_L$, $\cos\theta_K$ and ϕ. From that fit the Chebyshev polynomial coefficients for the combinatorial background and the angular parameters F_L, S_3 and $S_{i=4,5,7,8}$ were determined. The signal and combinatorial background yields, and combinatorial background slope parameter λ were fixed to the values obtained from the mass-prefits, given in Table 7.1.

The simulated total peaking background contribution to the B_d^0 mass, $\cos\theta_L$, $\cos\theta_K$ and ϕ from the decays listed in Table 6.3 wasn't included in the nominal fit; instead a systematic error was assigned to account for their effect, as described in Section 8.3.

The fit results from the four folded PDFs, in terms of F_L and the S_i observables, where $i = 3, 4, 5, 7, 8$, are given in Section 9.1. The optimised observable results, in terms of P_1 and P_i', are given in Section 9.2. A comparison of the results presented here with other experimental and theoretical results is given in Section 9.3.

9.1 S Observables

The values of F_L, S_3 and S_i fitted for the different folds are shown in Table 9.1 for each q^2 bin. The four different folded PDFs result in consistent fitted results and statistical uncertainties. The fitted values of F_L were found to be lower than SM

expectations across all bins. These deviations were observed to be less than 2 σ in the 2 $(GeV/c^2)^2$ wide bins, demonstrating reasonable consistency with the SM. The largest deviation observed was 3 σ in the widest q^2 bin, $q^2 \in [0.04, 6.00]$ $(GeV/c^2)^2$.

The equivalent table of angular parameters once the appropriate dilution was factored out of the S_4 and S_5 results is shown in Table 9.2. The dilution was assigned to correct for kaon-pion misidentification and was evaluated using Eq. (6.4), where the mistag fractions derived from SM $B^0_d \to K^{*0}\mu^+\mu^-$ and $\overline{B}^0_d \to \overline{K}^{*0}\mu^+\mu^-$ MC in Table 6.1 were combined. Here, the F_L, S_3, S_7 and S_8 results remain unchanged, but the S_4 and S_5 fitted values and statistical uncertainties are inflated.

TABLE 9.1: Angular parameters F_L, S_3 and S_i from fits to data, where i = 4, 5, 7, 8 depending on the PDF employed. The results are categorised by q^2 bin.

q^2 bin $((GeV/c^2)^2)$	PDF	$F_L \pm$ error	$S_3 \pm$ error	$S_i \pm$ error
$[0.04, 2.00]$	S_4	0.422 ± 0.083	-0.015 ± 0.086	0.151 ± 0.198
	S_5	0.443 ± 0.083	-0.034 ± 0.086	0.262 ± 0.103
	S_7	0.427 ± 0.084	0.018 ± 0.085	-0.087 ± 0.102
	S_8	0.405 ± 0.084	0.025 ± 0.085	-0.110 ± 0.185
$[2.00, 4.00]$	S_4	0.622 ± 0.104	-0.131 ± 0.096	-0.366 ± 0.149
	S_5	0.638 ± 0.108	-0.159 ± 0.098	-0.124 ± 0.117
	S_7	0.623 ± 0.103	-0.165 ± 0.099	0.151 ± 0.136
	S_8	0.619 ± 0.100	-0.149 ± 0.099	0.408 ± 0.155
$[4.00, 6.00]$	S_4	0.444 ± 0.128	0.003 ± 0.122	0.318 ± 0.163
	S_5	0.471 ± 0.127	-0.002 ± 0.123	0.100 ± 0.139
	S_7	0.424 ± 0.127	0.038 ± 0.119	0.028 ± 0.134
	S_8	0.439 ± 0.126	0.040 ± 0.120	-0.092 ± 0.162
$[0.04, 4.00]$	S_4	0.519 ± 0.066	-0.065 ± 0.065	-0.148 ± 0.122
	S_5	0.520 ± 0.066	-0.072 ± 0.065	0.125 ± 0.082
	S_7	0.516 ± 0.066	-0.053 ± 0.064	0.006 ± 0.084
	S_8	0.500 ± 0.066	-0.053 ± 0.064	0.150 ± 0.129
$[1.10, 6.00]$	S_4	0.558 ± 0.072	-0.052 ± 0.069	0.027 ± 0.108
	S_5	0.565 ± 0.072	-0.056 ± 0.069	0.003 ± 0.082
	S_7	0.558 ± 0.072	-0.038 ± 0.068	0.015 ± 0.082
	S_8	0.555 ± 0.072	-0.042 ± 0.068	0.090 ± 0.108
$[0.04, 6.00]$	S_4	0.504 ± 0.063	-0.058 ± 0.060	0.026 ± 0.102
	S_5	0.508 ± 0.063	-0.062 ± 0.060	0.107 ± 0.073
	S_7	0.495 ± 0.063	-0.037 ± 0.059	0.016 ± 0.073
	S_8	0.487 ± 0.062	-0.035 ± 0.059	0.053 ± 0.104

TABLE 9.2: Angular parameters F_L, S_3 and $S_{i=4,5,7,8}$ from fits to data with the dilution factored out of the affected parameters S_4 and S_5. The results are categorised by q^2 bin.

q^2 bin $((GeV/c^2)^2)$	PDF	$F_L \pm$ error	$S_3 \pm$ error	$S_i \pm$ error
$[0.04, 2.00]$	S_4	0.422 ± 0.083	-0.015 ± 0.086	0.192 ± 0.252
	S_5	0.443 ± 0.083	-0.034 ± 0.086	0.333 ± 0.131
	S_7	0.427 ± 0.084	0.018 ± 0.085	-0.087 ± 0.102
	S_8	0.405 ± 0.084	0.025 ± 0.085	-0.110 ± 0.185
$[2.00, 4.00]$	S_4	0.622 ± 0.104	-0.131 ± 0.096	-0.465 ± 0.189
	S_5	0.638 ± 0.108	-0.159 ± 0.098	-0.158 ± 0.149
	S_7	0.623 ± 0.103	-0.165 ± 0.099	0.151 ± 0.136
	S_8	0.619 ± 0.100	-0.149 ± 0.099	0.408 ± 0.155
$[4.00, 6.00]$	S_4	0.444 ± 0.128	-0.003 ± 0.122	0.404 ± 0.207
	S_5	0.471 ± 0.127	-0.002 ± 0.123	0.127 ± 0.177
	S_7	0.424 ± 0.127	0.038 ± 0.119	0.028 ± 0.134
	S_8	0.439 ± 0.126	0.040 ± 0.120	-0.092 ± 0.162
$[0.04, 4.00]$	S_4	0.519 ± 0.066	-0.065 ± 0.065	-0.188 ± 0.155
	S_5	0.520 ± 0.066	-0.072 ± 0.065	0.159 ± 0.104
	S_7	0.516 ± 0.066	-0.053 ± 0.064	0.006 ± 0.084
	S_8	0.500 ± 0.066	-0.053 ± 0.064	0.150 ± 0.129
$[1.10, 6.00]$	S_4	0.558 ± 0.072	-0.052 ± 0.069	0.034 ± 0.137
	S_5	0.565 ± 0.072	-0.056 ± 0.069	0.004 ± 0.104
	S_7	0.558 ± 0.072	-0.038 ± 0.068	0.015 ± 0.082
	S_8	0.555 ± 0.072	-0.042 ± 0.068	0.090 ± 0.108
$[0.04, 6.00]$	S_4	0.504 ± 0.063	-0.058 ± 0.060	0.033 ± 0.130
	S_5	0.508 ± 0.063	-0.062 ± 0.060	0.136 ± 0.093
	S_7	0.495 ± 0.063	-0.037 ± 0.059	0.016 ± 0.073
	S_8	0.487 ± 0.062	-0.035 ± 0.059	0.053 ± 0.104

The fitted mass, $\cos\theta_L$, $\cos\theta_K$ and ϕ distributions are shown for the S_4 folded analysis in Figures 9.1 through 9.4 for each q^2 bin studied. In each case, the data (black) is shown with the combinatorial background fit (red dashed line), signal fit (black dashed line) and total fitted PDF (blue line).

As discussed in Chapter 4, the B candidate mass range was initially defined as $[4900, 5700]$ MeV/c^2 in a blind analysis. However, unblinding exposed an unknown background in the fits to data, peaking at low B masses and in the $\cos\theta_L$ distribution at around $\cos\theta_L = 0.7$. Owing to time constraints, the mass range was reduced to $[5150, 5700]$ MeV/c^2, as seen in Figure 9.1 for the S_4 folded PDF, in order to remove the majority of this background and the fits were repeated in an unblind analysis. A systematic uncertainty to account for the effect of this new mass was assigned, as detailed in Section 8.10.

The background peaking at low B masses is the result of a neglected component to the combinatorial background. In addition to the fully combinatorial contribution consisting of a smoothly varying distribution in the mass and helicity angle fit variables, there can also be a contribution that peaks in the variables related to the $\mu^+\mu^-$ combination or to the $K^+\pi^-$ combination. The peaking background discovered here can be interpreted as PRDs in which $B \to D \to X$. A full discussion of the PRDs is given in Chapter 10, in which work that has been ongoing by the ATLAS Collaboration since this thesis was first submitted is detailed.

The $\cos\theta_L$ distributions are shown in Figure 9.2 for the S_4 folded PDF. A slight excess of events is seen in the data at around $\cos\theta_L = 0.7$ compared to the total fitted PDF. This is attributed to the remaining PRD contributions that were not removed from reducing B mass range.

The corresponding $\cos\theta_K$ distributions are shown in Figure 9.3. An excess of events is seen in the data in the last q^2 bin as $\cos\theta_K$ approaches $+1.0$. A small excess of events was expected here from the $B^+ \to K^+\mu^+\mu^-$ peaking background (see Figure 5.15), but at the level of approximately 4 events across the whole q^2 range. This contribution was accounted for in the peaking background systematic uncertainty calculated using embedded background MC toys. An excess of approximately 20 events across this full q^2 range remains unaccounted for in Figure 9.3. This peaking background was found to feed into the signal region from the K^{*0} and B mass sidebands.

Since this result was produced, two additional systematic uncertainties have been introduced by the ATLAS Collaboration to account for the peaking backgrounds seen here in $\cos\theta_L$ and $\cos\theta_K$. The details of these systematic uncertainties are given in Chapter 10.

The fitted ϕ distributions using the S_4 folded PDF are given in Figure 9.4 for each q^2 bin. The ϕ distributions are unaffected by the various background issues mentioned above.

The same trends are observed in the fitted observables for all PDFs. The equivalent distributions for the S_5, S_7 and S_8 PDFs are shown in Appendix D in Figures D.1 - D.4, D.5 - D.8 and D.9 - D.12, respectively.

S_4 PDF results

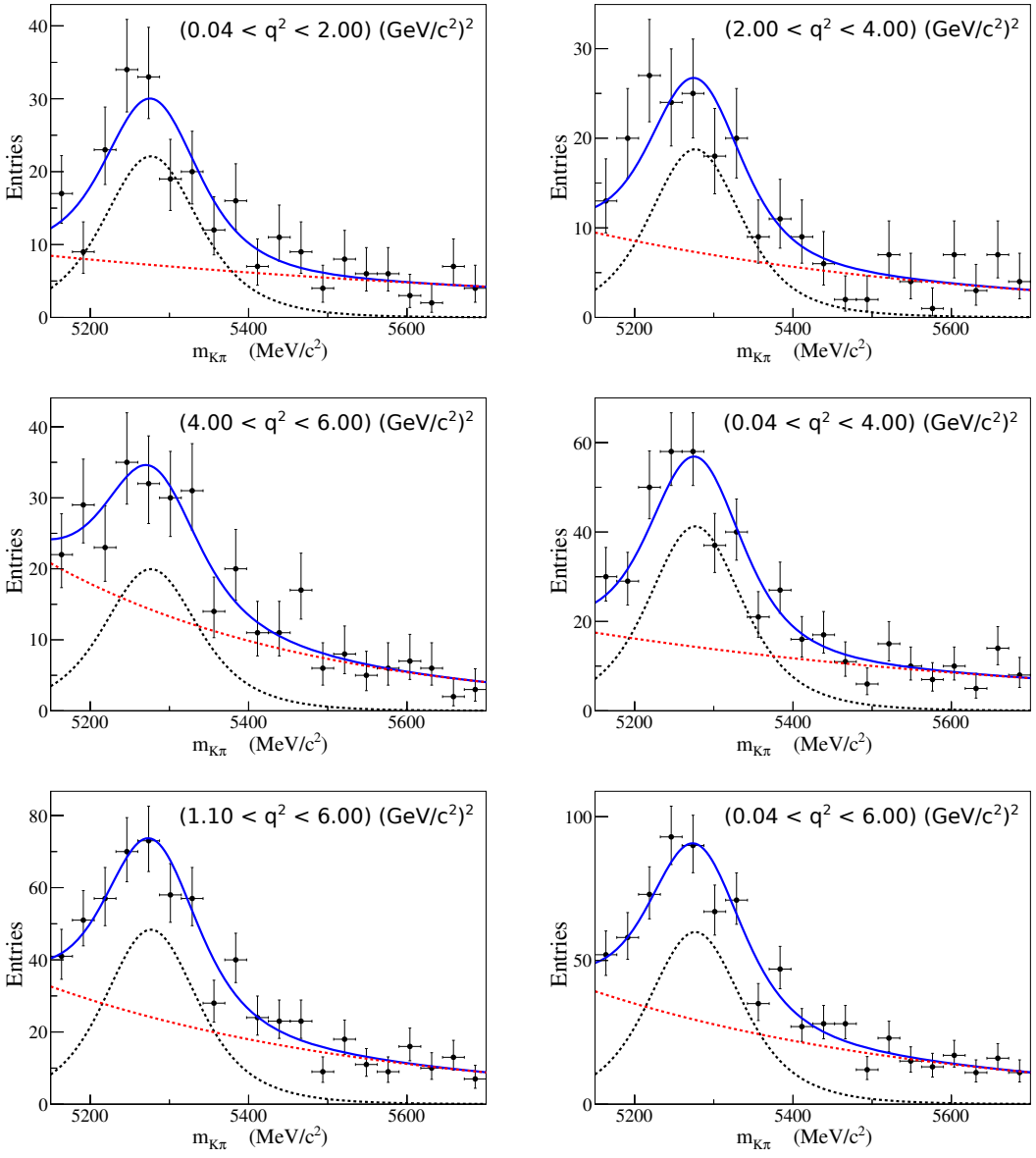

FIGURE 9.1: Mass fits to data using the S_4 folded PDF for q^2 bins $[0.04, 2.00]$ $(GeV/c^2)^2$ (top-left), $[2.00, 4.00]$ $(GeV/c^2)^2$ (top-right), $[4.00, 6.00]$ $(GeV/c^2)^2$ (middle-left), $[0.04, 4.00]$ $(GeV/c^2)^2$ (middle-right), $[1.10, 6.00]$ $(GeV/c^2)^2$ (bottom-left) and $[0.04, 6.00]$ $(GeV/c^2)^2$ (bottom-right). The black (dashed) line corresponds to the fitted signal, the red (dashed) line to the combinatorial background and the blue (solid) line to the total fitted PDF.

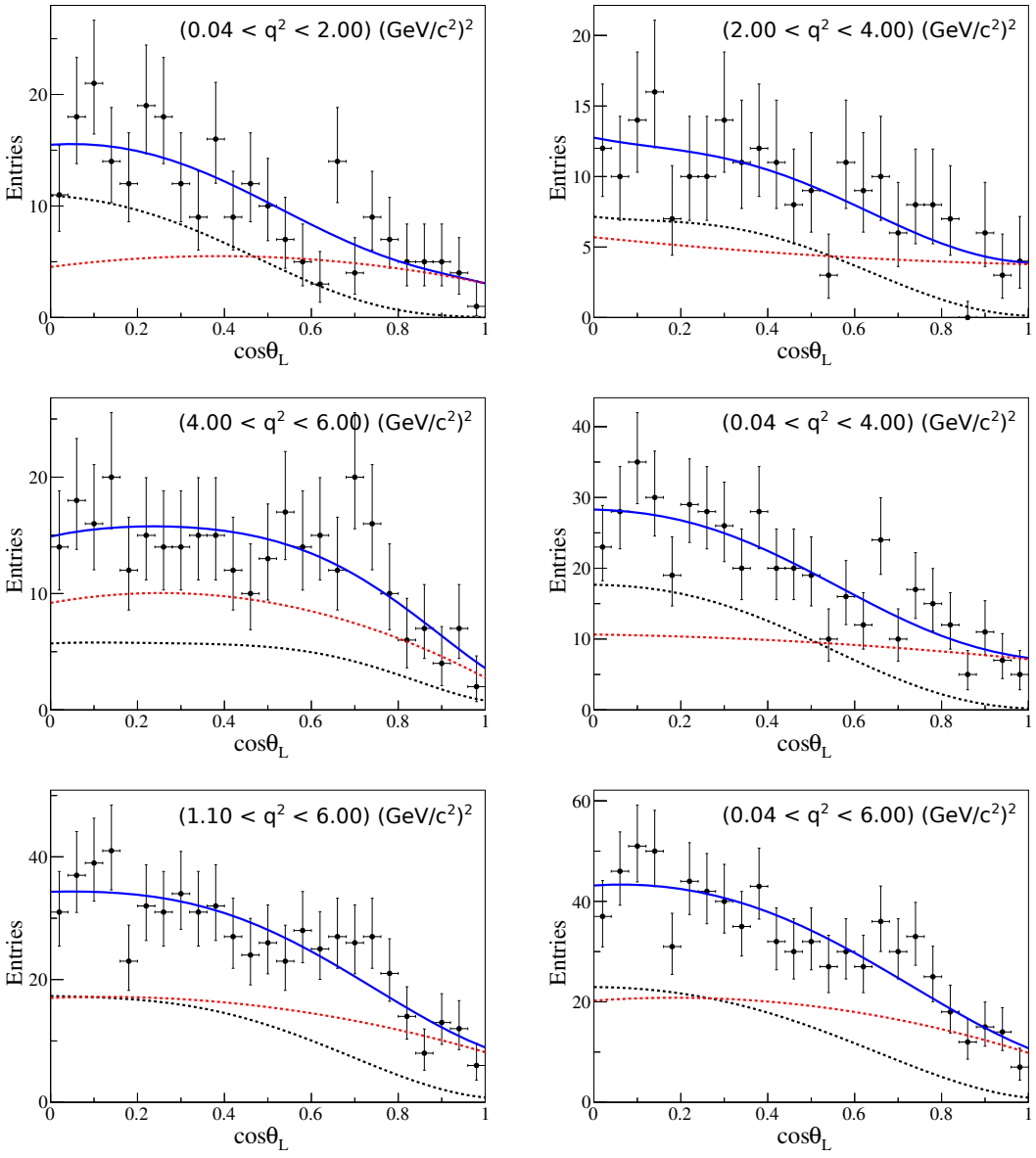

FIGURE 9.2: The $\cos\theta_L$ projection from angular fits to data using the S_4 folded PDF for q^2 bins $[0.04, 2.00]$ $(GeV/c^2)^2$ (top-left), $[2.00, 4.00]$ $(GeV/c^2)^2$ (top-right), $[4.00, 6.00]$ $(GeV/c^2)^2$ (middle-left), $[0.04, 4.00]$ $(GeV/c^2)^2$ (middle-right), $[1.10, 6.00]$ $(GeV/c^2)^2$(bottom-left) and $[0.04, 6.00]$ $(GeV/c^2)^2$(bottom-right). The black (dashed) line corresponds to the fitted signal, the red (dashed) line to the combinatorial background and the blue (solid) line to the total fitted PDF.

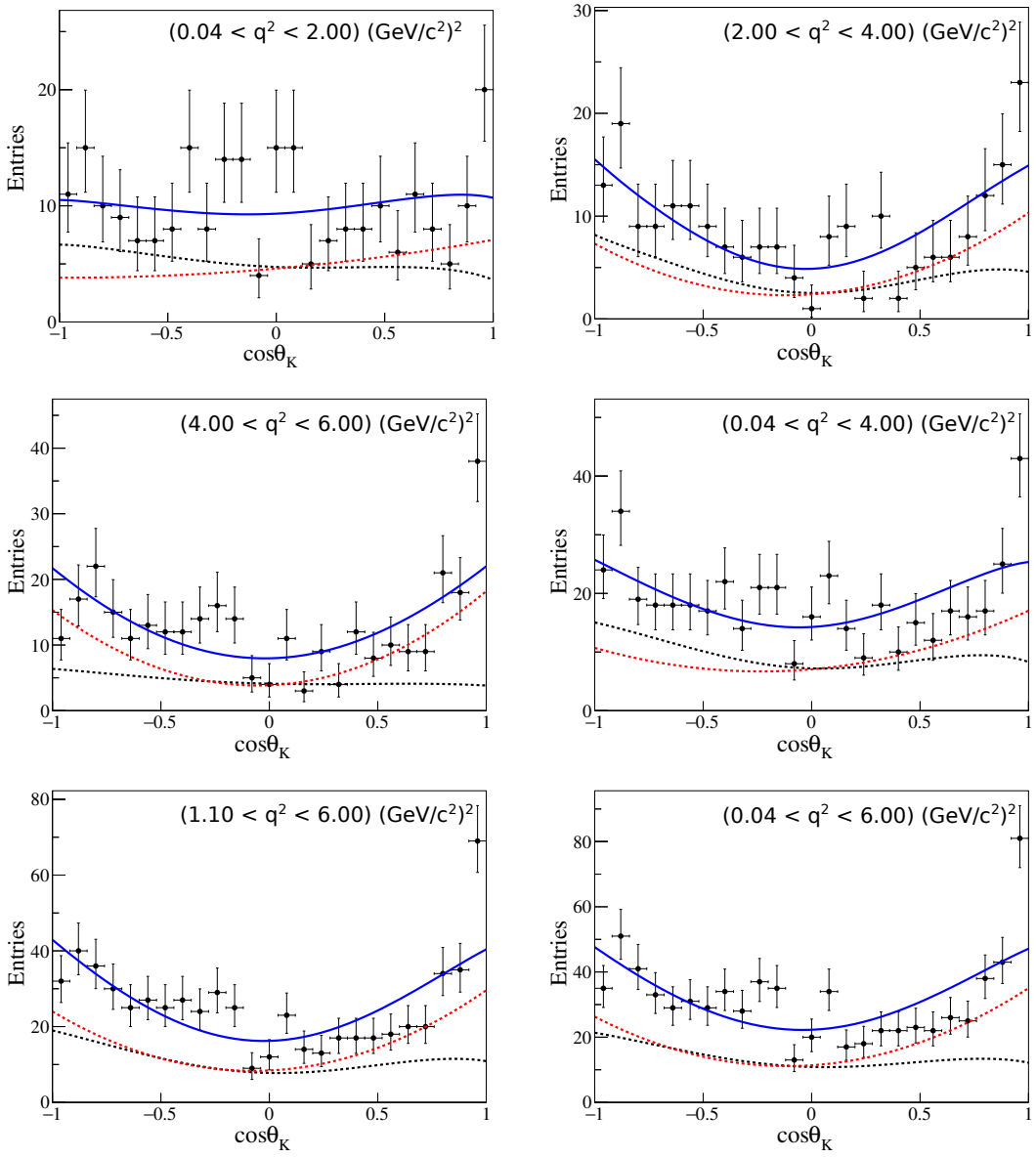

FIGURE 9.3: The $\cos\theta_K$ projection from angular fits to data using the S_4 folded PDF for q^2 bins $[0.04, 2.00]$ $(GeV/c^2)^2$ (top-left), $[2.00, 4.00]$ $(GeV/c^2)^2$ (top-right), $[4.00, 6.00]$ $(GeV/c^2)^2$ (middle-left), $[0.04, 4.00]$ $(GeV/c^2)^2$ (middle-right), $[1.10, 6.00]$ $(GeV/c^2)^2$ (bottom-left) and $[0.04, 6.00]$ $(GeV/c^2)^2$ (bottom-right). The black (dashed) line corresponds to the fitted signal, the red (dashed) line to the combinatorial background and the blue (solid) line to the total fitted PDF.

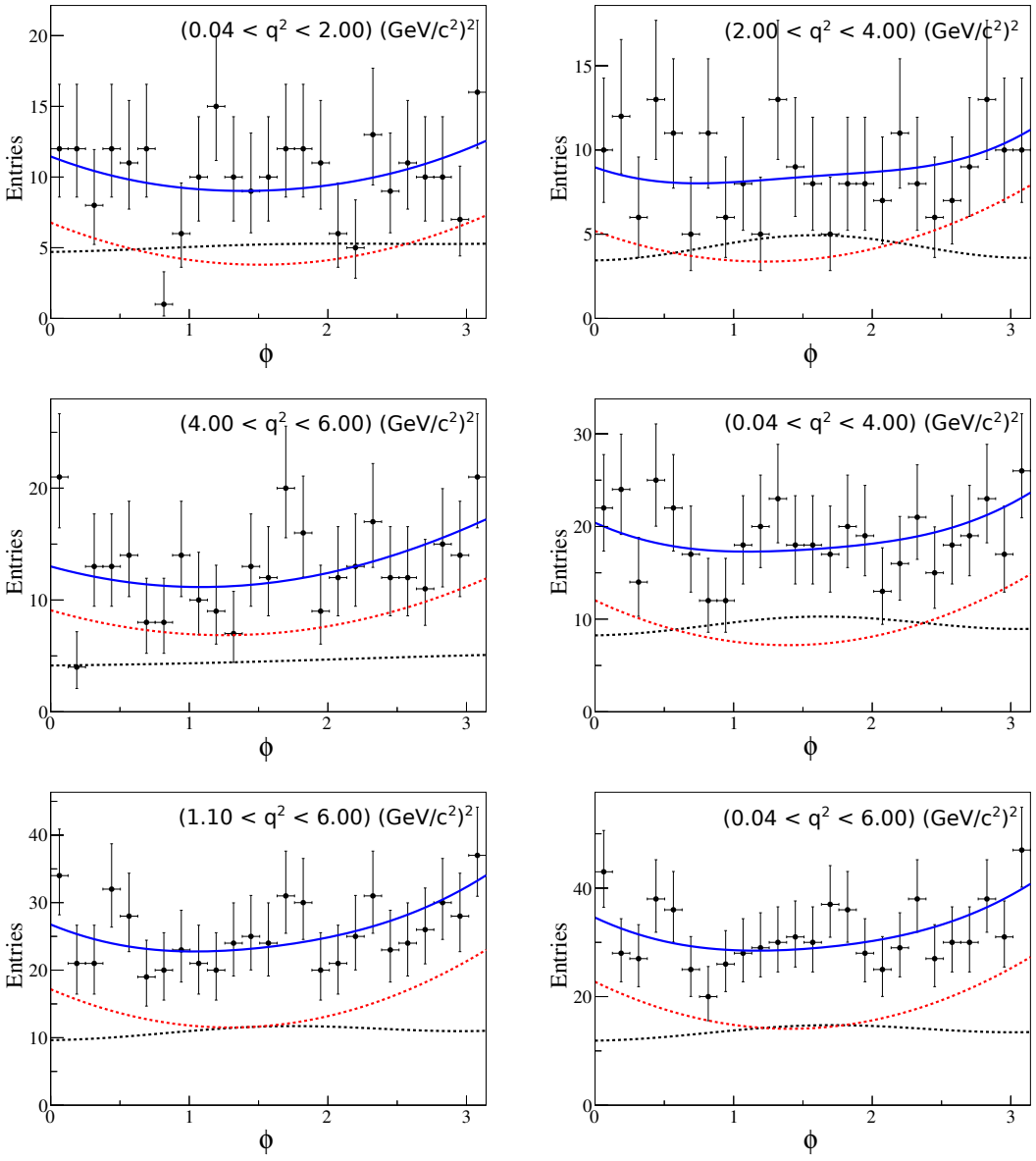

FIGURE 9.4: The ϕ projection from angular fits to data using the S_4 folded PDF for q^2 bins $[0.04, 2.00]$ $(GeV/c^2)^2$ (top-left), $[2.00, 4.00]$ $(GeV/c^2)^2$ (top-right), $[4.00, 6.00]$ $(GeV/c^2)^2$ (middle-left), $[0.04, 4.00]$ $(GeV/c^2)^2$ (middle-right), $[1.10, 6.00]$ $(GeV/c^2)^2$ (bottom-left) and $[0.04, 6.00]$ $(GeV/c^2)^2$ (bottom-right). The black (dashed) line corresponds to the fitted signal, the red (dashed) line to the combinatorial background and the blue (solid) line to the total fitted PDF.

9.2 P Observables

The optimised observables P_1 and $P'_{i=4,5,6,8}$ were obtained using the relation in Eq. (2.53) with the dilution corrected $S_{i=4,5,7,8}$ observables in Table 9.2; the optimised observable results are shown in Table 9.3 for each q^2 bin. The fits from the four different PDFs produce results consistent with each other for each q^2 bin with respect to their statistical uncertainty.

A comparison of these results with those obtained by the LHCb Collaboration as well as other experimental and theoretical results is given in Section 9.3.

9.3 Theoretical and Experimental Comparison of Results

The fitted ATLAS results presented in this thesis were compared to the experimental results from the angular analysis of $B^0_d \to K^{*0}\mu^+\mu^-$ performed by the BaBar [38], CMS [39], LHCb [40] and Belle [41] experiments. The results for F_L are shown together in Figure 9.5, the $S_{i=3,4,5,7,8}$ observables are shown in Figures 9.6 to 9.10 and the $P^{(\prime)}_{j=1,4,5,6,8}$ parameters in Figures 9.11 through 9.15.

Theoretical predictions are shown from three collaborations. The results labelled 'CFFMPSV fit' correspond to the theoretical approaches of Ciuchini et al. in Ref. [45], those labelled 'theory JC' correspond to the work of Jäger and Camalich described in Ref. [44] and finally the results labelled 'theory DHMV' correspond to the analysis performed by Descotes-Genon et al., described in Ref. [43]. DHMV and JC both use QCD factorisation, where the latter focuses on the impact of long distance corrections using a helicity amplitude approach. CFFMPSV takes a different approach, using the QCD factorisation framework to perform consistency checks to the LHCb data with theory expectations. This approach also allows information from a given parameter of interest to be excluded in order to make a prediction of the value of that parameter.

With the exception of the fitted values of S_4/P'_4 and S_5/P'_5 for $q^2 \in [4.00, 6.00]$ $(GeV/c^2)^2$ and S_8/P'_8 for $q^2 \in [2.00, 4.00]$ $(GeV/c^2)^2$, good agreement is observed between the results reported here and the theoretical predictions.

TABLE 9.3: The optimised observables P_1 and P_i', where i = 4, 5, 6, 8 for S_4, S_5, S_7 and S_8 folded PDFs respectively. The results are derived from fits to data through the relation given in Eq. (2.53) for each q^2 bin.

q^2 bin $((GeV/c^2)^2)$	PDF	$P_1 \pm$ error	$P_i' \pm$ error
$[0.04, 2.00]$	S_4	-0.052 ± 0.298	0.389 ± 0.510
	S_5	-0.122 ± 0.309	0.671 ± 0.264
	S_7	0.063 ± 0.297	-0.176 ± 0.206
	S_8	0.084 ± 0.286	-0.224 ± 0.377
$[2.00, 4.00]$	S_4	-0.688 ± 0.503	-0.960 ± 0.394
	S_5	-0.878 ± 0.531	-0.328 ± 0.310
	S_7	-0.875 ± 0.516	0.312 ± 0.281
	S_8	-0.782 ± 0.514	0.840 ± 0.322
$[4.00, 6.00]$	S_4	-0.011 ± 0.439	0.814 ± 0.418
	S_5	-0.008 ± 0.465	0.255 ± 0.354
	S_7	0.132 ± 0.413	0.057 ± 0.271
	S_8	0.143 ± 0.428	-0.185 ± 0.326
$[0.04, 4.00]$	S_4	-0.270 ± 0.270	-0.377 ± 0.310
	S_5	-0.300 ± 0.271	0.318 ± 0.209
	S_7	-0.219 ± 0.264	0.012 ± 0.168
	S_8	-0.212 ± 0.256	0.300 ± 0.258
$[1.10, 6.00]$	S_4	-0.235 ± 0.312	0.069 ± 0.277
	S_5	-0.257 ± 0.317	0.008 ± 0.210
	S_7	-0.172 ± 0.308	0.030 ± 0.165
	S_8	-0.189 ± 0.306	0.181 ± 0.217
$[0.04, 6.00]$	S_4	-0.234 ± 0.242	0.066 ± 0.259
	S_5	-0.252 ± 0.244	0.272 ± 0.186
	S_7	-0.147 ± 0.234	0.032 ± 0.146
	S_8	-0.136 ± 0.230	0.106 ± 0.208

A deviation of 2.6 σ is observed between the S_4/P_4' measurement and expectation from DHMV for $q^2 \in [4.00, 6.00]$ $(GeV/c^2)^2$, neglecting trial factors. A deviation of 2.6 σ is also observed between the S_8/P_8' measurement and expectation from DHMV for $q^2 \in [2.00, 4.00]$ $(GeV/c^2)^2$. However, compatibility between this result

and that reported by the LHCb Collaboration is observed, as seen in Figures 9.10 and 9.15.

An excess of 2.7 σ relative to SM expectations from DHMV is observed for S_5/P_5' in the same bin reported by the LHCb Collaboration [40]. The ATLAS, LHCb and Belle measurements shown in Figures 9.8 and 9.13, while not in perfect agreement with theory, are typically within three standard deviations of the expectations, accounting for both experimental and theoretical uncertainties and neglecting trial factors.

The discrepancies quoted here between the result presented in this thesis and SM expectations from DHMV are the most significant available, with smaller deviations observed between measurement and the theoretical expectations from JC and CFFMPSV.

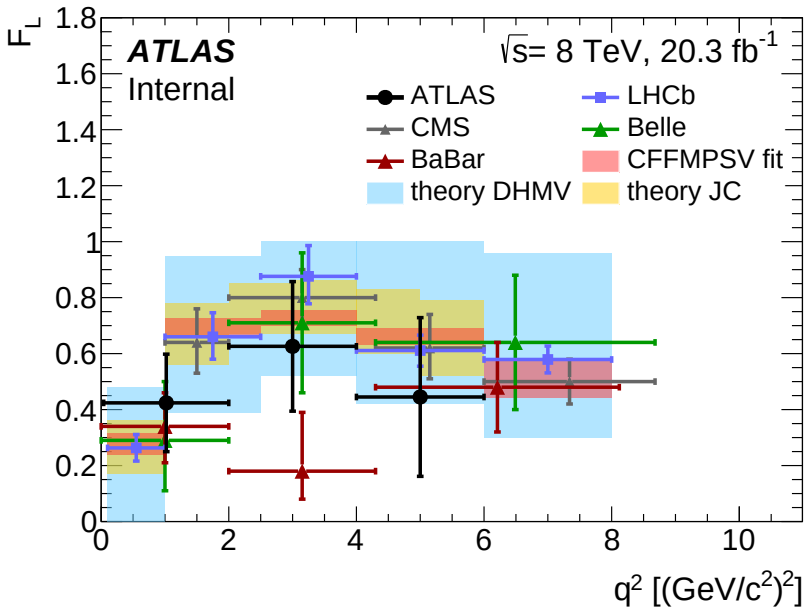

FIGURE 9.5: A theoretical and experimental comparison of F_L. The (red) ATLAS data points are the average fitted F_L values from all four folded PDFs used in this thesis. The thin error lines represent the combined statistical and systematic uncertainty whilst the thick error lines represent the statistical uncertainty alone. The ATLAS results are compared to the results from the BaBar [38], CMS [39], LHCb [40] and Belle [41] Collaborations, as well as three different theoretical approaches [43–45].

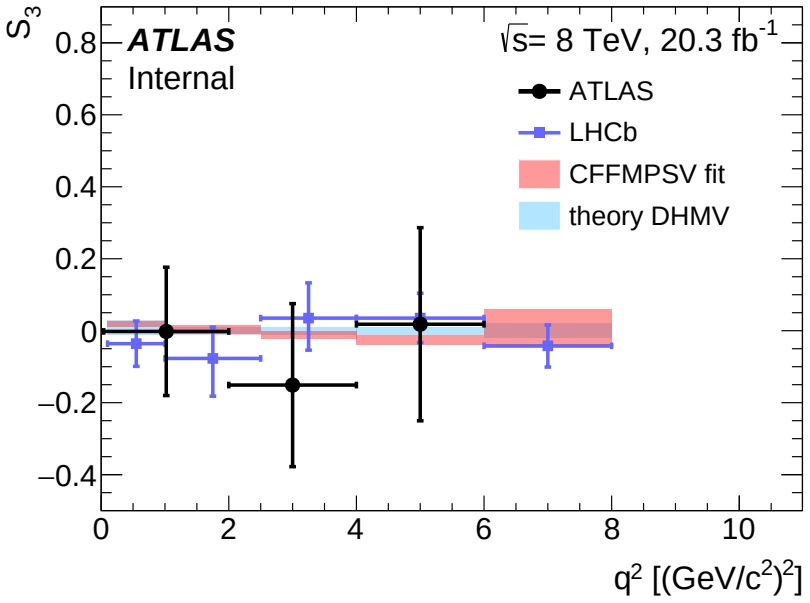

FIGURE 9.6: A theoretical and experimental comparison of S_3. The (red) ATLAS data points are the average fitted S_3 values from all four folded PDFs used in this thesis. The thin error lines represent the combined statistical and systematic uncertainty whilst the thick error lines represent the statistical uncertainty alone. The ATLAS results are compared to the results from the LHCb Collaboration [40], as well as two different theoretical approaches [43, 45].

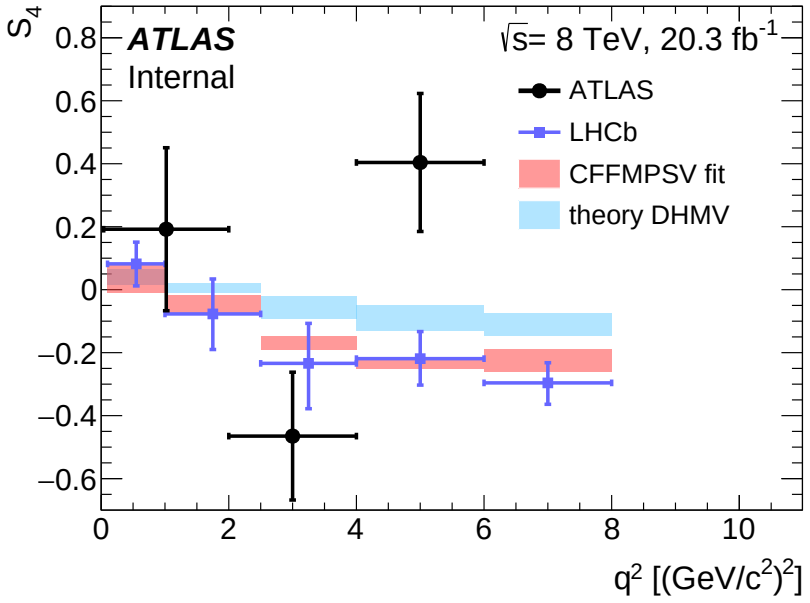

FIGURE 9.7: A theoretical and experimental comparison of S_4. The (red) ATLAS data points are the fitted S_4 values from the S_4 folded PDF. The thin error lines represent the combined statistical and systematic uncertainty whilst the thick error lines represent the statistical uncertainty alone. The ATLAS results are compared to the results from the LHCb Collaboration [40], as well as two different theoretical approaches [43, 45].

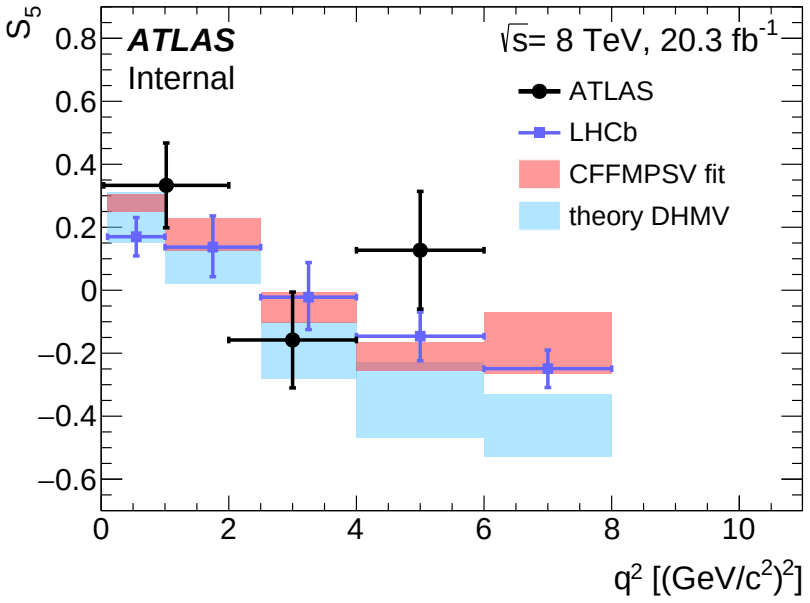

FIGURE 9.8: A theoretical and experimental comparison of S_5. The (red) ATLAS data points are the fitted S_5 values from the S_5 folded PDF. The thin error lines represent the combined statistical and systematic uncertainty whilst the thick error lines represent the statistical uncertainty alone. The ATLAS results are compared to the results from the LHCb Collaboration [40], as well as two different theoretical approaches [43, 45].

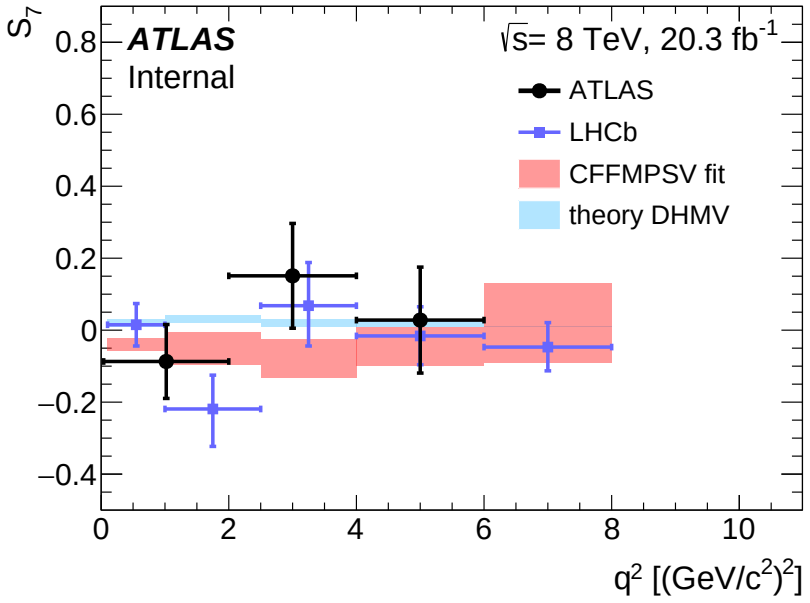

FIGURE 9.9: A theoretical and experimental comparison of S_7. The (red) ATLAS data points are the fitted S_7 values from the S_7 folded PDF. The thin error lines represent the combined statistical and systematic uncertainty whilst the thick error lines represent the statistical uncertainty alone. The ATLAS results are compared to the results from the LHCb Collaboration [40], as well as two different theoretical approaches [43, 45].

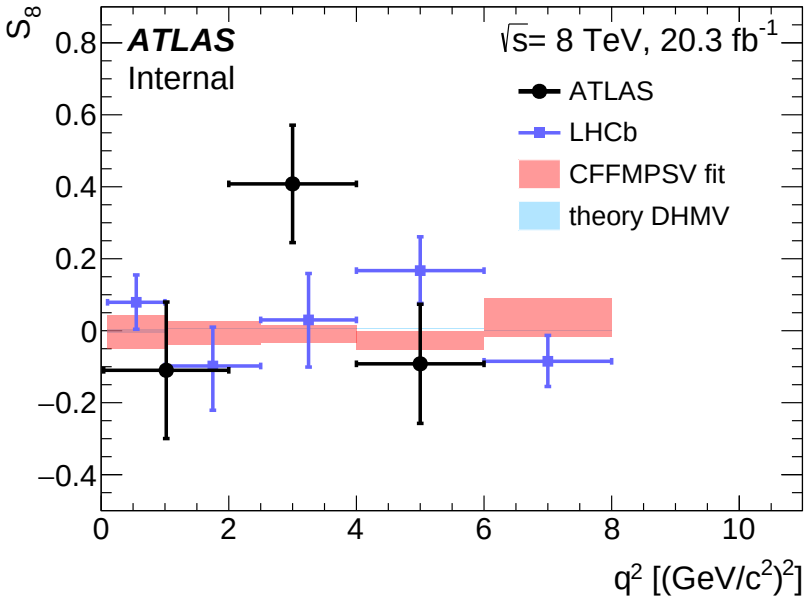

FIGURE 9.10: A theoretical and experimental comparison of S_8. The (red) ATLAS data points are the fitted S_8 values from the S_8 folded PDF. The thin error lines represent the combined statistical and systematic uncertainty whilst the thick error lines represent the statistical uncertainty alone. The ATLAS results are compared to the results from the LHCb Collaboration [40], as well as two different theoretical approaches [43, 45].

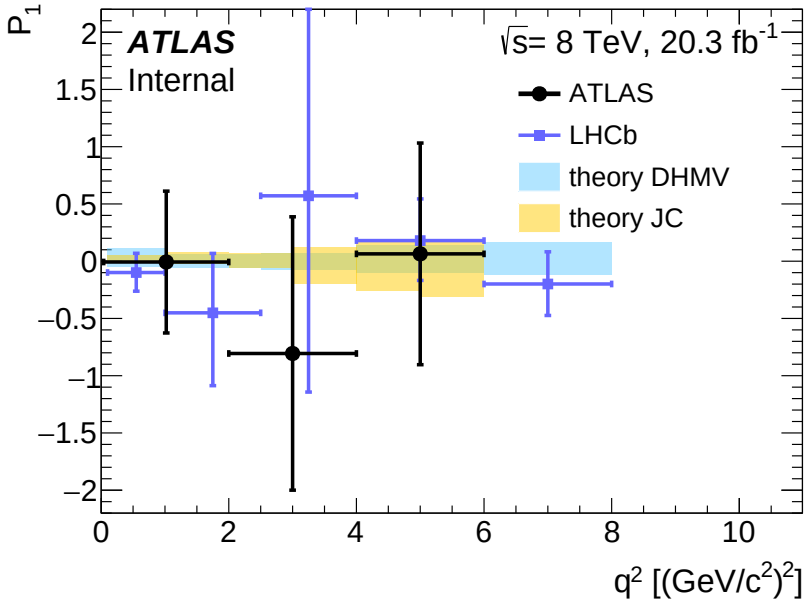

FIGURE 9.11: A theoretical and experimental comparison of P_1. The (red) ATLAS data points are the average fitted P_1 values from all four folded PDFs used in this thesis. The thin error lines represent the combined statistical and systematic uncertainty whilst the thick error lines represent the statistical uncertainty alone. The ATLAS results are compared to the results from the LHCb Collaboration [40], as well as two different theoretical approaches [43, 44].

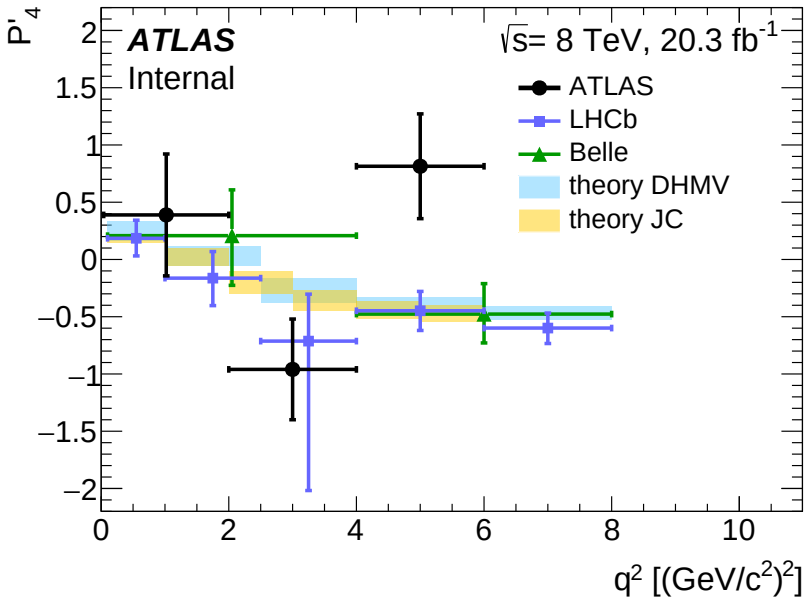

FIGURE 9.12: A theoretical and experimental comparison of P_4'. The (red) ATLAS data points are the fitted P_4' values from the converted S_4 folded PDF results. The thin error lines represent the combined statistical and systematic uncertainty whilst the thick error lines represent the statistical uncertainty alone. The ATLAS results are compared to the results from the LHCb [40] and Belle [41] Collaborations, as well as two different theoretical approaches [43, 44].

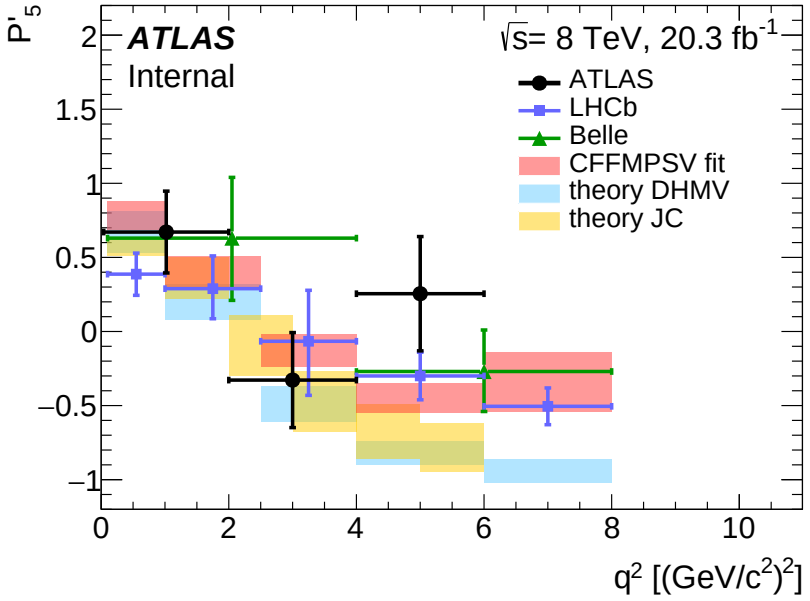

FIGURE 9.13: A theoretical and experimental comparison of P_5'. The (red) ATLAS data points are the fitted P_5' values from the converted S_5 folded PDF results. The thin error lines represent the combined statistical and systematic uncertainty whilst the thick error lines represent the statistical uncertainty alone. The ATLAS results are compared to the results from the LHCb [40] and Belle [41] Collaborations, as well as three different theoretical approaches [43–45].

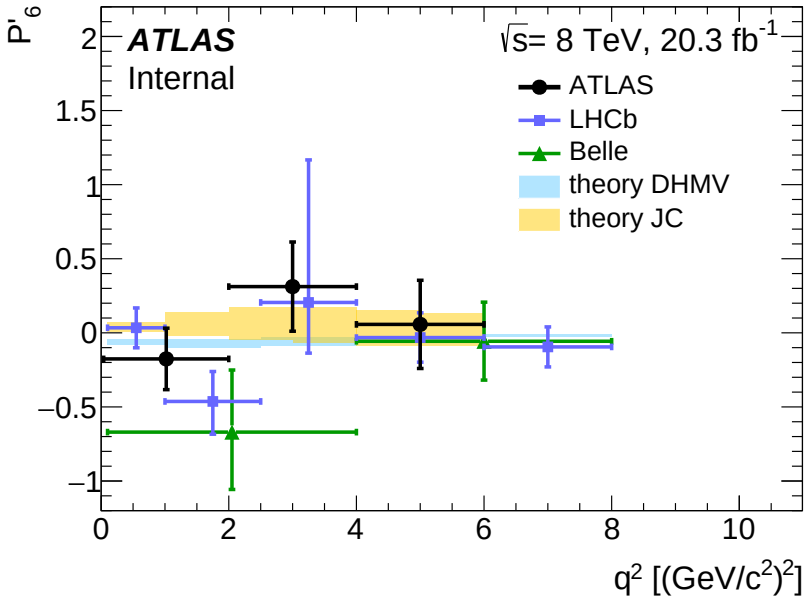

FIGURE 9.14: A theoretical and experimental comparison of P_6'. The (red) ATLAS data points are the fitted P_6' values from the converted S_7 folded PDF results. The thin error lines represent the combined statistical and systematic uncertainty whilst the thick error lines represent the statistical uncertainty alone. The ATLAS results are compared to the results from the LHCb [40] and Belle [41] Collaborations, as well as two different theoretical approaches [43, 44].

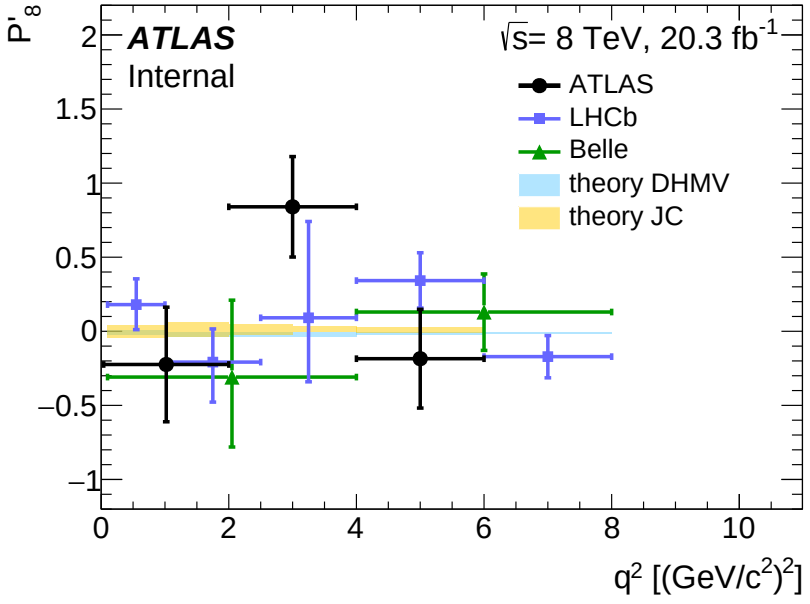

FIGURE 9.15: A theoretical and experimental comparison of P_8'. The (red) ATLAS data points are the fitted P_8' values from the converted S_8 folded PDF results. The thin error lines represent the combined statistical and systematic uncertainty whilst the thick error lines represent the statistical uncertainty alone. The ATLAS results are compared to the results from the LHCb [40] and Belle [41] Collaborations, as well as two different theoretical approaches [43, 44].

Chapter 10

Discussion and Future Work

This chapter addresses the unexpected peaking structures observed in the results presented in Chapter 9. A discussion of the studies performed by the ATLAS Collaboration to understand the backgrounds is given in Section 10.1.

Additionally, limitations of the current analysis and directions for future iterations are outlined in Section 10.2.

10.1 Peaking Background in $\cos\theta_L$ and $cos\theta_K$

After unblinding, a combinatorial background peaking at both $\cos\theta_L = 0.7$ and high values $\cos\theta_K$ was observed. The majority of the background peaking at $\cos\theta_L = 0.7$ was removed by reducing the B mass fit range from $[4900, 5700]\ MeV/c^2$ to $[5150, 5700]\ MeV/c^2$. However, time constraints meant a full investigation into this background couldn't be finalised. Furthermore, the peaking background in the $\cos\theta_K$ distribution was not accounted for.

Since the submission of this thesis, the ATLAS Collaboration has performed a systematic study in order to understand the combinatorial background. This study resulted in at least two additional sources of combinatorial background being found. The first can be interpreted as PRDs, where $B \to D \to X$.

This component was observed in the left $M_{K\pi\mu\mu}$ sideband, peaking around $|\cos\theta_L| = 0.7$, with the number of events found to increase with increasing q^2. This can be seen in Figure 10.1, where $M_{K\pi\mu\mu}$ and q^2 are plotted versus $\cos\theta_L$.

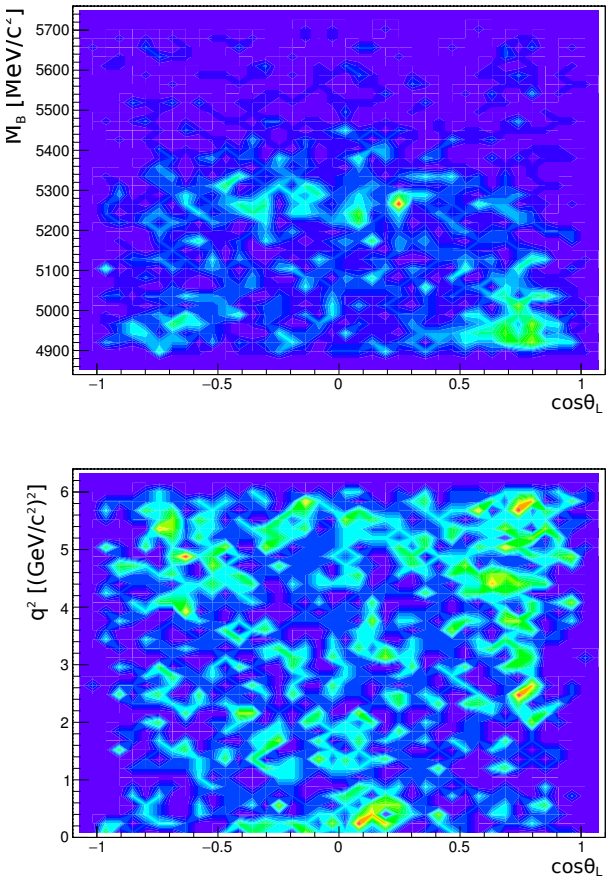

FIGURE 10.1: The distributions of $M_{K\pi\mu\mu}$ vs $\cos\theta_L$ (top) and q^2 vs $\cos\theta_L$ (bottom), highlighting regions where there is an excess of events at low mass (below the B peak) that also peak in $\cos\theta_L$.

The PRD hypothesis was tested by assigning a pion or kaon mass to tracks forming the signal candidate and comparing the invariant mass distributions of two or three track combinations with the signal MC.

Contributions from the following decays were found, where the notation 'K_π' can be interpreted as a kaon track with a π mass assignment and so on:

- $D^0 \to K\pi$: $m(K_\pi\pi_K)$
- $D^\pm \to K\pi\pi$: $m(K\pi\mu_\pi)$, $m(\pi_K K_\pi\mu_\pi)$, $m(K_\pi\pi\mu_K)$
- $D_s^\pm \to KK\pi$: $m(K\pi_K\mu_\pi)$, $m(K\pi\mu_K)$, $m(K_\pi\pi_K\mu_K)$
- $D_s^{*+} \to KK\pi$: $m(K\pi_K\mu_\pi)$, $m(K\pi\mu_K)$, $m(K_\pi\pi_K\mu_K)$

The second source of combinatorial background found can be interpreted as $B^+ \to K^+\mu^+\mu^-$ and $B^+ \to \pi^+\mu^+\mu^-$ decays with a track from the event mimicking a pion

or kaon from the signal decay. This source contributes to the high $M_{K\pi\mu\mu}$ sideband and peaks at high values of $\cos\theta_K$.

Due to the unavailability of inclusive $B \to D \to X$ MC samples to confirm these hypotheses, a systematic uncertainty was derived to account for the PRDs. A veto width was optimised to remove the observed background and as a result, events in a window of 30 MeV/c^2 around the mass of the D meson and 50 MeV/c^2 around the mass of the B^+ meson were removed for the aforementioned combinations.

In order to estimate the effect of the PRD background, the nominal results were compared to those obtained from a fit to data with the B^+ and D vetoes applied. The differences obtained were used as a systematic uncertainty. The second fit used acceptance functions obtained from the signal MC with the same veto applied to the selection process as for the data. The resulting uncertainties were found to dominate the measurement of F_L at lower values of q^2, with values reaching 0.18. The uncertainties calculated for the rest of the observables were of the same order as those shown in Chapter 8.

The component peaking at high values of $\cos\theta_K$ was also addressed by assigning a systematic error. This second systematic error was evaluated as the difference between the nominal fit result and that obtained when removing the peak in $\cos\theta_K$ by imposing a constraint that $\cos\theta_K < 0.9$.

This systematic uncertainty was found to dominate the measurements of F_L and S_8 at higher values of q^2, but once again with other uncertainties at a level consistent with previous systematic uncertainties shown in Chapter 8.

10.2 Future Work

The next angular analysis of $B_d^0 \to K^{*0}\mu^+\mu^-$ performed by the ATLAS Collaboration will use data collected at a pp centre-of-mass energy of $\sqrt{s} = 13\ TeV$ during Run 2 at the LHC.

The ATLAS ID was updated with a new subdetector, the Insertable B-Layer (IBL) during the first long shutdown at the LHC [92]. The IBL, built to cope with high radiation and occupancy, was installed between the existing Pixel detector and a new smaller radius beam-pipe. The potential benefit of the additional pixel detector layer on this measurement should be studied for Run 2.

Providing the trigger efficiency is adequate for the whole run, the increased luminosity will lead to a significantly larger data sample. Studies should be done to determine the signal event yield required to migrate from a folded analysis, as presented here, to a full angular analysis, as performed by the LHCb Collaboration in Ref. [40]. Furthermore, if the event yields are sufficient, it will be beneficial to move towards a 1 $(GeV/c^2)^2$ binning regime. Fine binning is good for studying the resonant sub-structure in the q^2 distribution and is something the LHCb Collaboration have already achieved. The framework to perform the full angular analysis in 1 $(GeV/c^2)^2$ wide bins was created during this analysis, thus this is a conceivable goal with the increased data sets.

The event selection will need to be re-optimised, paying particular attention to the current dominant systematic uncertainties, as shown in Table 10.1. The systematic uncertainties documented in Table 10.1 are given in order of their contribution, from most to least dominant, where both the uncertainties from this thesis and those evaluated by the ATLAS Collaboration since (see Section 10.1 above) are included. The numbers quoted represent the highest uncertainty measured for each observable across all q^2 bins and folded PDF results.

The two most contributing sources of systematic uncertainty were introduced to account for the peaking combinatorial background in the $\cos\theta_L$ and $\cos\theta_K$ distributions. The combinatorial $K\pi$ background and D/B^+ veto systematic uncertainties dominate the F_L and S_8 observables in particular.

The vetoes were introduced after the PRDs were discovered on unblinding. In a future analysis, these vetoes can be optimised in the early stages of the event selection in order to reduce the final systematic uncertainty. A thorough study

TABLE 10.1: Systematic uncertainties for F_L and S_i from different sources considered.

Source	F_L	S_3	S_4	S_5	S_7	S_8
Combinatorial $K\pi$ background	< 0.18	< 0.04	≤ 0.05	≤ 0.03	≤ 0.06	< 0.13
D and B^+ veto	< 0.13	< 0.04	< 0.05	< 0.03	< 0.01	< 0.05
Background PDF shape	≤ 0.07	≤ 0.04	≤ 0.03	≤ 0.02	≤ 0.03	≤ 0.01
Acceptance function	≤ 0.01	< 0.01	≤ 0.07	< 0.01	< 0.01	< 0.01
Mass fit range (PRD)	≤ 0.03	< 0.06	< 0.02	< 0.06	< 0.05	≤ 0.05
Alignment and B field calibration	≤ 0.02	< 0.04	≤ 0.05	≤ 0.03	≤ 0.04	< 0.03
Fit bias	≤ 0.02	≤ 0.02	< 0.02	< 0.02	< 0.01	< 0.04
Data/MC differences for p_T	≤ 0.02	< 0.01	≤ 0.01	< 0.01	< 0.01	< 0.01
S-wave	≤ 0.01	≤ 0.01	< 0.01	< 0.01	≤ 0.01	≤ 0.02
Nuisance parameters	≤ 0.01	≤ 0.02	< 0.01	< 0.01	< 0.01	< 0.01
Λ_b, B^+ and B_s background	≤ 0.01	< 0.01	< 0.01	< 0.01	< 0.01	< 0.01
Misreconstructed signal	< 0.01	< 0.01	< 0.01	< 0.01	< 0.01	< 0.01
Dilution	–	–	< 0.01	< 0.01	–	–

into understanding the combinatorial $K\pi$ background and how to control the peak at higher values of $\cos\theta_K$ will also need to be undertaken.

A good understanding of these two sources of systematic uncertainty will likely feed into the background PDF shape, reducing this contribution to the total systematic uncertainty as well.

The acceptance function systematic uncertainties are generally small, with the exception of that associated with the S_4 observable, which is larger than the other observables. This is likely due to the extra ϕ term in the S_4 acceptance function, adding an additional layer of complexity to the fit. A study into this effect would be beneficial.

Given that Λ_b decays are known to provide the largest source of peaking background in the $B^0_d \to K^{*0}\mu^+\mu^-$ analysis performed by the LHCb Collaboration [40], it's important to obtain a broader range of Λ_b MC samples or a generic Λ_b MC sample in order to reliably investigate its contribution. These samples will need to be produced using SM-like decay models, as the phase space models are known to have an unreliable q^2 distribution (see Section 5.3).

Finally, the q^2 range studied here was limited to $(0.04 < q^2 < 6.00)$ $(GeV/c^2)^2$ in order to remove contributions from the J/ψ and $\psi(2S)$ charm resonances. This was done largely because of time constraints given the lack of foundations to the

analysis. Extending the range to at least $(0.04 < q^2 < 8.00)$ $(GeV/c^2)^2$ would be advantageous in terms of making comparisons with theory as the LHCb analysis reported the largest discrepancy with theory in the $q^2 \in [6.00, 8.00]$ $(GeV/c^2)^2$ bin.

Chapter 11

Conclusion

An angular analysis of the decay $B^0_d \to K^0(\to K^+\pi^-)\mu^+\mu^-$ has been presented. The $B^0_d \to K^0(\to K^+\pi^-)\mu^+\mu^-$ analysis used 20.3 fb^{-1} of Run 1 data collected at the LHC during pp collisions with a centre-of-mass energy $\sqrt{s} = 8\ TeV$ using the ATLAS detector.

The angular observables F_L and $S_{3,4,5,7,8}$ were extracted in six bins of q^2, within the full range $0.04 < q^2 < 6.00\ (GeV/c^2)^2$. The three q^2 bins $[0.04, 2.00]\ (GeV/c^2)^2$, $[2.00, 4.00]\ (GeV/c^2)^2$ and $[4.00, 6.00]\ (GeV/c^2)^2$ were studied in addition to three overlapping bins $[0.04, 4.00]\ (GeV/c^2)^2$, $[1.10, 6.00]\ (GeV/c^2)^2$ and $[0.04, 6.00](GeV/c^2)^2$ in order to report results in ranges compatible with other experiments and theoretical predictions.

The observables were determined from an unbinned maximum likelihood fit using four folded parameterisations of the full angular distribution. The fit results were used to obtain corresponding values for the optimised observables P_1 and $P'_{4,5,6,8}$.

With the exception of the P'_4 and P'_5 measurements in $q^2 \in [4.00, 6.00]\ (GeV/c^2)^2$ and P'_8 in $q^2 \in [2.00, 4.00]\ (GeV/c^2)^2$ there is good agreement between theory and measurement. The excess observed for P'_5 is in the same bin and direction as reported by the LHCb Collaboration in Ref. [40], and it is approximately 3.4 standard deviations away from the calculation of Descotes-Genon et al [43]. All measurements are found to be within three standard deviation of the range covered by the available predictions. Hence, including experimental and theoretical uncertainties, the results presented here are found to be in accordance with the expectations of the SM contributions to this decay.

The theoretical groups working on interpreting this decay are not in perfect agreement with each other, and in time this situation is expected to evolve. With data from Run 2 at the LHC it will be interesting to see how the tension indicated by the LHCb Collaboration relative to the DHMV calculation evolves. Likewise how the data from experiments evolve with respect to the theory calculations and phenomenological fit interpretation may provide insight to deficiencies in theory, experiment or as is hoped, some sign of new physics. The LHCb and, once it comes online, Belle II experiments will be able to measure $B^0_d \to K^{*0} e^+ e^-$ and in doing so will be able to provide comparisons of results from the di-muon and di-electron modes.

Appendix A

Neglected Backgrounds

An extensive list of decays with a similar topology to the signal were considered as potential peaking backgrounds, as described in Chapter 5. These decays were broadly categorised by considering the following:

- A change in the spectator quark.
- A change in the non-spectator quark.
- Hadron misidentification.
- Three body decays, in which an independent fourth particle is misreconstructed as part of the decay.
- Five body decays, in which one particle is neglected in the reconstruction.

This section documents the channels that were considered but omitted owing to significant differences between their invariant mass ranges and the signal mass region at generator level, through incompatible daughter particles or through branching fractions too small relative to the signal channel. Decays that were considered but found to be negligible are summarised in Tables A.1, A.2 and A.3 for B^0_d, B^0_s and B^+_u decays respectively. The EvtGen decay model for MC generation and the relevant branching fractions [19] are given.

TABLE A.1: B_d^0 decays that were considered as potential peaking backgrounds, but ultimately neglected. The EvtGen decay model available for each decay is given along with the total branching fraction calculated for the B_d^0 decay and all subsequent decays that lead to a signal-like final state.

Decay	EvtGen Models	Total $\Gamma_i/\Gamma \pm \sigma_{\Gamma_i/\Gamma}$
$B_d^0 \to J/\psi K^+\pi^-, \quad J/\psi \to \mu^+\mu^-$	PHSP, PHOTOS VLL	$(7.15 \pm 3.58) \times 10^{-5}$
$B_d^0 \to J/\psi K^{*+}\pi^-, \quad J/\psi \to \mu^+\mu^-, \quad K^{*+} \to (K\pi)^+$	PHSP, PHOTOS VLL, VSS	$(4.76 \pm 2.38) \times 10^{-5}$
$B_d^0 \to J/\psi K^0\rho^0, \quad J/\psi \to \mu^+\mu^-, \quad \rho^0 \to \pi^+\pi^-$	PHSP, PHOTOS VLL, VSS	$(3.22 \pm 1.79) \times 10^{-5}$
$B_d^0 \to J/\psi K^0\pi^+\pi^-, \quad J/\psi \to \mu^+\mu^-$	PHSP, PHOTOS VLL	$(2.62 \pm 0.24) \times 10^{-5}$
$B_d^0 \to \chi_{c1}K^-\pi^+, \quad \chi_{c1} \to J/\psi\gamma, \quad J/\psi \to \mu^+\mu^-$	PHSP, VVP, PHOTOS VLL	$(7.68 \pm 0.85) \times 10^{-6}$
$B_d^0 \to \chi_{c1}K^{*0}, \quad K^{*0} \to K^+\pi^-, \quad \chi_{c1} \to J/\psi\gamma, \quad J/\psi \to \mu^+\mu^-$	SVV_HELAMP, VSS, VVP, PHOTOS VLL	$(4.89 \pm 0.46) \times 10^{-6}$
$B_d^0 \to \psi(2S)K^+\pi^-, \quad \psi(2S) \to \mu^+\mu^-$	PHSP, PHOTOS VLL	$(4.58 \pm 0.61) \times 10^{-6}$
$B_d^0 \to J/\psi\pi^+\pi^-, \quad J/\psi \to \mu^+\mu^-$	PHSP, PHOTOS VLL	$(2.40 \pm 0.11) \times 10^{-6}$
$B_d^0 \to J/\psi\rho^0, \quad J/\psi(\to \mu^+\mu^-), \quad \rho^0 \to \pi^+\pi^-$	SVV_HELAMP, PHOTOS VLL, VSS	$(1.51 \pm 0.08) \times 10^{-6}$
$B_d^0 \to \chi_{c2}K^{*0}, \quad K^{*0} \to K^+\pi^-, \quad \chi_{c2} \to J/\psi\gamma, \quad J/\psi \to \mu^+\mu^-$	SVS, VSS, PHSP, PHOTOS VLL	$(5.72 \pm 1.39) \times 10^{-7}$
$B_d^0 \to \chi_{c0}K^{*0}, \quad K^{*0} \to K^+\pi^-, \quad \chi_{c0} \to J/\psi\gamma, \quad J/\psi \to \mu^+\mu^-$	SVS, VSS, PHSP, PHOTOS VLL	$(1.29 \pm 0.31) \times 10^{-7}$
$B_d^0 \to J/\psi f^0(980), \quad f^0 \to \pi^+\pi^-, \quad J/\psi \to \mu^+\mu^-$	PHSP, PHSP, PHOTOS VLL	$< 6.56 \times 10^{-8}$
$B_d^0 \to \rho^0\ X(214), \quad \rho^0 \to \pi^+\pi^-, \quad X(214) \to \mu^+\mu^-$	PHSP, VSS, PHSP	$< 1.73 \times 10^{-8}$
$B_d^0 \to \omega(K\pi)_0^{*0}, \quad \omega \to \mu^+\mu^-$	PHSP, PHSP	$(1.66 \pm 0.61) \times 10^{-9}$
$B_d^0 \to \eta K^{*0}, \quad \eta \to \mu^+\mu^-\gamma, \quad K^{*0} \to K^+\pi^-$	SVS, PHOTOS PHSP, VSS	$(8.68 \pm 2.17) \times 10^{-10}$

TABLE A.2: B_s^0 decays that were considered as potential peaking backgrounds, but ultimately neglected. The EvtGen decay model available for each decay is given along with the total branching fraction calculated for the B_s^0 decay and all subsequent decays that lead to a signal-like final state.

Decay	EvtGen Model	Total $\Gamma_i/\Gamma \pm \sigma_{\Gamma_i/\Gamma}$
$B_s^0 \to J/\psi\phi, \quad J/\psi \to \mu^+\mu^-, \quad \phi \to K^+K^-$	SVV_HELAMP, PHOTOS VLL, VSS	$(2.90 \pm 0.93) \times 10^{-5}$
$B_s^0 \to J/\psi\phi, \quad J/\psi \to \mu^+\mu^-, \quad \phi \to K_SK_L$	SVV_HELAMP, PHOTOS VLL, VSS	$(2.03 \pm 0.65) \times 10^{-5}$
$B_s^0 \to J/\psi\phi, \quad J/\psi \to \mu^+\mu^-, \quad \phi \to \pi^+\pi^-\pi^0$	SVV_HELAMP, PHOTOS VLL, PHSP	$< 5.93 \times 10^{-5}$
$B_s^0 \to J/\psi f_2'(1525), \quad J/\psi \to \mu^+\mu^-, \quad f_2'(1525) \to K^+K^-$	PHSP, PHOTOS VLL, TSS	$(1.37 \pm 0.48) \times 10^{-5}$
$B_s^0 \to J/\psi\pi^+\pi^-, \quad J/\psi \to \mu^+\mu^-$	PHSP, PHOTOS VLL	$(1.19 \pm 0.36) \times 10^{-5}$
$B_s^0 \to J/\psi\eta', \quad J/\psi \to \mu^+\mu^-, \quad \eta' \to \pi^+\pi^-$	SVS, PHOTOS VLL, PHSP	$(8.65 \pm 1.28) \times 10^{-6}$
$B_s^0 \to J/\psi\eta', \quad J/\psi \to \mu^+\mu^-, \quad \eta' \to \pi^+\pi^-\pi^0$	SVS, PHOTOS VLL, PHSP	$(7.66 \pm 1.39) \times 10^{-8}$
$B_s^0 \to J/\psi f_0(980), \quad J/\psi \to \mu^+\mu^-, \quad f_0(980) \to \pi^+\pi^-$	SVS, PHOTOS VLL, PHSP	$(7.65 \pm 2.37) \times 10^{-6}$
$B_s^0 \to J/\psi\eta, \quad J/\psi \to \mu^+\mu^-, \quad \eta \to \pi^+\pi^-\pi^0$	SVS, PHOTOS VLL, ETA_DALITZ	$(5.44 \pm 0.96) \times 10^{-6}$
$B_s^0 \to J/\psi K^{*0}, \quad K^{*0} \to K^+\pi^-, \quad J/\psi \to \mu^+\mu^-$	PHSP, VSS, PHOTOS VLL	$(2.61 \pm 0.53) \times 10^{-6}$
$B_s^0 \to J/\psi f_0(1370), \quad f_0(1370) \to \pi^+\pi^-, \quad J/\psi \to \mu^+\mu^-$	PHSP, PHSP, PHOTOS VLL	$(2.31 \pm 0.53) \times 10^{-6}$
$B_s^0 \to \psi(2S)\phi, \quad \psi \to \mu^+\mu^-, \quad \phi \to K^+K^-$	SVV_HELAMP, PHOTOS VLL, VSS	$(1.91 \pm 0.65) \times 10^{-6}$
$B_s^0 \to \psi(2S)\phi, \quad \psi \to \mu^+\mu^-, \quad \phi \to K_SK_L$	SVV_HELAMP, PHOTOS VLL, VSS	$(1.33 \pm 0.45) \times 10^{-6}$
$B_s^0 \to \psi(2S)\phi, \quad \psi \to \mu^+\mu^-, \quad \phi \to \pi^+\pi^-\pi^0$	SVV_HELAMP, PHOTOS VLL, PHSP	$< 3.90 \times 10^{-6}$
$B_s^0 \to J/\psi\eta, \quad J/\psi \to \mu^+\mu^-, \quad \eta \to \pi^+\pi^-\pi^0$	SVS, PHOTOS VLL, ETA_DALITZ	$(1.00 \pm 0.18) \times 10^{-6}$
$B_s^0 \to \phi\mu^+\mu^-, \quad \phi \to \pi^+\pi^-\pi^0$	BTOSLLALI, PHSP	$< 1.13 \times 10^{-6}$
$B_s^0 \to \phi\mu^+\mu^-, \quad \phi \to K_SK_L$	BTOSLLALI, VSS	$(3.86 \pm 1.37) \times 10^{-7}$
$B_s^0 \to K^{*0}\phi, \quad \phi \to K^+K^-, \quad K^{*0} \to K^+\pi^-$	SVV_HELAMP, VSS, VSS	$(3.17 \pm 0.21) \times 10^{-7}$
$B_s^0 \to J/\psi f_2(1270), \quad J/\psi \to \mu^+\mu^-, \quad f_2(1270) \to \pi^+\pi^-$	PHSP, PHOTOS VLL, TSS	$(5.93 \pm 2.97) \times 10^{-8}$
$B_s^0 \to \overline{K}^{*0}\rho^0, \quad \overline{K}^{*0} \to K^-\pi^+, \quad \rho^0 \to \mu^+\mu^-$	SVV_HELAMP, VSS, PHSP	$(3.49 \pm 2.15) \times 10^{-8}$

TABLE A.3: B_u^+ decays that were considered as potential peaking backgrounds, but ultimately neglected. The EvtGen decay model available for each decay is given along with the total branching fraction calculated for the B_u^+ decay and all subsequent decays that lead to a signal-like final state.

Decay	EvtGen Model	Total $\Gamma_i/\Gamma \pm \sigma_{\Gamma_i/\Gamma}$
$B_u^+ \to \psi(2S)K^{*+}, \quad \psi(2S) \to \mu^+\mu^-, \quad K^{*+} \to K^0\pi^+$	SVV_HELAMP, PHOTOS VLL, VSS	$(3.97 \pm 0.83) \times 10^{-5}$
$B_u^+ \to \psi(2S)K^+, \quad \psi \to \mu^+\mu^-$	SVS, PHOTOS VLL	$(3.72 \pm 0.15) \times 10^{-5}$
$B_u^+ \to \psi(2S)K^+\pi^+\pi^-, \quad \psi(2S) \to \mu^+\mu^-$	PHSP, PHOTOS VLL	$(2.55 \pm 0.30) \times 10^{-5}$
$B_u^+ \to J/\psi K^{*+}, \quad J/\psi \to \mu^+\mu^-, \quad K^{*+} \to K^0\pi^+$	SVV_HELAMP, PHOTOS VLL, VSS	$(1.12 \pm 0.14) \times 10^{-5}$
$B_u^+ \to \chi_{c1}K^+, \quad J/\psi \to \mu^+\mu^- \quad \chi_{c1} \to J/\psi\gamma$	SVS, PHOTOS VLL, VVP	$(9.88 \pm 0.64) \times 10^{-6}$
$B_u^+ \to J/\psi a_1(1260)^+, \quad J/\psi \to \mu^+\mu^-, \quad a_1(1260)^+ \to \pi^+\pi^-\pi^0$	PHSP, PHOTOS VLL, PHSP	$(9.36 \pm 1.08) \times 10^{-6}$
$B_u^+ \to K^{*-}\mu^+\mu^-, \quad K^{*-} \to \overline{K}^0\pi^-$	PHSP, VSS	8.30×10^{-6}
$B_u^+ \to J/\psi K^+, \quad J/\psi \to \mu^+\mu^-$	SVS, PHOTOS VLL	$(8.02 \pm 1.0) \times 10^{-6}$
$B_u^+ \to K^+\pi^+\pi^-, \quad J/\psi \to \mu^+\mu^-$	PHSP, PHOTOS VLL	$(6.32 \pm 1.25) \times 10^{-6}$
$B_u^+ \to J/\psi K^+(1270), \quad K^+(1270) \to \rho^+K^0$	SVV_HELAMP, VVS_PWAVE	$(5.90 \pm 1.96) \times 10^{-6}$
$B_u^+ \to K^{*+}\rho^0, \quad K^{*+} \to K^0\pi^+, \quad \rho^0 \to \pi^+\pi^-$	SVV_HELAMP, VSS, VSS	$(4.60 \pm 1.10) \times 10^{-6}$
$B_u^+ \to \psi(2S)\pi^+, \quad \psi \to \mu^+\mu^-$	PHSP, PHOTOS VLL	$(1.45 \pm 0.18) \times 10^{-6}$
$B_u^+ \to \pi^-\mu^+\mu^-$	PHSP	$< 1.30 \times 10^{-6}$
$B_u^+ \to X(3872)K^+, \quad X(3872) \to J/\psi\pi^+\pi^-, \quad J/\psi \to \mu^+\mu^-$	PHSP, PHSP, PHOTOS VLL	$(5.10 \pm 0.48) \times 10^{-7}$
$B_u^+ \to X(3872)K^+, \quad X(3872) \to \psi(2S)\gamma, \quad J/\psi \to \mu^+\mu^-$	PHSP, PHSP, PHOTOS VLL	3.14×10^{-8}
$B_u^+ \to X(3872)K^+, \quad X(3872) \to J/\psi\gamma, \quad J/\psi \to \mu^+\mu^-$	PHSP, PHSP, PHOTOS VLL	$(1.25 \pm 0.24) \times 10^{-7}$
$B_u^+ \to \chi_{c1}\pi^+, \quad \chi_{c1} \to J/\psi\gamma$	PHSP, VVP	$(4.54 \pm 1.05) \times 10^{-7}$
$B_u^+ \to J/\psi\phi K^+, \quad \phi \to K^+K^-, \quad J/\psi \to \mu^+\mu^-$	PHSP, VSS, PHOTOS VLL	$(4.06 \pm 1.41) \times 10^{-7}$
$B_u^+ \to J/\psi\rho^+, \quad \rho^+ \to \pi^+\pi^0, \quad J/\psi \to \mu^+\mu^-$	SVV_HELAMP, VSS, PHOTOS VLL	$(3.90 \pm 0.77) \times 10^{-7}$
$B_u^+ \to J/\psi K^+(1400), \quad K^+(1400) \to K^{*0}\pi^+, \quad K^{*0} \to K^+\pi^-, \quad J/\psi \to \mu^+\mu^-$	SVV_HELAMP, VVS_PWAVE, VSS, PHOTOS VLL	$(3.67 \pm 0.48) \times 10^{-7}$
$B_u^+ \to J/\psi\pi^+, \quad J/\psi \to \mu^+\mu^-$	SVS, PHOTOS VLL	$(3.20 \pm 0.48) \times 10^{-7}$
$B_u^+ \to X(3872)K^*, \quad X(3872) \to J/\psi\gamma, \quad K^{*+} \to K^0\pi^+, \quad J/\psi \to \mu^+\mu^-$	PHSP, PHSP, VSS, PHOTOS VLL	$(2.85 \pm 0.30) \times 10^{-8}$
$B_u^+ \to \chi_{c0}K^{*+}, \quad \chi_{c0} \to J/\psi\gamma, \quad K^{*+} \to K^0\pi^+, J/\psi \to \mu^+\mu^-$	SVV_HELAMP, PHSP, VSS, PHOTOS VLL	$(2.31 \pm 0.48) \times 10^{-7}$
$B_u^+ \to X(3872)K^{*+}, \quad X(3872) \to J/\psi\gamma, \quad K^{*+} \to K^0\pi^+, \quad J/\psi \to \mu^+\mu^-$	PHSP, PHSP, VSS, PHOTOS VLL	$(2.18 \pm 0.25) \times 10^{-7}$
$B_u^+ \to h_cK^+, \quad h_c \to J/\psi\pi^+\pi^-, \quad J/\psi \to \mu^+\mu^-$	PHSP, PHSP, PHOTOS VLL	$(2.02 \pm 0.20) \times 10^{-7}$
$B_u^+ \to \chi_{c0}K^{*+}, \quad \chi_{c0} \to J/\psi\gamma, \quad J/\psi \to \mu^+\mu^-, \quad K^{*+} \to K^0\pi^+$	SVS, PHSP, PHOTOS VLL, VSS	$(1.62 \pm 0.09) \times 10^{-7}$
$B_u^+ \to \chi_{c2}K^{*+}, \quad \chi_{c2} \to J/\psi\gamma, \quad J/\psi \to \mu^+\mu^-, \quad K^{*+} \to K^0\pi^+$	PHSP, PHSP, PHOTOS VLL, VSS	$(1.41 \pm 0.57) \times 10^{-7}$
$B_u^+ \to \chi_{c0}K^+, \quad \chi_{c0} \to J/\psi\gamma, \quad J/\psi \to \mu^+\mu^-$	PHSP, PHSP, PHOTOS VLL	$(1.15 \pm 0.13) \times 10^{-7}$
$B_u^+ \to J/\psi\pi^+\pi^0, \quad J/\psi \to \mu^+\mu^-$	PHSP, PHOTOS VLL	$(5.69 \pm 0.66) \times 10^{-8}$
$B_u^+ \to \pi^+\mu^+\mu^0$	PHSP	$(2.40 \pm 0.60) \times 10^{-8}$
$B_u^+ \to \chi_{c2}K^+, \quad \chi_{c2} \to J/\psi\gamma, \quad J/\psi \to \mu^+\mu^-$	STS, PHSP, PHOTOS VLL	$(1.29 \pm 0.70) \times 10^{-8}$

Appendix B

Acceptance Maps

A full description of how the acceptance maps were made is given in Sec. 6.2.1. The acceptance maps for $\cos\theta_L$, $\cos\theta_K$ and ϕ are shown for each of the four folded PDFs, in terms of S_4, S_5, S_7 and S_8, below.

S_4 Folded PDF

See Sec. 6.2.1.

S_5 Folded PDF

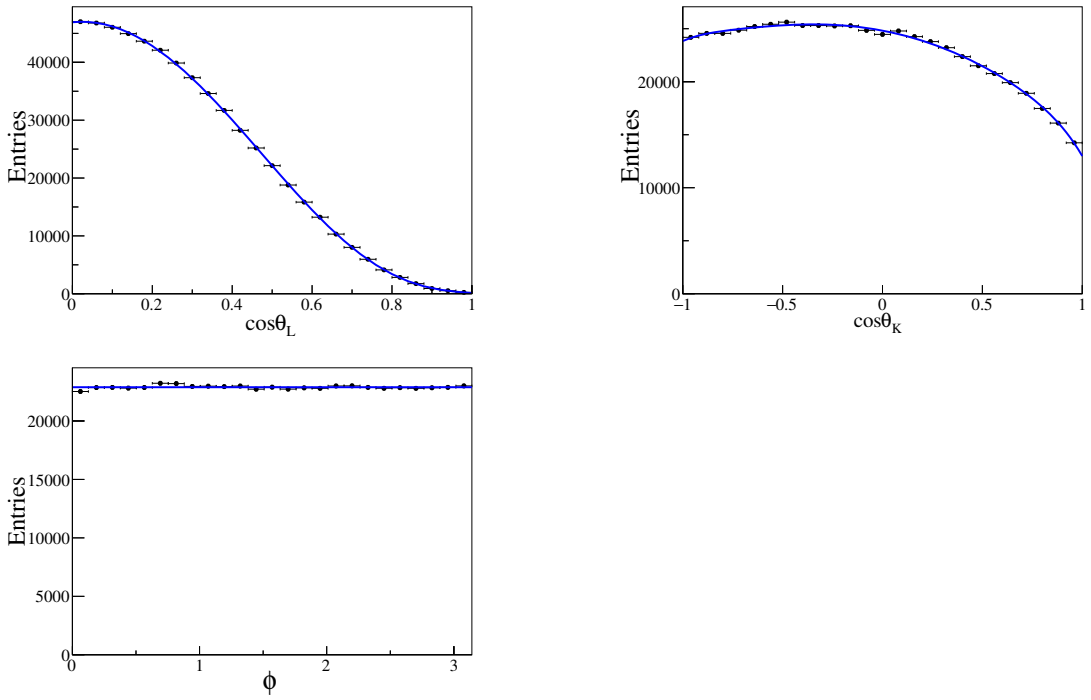

FIGURE B.1: 6th order polynomial fits to the folded S_5 $B^0_d \to K^{*0}$ $\mu^+\mu^-$ (EvtGen, flat) MC for $q^2 \in [0.04, 2.00]$ $(GeV/c^2)^2$.

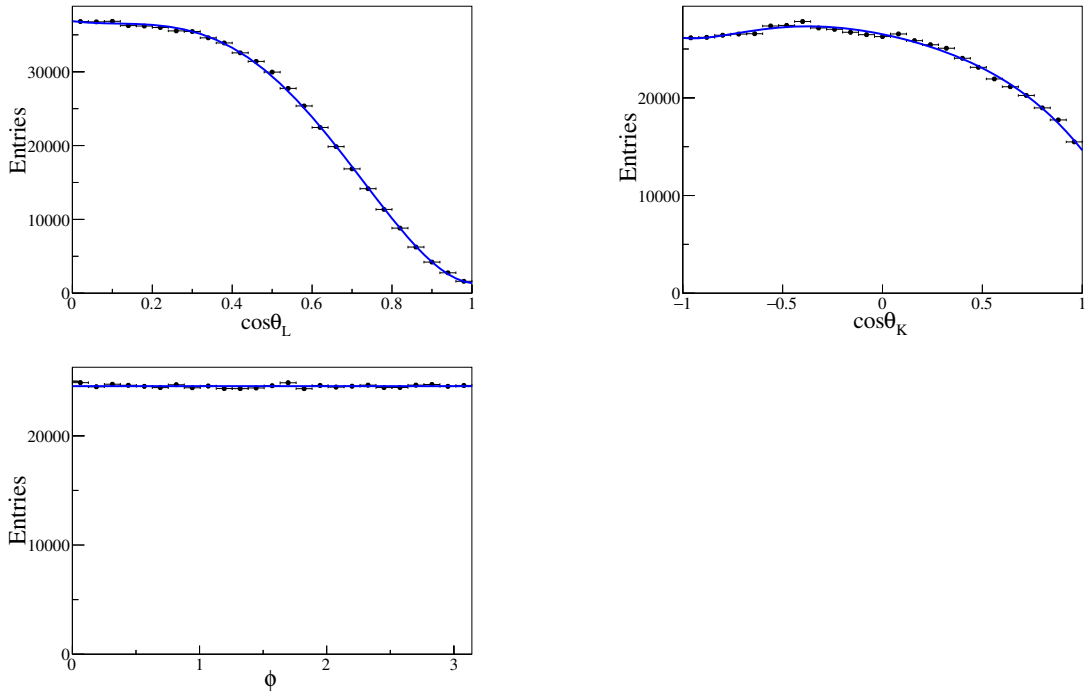

FIGURE B.2: 6th order polynomial fits to the folded S_5 $B^0_d \to K^{*0}$ $\mu^+\mu^-$ (EvtGen, flat) MC for $q^2 \in [2.00, 4.00]$ $(GeV/c^2)^2$.

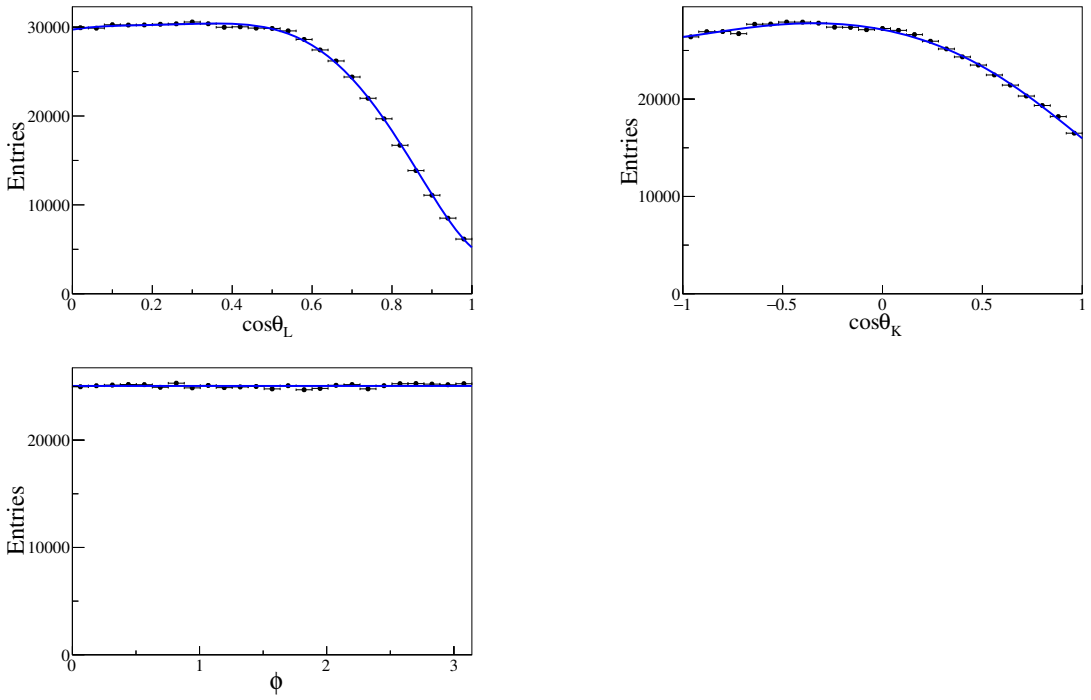

FIGURE B.3: 6th order polynomial fits to the folded S_5 $B^0_d \to K^{*0}\ \mu^+\mu^-$ (EvtGen, flat) MC for $q^2 \in [4.00, 6.00]$ $(GeV/c^2)^2$.

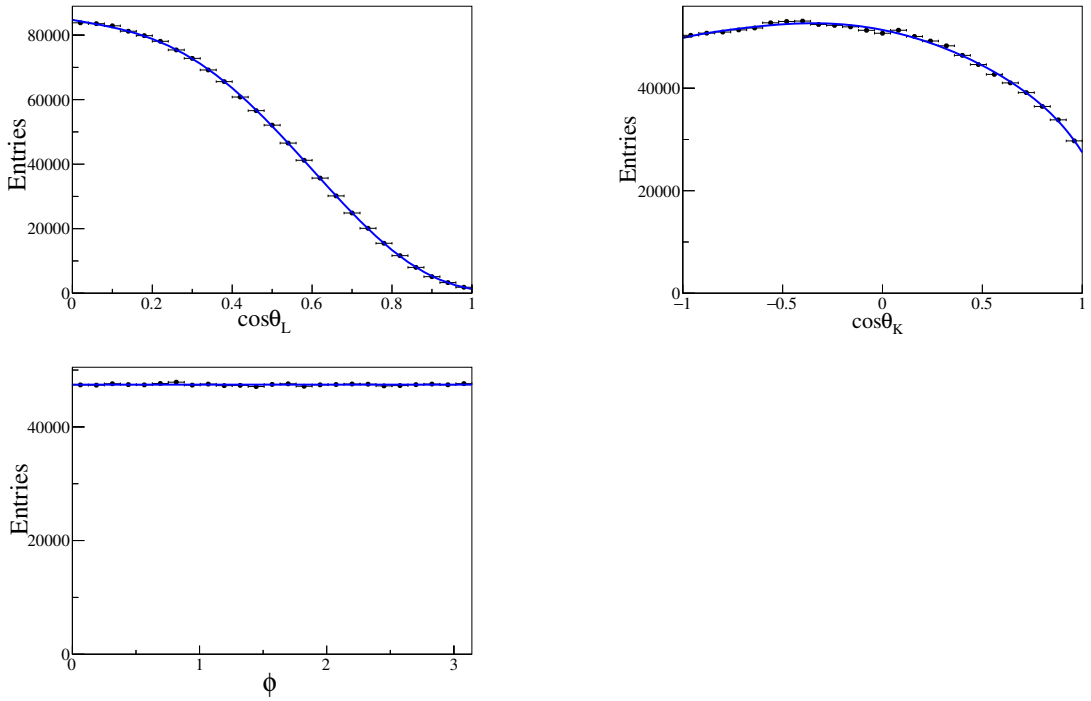

FIGURE B.4: 6th order polynomial fits to the folded S_5 $B^0_d \to K^{*0}\ \mu^+\mu^-$ (EvtGen, flat) MC for $q^2 \in [0.04, 4.00]$ $(GeV/c^2)^2$.

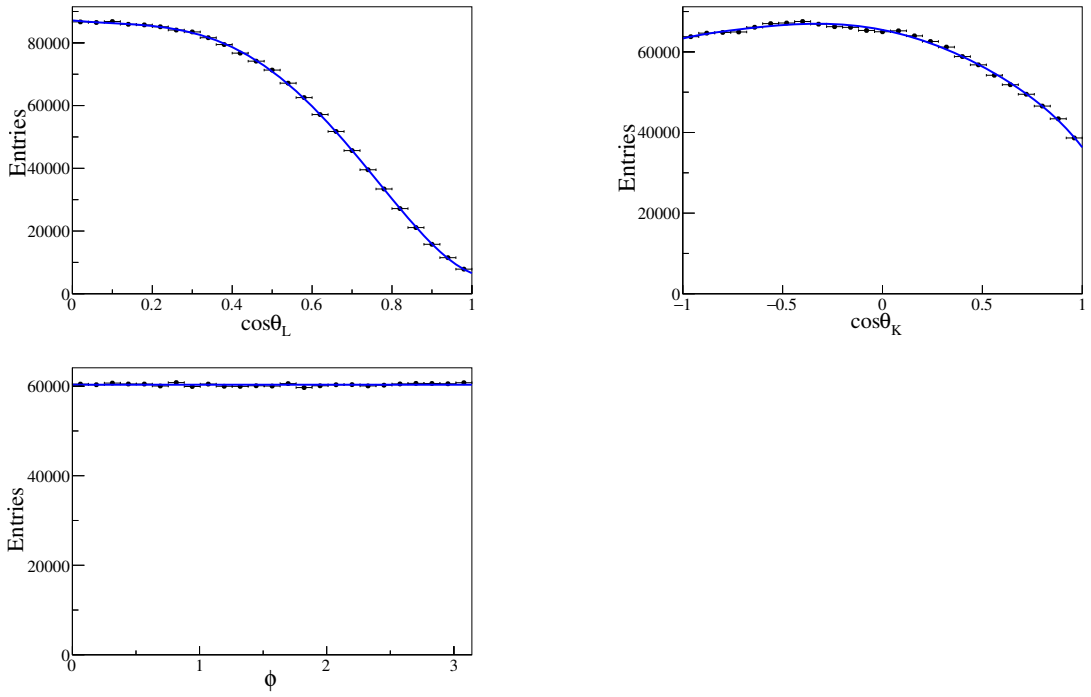

FIGURE B.5: 6th order polynomial fits to the folded S_5 $B^0_d \to K^{*0}\ \mu^+\mu^-$ (EvtGen, flat) MC for $q^2 \in [1.10, 6.00]$ $(GeV/c^2)^2$.

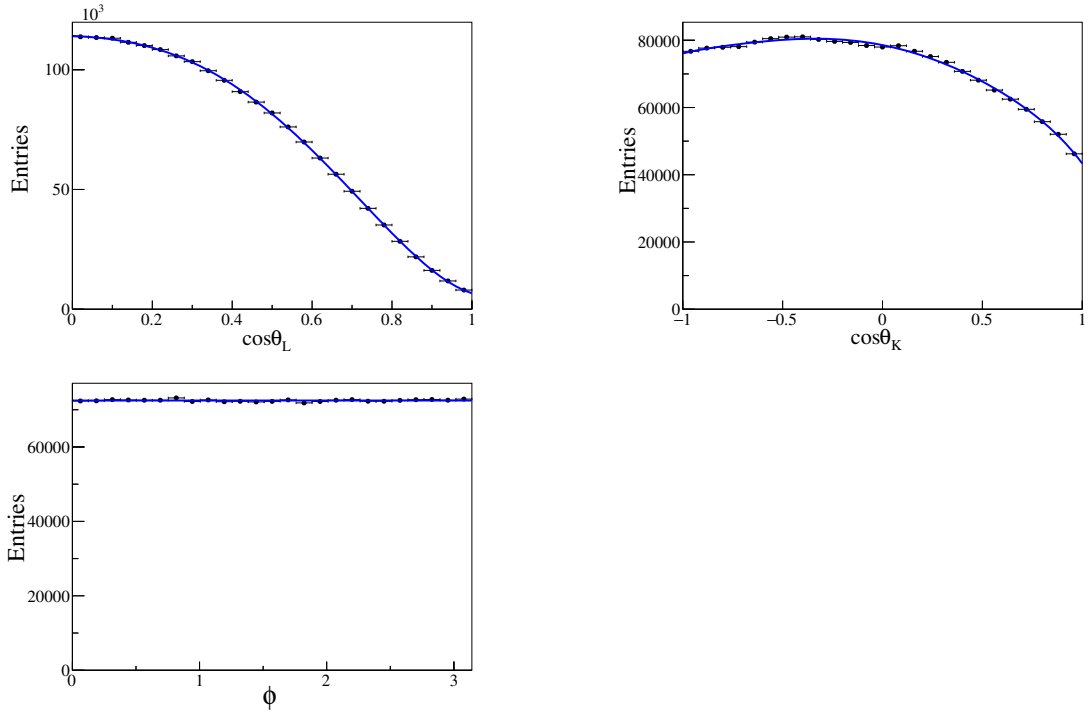

FIGURE B.6: 6th order polynomial fits to the folded S_5 $B^0_d \to K^{*0}\ \mu^+\mu^-$ (EvtGen, flat) MC for $q^2 \in [0.04, 6.00]$ $(GeV/c^2)^2$.

S_7 Folded PDF

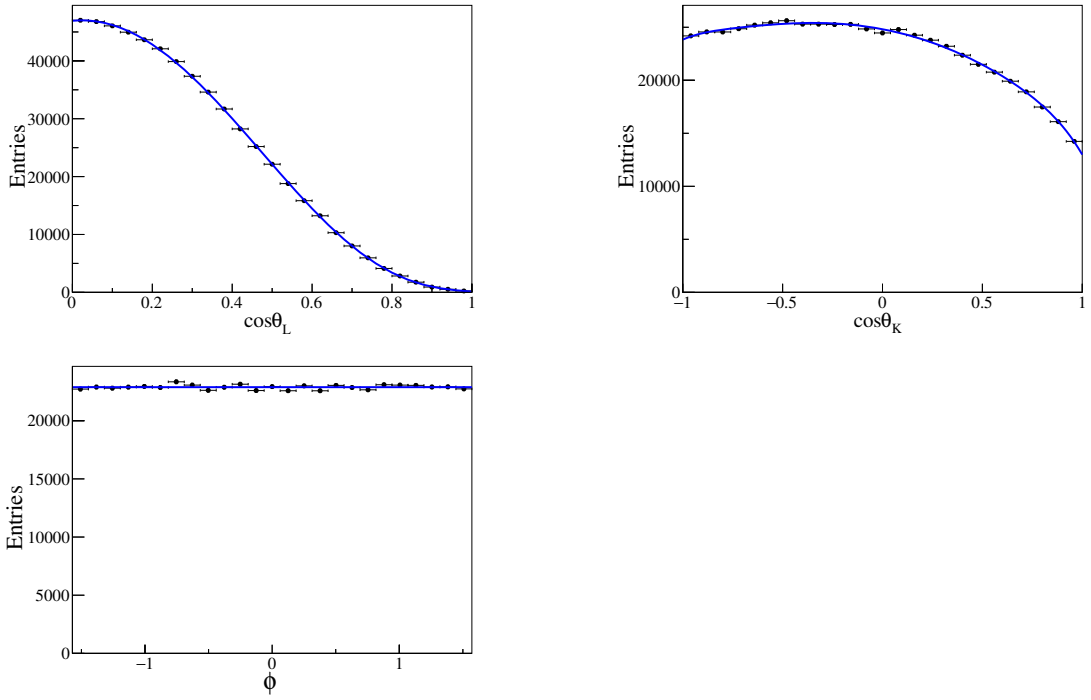

FIGURE B.7: 6th order polynomial fits to the folded S_7 $B^0_d \to K^{*0}$ $\mu^+\mu^-$ (EvtGen, flat) MC for $q^2 \in [0.04, 2.00]$ $(GeV/c^2)^2$.

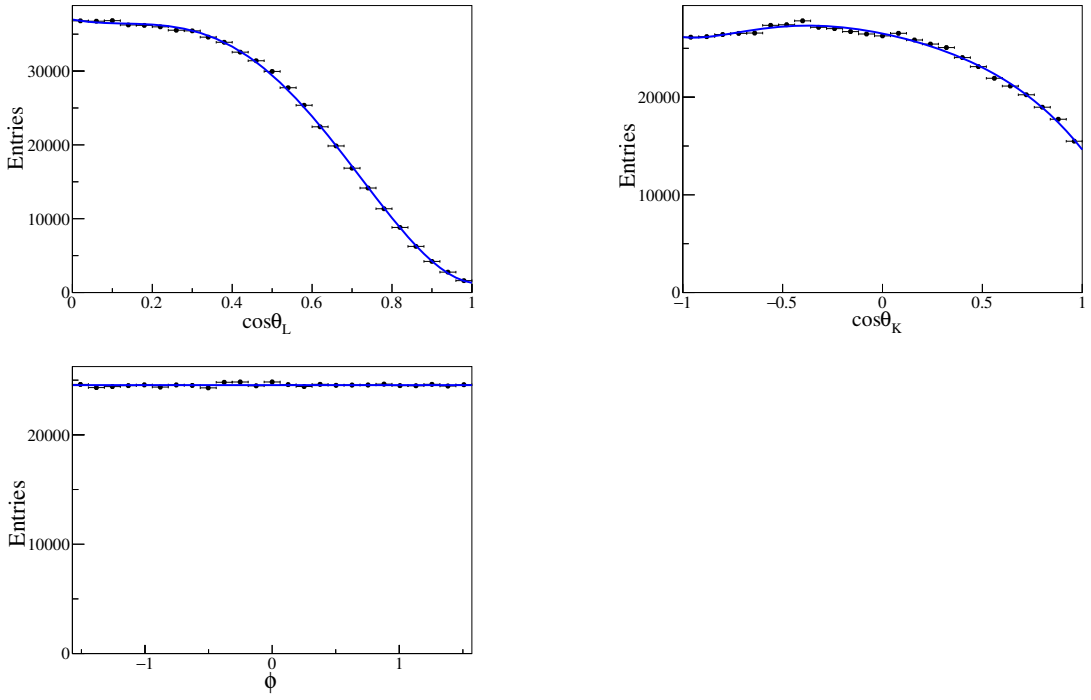

FIGURE B.8: 6th order polynomial fits to the folded S_7 $B^0_d \to K^{*0}$ $\mu^+\mu^-$ (EvtGen, flat) MC for $q^2 \in [2.00, 4.00]$ $(GeV/c^2)^2$.

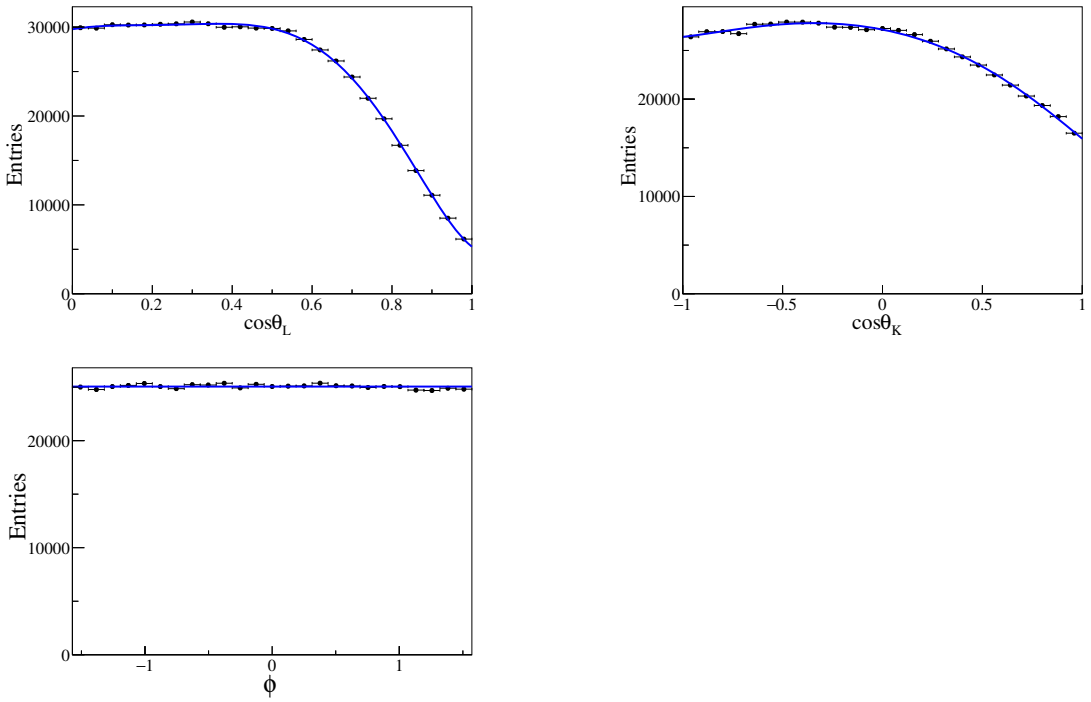

FIGURE B.9: 6th order polynomial fits to the folded S_7 $B^0_d \to K^{*0}\ \mu^+\mu^-$ (EvtGen, flat) MC for $q^2 \in [4.00, 6.00]$ $(GeV/c^2)^2$.

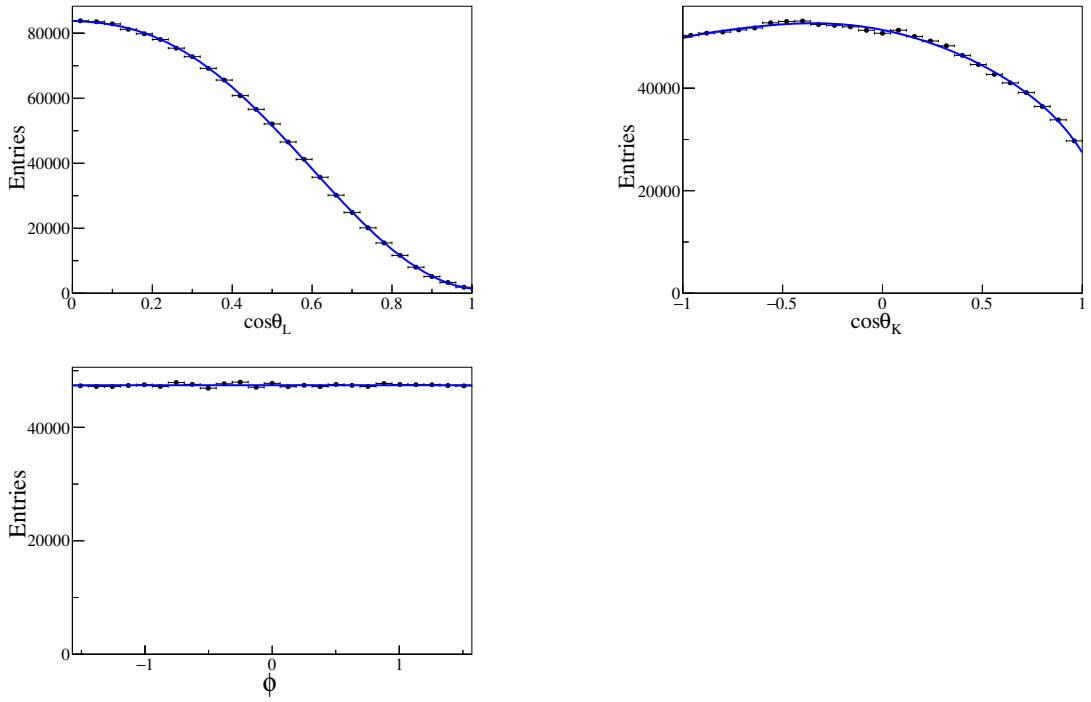

FIGURE B.10: 6th order polynomial fits to the folded S_7 $B^0_d \to K^{*0}\ \mu^+\mu^-$ (EvtGen, flat) MC for $q^2 \in [0.04, 4.00]$ $(GeV/c^2)^2$.

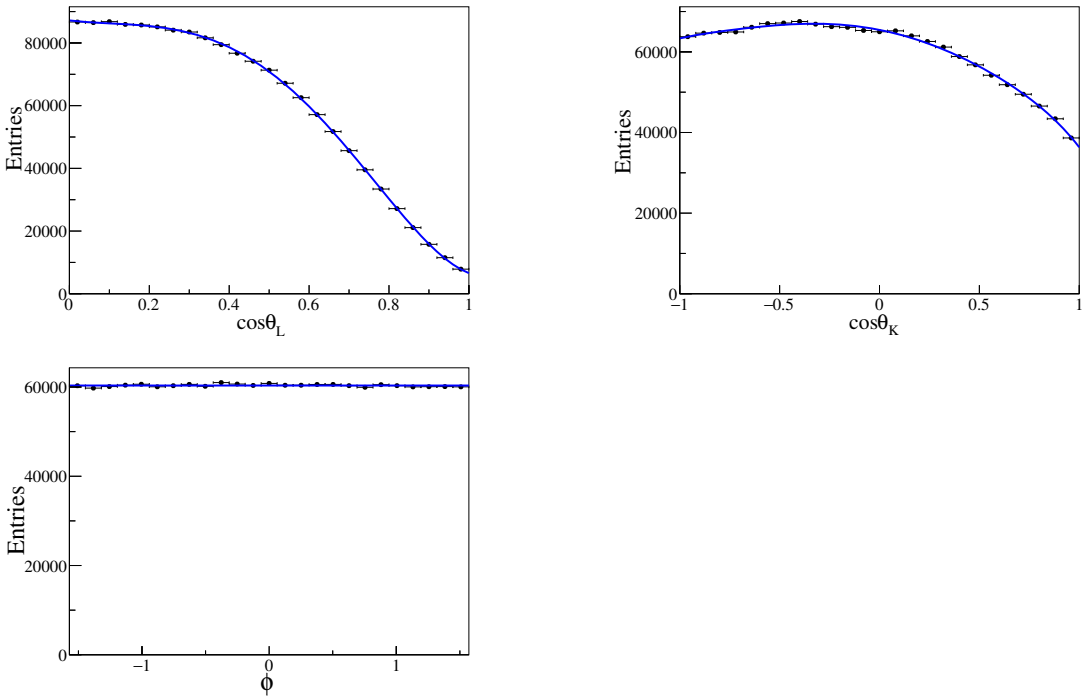

FIGURE B.11: 6th order polynomial fits to the folded S_7 $B^0_d \to K^{*0}$ $\mu^+\mu^-$ (EvtGen, flat) MC for $q^2 \in [1.10, 6.00]$ $(GeV/c^2)^2$.

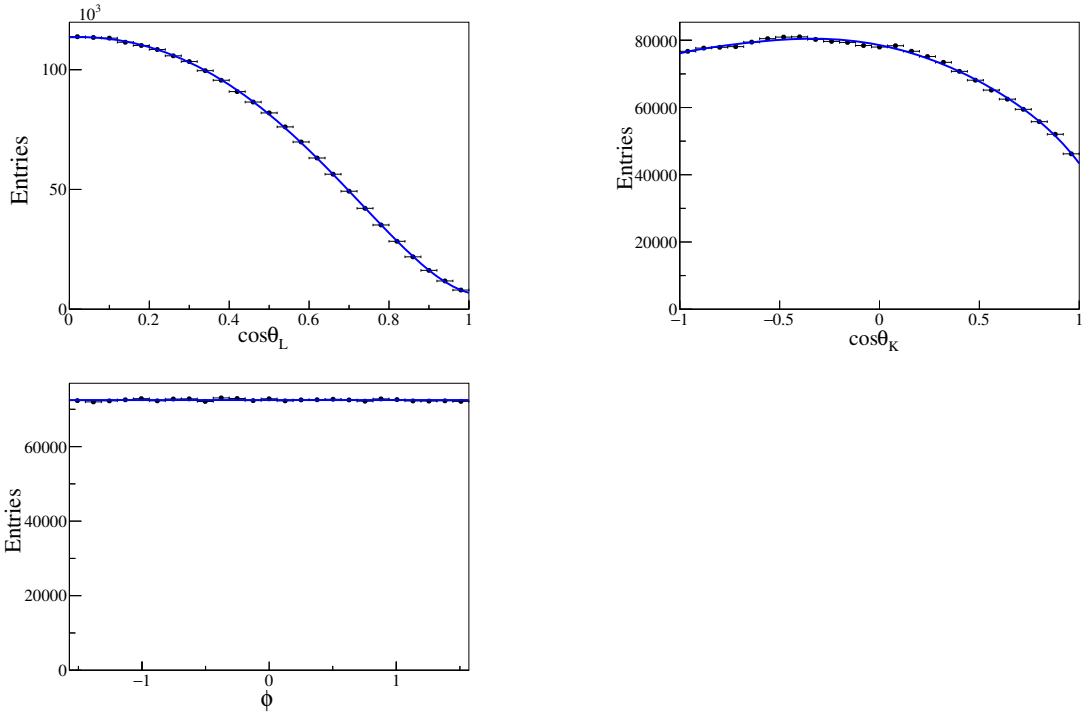

FIGURE B.12: 6th order polynomial fits to the folded S_7 $B^0_d \to K^{*0}$ $\mu^+\mu^-$ (EvtGen, flat) MC for $q^2 \in [0.04, 6.00]$ $(GeV/c^2)^2$.

S_8 Folded PDF

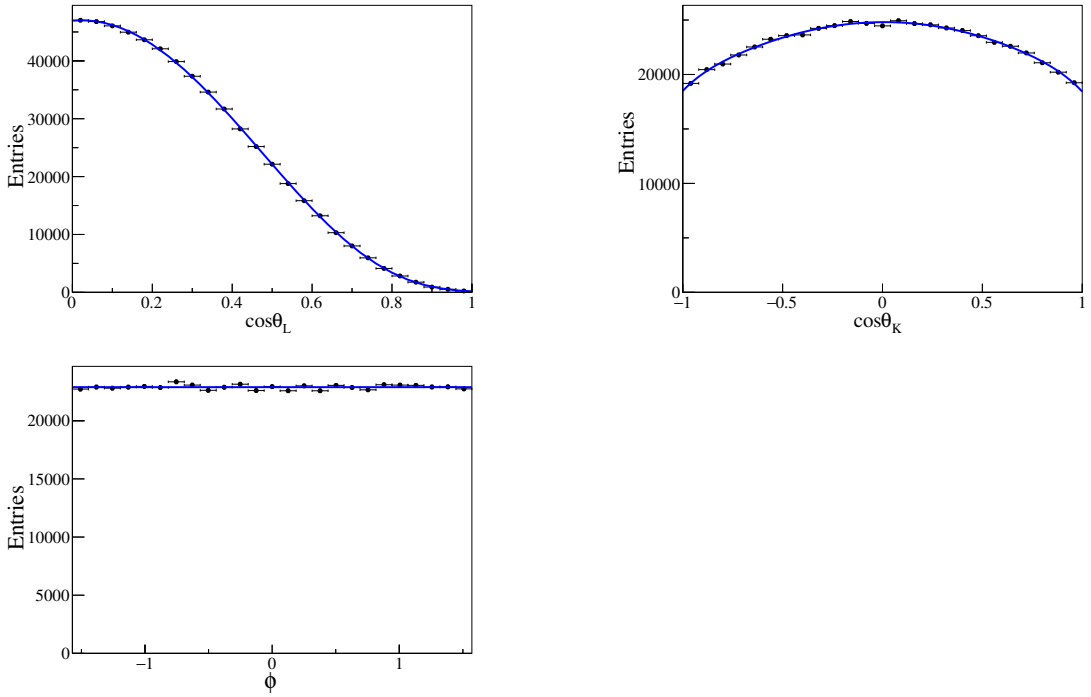

FIGURE B.13: 6th order polynomial fits to the folded S_8 $B_d^0 \to K^{*0}\ \mu^+\mu^-$ (EvtGen, flat) MC for $q^2 \in [0.04, 2.00]$ $(GeV/c^2)^2$.

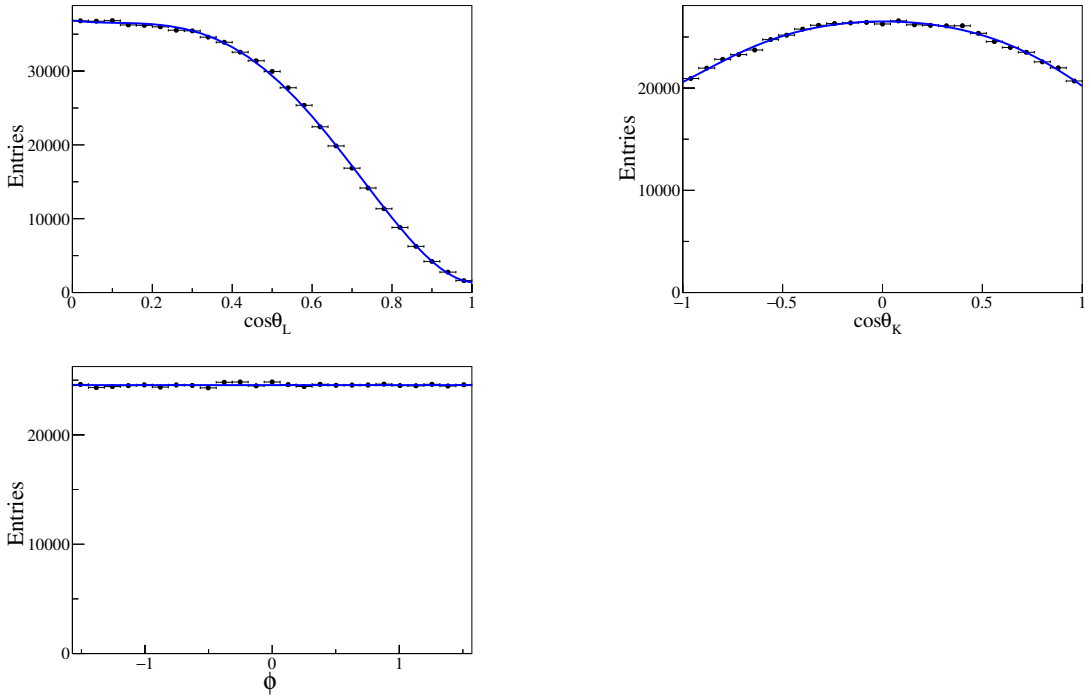

FIGURE B.14: 6th order polynomial fits to the folded S_8 $B_d^0 \to K^{*0}\ \mu^+\mu^-$ (EvtGen, flat) MC for $q^2 \in [2.00, 4.00]$ $(GeV/c^2)^2$.

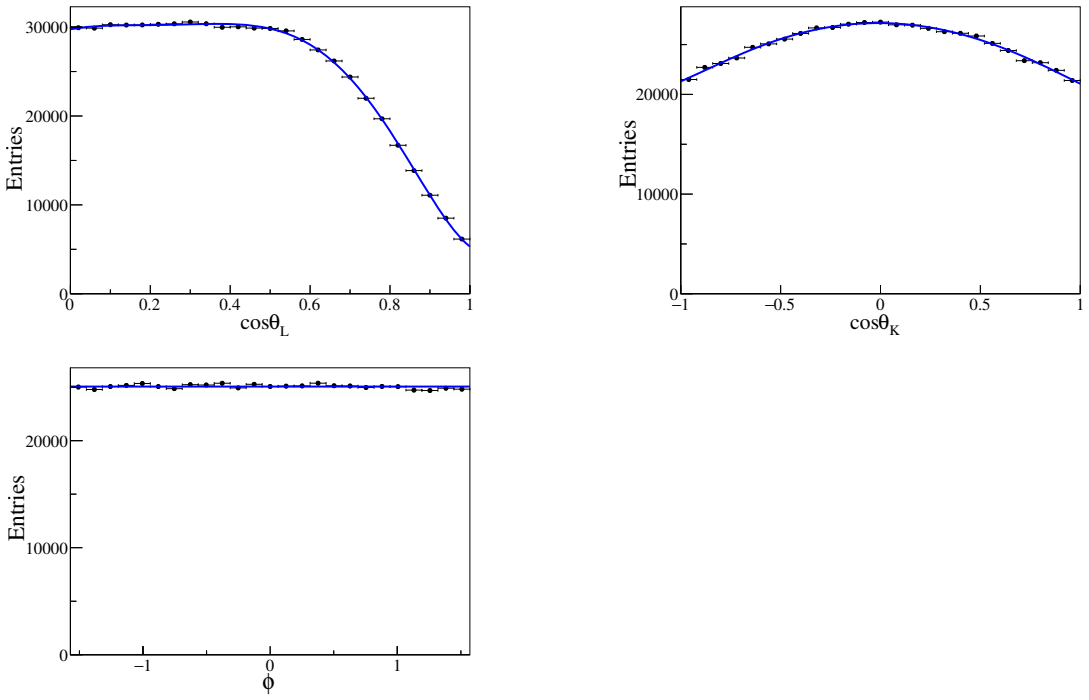

FIGURE B.15: 6th order polynomial fits to the folded S_8 $B^0_d \to K^{*0}$ $\mu^+\mu^-$ (EvtGen, flat) MC for $q^2 \in [4.00, 6.00]$ $(GeV/c^2)^2$.

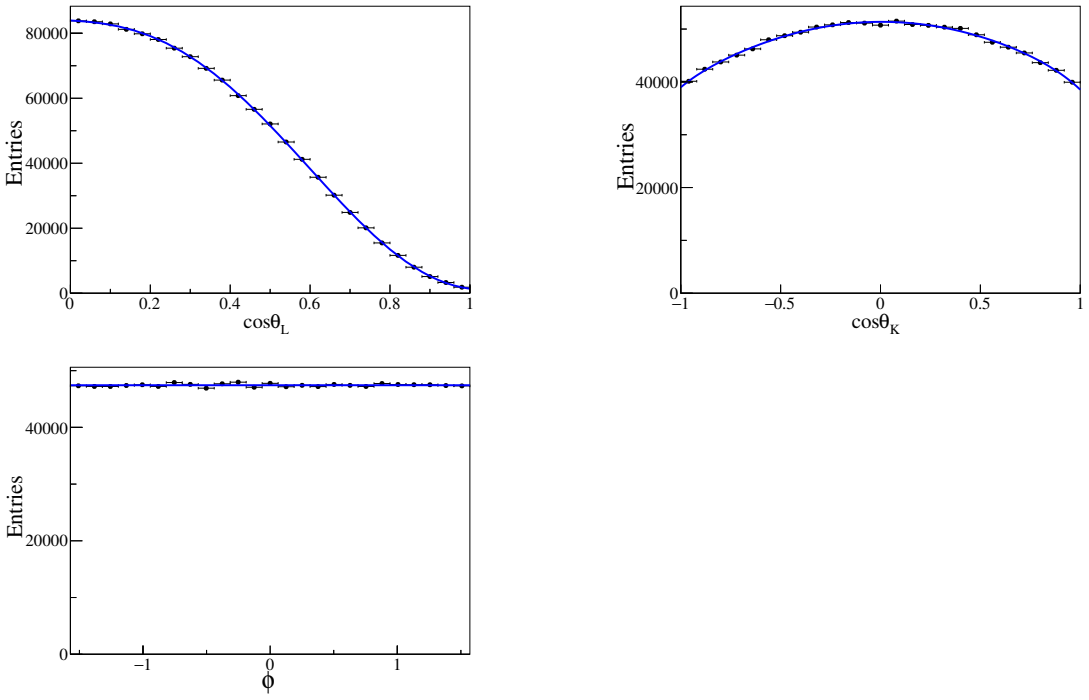

FIGURE B.16: 6th order polynomial fits to the folded S_8 $B^0_d \to K^{*0}$ $\mu^+\mu^-$ (EvtGen, flat) MC for $q^2 \in [0.04, 4.00]$ $(GeV/c^2)^2$.

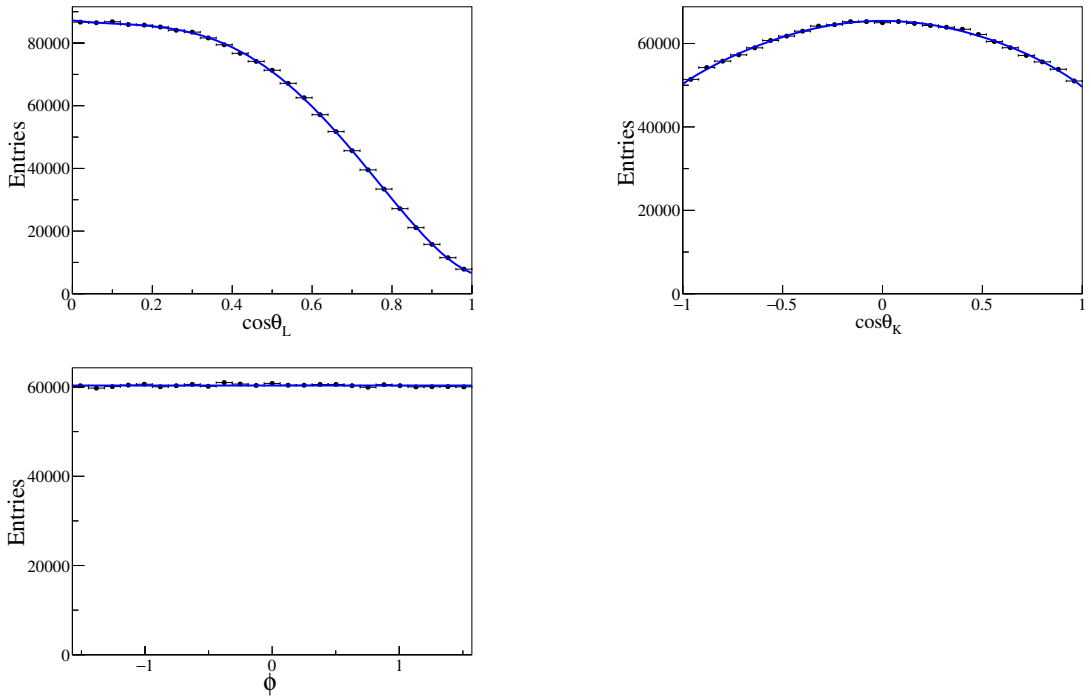

FIGURE B.17: 6th order polynomial fits to the folded S_8 $B^0_d \to K^{*0}$ $\mu^+\mu^-$ (EvtGen, flat) MC for $q^2 \in [1.10, 6.00]$ $(GeV/c^2)^2$.

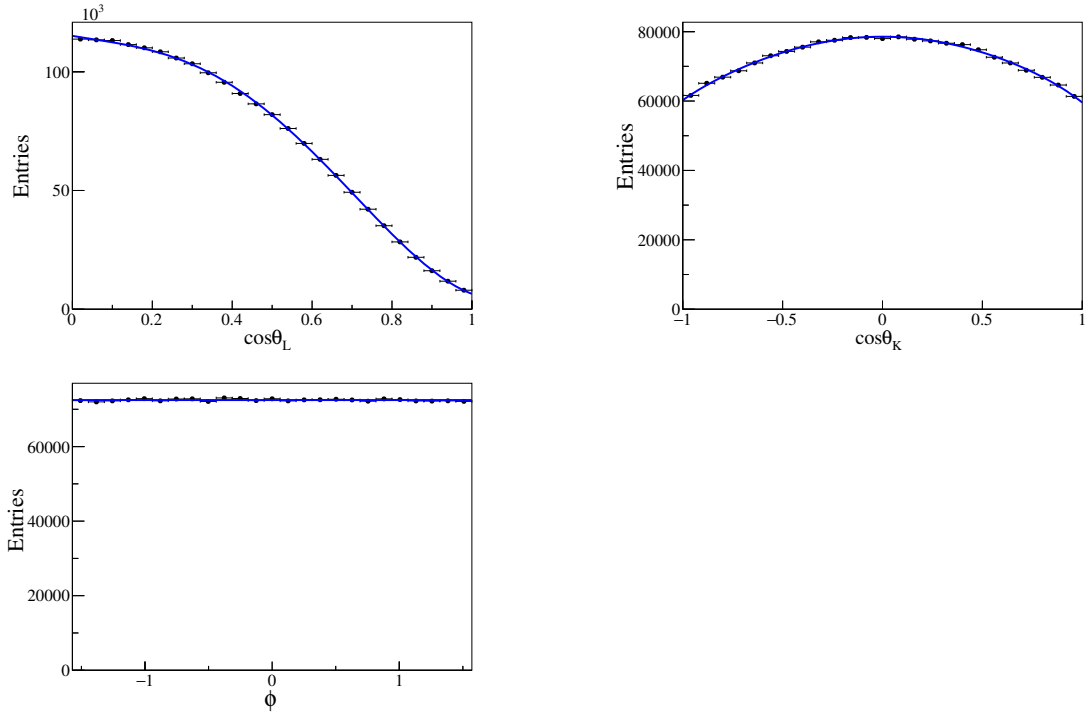

FIGURE B.18: 6th order polynomial fits to the folded S_8 $B^0_d \to K^{*0}$ $\mu^+\mu^-$ (EvtGen, flat) MC for $q^2 \in [0.04, 6.00]$ $(GeV/c^2)^2$.

Appendix C

Systematic Uncertainties

This chapter documents systematic uncertainties that were evaluated for this analysis, as described in Chapter 8.

Tables of the systematic uncertainties on each variable from each source considered are given below in Sections C.1 through C.10. A full description of the ten sources of systematic uncertainty can be found in the following Sections:

- PDF nuisance parameters (See Sec. 8.1).
- Background description in the angular distributions (See Sec. 8.2).
- Peaking background (See Sec. 8.3).
- Data-MC differences (See Sec. 8.4).
- Fit bias (See Sec. 8.5).
- Kaon-pion misidentification (See Sec. 8.6).
- S-wave contribution (See Sec. 8.7).
- Misreconstructed decays (See Sec. 8.8).
- Acceptance functions (See Sec 8.9).
- Mass fit range (See Sec. 8.10).

C.1 PDF Nuisance Parameters

TABLE C.1: The systematic uncertainties on the fitted angular observables arising from the model nuisance parameters in the nominal angular fit. The results are shown for F_L, S_3 and S_i, where $i = 4, 5, 7, 8$ according to the folded PDF used, for each q^2 bin.

q^2 range $((GeV/c^2)^2$	PDF	$\sigma(F_L)$	$\sigma(S_3)$	$\sigma(S_i)$
$[0.04, 2.00])$	S_4	$^{+0.007}_{-0.004}$	$^{+0.011}_{-0.010}$	$^{+0.002}_{-0.002}$
	S_5	$^{+0.010}_{-0.012}$	$^{+0.010}_{-0.010}$	$^{+0.002}_{-0.001}$
	S_7	$^{+0.003}_{-0.004}$	$^{+0.017}_{-0.015}$	$^{+0.002}_{-0.002}$
	S_8	$^{+0.006}_{-0.005}$	$^{+0.019}_{-0.018}$	$^{+0.002}_{-0.003}$
$[2.00, 4.00]$	S_4	$^{+0.020}_{-0.023}$	$^{+0.012}_{-0.014}$	$^{+0.005}_{-0.004}$
	S_5	$^{+0.002}_{-0.002}$	$^{+0.013}_{-0.014}$	$^{+0.006}_{-0.005}$
	S_7	$^{+0.010}_{-0.010}$	$^{+0.013}_{-0.014}$	$^{+0.005}_{-0.005}$
	S_8	$^{+0.028}_{-0.030}$	$^{+0.012}_{-0.013}$	$^{+0.005}_{-0.004}$
$[4.00, 6.00]$	S_4	$^{+0.018}_{-0.020}$	$^{+0.022}_{-0.022}$	$^{+0.007}_{-0.007}$
	S_5	$^{+0.004}_{-0.005}$	$^{+0.008}_{-0.009}$	$^{+0.007}_{-0.007}$
	S_7	$^{+0.003}_{-0.003}$	$^{+0.008}_{-0.008}$	$^{+0.006}_{-0.006}$
	S_8	$^{+0.012}_{-0.009}$	$^{+0.008}_{-0.009}$	$^{+0.006}_{-0.006}$
$[0.04, 4.00]$	S_4	$^{+0.007}_{-0.007}$	$^{+0.003}_{-0.003}$	$^{+0.001}_{-0.001}$
	S_5	$^{+0.007}_{-0.007}$	$^{+0.010}_{-0.010}$	$^{+0.002}_{-0.002}$
	S_7	$^{+0.003}_{-0.003}$	$^{+0.010}_{-0.010}$	$^{+0.001}_{-0.001}$
	S_8	$^{+0.008}_{-0.007}$	$^{+0.011}_{-0.011}$	$^{+0.001}_{-0.001}$
$[1.10, 6.00]$	S_4	$^{+0.002}_{-0.002}$	$^{+0.005}_{-0.006}$	$^{+0.003}_{-0.003}$
	S_5	$^{+0.002}_{-0.002}$	$^{+0.011}_{-0.011}$	$^{+0.003}_{-0.003}$
	S_7	$^{+0.003}_{-0.003}$	$^{+0.011}_{-0.011}$	$^{+0.003}_{-0.002}$
	S_8	$^{+0.004}_{-0.002}$	$^{+0.011}_{-0.013}$	$^{+0.003}_{-0.004}$
$[0.04, 6.00]$	S_4	$^{+0.002}_{-0.002}$	$^{+0.009}_{-0.009}$	$^{+0.002}_{-0.002}$
	S_5	$^{+0.004}_{-0.005}$	$^{+0.009}_{-0.009}$	$^{+0.002}_{-0.002}$
	S_7	$^{+0.002}_{-0.002}$	$^{+0.009}_{-0.009}$	$^{+0.001}_{-0.002}$
	S_8	$^{+0.002}_{-0.002}$	$^{+0.009}_{-0.010}$	$^{+0.001}_{-0.002}$

C.2 Background Description in Angular Distributions

TABLE C.2: The systematic uncertainties from the background description in the angular distributions. The results show the difference between the fitted angular observables when using a 2^{nd} order and a 3^{rd} order Chebyshev polynomial function to model the combinatorial background in the angular distributions. The systematic uncertainties are categorised by q^2 bin for each $S_{i=4,5,7,8}$ folded PDF.

q^2 range $((GeV/c^2)^2$	PDF	$\sigma(F_L)$	$\sigma(S_3)$	$\sigma(S_i)$
$[0.04, 2.00]$	S_4	-0.009	0.005	0.023
	S_5	-0.010	0.009	-0.013
	S_7	-0.003	0.020	-0.006
	S_8	0.013	0.021	-0.002
$[2.00, 4.00]$	S_4	-0.046	0.009	-0.018
	S_5	-0.035	-0.005	0.001
	S_7	-0.055	0.009	0.032
	S_8	-0.006	-0.003	0.002
$[4.00, 6.00]$	S_4	-0.069	-0.032	0.012
	S_5	-0.064	-0.036	-0.016
	S_7	-0.033	-0.044	0.012
	S_8	-0.010	-0.009	0.005
$[0.04, 4.00]$	S_4	-0.025	0.004	-0.028
	S_5	-0.027	0.003	-0.002
	S_7	-0.024	0.008	0.014
	S_8	-0.002	0.004	0.000
$[1.10, 6.00]$	S_4	-0.052	0.011	-0.017
	S_5	-0.049	0.005	0.012
	S_7	-0.043	0.004	0.016
	S_8	-0.012	-0.006	0.002
$[0.04, 6.00]$	S_4	-0.035	-0.003	-0.013
	S_5	-0.035	-0.006	-0.001
	S_7	-0.027	-0.003	0.012
	S_8	-0.004	-0.001	-0.000

C.3 Peaking Background Contribution

TABLE C.3: The systematic uncertainties attributed with the peaking background contribution. The uncertainties are evaluated as the difference between the fitted angular observables in PDF and embedded toys for each $S_{i=4,5,7,8}$ folded PDF. The results are categorised by q^2 bin.

q^2 range $((GeV/c^2)^2)$	PDF	$\sigma(F_L)$	$\sigma(S_3)$	$\sigma(S_i)$
$[0.04, 2.00]$	S_4	-0.002	0.000	0.001
	S_5	-0.002	0.001	0.001
	S_7	-0.001	0.001	-0.001
	S_8	-0.002	0.001	0.000
$[2.00, 4.00]$	S_4	-0.007	0.001	-0.001
	S_5	-0.004	0.004	0.004
	S_7	-0.007	0.000	0.000
	S_8	-0.004	0.000	-0.001
$[4.00, 6.00]$	S_4	-0.012	0.001	-0.001
	S_5	-0.009	0.001	0.000
	S_7	-0.013	0.001	-0.001
	S_8	-0.009	-0.001	0.000
$[0.04, 4.00]$	S_4	0.002	0.000	0.000
	S_5	0.002	0.000	0.000
	S_7	0.002	-0.001	0.000
	S_8	0.001	0.000	0.000
$[1.10, 6.00]$	S_4	-0.011	0.001	-0.001
	S_5	-0.011	0.000	0.000
	S_7	-0.011	0.000	0.000
	S_8	-0.011	0.000	0.000
$[0.04, 6.00]$	S_4	-0.005	0.000	0.000
	S_5	-0.005	0.000	0.000
	S_7	-0.005	0.000	0.000
	S_8	-0.006	0.000	0.000

C.4 Data-MC Agreement

TABLE C.4: The systematic uncertainties associated with data-MC differences. The uncertainties are evaluated as the difference between the fitted angular observables before and after the MC is reweighted to match the data.

q^2 range $((GeV/c^2)^2)$	PDF	$\sigma(F_L)$	$\sigma(S_3)$	$\sigma(S_i)$
$[0.04, 2.00]$	S_4	-0.015	-0.001	-0.008
	S_5	-0.015	-0.001	-0.003
	S_7	-0.015	-0.001	-0.001
	S_8	-0.015	-0.001	0.000
$[2.00, 4.00]$	S_4	-0.017	-0.001	-0.013
	S_5	-0.017	0.000	0.002
	S_7	-0.017	0.000	0.000
	S_8	-0.017	0.000	0.001
$[4.00, 6.00]$	S_4	-0.021	0.000	-0.009
	S_5	-0.020	0.001	-0.002
	S_7	-0.020	0.001	-0.000
	S_8	-0.020	0.001	-0.004
$[0.04, 4.00]$	S_4	-0.015	0.000	-0.011
	S_5	-0.016	-0.001	0.000
	S_7	-0.016	-0.001	0.000
	S_8	-0.016	-0.001	0.001
$[1.10, 6.00]$	S_4	-0.016	0.000	-0.010
	S_5	-0.017	0.000	-0.001
	S_7	-0.017	0.000	0.000
	S_8	-0.017	0.000	-0.002
$[0.04, 6.00]$	S_4	-0.015	0.000	-0.010
	S_5	-0.016	-0.001	-0.001
	S_7	-0.016	-0.001	0.000
	S_8	-0.016	-0.001	-0.002

C.5 Fit Bias

TABLE C.5: The systematic uncertainties associated with the intrinsic fit bias of the likelihood estimator. The uncertainties are evaluated as the difference between the fitted angular observables in PDF toy MC studies before and after the fit bias was corrected for.

q^2 range $((GeV/c^2)^2)$	PDF	$\sigma(F_L)$	$\sigma(S_3)$	$\sigma(S_i)$
$[0.04, 2.00]$	S_4	-0.003	-0.001	-0.014
	S_5	-0.008	0.003	0.011
	S_7	-0.012	0.007	-0.000
	S_8	-0.021	0.019	-0.032
$[2.00, 4.00]$	S_4	0.013	0.012	0.004
	S_5	-0.007	-0.019	-0.012
	S_7	0.015	-0.013	-0.002
	S_8	0.004	-0.008	0.006
$[4.00, 6.00]$	S_4	-0.013	-0.011	-0.004
	S_5	-0.006	-0.001	-0.009
	S_7	-0.013	0.006	0.026
	S_8	-0.004	0.021	0.008
$[0.04, 4.00]$	S_4	0.003	-0.002	-0.010
	S_5	-0.002	0.002	0.018
	S_7	0.001	-0.001	-0.008
	S_8	0.003	0.021	0.015
$[1.10, 6.00]$	S_4	-0.003	-0.008	0.004
	S_5	-0.003	-0.005	0.010
	S_7	0.001	0.003	-0.005
	S_8	0.004	0.008	-0.036
$[0.04, 6.00]$	S_4	-0.011	-0.014	0.012
	S_5	0.000	-0.003	0.005
	S_7	-0.010	-0.006	0.005
	S_8	0.002	-0.005	-0.013

C.6 Kaon-Pion Misidentification

TABLE C.6: The systematic uncertainties associated with the dilution on data, assigned to correct for kaon-pion misidentification. The uncertainties were assigned to S_4 and S_5 observables only and were evaluated for each q^2 bin separately.

q^2 range $((GeV/c^2)^2)$	$\sigma(S_{4,5})$
$[0.04, 2.00]$	0.003
$[2.00, 4.00]$	-0.001
$[4.00, 6.00]$	-0.001
$[0.04, 4.00]$	0.001
$[1.10, 6.00]$	0.000
$[0.04, 6.00]$	0.001

C.7 S-Wave

TABLE C.7: The systematic uncertainties from the S-wave contribution to the signal, summarised for each of the folded PDFs in bins of q^2.

q^2 range $((GeV/c^2)^2)$	PDF	$\sigma(F_L)$	$\sigma(S_3)$	$\sigma(S_i)$
$[0.04, 2.00]$	S_4	-0.001	-0.004	0.004
	S_5	0.002	0.007	0.002
	S_7	0.001	0.004	0.000
	S_8	-0.010	0.012	-0.009
$[2.00, 4.00]$	S_4	0.001	0.004	-0.005
	S_5	-0.007	-0.005	0.001
	S_7	-0.005	-0.004	-0.006
	S_8	-0.005	-0.009	0.007
$[4.00, 6.00]$	S_4	-0.012	-0.014	0.000
	S_5	0.005	-0.012	0.004
	S_7	-0.001	0.006	0.010
	S_8	-0.001	0.005	-0.009
$[0.04, 4.00]$	S_4	0.004	-0.002	0.005
	S_5	-0.004	0.004	0.002
	S_7	0.000	-0.003	-0.004
	S_8	0.001	0.008	0.020
$[1.10, 6.00]$	S_4	0.002	0.000	0.002
	S_5	0.000	0.000	0.001
	S_7	0.001	0.002	-0.004
	S_8	-0.007	0.003	-0.011
$[0.04, 6.00]$	S_4	0.002	-0.002	-0.003
	S_5	-0.001	-0.002	0.001
	S_7	-0.003	-0.003	-0.002
	S_8	-0.004	-0.002	-0.002

C.8 Misreconstructed Decays

TABLE C.8: The systematic uncertainties from misreconstructed decays, calculated as the difference between the fitted angular parameters from two sets of closure tests, in which fits to the SM signal MC were performed with acceptance parameters extracted from the SM signal MC and the SM $\overline{B}{}^0_d \to \overline{K}^{*0}\mu^+\mu^-$ MC.

q^2 range $((GeV/c^2)^2)$	PDF	$\sigma(F_L)$	$\sigma(S_3)$	$\sigma(S_i)$
$[0.04, 2.00]$	S_4	-0.001	0.000	-0.000
	S_5	-0.001	-0.000	0.000
	S_7	-0.001	0.000	-0.000
	S_8	-0.001	0.000	-0.000
$[2.00, 4.00]$	S_4	-0.003	0.001	-0.000
	S_5	0.008	0.002	0.004
	S_7	-0.003	-0.000	0.000
	S_8	-0.003	-0.000	0.000
$[4.00, 6.00]$	S_4	-0.007	-0.009	0.001
	S_5	-0.006	-0.000	-0.001
	S_7	-0.006	-0.000	0.000
	S_8	-0.006	-0.000	-0.000
$[0.04, 4.00]$	S_4	-0.001	0.002	0.000
	S_5	-0.002	-0.000	0.000
	S_7	-0.002	0.000	0.000
	S_8	-0.001	0.000	0.000
$[1.10, 6.00]$	S_4	-0.004	-0.003	0.001
	S_5	-0.003	-0.000	-0.000
	S_7	-0.003	-0.000	0.000
	S_8	-0.003	-0.000	0.000
$[0.04, 6.00]$	S_4	-0.003	-0.001	0.000
	S_5	-0.003	-0.000	0.000
	S_7	-0.003	-0.000	0.000
	S_8	-0.003	-0.000	0.000

C.9 Acceptance functions

TABLE C.9: The systematic uncertainties from the phase space signal MC derived acceptance functions.

q^2 range $((GeV/c^2)^2)$	PDF	$\sigma(F_L)$	$\sigma(S_3)$	$\sigma(S_i)$
$[0.04, 2.00]$	S_4	0.003	0.000	-0.051
	S_5	0.003	-0.001	0.001
	S_7	0.003	-0.001	0.000
	S_8	0.003	-0.001	-0.002
$[2.00, 4.00]$	S_4	0.008	0.001	-0.070
	S_5	0.007	0.003	0.001
	S_7	0.007	0.003	0.000
	S_8	0.007	0.003	-0.001
$[4.00, 6.00]$	S_4	0.014	0.002	-0.069
	S_5	0.013	0.005	-0.004
	S_7	0.013	0.005	-0.000
	S_8	0.013	0.005	0.003
$[0.04, 4.00]$	S_4	0.006	0.001	-0.062
	S_5	0.006	0.001	0.001
	S_7	0.006	0.001	0.000
	S_8	0.006	0.001	-0.001
$[1.10, 6.00]$	S_4	0.010	0.001	-0.068
	S_5	0.010	0.003	-0.001
	S_7	0.010	0.003	-0.000
	S_8	0.010	0.003	0.001
$[0.04, 6.00]$	S_4	0.009	0.001	-0.065
	S_5	0.009	0.002	-0.001
	S_7	0.009	0.002	0.000
	S_8	0.009 1	0.002	0.000

C.10 Mass Fit Range

TABLE C.10: The systematic uncertainties associated with varying the mass fit range. The results show the difference between the nominal angular fit results and fit results when the tighter mass range $[5200, 5700]$ MeV/c^2 was imposed.

q^2 range $((GeV/c^2)^2)$	PDF	$\sigma(F_L)$	$\sigma(S_3)$	$\sigma(S_i)$
$[0.04, 2.00]$	S_4	-0.000	-0.004	0.005
	S_5	-0.003	-0.001	-0.026
	S_7	0.004	0.001	-0.010
	S_8	0.014	-0.008	0.026
$[2.00, 4.00]$	S_4	-0.011	-0.054	0.007
	S_5	-0.007	-0.055	-0.027
	S_7	-0.007	-0.051	0.040
	S_8	0.008	-0.050	0.050
$[4.00, 6.00]$	S_4	0.020	0.032	0.009
	S_5	0.005	0.037	0.056
	S_7	0.013	0.049	0.052
	S_8	0.034	0.051	0.030
$[0.04, 4.00]$	S_4	0.003	-0.029	0.018
	S_5	0.004	-0.030	-0.027
	S_7	0.004	-0.030	0.024
	S_8	0.008	-0.032	0.015
$[1.10, 6.00]$	S_4	0.012	-0.007	-0.002
	S_5	0.010	-0.006	0.006
	S_7	0.014	-0.002	0.039
	S_8	0.027	-0.002	0.039
$[0.04, 6.00]$	S_4	0.007	-0.012	0.003
	S_5	0.007	-0.014	0.005
	S_7	0.007	-0.008	0.033
	S_8	0.016	-0.009	0.032

Appendix D

Fits to Data

This Chapter documents the B mass and helicity angle fits to data. The values of F_L, S_3 and S_i fitted for the four different folded PDFS are shown in Table 9.2 for each q^2 bin, where the dilution is also accounted for.

The fitted mass, $\cos\theta_L$, $\cos\theta_K$ and ϕ distributions are shown for the S_4 folded analysis in Figures 9.1 through 9.4 in Chapter 9, where a discussion of the results is also given.

The equivalent distributions are shown in Figures D.1 - D.4, D.5 - D.8 and D.9 - D.12 for the S_5, S_7 and S_8 PDFs, respectively. The same trends are observed in the fitted observables for all PDFs.

S_5 PDF results

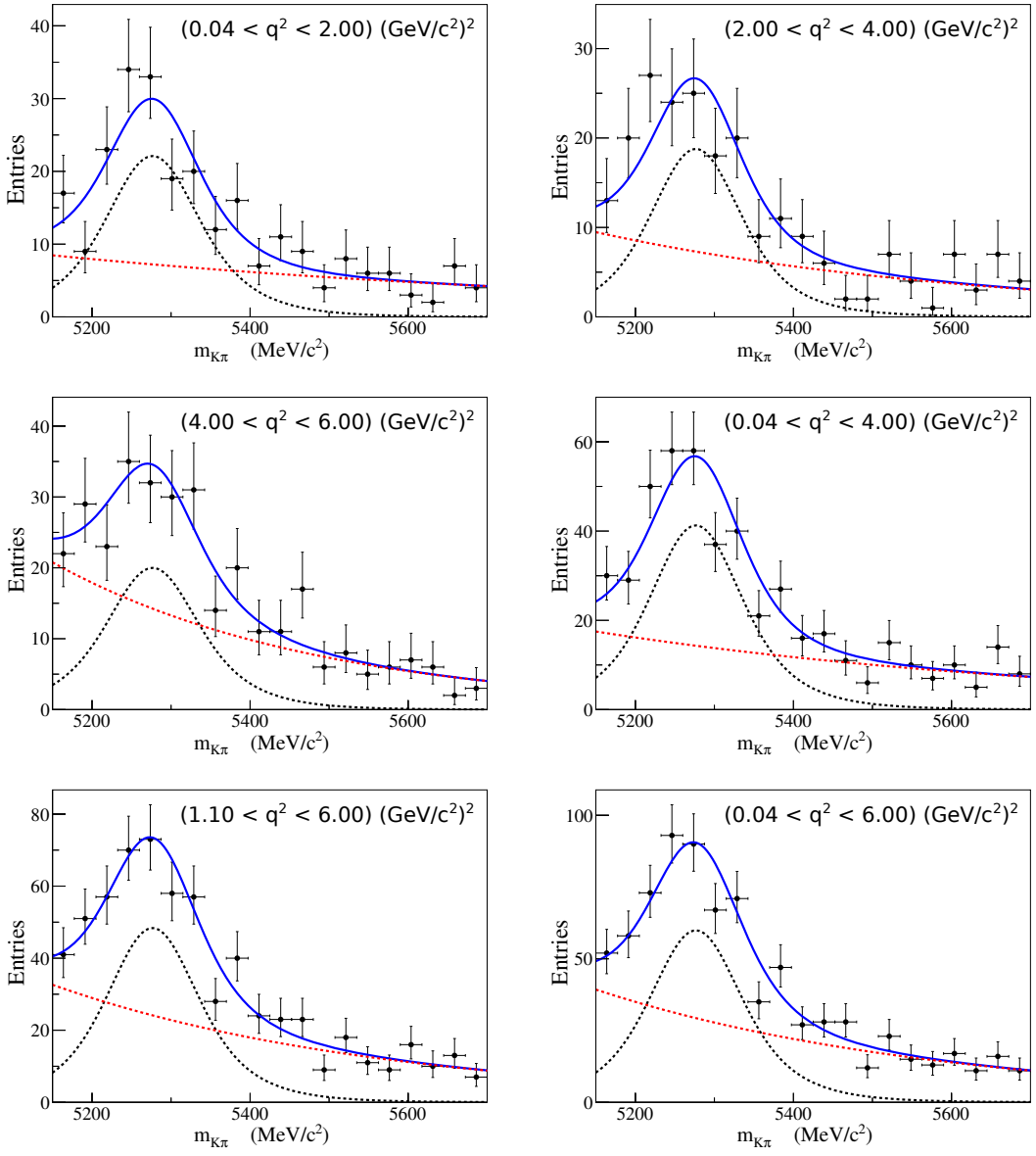

FIGURE D.1: Mass fits to data using the S_5 folded PDF for q^2 bins $[0.04, 2.00]$ $(GeV/c^2)^2$ (top-left), $[2.00, 4.00]$ $(GeV/c^2)^2$ (top-right), $[4.00, 6.00]$ $(GeV/c^2)^2$ (middle-left), $[0.04, 4.00]$ $(GeV/c^2)^2$ (middle-right), $[1.10, 6.00]$ $(GeV/c^2)^2$ (bottom-left) and $[0.04, 6.00]$ $(GeV/c^2)^2$ (bottom-right). The black (dashed) line corresponds to the fitted signal, the red (dashed) line to the combinatorial background and the blue (solid) line to the total fitted PDF.

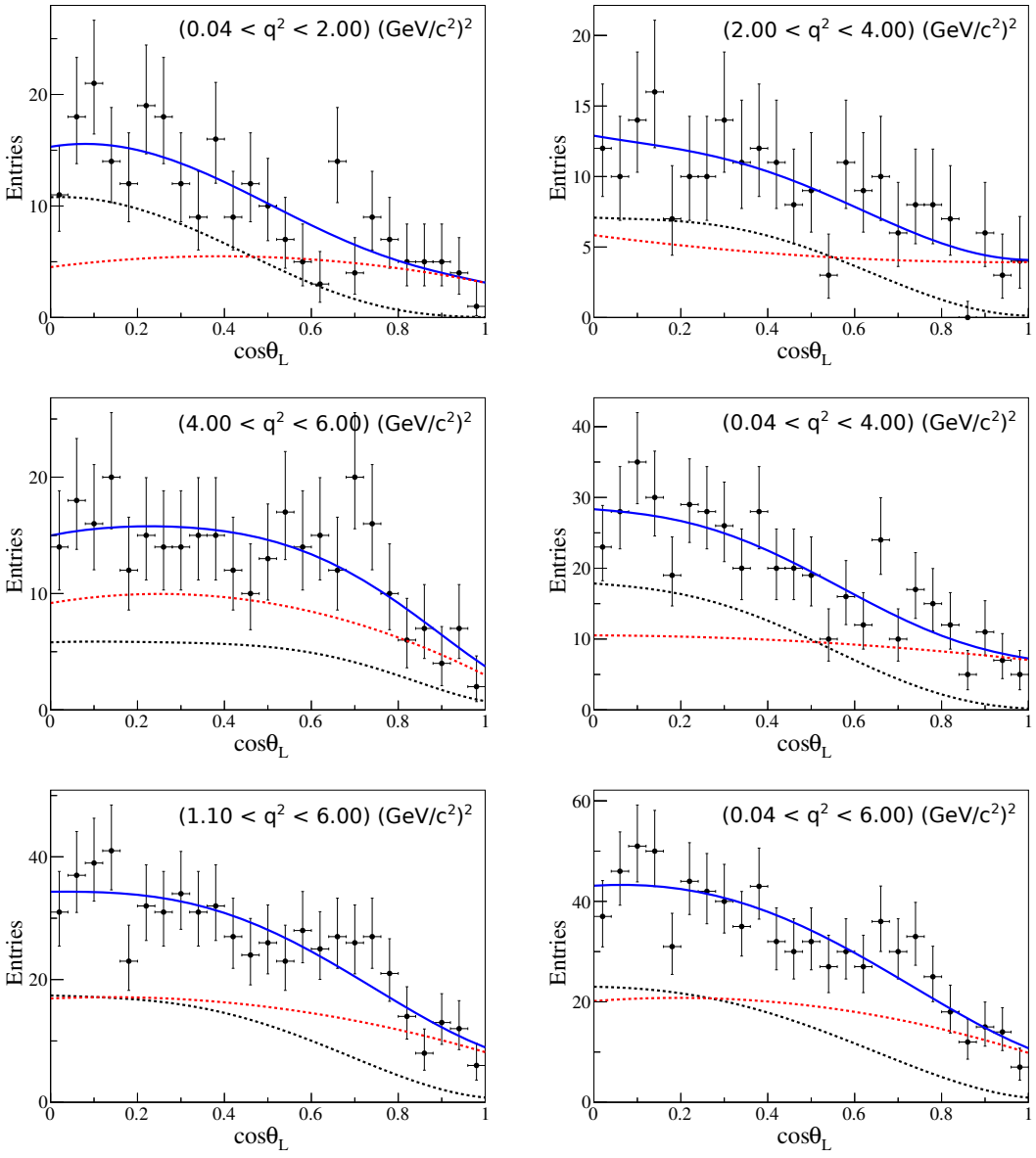

FIGURE D.2: The $\cos\theta_L$ projection from angular fits to data using the S_5 folded PDF for q^2 bins $[0.04, 2.00]$ $(GeV/c^2)^2$ (top-left), $[2.00, 4.00]$ $(GeV/c^2)^2$ (top-right), $[4.00, 6.00]$ $(GeV/c^2)^2$ (middle-left), $[0.04, 4.00]$ $(GeV/c^2)^2$ (middle-right), $[1.10, 6.00]$ $(GeV/c^2)^2$(bottom-left) and $[0.04, 6.00]$ $(GeV/c^2)^2$(bottom-right). The black (dashed) line corresponds to the fitted signal, the red (dashed) line to the combinatorial background and the blue (solid) line to the total fitted PDF.

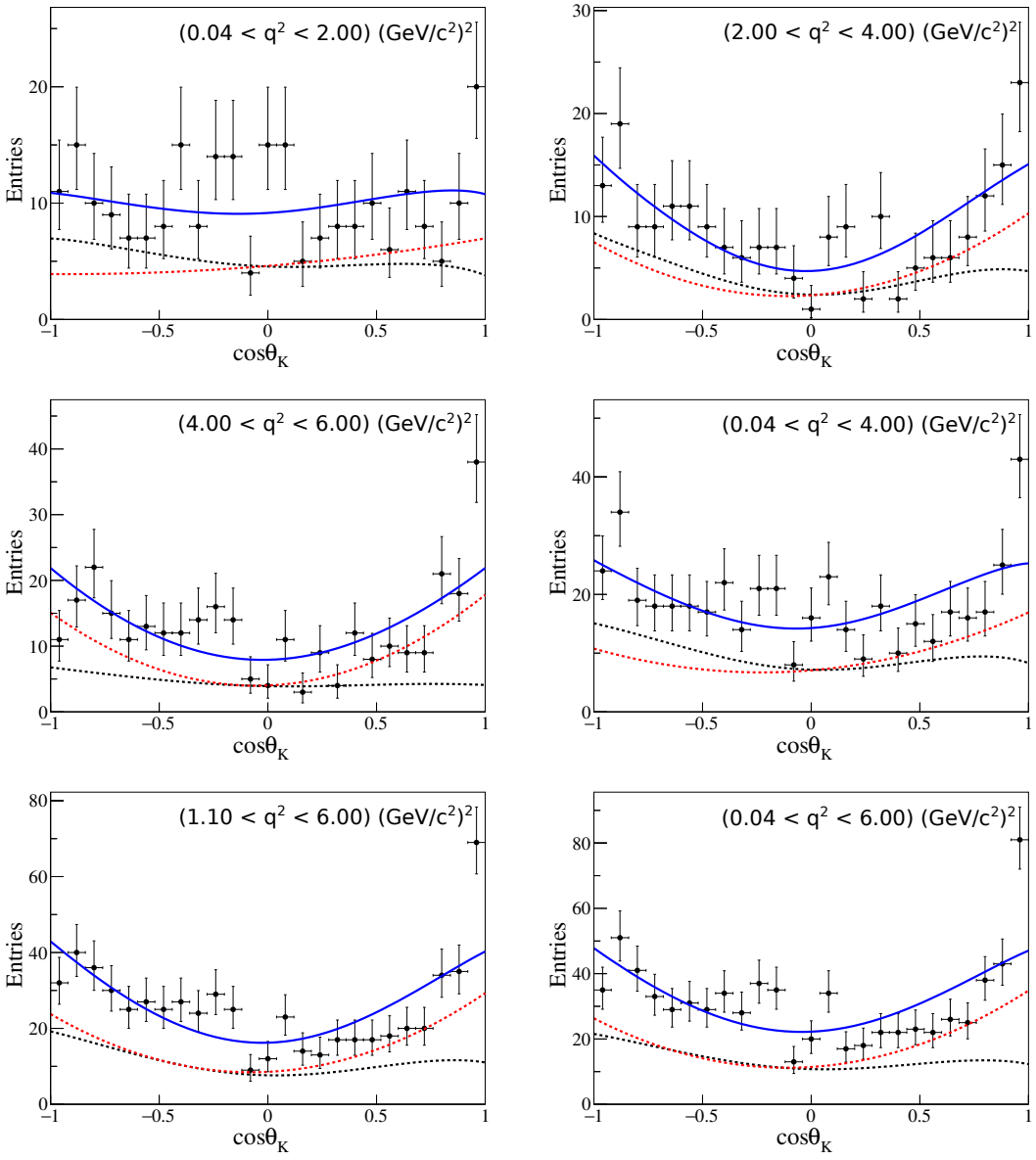

FIGURE D.3: The $\cos\theta_K$ projection from angular fits to data using the S_5 folded PDF for q^2 bins $[0.04, 2.00]$ $(GeV/c^2)^2$ (top-left), $[2.00, 4.00]$ $(GeV/c^2)^2$ (top-right), $[4.00, 6.00]$ $(GeV/c^2)^2$ (middle-left), $[0.04, 4.00]$ $(GeV/c^2)^2$ (middle-right), $[1.10, 6.00]$ $(GeV/c^2)^2$ (bottom-left) and $[0.04, 6.00]$ $(GeV/c^2)^2$ (bottom-right). The black (dashed) line corresponds to the fitted signal, the red (dashed) line to the combinatorial background and the blue (solid) line to the total fitted PDF.

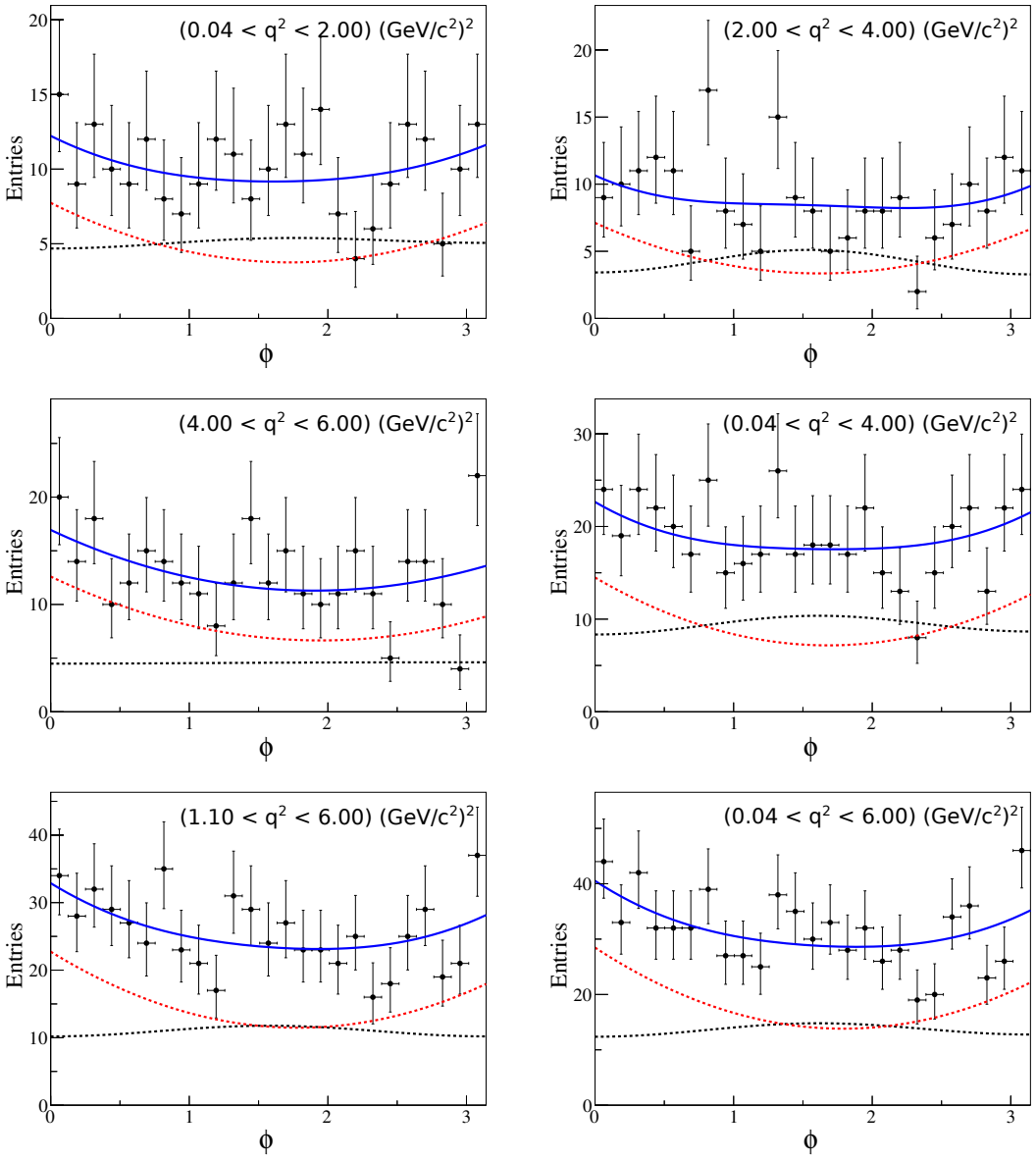

FIGURE D.4: The ϕ projection from angular fits to data using the S_5 folded PDF for q^2 bins $[0.04, 2.00]$ $(GeV/c^2)^2$ (top-left), $[2.00, 4.00]$ $(GeV/c^2)^2$ (top-right), $[4.00, 6.00]$ $(GeV/c^2)^2$ (middle-left), $[0.04, 4.00]$ $(GeV/c^2)^2$ (middle-right), $[1.10, 6.00]$ $(GeV/c^2)^2$ (bottom-left) and $[0.04, 6.00]$ $(GeV/c^2)^2$ (bottom-right). The black (dashed) line corresponds to the fitted signal, the red (dashed) line to the combinatorial background and the blue (solid) line to the total fitted PDF.

S_7 PDF results

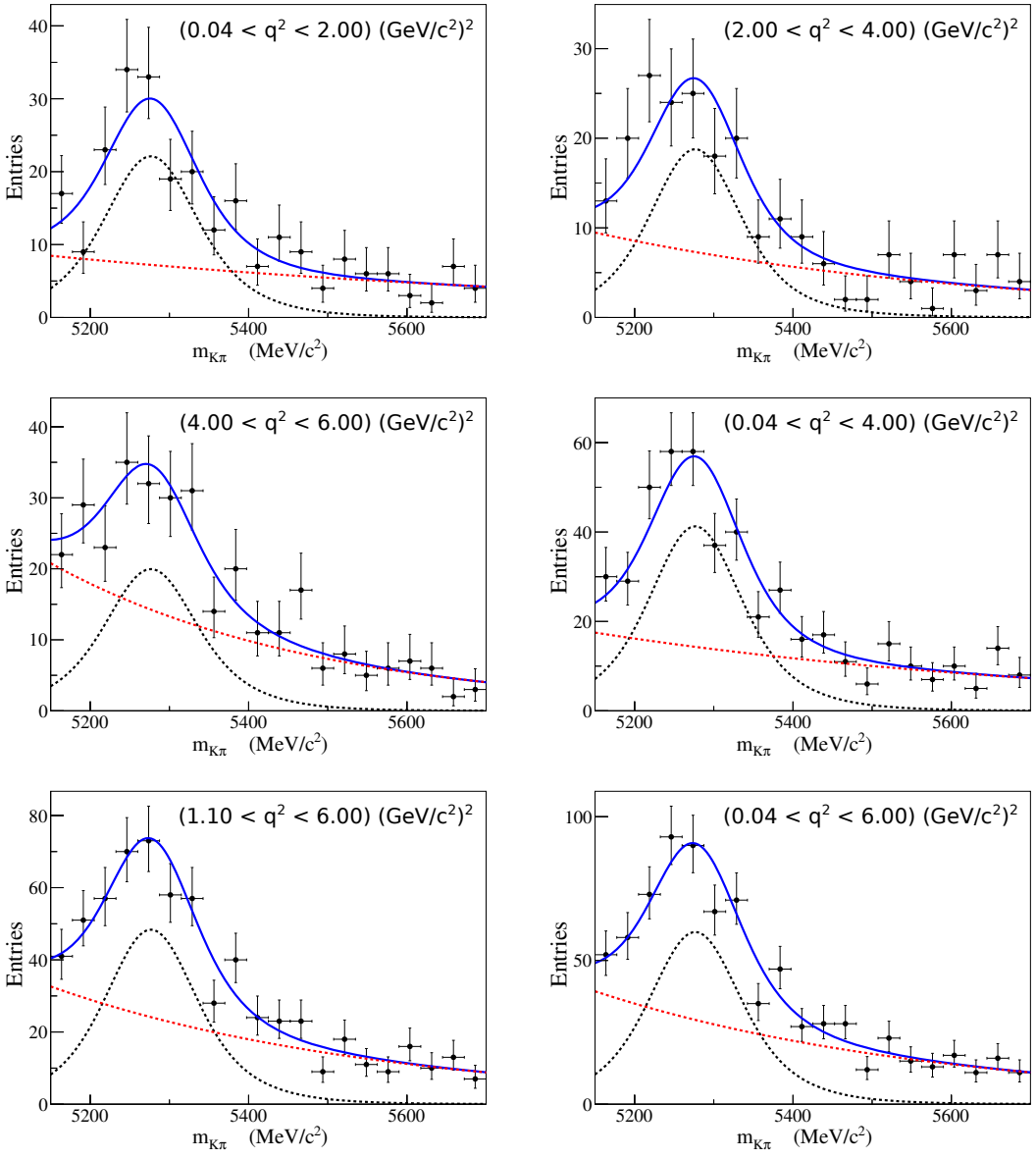

FIGURE D.5: Mass fits to data using the S_7 folded PDF for q^2 bins $[0.04, 2.00]$ $(GeV/c^2)^2$ (top-left), $[2.00, 4.00]$ $(GeV/c^2)^2$ (top-right), $[4.00, 6.00]$ $(GeV/c^2)^2$ (middle-left), $[0.04, 4.00]$ $(GeV/c^2)^2$ (middle-right), $[1.10, 6.00]$ $(GeV/c^2)^2$ (bottom-left) and $[0.04, 6.00]$ $(GeV/c^2)^2$ (bottom-right). The black (dashed) line corresponds to the fitted signal, the red (dashed) line to the combinatorial background and the blue (solid) line to the total fitted PDF.

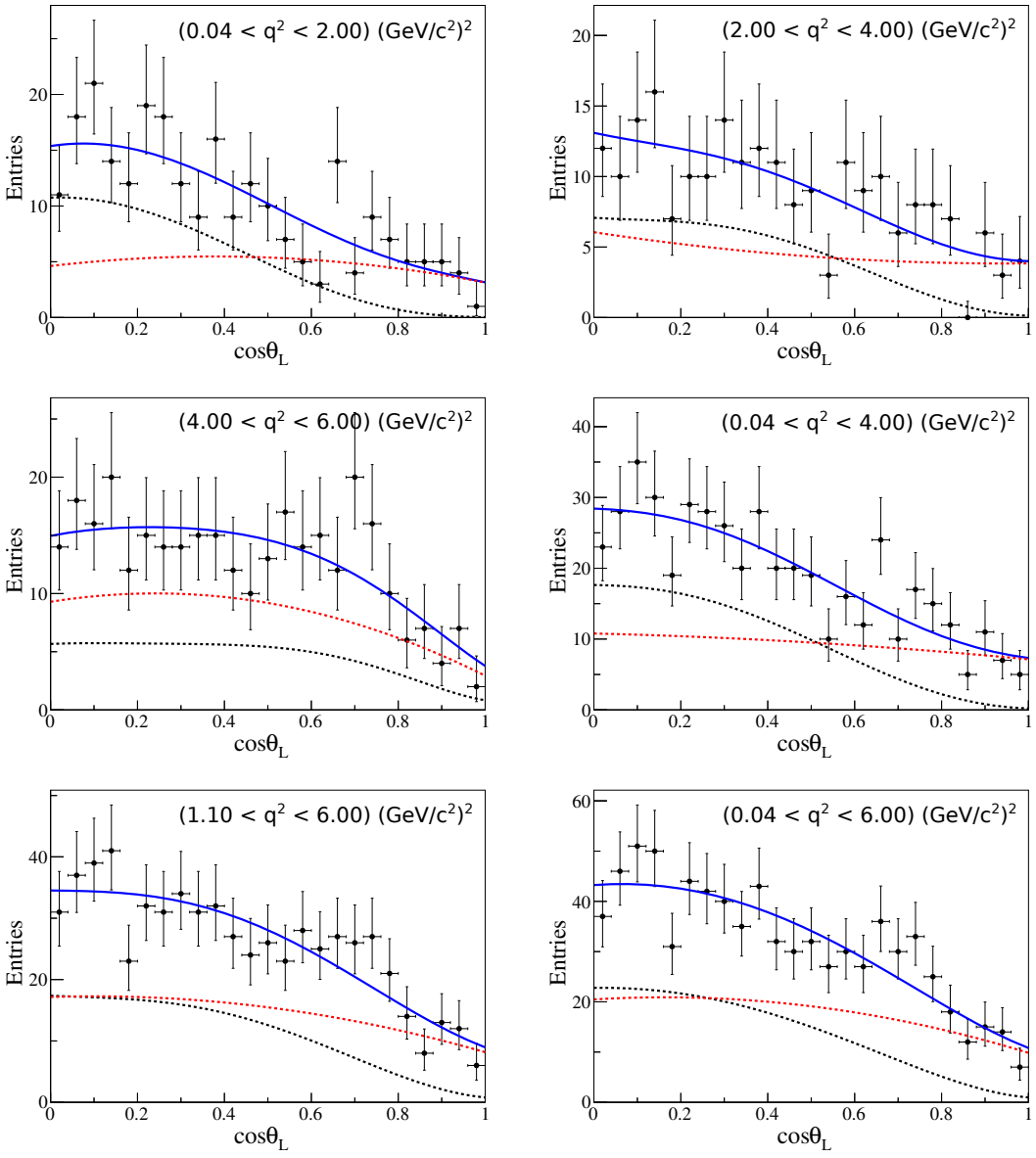

FIGURE D.6: The $\cos\theta_L$ projection from angular fits to data using the S_7 folded PDF for q^2 bins $[0.04, 2.00]$ $(GeV/c^2)^2$ (top-left), $[2.00, 4.00]$ $(GeV/c^2)^2$ (top-right), $[4.00, 6.00]$ $(GeV/c^2)^2$ (middle-left), $[0.04, 4.00]$ $(GeV/c^2)^2$ (middle-right), $[1.10, 6.00]$ $(GeV/c^2)^2$(bottom-left) and $[0.04, 6.00]$ $(GeV/c^2)^2$(bottom-right). The black (dashed) line corresponds to the fitted signal, the red (dashed) line to the combinatorial background and the blue (solid) line to the total fitted PDF.

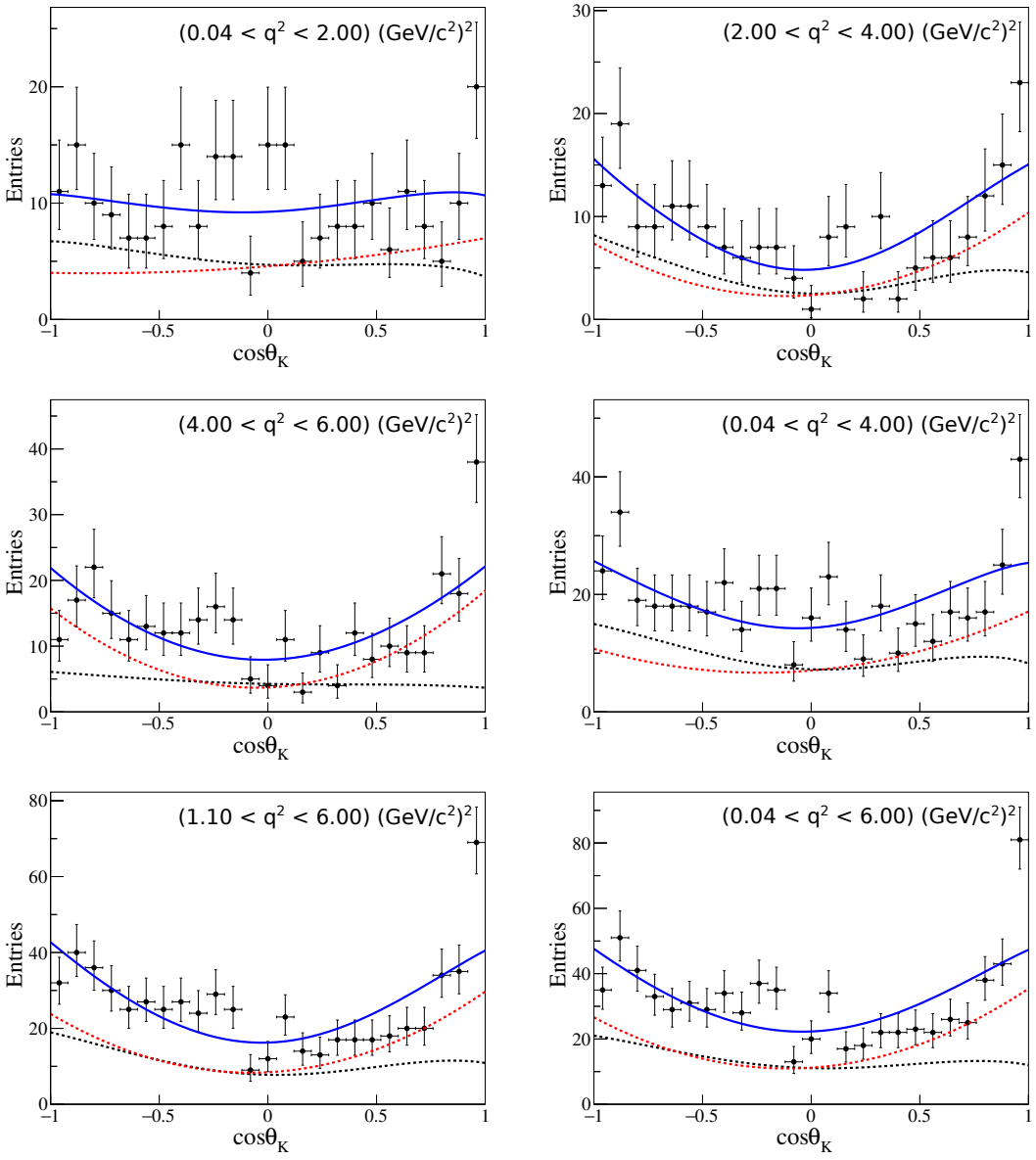

FIGURE D.7: The $\cos\theta_K$ projection from angular fits to data using the S_7 folded PDF for q^2 bins $[0.04, 2.00]$ $(GeV/c^2)^2$ (top-left), $[2.00, 4.00]$ $(GeV/c^2)^2$ (top-right), $[4.00, 6.00]$ $(GeV/c^2)^2$ (middle-left), $[0.04, 4.00]$ $(GeV/c^2)^2$ (middle-right), $[1.10, 6.00]$ $(GeV/c^2)^2$ (bottom-left) and $[0.04, 6.00]$ $(GeV/c^2)^2$ (bottom-right). The black (dashed) line corresponds to the fitted signal, the red (dashed) line to the combinatorial background and the blue (solid) line to the total fitted PDF.

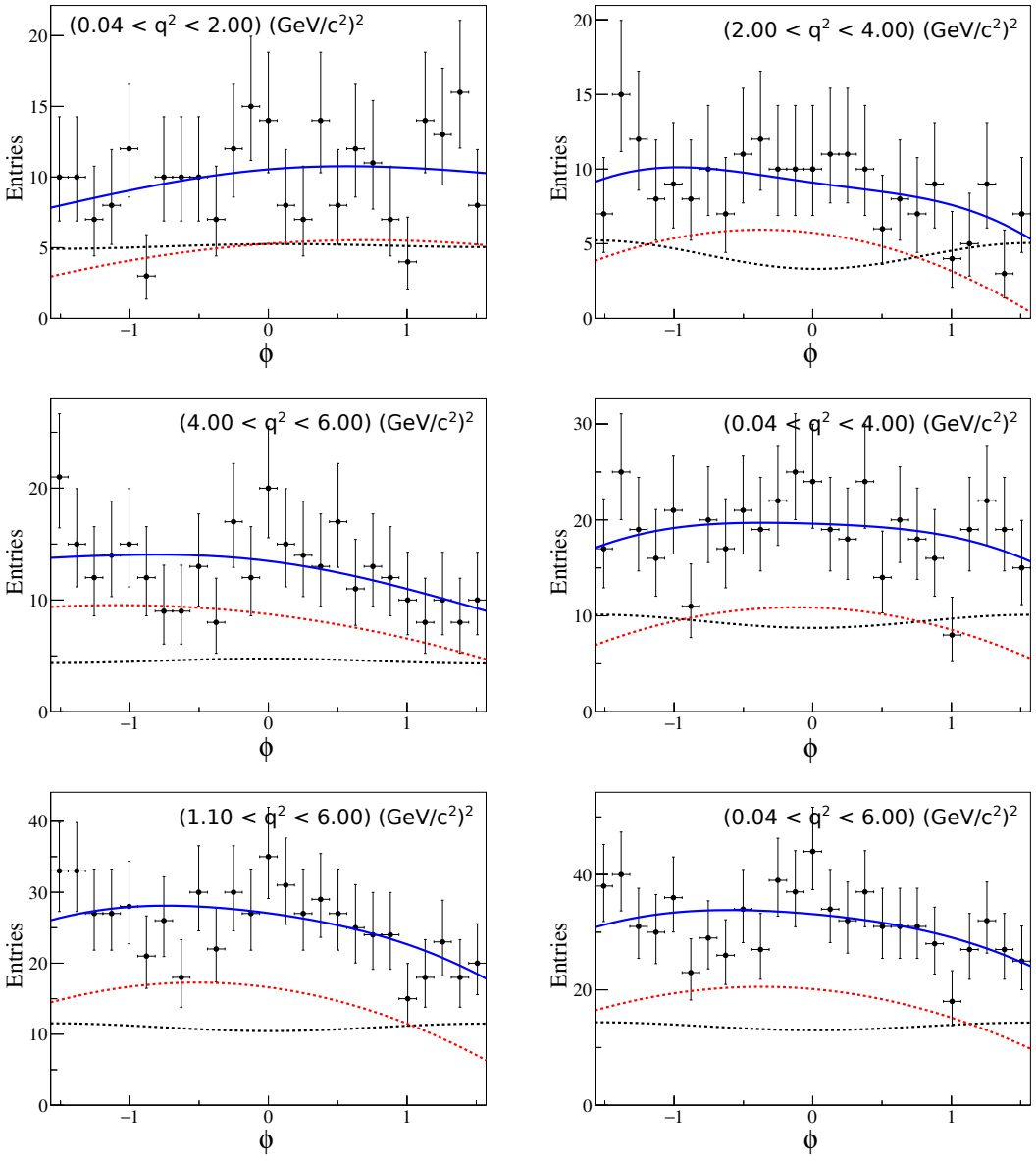

FIGURE D.8: The ϕ projection from angular fits to data using the S_7 folded PDF for q^2 bins $[0.04, 2.00]$ $(GeV/c^2)^2$ (top-left), $[2.00, 4.00]$ $(GeV/c^2)^2$ (top-right), $[4.00, 6.00]$ $(GeV/c^2)^2$ (middle-left), $[0.04, 4.00]$ $(GeV/c^2)^2$ (middle-right), $[1.10, 6.00]$ $(GeV/c^2)^2$ (bottom-left) and $[0.04, 6.00]$ $(GeV/c^2)^2$ (bottom-right). The black (dashed) line corresponds to the fitted signal, the red (dashed) line to the combinatorial background and the blue (solid) line to the total fitted PDF.

S_8 PDF results

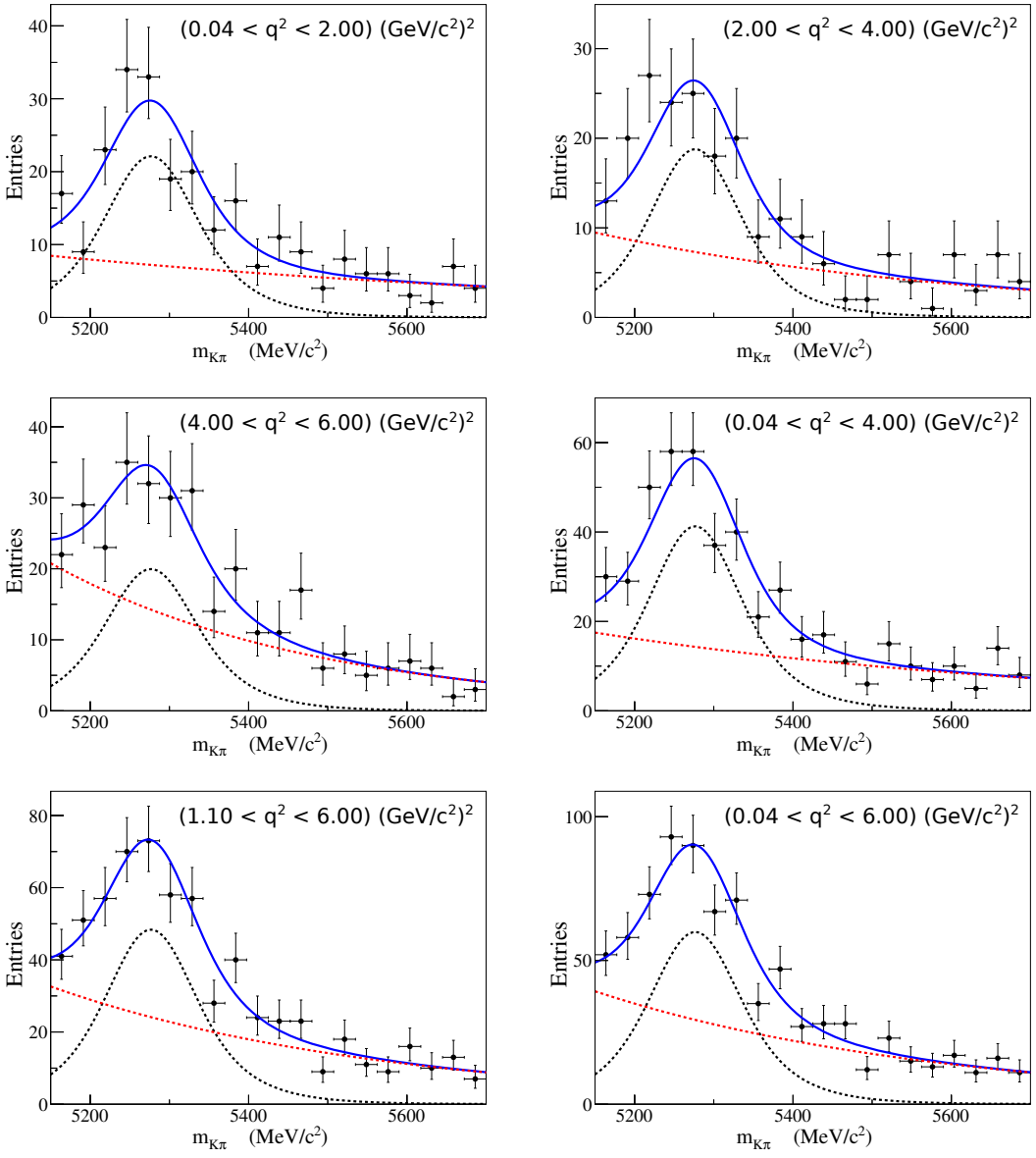

FIGURE D.9: Mass fits to data using the S_8 folded PDF for q^2 bins $[0.04, 2.00]$ $(GeV/c^2)^2$ (top-left), $[2.00, 4.00]$ $(GeV/c^2)^2$ (top-right), $[4.00, 6.00]$ $(GeV/c^2)^2$ (middle-left), $[0.04, 4.00]$ $(GeV/c^2)^2$ (middle-right), $[1.10, 6.00]$ $(GeV/c^2)^2$ (bottom-left) and $[0.04, 6.00]$ $(GeV/c^2)^2$ (bottom-right). The black (dashed) line corresponds to the fitted signal, the red (dashed) line to the combinatorial background and the blue (solid) line to the total fitted PDF.

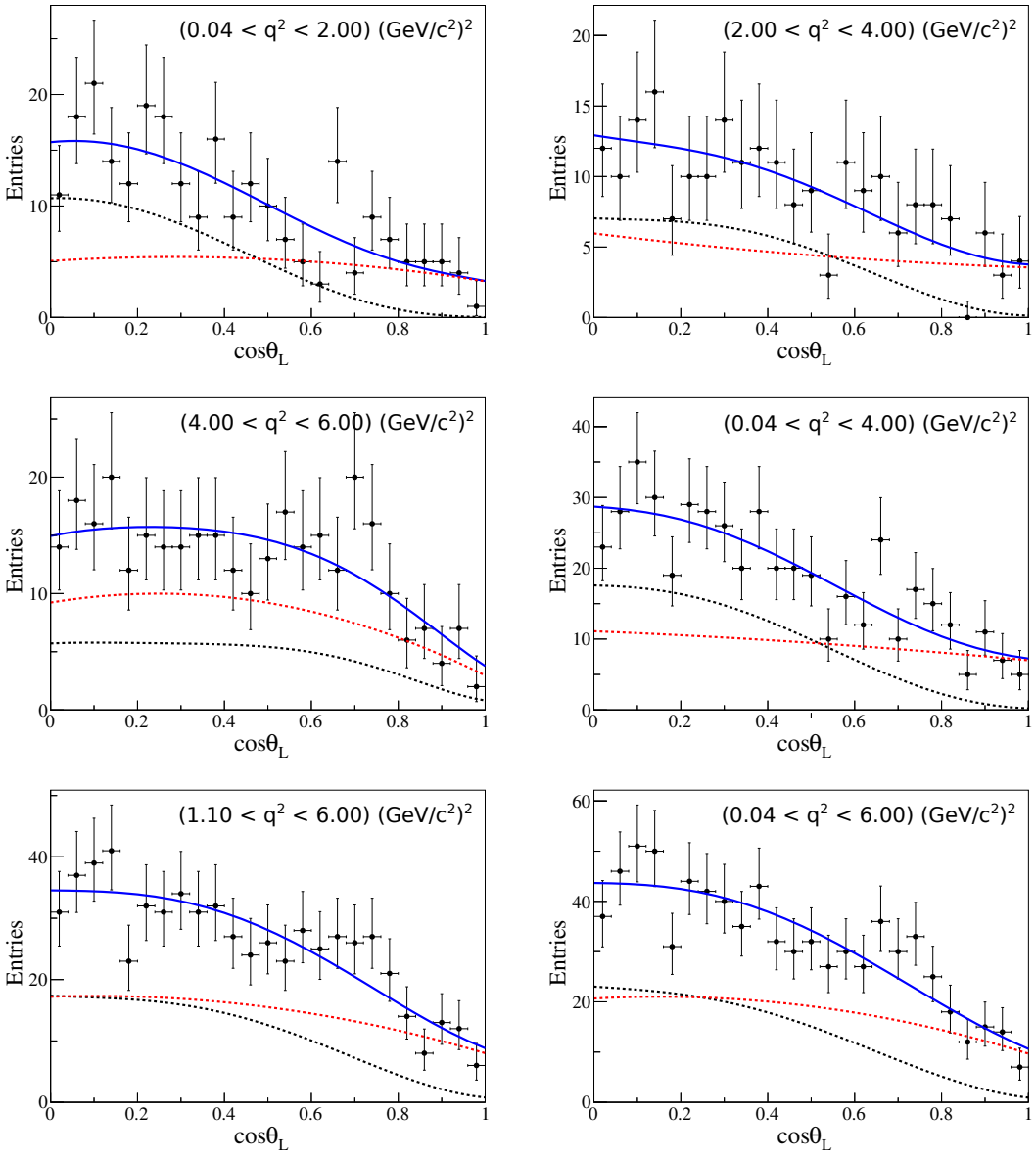

FIGURE D.10: The $\cos\theta_L$ projection from angular fits to data using the S_8 folded PDF for q^2 bins $[0.04, 2.00]$ $(GeV/c^2)^2$ (top-left), $[2.00, 4.00]$ $(GeV/c^2)^2$ (top-right), $[4.00, 6.00]$ $(GeV/c^2)^2$ (middle-left), $[0.04, 4.00]$ $(GeV/c^2)^2$ (middle-right), $[1.10, 6.00]$ $(GeV/c^2)^2$(bottom-left) and $[0.04, 6.00]$ $(GeV/c^2)^2$(bottom-right). The black (dashed) line corresponds to the fitted signal, the red (dashed) line to the combinatorial background and the blue (solid) line to the total fitted PDF.

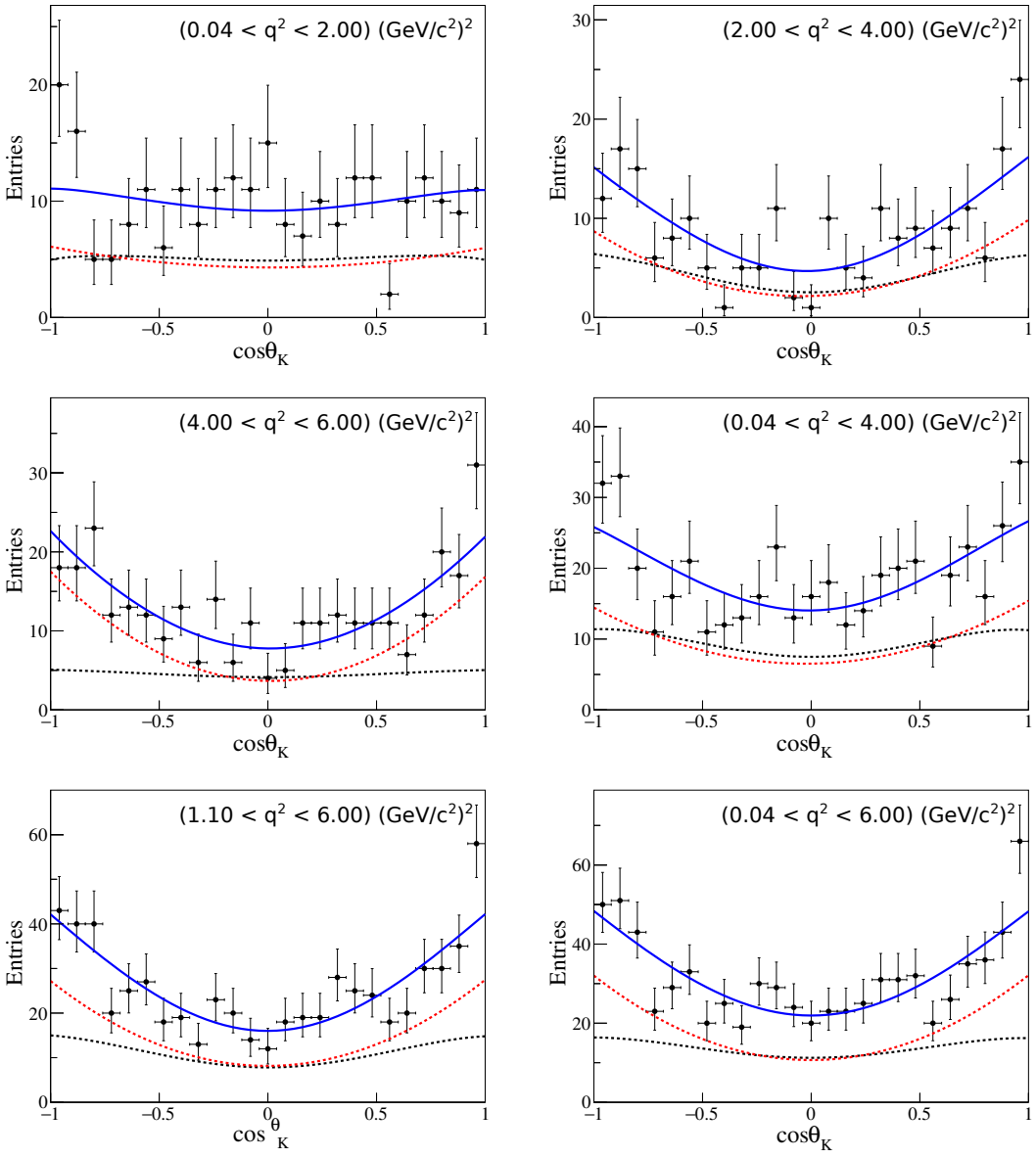

FIGURE D.11: The $\cos\theta_K$ projection from angular fits to data using the S_8 folded PDF for q^2 bins $[0.04, 2.00]$ $(GeV/c^2)^2$ (top-left), $[2.00, 4.00]$ $(GeV/c^2)^2$ (top-right), $[4.00, 6.00]$ $(GeV/c^2)^2$ (middle-left), $[0.04, 4.00]$ $(GeV/c^2)^2$ (middle-right), $[1.10, 6.00]$ $(GeV/c^2)^2$ (bottom-left) and $[0.04, 6.00]$ $(GeV/c^2)^2$ (bottom-right). The black (dashed) line corresponds to the fitted signal, the red (dashed) line to the combinatorial background and the blue (solid) line to the total fitted PDF.

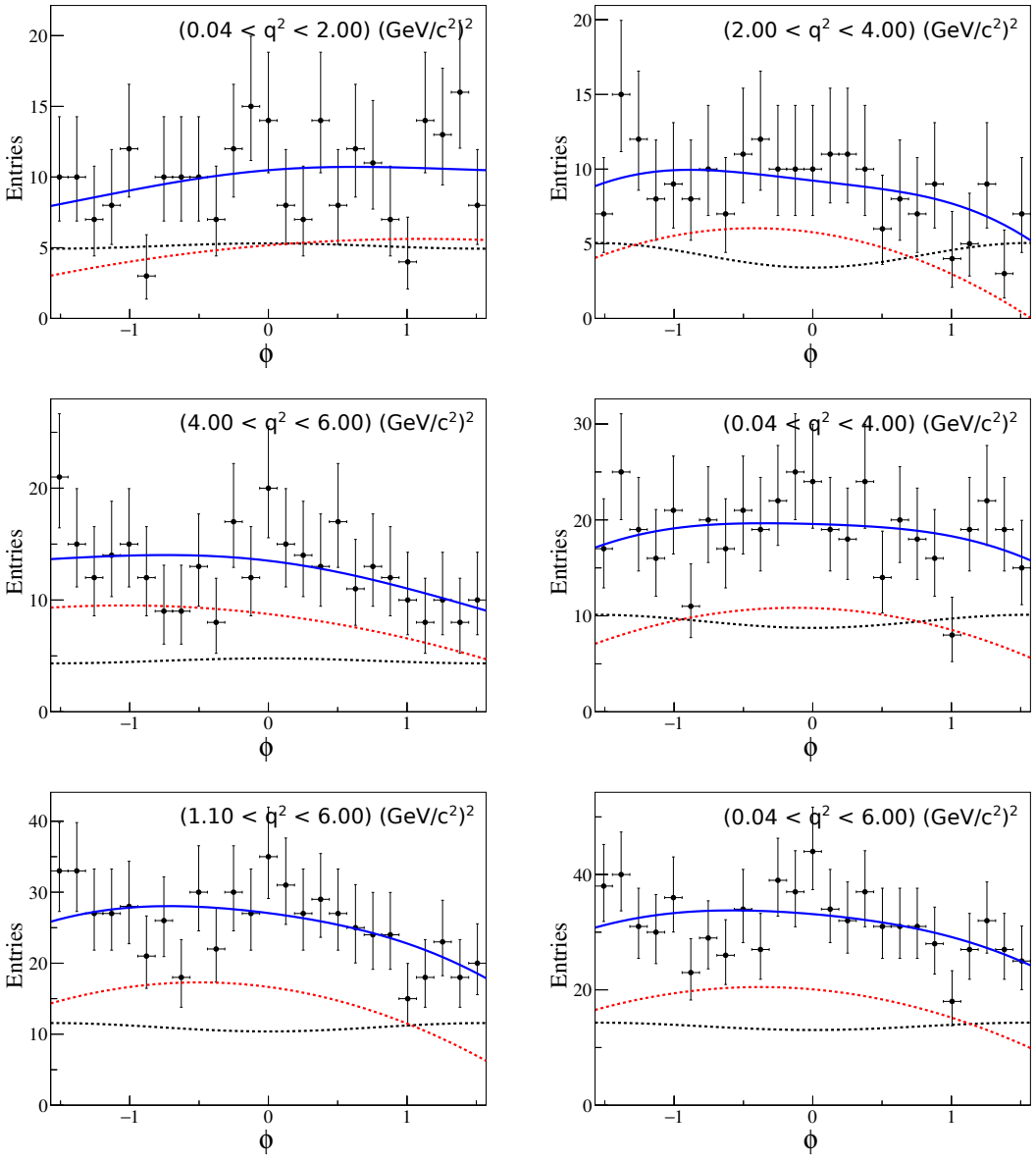

FIGURE D.12: The ϕ projection from angular fits to data using the S_8 folded PDF for q^2 bins $[0.04, 2.00]$ $(GeV/c^2)^2$ (top-left), $[2.00, 4.00]$ $(GeV/c^2)^2$ (top-right), $[4.00, 6.00]$ $(GeV/c^2)^2$ (middle-left), $[0.04, 4.00]$ $(GeV/c^2)^2$ (middle-right), $[1.10, 6.00]$ $(GeV/c^2)^2$ (bottom-left) and $[0.04, 6.00]$ $(GeV/c^2)^2$ (bottom-right). The black (dashed) line corresponds to the fitted signal, the red (dashed) line to the combinatorial background and the blue (solid) line to the total fitted PDF.

Bibliography

[1] T. Y. Cao. Conceptual Developments of 20th Century Field Theories. pages 320–321. Cambridge University Press, (1997).

[2] C. Quigg. The State of the Standard Model. In *AIP Conf. Proc.*, volume 542, pages 3–28. AIP, (2000).

[3] R. Englert, F., Brout. Broken Symmetry and the Mass of Gauge Vector Mesons. *Phys. Rev. Lett.*, **13**:321–323, (1964).

[4] P. Higgs. Broken Symmetries and the Masses of Gauge Bosons. *Phys. Rev. Lett.*, **13**:508–509, (1964).

[5] T. Guralnik, G.S., Hagen, C.R., Kibble. Global Conservation Laws and Massless Particles. *Phys. Rev. Lett.*, **13**:585–587, (1964).

[6] LHC Collaboration. LHC Design Report. *LHC Infrastruct. Gen. Serv.*, **2**, (2004).

[7] CMS Collaboration. Observation of a new boson at a mass of 125 GeV with the CMS experiment at the LHC. *Phys. Lett. B*, **716**(1):30–61, (2012).

[8] ATLAS Collaboration. Observation of a new particle in the search for the Standard Model Higgs boson with the ATLAS detector at the LHC. *Phys. Lett. B*, **716**(1):1–29, (2012).

[9] Nobelprize.org. The 2013 Nobel Prize in Physics - Press Release, (2014).

[10] CDF and D0 Collaborations. Combination of CDF and D0 W-Boson Mass Measurements. *Phys. Rev. D*, **88**(5):052018, (2013).

[11] S. Schael, R. Barate, R. Brunelière, et al. Precision electroweak measurements on the Z resonance. *Phys. Rep.*, **427**(5-6):257–454, (2006).

[12] D. Hanneke, S. Fogwell Hoogerheide, and G. Gabrielse. Cavity control of a single-electron quantum cyclotron: Measuring the electron magnetic moment. *Phys. Rev. A*, **83**(5):052122, (2011).

[13] Planck Collaboration, R. Adam, P. A. R. Ade, et al. Planck 2013 results. I. Overview of products and scientific results. *Astron. Astrophys.*, **571**:A1, (2013).

[14] M. Bona, J. Garra Tico, E. Grauges Pous, et al. SuperB, A High-Luminosity Heavy Flavour Factory. Technical report, (2007).

[15] F. Wilson. Arachnid Project. *https//www.spider.ac.uk/display/arachnid [Accessed 12 Nov 2014]*., (2012).

[16] J. Mylroie-Smith, S. Kolya, J. Velthuis, et al. First tests of CHERWELL, a Monolithic Active Pixel Sensor: A CMOS Image Sensor (CIS) using 180nm technology. *Nucl. Instruments Methods Phys. Res. Sect. A Accel. Spectrometers, Detect. Assoc. Equip.*, **731**:137–140, (2013).

[17] T. Nooney, S. Kolya, J. Velthuis, et al. First Results from Cherwell, a Monolithic Active Pixel Sensor for Particle Physics. In *Eur. Phys. Soc. Conf. High Energy Phys.*, page 507, (2013).

[18] ATLAS Collaboration. The ATLAS Experiment at the CERN Large Hadron Collider. *J. Instrum.*, **3**, (2008).

[19] K.A. Olive et al. (Particle Data Group). Review of Particle Physics. *Chin. Phys. C*, **38**(9), (2015).

[20] Nobelprize.org. The 2015 Nobel Prize in Physics - Press Release, (2016).

[21] E. Noether. Invariante Variationsprobleme. *Nachr. D. König. Gesellsch. D. Wiss. Zu Göttingen, Math-phys. Klasse.*, (1918).

[22] L. M. S. L. Glashow, J. Iliopoulos. Weak Interactions with Lepton-Hadron Symmetry. *Phys. Rev. D*, **2**:1285, (1970).

[23] Nicola Cabibbo. Unitary Symmetry and Leptonic Decays. *Phys. Rev. Lett.*, **10**:531, (1963).

[24] Nicola Cabibbo. Unitary Symmetry and Nonleptonic Decays. *Phys. Rev. Lett.*, **12**:62, (1964).

[25] M. Kobayashi and T. Maskawa. CP Violation in the Renormalizable Theory of Weak Interaction. *Prog. Theor. Phys.*, **49**:652, (1973).

[26] L.-L. Chau and W.-Y. Keung. Comments on the Parametrization of the Kobayashi-Maskawa Matrix. *Phys. Rev. Lett.*, **53**:1802, (1984).

[27] F. Krüger, L. M. Sehgal, N. Sinha, and R. Sinha. Angular Distribution and CP Asymmetries in the Decays $B^0 \to K^-\pi^+e^-e^+$ and $B^0 \to \pi^-\pi^+e^-e^+$. *Phys. Rev. D*, **61**:114028, (2000).

[28] C. Bobeth, M. Misiak, and J. Urban. Photonic penguins at two loops and m_t-dependence of BR$[B \to X_s l^+l^-]$. *Nucl. Phys. B*, **574**(1-2):291–330, (2000).

[29] W. Altmannshofer, P. Ball, A. Bharucha, et al. Symmetries and Asymmetries of $B \to K^*\mu^+\mu^-$ Decays in the Standard Model and Beyond. *J. High Energy Phys.*, **0901**:019, (2009).

[30] W. Altmannshofer and D. M. Straub. New physics in $b \to s$ transitions after LHC run 1. *Eur. Phys. J. C*, **75**(8):382, (2015).

[31] F. Krüger and J. Matias. Probing new physics via the transverse amplitudes of of $B^0 \to K^{*0}(\to K^-\pi^+)l^+l^-$ at Large Recoil. *Phys. Rev. D*, **71**(9):094009, (2005).

[32] S. Descotes-Genon, T. Hurth, J. Matias, and J. Virto. Optimizing the basis of $B \to K^*ll$ observables in the full kinematic range. *J. High Energy Phys.*, **1305**:137, (2013).

[33] S. Descotes-Genon, J. Matias, M. Ramon, and J. Virto. Implications from clean observables for the binned analysis of $B \to K^*ll$ at large recoil. *J. High Energy Phys.*, **1301**:048, (2013).

[34] T. Blake, T. Gershon, and G. Hiller. Rare b hadron decays at the LHC. *Annu. Rev. Nucl. Part. Sci.*, **65**:113, (2015).

[35] B. Grinstein and D. Pirjol. Exclusive rare $B \to K^*e^+e^-$ decays at low recoil: controlling the long-distance effects. *Phys. Rev. D*, **70**:114005, (2004).

[36] A. Ali, P. Ball, L. T. Handoko, and G. Hiller. A Comparative Study of the Decays $B \to (K, K^*)l^+l^-$ in Standard Model and Supersymmetric Theories. *Phys. Rev. D*, **61**:074024, (2000).

[37] R. Aaij, B. Adeva, M. Adinolfi, et al. Measurement of Form-Factor-Independent Observables in the Decay $B^0 \to K^{*0}\ \mu^+\ \mu^-$. *Phys. Rev. Lett.*, **111**(19):191801, (2013).

[38] BaBar Collaboration. Measurement of Angular Asymmetries in the Decays $B \to K^0 l^+ l^-$. *Phys. Rev. D*, **93**:052015, (2016).

[39] CMS Collaboration. Angular analysis of the decay $B^0 \to K^0 \mu^+ \mu^-$ from pp collisions at $\sqrt{s} = 8$ TeV. *Phys. Lett. B*, **753**:424–448, (2016).

[40] LHCb Collaboration. Angular analysis of the $B^0 \to K^{*0} \mu^+ \mu^-$ decay using $3\,\mathrm{fb}^{-1}$ of integrated luminosity. *J. High Energy Phys.*, **02**:104, (2016).

[41] Belle Collaboration, A. Abdesselam, I. Adachi, et al. Angular analysis of $B^0 \to K^*(892)^0 \ell^+ \ell^-$. *BELLE-CONF-1603*, (2016).

[42] S. Descotes-Genon, L. Hofer, J. Matias, and J. Virto. On the impact of power corrections in the prediction of $B \to K^* \mu^+ \mu^-$ observables. *J. High Energy Phys.*, **12**:125, (2014).

[43] S. Descotes-Genon, L. Hofer, J. Matias, and J. Virto. Global analysis of $b \to s\ell\ell$ anomalies. *J. High Energy Phys.*, **1606**:092, (2016).

[44] S. Jäger and J. M. Camalich. Reassessing the discovery potential of the $B \to K^* l^+ l^-$ decays in the large-recoil region: SM challenges and BSM opportunities. *Phys. Rev. D*, **93**:014028, (2016).

[45] M. Ciuchini, M. Fedele, E. Franco, et al. $B \to K^* \ell^+ \ell^-$ decays at large recoil in the Standard Model: a theoretical reappraisal. *J. High Energy Phys.*, **1606**:116, (2016).

[46] L. Evans and P. Bryant. LHC Machine. *J. Instrum.*, **3**(08):S08001–S08001, (2008).

[47] M. Schott and M. Dunford. Review of single vector boson production in pp collisions at $\sqrt{s} = 7$ TeV. *Eur. Phys. J. C*, **74**(7):2916, (2014).

[48] ATLAS Muon Collaboration. ATLAS Muon Detector Commissioning. In *Meet. Div. Part. Fields Am. Phys. Soc.*, pages 1–6, (2009).

[49] ATLAS Collaboration. Measurement of the Inelastic Proton-Proton Cross Section at with the ATLAS Detector. *ATLAS-CONF-2011-002*, (2011).

[50] ATLAS Collaboration. The ATLAS Inner Detector commissioning and calibration. *Eur. Phys. J. C*, **70**(3):787–821, (2010).

[51] G. Aad, M. Ackers, F. A. Alberti, et al. ATLAS pixel detector electronics and sensors. *J. Instrum.*, **3**(07):P07007–P07007, (2008).

[52] ATLAS Collaboration. Operation and performance of the ATLAS semiconductor tracker. *J. Instrum.*, **9**(08):P08009–P08009, (2014).

[53] ATLAS TRT Collaboration. The ATLAS Transition Radiation Tracker. *Astroparticle, Part. Sp. Physics, Detect. Med. Phys. Appl.*, **2**:497–501, (2003).

[54] S. Wakely, S. Plewnia, D. Müller, J. Hörandel, and F. Gahbauer. Transition radiation detectors for energy measurements at high Lorentz factors. *Nucl. Instruments Methods Phys. Res. Sect. A Accel. Spectrometers, Detect. Assoc. Equip.*, **531**(3):435–444, (2004).

[55] J. Colas, L. Di Ciaccio, M. El Kacimi, et al. Position resolution and particle identification with the ATLAS EM calorimeter. *Nucl. Instruments Methods Phys. Res. Sect. A Accel. Spectrometers, Detect. Assoc. Equip.*, **550**(1-2):96–115, (2005).

[56] M. Aharrouche, J. Colas, L. Di Ciaccio, et al. Energy linearity and resolution of the ATLAS electromagnetic barrel calorimeter in an electron test-beam. *Nucl. Instruments Methods Phys. Res. Sect. A Accel. Spectrometers, Detect. Assoc. Equip.*, **568**(2):601–623, (2006).

[57] A. Succurro. The ATLAS Tile Hadronic Calorimeter performance in the LHC Collision Era. *Proc. 2nd Int. Conf. Technol. Instrum. Part. Phys. (TIPP 2011)*, **37**:229–237, (2012).

[58] E. Diehl. Calibration and Performance of the ATLAS Muon Spectrometer. *Proc. DPF-2011 Conf.*, (2011).

[59] T. Argyropoulos, K. A. Assamagan, B. H. Benedict, et al. Cathode Strip Chambers in ATLAS: Installation, Commissioning and in Situ Performance. *IEEE Trans. Nucl. Sci.*, **56**(3):1568–1574, (2009).

[60] E. Etzion, Y. Benhammou, J. Ginzburg, et al. The certification of ATLAS thin gap chambers produced in Israel and China. *IEEE Symp. Conf. Rec. Nucl. Sci. 2004.*, **1**:236–241, (2004).

[61] Will Buttinger. The ATLAS Level-1 Trigger System. *J. Phys. Conf. Ser.*, **396**(1):012010, (2012).

[62] MJ Woudstra. Performance of the ATLAS muon trigger in pp collisions at $\sqrt{s} = 8$ TeV. *J. Phys. Conf. Ser.*, **513**:012040, (2014).

[63] D. Zeppenfeld. Standard Model at Hadron Colliders, (2005).

[64] T. Sjöstrand, S. Mrenna, and P. Skands. A Brief Introduction to PYTHIA 8.1. *Comput.Phys.Commun.*, **178**:852–867, (2008).

[65] J. Pumplin, D. R. Stump, J. Huston, et al. New Generation of Parton Distributions with Uncertainties from Global QCD Analysis. *J. High Energy Phys.*, **07**:012, (2002).

[66] ATLAS Collaboration. Summary of ATLAS Pythia 8 tunes. *ATL-PHYS-PUB-2012-003*, (2012).

[67] D. J. Lange. The EvtGen particle decay simulation package. *Nucl. Instrum. Meth. A*, **462**:152, (2001).

[68] S. Agostinelli, J. Allison, K. Amako, et al. Geant4 - a simulation toolkit. *Nucl. Instruments Methods Phys. Res. A*, **506**(3):250–303, (2003).

[69] W. Lukas. Fast Simulation for ATLAS: Atlfast-II and ISF. In *Comput. High Energy Nucl. Phys.*, page 022031, (2012).

[70] K. Edmonds, S. Fleischmann, T. Lenz, et al. The fast ATLAS track simulation (FATRAS). *ATL-SOFT-PUB-2008-001*, **002**, (2008).

[71] ATLAS Collaboration. The ATLAS Simulation Infrastructure. *Eur. Phys. J. C*, **70**:823–874, (2010).

[72] ATLAS Collaboration. The simulation principle and performance of the ATLAS fast calorimeter simulation FastCaloSim. *ATL-PHYS-PUB-2010-013*, **013**, (2010).

[73] P. Bernat. Architecture and Performance of the Inner Detector Trigger of the ATLAS detector. In *Comput. High Energy Nucl. Phys.*, page 032, (2012).

[74] ATLAS Collaboration. Topological cell clustering in the ATLAS calorimeters and its performance in LHC Run 1. *CERN-PH-EP*, **304**, (2015).

[75] P. Calafiura, W. Lavrijsen, C. Leggett, M. Marino, and D. Quarrie. The Athena control framework in production, new developments and lessons learned. In *Conf. Comput. High-Energy Nucl. Phys.*, pages 456–458, (2005).

[76] G. Barrand, I. Belyaev, P. Binko, et al. GAUDI - A Software Architecture and Framework for building HEP Data Processing Applications. *Comput. Phys. Commun.*, **140**:45–55, (2001).

[77] ATLAS Collaboration. Measurement of the muon reconstruction performance of the ATLAS detector using 2011 and 2012 LHC proton-proton collision data. *Eur.Phys.J. C*, **74**:3130, (2014).

[78] ATLAS Collaboration. Observation of the B_d^0 and B_s^0 mesons in the decays $B_d^0 \to J/\psi K^0$ and $B_s^0 \to J/\psi\phi$ in ATLAS. *ATLAS-CONF-2011-050*, (2011).

[79] ATLAS Collaboration. Study of the rare decays of B_s^0 and B^0 into muon pairs from data collected during the LHC Run 1 with the ATLAS detector. *CERN-EP-2016-064*, (2016).

[80] ATLAS Collaboration. Determination of the ratio of b-quark fragmentation fractions f_s/f_d in pp collisions at $\sqrt{s} = 7$ TeV with the ATLAS detector. *Phys. Rev. Lett.*, **115**:262001, (2015).

[81] LHCb Collaboration. Study of the kinematic dependences of Λ_b^0 production in pp collisions and a measurement of the $\Lambda_b^0 \to \Lambda_c^+\pi^-$ branching fraction. *J. High Energy Phys.*, **08**:143, (2014).

[82] CDF Collaboration. Measurement of Ratios of Fragmentation Fractions for Bottom Hadrons in $p\overline{p}$ Collisions at $\sqrt{s}$=1.96 TeV. *Phys. Rev. D*, **77**:072003, (2008).

[83] M. Jacob and G. Wick. On the general theory of collisions for particles with spin. *Ann. Phys. (N. Y).*, **7**(4):404–428, (1959).

[84] A. Ali, E. Lunghi, C. Greub, and G. Hiller. Improved Model-Independent Analysis of Semileptonic and Radiative Rare B Decays. *Phys. Rev. D*, **66**:034002, (2001).

[85] LHCb Collaboration. Differential branching fraction and angular analysis of $\Lambda_b^0 \to \Lambda\mu^+\mu^-$ decays. *J. High Energy Phys.*, **1506**:115, (2015).

[86] W. Detmold, C. J. D. Lin, S. Meinel, and M. Wingate. $\Lambda_b \to \Lambda l^+ l^-$ form factors and differential branching fraction from lattice QCD. *Phys. Rev. D*, **87**:074502, (2012).

[87] A. Usanova. Statistical errors in $B_d^0 \to K^0 \mu^+ \mu^-$ analysis for the Run II. *ATL-COM-PHYS-2014-032*.

[88] CMS Collaboration. Angular analysis and branching fraction measurement of the decay $B^0 \to K^{*0} \mu^+ \mu^-$. *Phys. Lett. B*, **727**:77, (2013).

[89] G. Punzi. Comments on Likelihood fits with variable resolution. In *Stat. Probl. Part. physics, Astrophys. Cosmol.*, pages 235–237, (2003).

[90] B. Aubert, M. Bona, Y. Karyotakis, et al. Angular distributions in the decay $B \to K^* l^+ l^-$. *Phys. Rev. D*, **79**(3):031102, (2009).

[91] D. Straub, R. Zwicky, and A. Bharucha. $B \to V \ell^+ \ell^-$ in the Standard Mode from Light-Cone Sum Rules. *J. High Energy Phys.*, **1608**:098, (2016).

[92] M. Capeans, G. Darbo, K. Einsweiller, et al. ATLAS Insertable B-Layer Technical Design Report. Technical report, (2010).